LiFi Transceiver Designs for 6G Wireless Networks

Mohamed Amine Arfaoui

A Thesis

in

The Department

of

Information and Systems Engineering

Presented in Partial Fulfillment of the Requirements For the Degree of
Doctor of Philosophy (Information Systems Engineering)
at
Gina Cody School of Engineering and Computer Science
Concordia University
Montréal, Québec, Canada

August 2022

CONCORDIA UNIVERSITY
SCHOOL OF GRADUATE STUDIES

This is to certify that the thesis prepared

By: **Mohamed Amine Arfaoui**

Entitled: **LiFi Transceiver Designs for 6G Wireless Networks**

and submitted in partial fulfillment of the requirements for the degree of

Doctor of Philosophy (Information and Systems Engineering)

complies with the regulations of the University and meets the accepted standards with respect to originality and quality.

Signed by the final examining committee:

_____ Chair
Dr. Ahmed Soliman

_____ External Examiner
Dr. Murat Uysal

_____ External to Program
Dr. Reza Soleymani

_____ Examiner
Dr. Abdessamad Ben Hamza

_____ Examiner
Dr. Nizar Bouguila

_____ Supervisor
Dr. Chadi Assi

_____ Co-Supervisor
Dr. Ali Ghrayeb

Approved by _____

Dr. Abdessamad Ben Hamza, Chair

Department of Information and Systems Engineering

13/07/2022 _____

Dr. Mourad Debbabi, Dean

Gina Cody School of Engineering and Computer Science

Abstract

LiFi Transceiver Designs for 6G Wireless Networks

Mohamed Amine Arfaoui, Ph.D.

Concordia University, 2022

Due to the dramatic increase in high data rate services, and in order to meet the demands of the sixth-generation (6G) wireless networks, researchers from both academia and industry have been exploring advanced transmission techniques, new network architectures and new frequency bands, such as the millimeter wave (mmWave), the infrared, and the visible light bands. Light-fidelity (LiFi) particularly is an emerging, novel, bidirectional, high-speed and fully networked optical wireless communication (OWC) technology that has been introduced as a promising solution for 6G networks, especially for indoor connectivity, owing to the large unexploited spectrum that translates to significantly high data rates.

Although there has been a big leap in the maturity of the LiFi technology, there is still a considerable gap between the available LiFi technology and the required demands of 6G networks. Motivated by this, this dissertation aims to bridge between the current research literature of LiFi and the expected demands of 6G networks. Specifically, the key goal of this dissertation is to fill some shortcomings in the LiFi technology, such as channel modeling, transceiver designs, channel state information (CSI) acquisition, localization, quality-of-service (QoS), and performance optimization. Our work is devoted to address and solve some of these limitations. Towards achieving this goal, this dissertation makes significant contributions to several areas of LiFi. First, it develops novel and measurements-based channel models for LiFi systems that are required for performance analysis and handover management. Second, it proposes a novel design for LiFi devices that is capable of alleviating the real behaviour of users and the impurities of indoor propagation environments. Third, it proposes intelligent, accurate and fast joint position and orientation techniques for LiFi devices, which improve the CSI estimation process and boost the indoor location-based and navigation-based services. Then, it proposes novel proactive optimization technique that can provide near-optimal and real-time service for indoor mobile LiFi users that are running some services with high data rates, such as

extended reality, video conferencing, and real-time video monitoring. Finally, it proposes advanced multiple access techniques that are capable of cancelling the effects of interference in indoor multi-user settings. The studied problems are tackled using various tools from probability and statistic theory, system design and integration theory, optimization theory, and deep learning. The Results demonstrate the effectiveness of the proposed designs, solutions, and techniques. Nevertheless, the findings in this dissertation highlight key guidelines for the effective design of LiFi while considering their unique propagation features.

Acknowledgments

First and foremost, all my gratitude goes to God the Almighty, Alhamdulillah. It is my utmost belief in Him and His boundless blessings that allowed me to finish this dissertation.

During my Ph.D. journey, I have been very fortunate to have met many great individuals. I would like to thank my supervisors, Dr. Chadi Assi and Dr. Ali Ghrayeb, for their guidance during the course of my research and for being my role models as great engineers, professors, and researchers. Through numerous discussions and meetings, I learned so much from them and I greatly appreciate all the advice and wisdom. I would also like to express my appreciation to our collaborators, Dr. Mohammad Dehghani Soltani and Dr. Majid Safari from University of Edinburgh, and Dr. Iman Tavakkolnia and Dr. Harald Haas from LiFi Research and Development Center in University of Strathclyde, for their support and mentorship during the course of this thesis. Their knowledge and work ethics have always inspired me. My gratitude also goes to my colleagues within our research lab in Concordia University, for their collaborations and friendship, wishing them the best of luck in their future endeavors. I wish to express my appreciation to every reviewer and editor for their valuable comments and suggestions towards my publications. I would like also to thank the members of my Ph.D. advisory committee for their valuable comments which have helped me to substantially improve the quality of this dissertation. I would finally like to express my deepest gratitude to my parents, my sisters, and my friends, to whom this work is dedicated. Without their unconditional support, kind words, and sound advice, I would not be the person I am today.

"To him that will, ways are not wanting."

- George Herbert, *Jacula Prudentum*, 1640 -

Contents

List of Figures

List of Tables

List of Abbreviations

3GPP	3rd Generation Partnership Project
5G	Fifth generation
6G	Sixth generation
ANN	Artificial neural network
AP	Access point
ASM	Adaptive SM
AWGN	Additive white Gaussian noise
BER	Bit error rate
C-NOMA	Cooperative non orthogonal multiple access
CCP	Convex-concave procedure
CDF	Cumulative distribution function
CNN	Convolution neural network
CoMP	Coordinated multipoint
CPU	Central processing unit
CSI	Channel state information
D2D	Device-to-device
DD	Direct detection
DL	Deep learning
FDMA	Frequency division multiple access
FOV	Field of view
ICI	Inter cell interference
IM	Intensity modulation
IoT	Internet of things
IUI	Inter-user interference
JT	Joint transmission

KSD	Kolmogorov-Smirnov distance
KNN	K-nearest neighbours
LED	Light emitting diode
LD	Laser diode
LiFi	Light fidelity
LOS	line of sight
LSTM	Long short term memory
MAE	Mean absolute error
ML	Machine learning
MLP	Mulitple layer perceptron
mmWave	Millimeter wave
MB	Modified Beta
MDR	Multi-directional receiver
MIMO	Multiple input multiple output
MRC	Maximum ratio combining
MSE	Mean square error
MTL	Modified truncated Laplace
MUI	Multi-user interference
NLOS	Non line of sight
NOMA	Non orthogonal multiple access
OMA	orthogonal multiple access
OOK	On-off keying
ORWP	Orientation-based random waypoint
OWC	Optical wireless communication
PAM	Pulse amplitude modulation
PD	Photo-diode
PDF	Probability density function
PO	Proactive optimization
QoS	Quality of Service
IR	Infrared
ReLU	Rectified Linear Unit
RF	Radio frequency

RNN	Recurrent neural network
RSMA	Rate splitting multiple access
RSS	Received signal strength
RWP	Random waypoint
SC	Superposition coding
SDMA	Space division multiple access
SGD	Stochastic gradient descent
SIC	Successive interference cancellation
SINR	signal to interference plus noise ratio
SM	Spatial modulation
SMB	Sum of modified Beta
SMTG	Sum of modified truncated Gaussian
SNR	Signal to noise ratio
SR	Screen receiver
tanh	Hyperbolic tangent
TDMA	time division multiple access
THz	Terahertz
UC	User clustering
UE	User equipement
VL	Visible light
ZF	Zero-forcing

List of Common Symbols

L_r Length of the indoor environment

W_r Width of the indoor environment

H_r Height of the indoor environment

N_t Number of transmit elements

N_r Number of receiving elements

I_DC DC bias

M Order of the pulse amplitude modulation

P_elec Transmit electrical power

P_opt Transmit optical power

d Distance

ϕ Angle of radiance

$\Phi_{1/2}$ Half-power semiangle

ψ Angle of incidence

Ψ Field of view

ϕ Angle of radiance

A_PD Area of the photo-diode

m Lambertian order

n_c Refractive index

T Transimpedance amplifier gain

R_p Photo-diode's responsivity

η electro-optical conversion factor

K Number of users

h Downlink channel gain

$\mathbf{H}$ Downlink channel matrix

g uplink channel gain

$\mathbf{G}$	uplink channel matrix
g^{D2D}	Device to device channel gain
$\mathbf{u}$	Vector of messages
$\mathbf{n}$	AWGN noise
$\mathbf{y}$	Downlink received signals
$\mathbf{z}$	Uplink received signals
$\mathbf{V}$	Precoding matrix
γ_{TX}	Transmit signal to noise ratio
γ_{RX}	Received signal to noise ratio
$\mathbf{r}$	Received signal to noise ratio at the access points
$\mathbf{s}$	Real valued transmitted signal
$\mathbf{x}$	Positive valued transmitted signal
B_{VL}	Visible light bandwidth
N_{VL}	Noise power spectral density in the Visible light bandwidth
B_{IR}	Infrared bandwidth
N_{IR}	Noise power spectral density in the infrared bandwidth
B_{RF}	Radio frequency bandwidth
N_{RF}	Noise power spectral density in the radio frequency bandwidth
h_{u}	Height of user
h_{a}	Height of access points
N	Prior time slot index
L	Posterior time slot index
Q_{d}	Size of the data set

Chapter 1

Introduction

1.1 The Road Toward 6G

As the fifth generation (5G) of wireless networks is currently under deployment, researchers from both academia and industry started shaping their vision on how the upcoming sixth generation (6G) would be [1]. The main goals of 6G networks are not only to fill the gap of the original and unfulfilled promises of 5G or to keep up with the continuous emergence of the Internet-of-Things (IoT) networks but also to be able to handle the exponential increase of both the number of devices connected to the Internet and the total data traffic [2]. In this regard, unlike previous generations of cellular networks, 6G networks are expected to seamlessly and ubiquitously connect everything and support very high data rates and diverse requirements on reliability and latency. They are also expected to support a myriad of services across different industries such as augmented or extended reality, autonomous driving, industrial automation, and remote healthcare, among others. In this regard, 6G networks would meet unprecedented demands for high quality wireless services. In other words, 6G networks must urgently provide high data rates, seamless connectivity, ubiquitous coverage, and ultra-low latency communications in order to reach the preset targets [2]. With the goal of meeting these high requirements, researchers from both industry and academia have been trying to explore new network architectures, such as ultra dense networks [3], novel transceiver designs, such as massive multiple-input-multiple-output (MIMO) [4], cell-free (CF) massive MIMO [5], reconfigurable intelligent surface (RIS) [6, 7], and holographic MIMO surface (HMIMOS) [8], advanced transmission techniques, such as non-orthogonal-multiple-access (NOMA) [9], and rate splitting multiple access (RSMA) [10], and high frequency bands, such as the

millimeter wave (mmWave) band [11], the terahertz (THz) [12] band, and the optical band, which includes the infrared (IR) and the visible light (VL) bands [13–15].

1.2 Light Fidelity (LiFi)

Light-fidelity (LiFi) is a novel bidirectional, high speed and fully networked optical wireless communication (OWC) technology, that uses the VL as the propagation medium in the downlink for the purposes of illumination and wireless communication [16]. It also uses IR light in the uplink so that the illumination constraint remains unaffected, especially in indoor environments, and also to avoid interference with the VL in the downlink [16]. LiFi offers a number of important benefits that have made it favorable for 6G networks [17]. These benefits include the very large, unregulated bandwidth available in the IR and the VL spectra (more than 2600 times greater than the whole radio-frequency (RF) spectrum), the high energy efficiency [18], the straightforward deployment that uses off-the-shelf light emitting diodes (LEDs) or laser diodes (LDs) at the transmitter side and photodiodes (PDs) at the receiver end, respectively, and the enhanced security as light does not penetrate through walls and opaque objects [19].

1.3 Potential Applications

LiFi has unique advantages to provide safe, secure, low-cost, and high-bandwidth communications. Many distributed applications from indoor to outdoor environments can benefit from LiFi, including broadband access, indoor localization, remote monitoring, control and sensing, vehicular communication, and underwater exploration. As depicted in Figure 1.1, the main potential applications of LiFi technology in different areas are described as follows [20]:

- **Indoor connectivity**: Any light source can be used to provide LiFi hotspots and the same communications and sensor infrastructure can be used to monitor and control both lighting and data communication simultaneously. A secure and very high data rate local area network (LAN) can be deployed where computers, printers, mobile phones, wearables, and other mobile devices are interconnected using LiFi. It can also be used to deal with the high demand of indoor wireless access to Internet

2
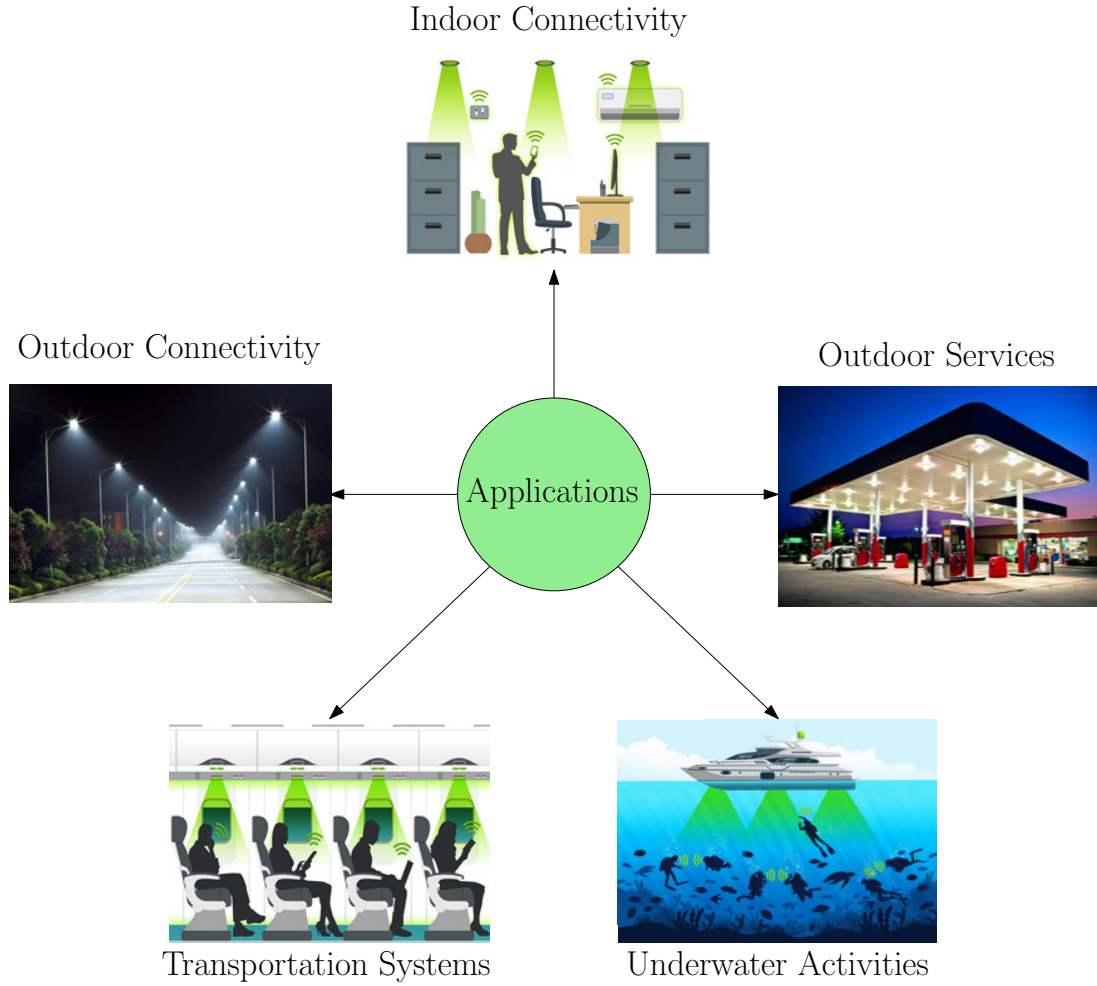
Figure 1.1: Main applications of LiFi technology.

and real-time bandwidth-intensive applications, such as Voice over IP (VoIP), video conference, extended reality (XR), and real-time video monitoring [20].

- **Outdoor connectivity**: Using the light sources that are deployed in the streets, wireless broadband connectivity can be offered for the nearby users. In addition, the street lights infrastructure can be exploited in outdoor localization, navigation, and crowd sensing applications, especially in the case of emergency or social events.

- **Transportation systems**: Through the light sources that are used in head and tail of vehicles, the street lamps, the signage, and the traffic signals, a smart traffic system can be deployed based on LiFi. As such, vehicles can communicate with each other about speed, routes and destinations of themselves to avoid traffic accidents and share traffic information that is unknown in advance for traffic management. Moreover, some infrastructures could share valuable information with passing vehi-

cles to help drivers and ensure road safety [21]. Other promising LiFi application is the use of the traveller lighting in aircrafts to transmit music and video, and exchange data with wired nodes in the aircraft cabin [22, 22, 23].

- **Underwater communication**: LiFi is an excellent alternative for high speed underwater communication compared to RF transmission and acoustic communication, which are expensive and have limited data rates. Several LiFi systems have been proposed for submarine communication, wireless sensor networks, remotely operated vehicles, and diver communication applications [24].

- **Public areas**: Museums, malls and other public areas can be equipped with accurate localization and navigation systems based on LiFi. A mobile indoor positioning system might help, for example, trigger a particular audio or video guide script in a museum, or help shoppers to find discounted items in a store [22, 22, 23]. In addition, it will be possible to provide information and communication in case of civil contingencies.

While LiFi technology bring efficient solutions to many real-life problems, it is not intended to replace RF technologies. Rather, LiFi can be viewed as a complementary technology to RF. There are applications where LiFi is more suitable than RF, whereas there are other applications where the opposite is true. For example, recent advances in wireless communication technologies have shown that mmWave communications, which is an RF technology, is the most efficient for air-to-ground communications [25, 26]. On the other hand, it has been shown through experiments that LiFi is efficient in indoor environments, such as airport halls and aircraft cabins [22, 23]. This suggest that neither technology can be considered as a replacement for the other. In fact, in some cases, one may need to combine both technologies to reap the best performance. It all depends on the underlying environment and application. As such, both technologies should be exploited together to meet the expectations of 6G networks.

1.4 Motivation and State of the Art

Although there has been a big leap in the maturity of the LiFi technology, there is still a considerable gap between the available LiFi technology and the required demands of IoT and 6G networks. In fact, several shortcomings of the current research literature

on LiFi make the current technology still far from satisfying the demands of IoT and 6G networks. Motivated by this, we aim in this thesis to provide transceiver designs for indoor LiFi applications that can alleviate the effects of both the real behaviour of typical users and the environment impurities. More importantly, such designs have to be capable of satisfying the demands of IoT and 6G networks, in terms of high data rates, ultra reliability, low latency, robust security and accurate localization.

In the following, we review the state-of-the-art of the current LiFi technology for indoor environments. The starting points of the proposed research are three research aspects related to LiFi technology. These research aspects are based on recent survey papers in the visible light communication (VLC) and LiFi literature, which are detailed in the following parts.

1.4.1 Channel Models

1.4.1.1 Overview

The survey paper [27] considers OWC channel scenarios and their utilization trade-off in terms of optical carrier, range, mobility, and power efficiency. Furthermore, it investigates the main optical channel characteristics that affect the OWC link performance. Moreover, this paper presents a comprehensive overview of the most important OWC channel measurement campaigns and channel models, primarily for wireless infrared communications and visible light communications. OWCs channel models are further compared in terms of computation speed, complexity, and accuracy. This survey considers indoor, outdoor, underground, and underwater communication environments.

1.4.1.2 Limitations and Gaps

From the comprehensive survey provided in [27], one of the key shortcomings of the current research literature on LiFi is the lack of appropriate statistical channel models for transceiver design, performance analysis and handover management purposes. In fact, the majority of the works reported in the literature of LiFi systems assume idealistic channel models that do not encompass the real behaviour of users. Precisely, the majority of studies assume that LiFi devices are always stationary and face the LiFi access points (APs). However, in real life scenarios, LiFi users may have a random motion and may hold their devices in a way that feels most comfortable. Nevertheless, unlike conventional

RF wireless systems, the LiFi channel is not isotropic, meaning that the device orientation affects the channel gain, and consequently the performance, significantly [28]. Such random behaviour along with the environment impurities, such as link blockage (light path blockage by opaque objects), can affect the desired performance remarkably and it should be analyzed carefully.

1.4.2 Position and Orientation Estimation

1.4.2.1 Overview

As Global Positioning System (GPS) cannot provide satisfying performance in indoor environments, indoor positioning technology, which utilizes indoor wireless signals instead of GPS signals, has grown rapidly recently. Meanwhile, using light devices, such as LEDs and LDs, the LiFi technology has been deemed to be a promising candidate for indoor positioning. The survey paper [29] provides a comprehensive study of a novel positioning technology based on white LED lights, which has attracted much attention from both academia and industry in recent years. The essential characteristics and principles of this system are deeply discussed, and relevant positioning algorithms and techniques are classified and elaborated. In addition, this paper undertakes a thorough investigation into current LED-based indoor positioning systems and compares their performance through many aspects, such as test environment, accuracy, and cost.

1.4.2.2 Limitations and Gaps

It is predictable that implementing a novel localization technology based on LiFi systems has a great potential, which has encouraged both academia and industry to step into the field [30]. However, as mentioned previously, the device orientation is a crucial factor in LiFi networks like any system employing high frequency bands (mmWave, THz, etc), which are possible candidates for future indoor communication that can fulfil the demand of 6G networks [28]. This makes the orientation estimation an important factor in maintaining the target high performance of LiFi systems. Hence, reporting the device orientation along with the position can remarkably help in improving user quality-of-service (QoS), resource allocation, and interference management for this kind of networks [28]. Based on the comprehensive survey [29], there are a number of limitations in the current literature. In fact, only the estimate of the position is considered, and hence, the esti-

mate of the UE's orientation remains unresolved. This is mainly due to the fact that the position and orientation estimation metrics of LiFi systems are non-linear functions with respect to the user's position and orientation [28], which leads to non-convex optimization problems with a lot of local optima. Nevertheless, the imperfect estimation of these uncertain parameters will result in a serious performance loss.

1.4.3   Performance Optimization

1.4.3.1   Overview

The survey paper [31] reviews the emerging research in the field of LiFi networks and lay out the challenges and some technological solutions. Specifically, it reviews at first the LiFi channel capacity derivation and discusses the performance metrics and the associated variables. The optimization of LiFi networks is also discussed, including resources and power allocation techniques, users association, coordination techniques, multiple access techniques, interference management, simultaneous energy harvesting and information transmission.

1.4.3.2   Limitations and Gaps

The LiFi propagation medium has been deemed as a randomly behaving entity among the source and the destination due to the mobility and random orientation of LiFi devices as well as the presence of blockages. These three factors combined together deteriorates the received signal quality. As a result, the channel quality fluctuates and the performance of advanced multiple access techniques in LiFi cellular networks is significantly affected. Unfortunately, in the current literature of LiFi technology, there is no effective multiple access techniques that can alleviate the effects of mobility and random orientation of LiFi devices, deal with the blockage issues, and perfectly manage the interference in LiFi cellular networks.

1.5   Thesis Contributions

The focus of this dissertation is to address the limitations of the state of the art of LiFi technology detailed in Section 1.4. In this context, the main contributions of the thesis, which are shown in Figure 1.2, are summarized as follows:
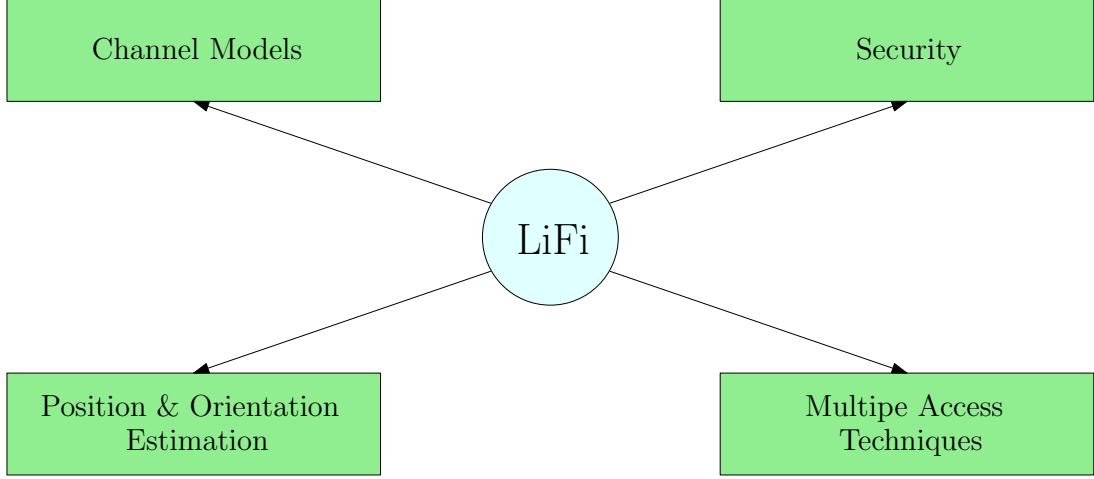
Figure 1.2: Graphical summary of problems addressed in the Thesis.

1. **Physical Layer Security**: One of the aspects that are missing from the LiFi literature is the security issues that face this technology. Hence, we have conducted a comprehensive and comparative study that covers almost all aspects of physical layer security (PLS) for LiFi systems, including different channel models, input distributions, network configurations, precoding/signaling strategies, secrecy capacity, and information rates, in a way that completely defines the overall state-of-the-art of the LiFi technology. This study is published in [32].

2. **Channel Models**: In Chapter 3, we have developed novel, realistic and measurement-based channel models for indoor LiFi systems. Precisely, the statistics of the channel gain are derived for the case of stationary and mobile users with random device orientation. For stationary users, two channel models are proposed as well, namely, the modified truncated Laplace (MTL) model and the modified Beta (MB) model. For mobile users, two channel models are proposed, namely, the sum of modified truncated Gaussian (SMTG) model and the sum of modified Beta (SMB) model. Based on the derived models, the impact of random orientation and spatial distribution of users is investigated, where we show that the aforementioned factors can strongly affect the channel gain and the system performance. Our findings for this aim were published in [33] and [34].

3. **Multi-Directional Receiver Design**: Aiming to alleviate the effects of mobility, random device orientation, and blockage, we have proposed in Chapter 4 a novel multi-directional receiver (MDR) structure, in which the PDs are located on differ-

ent sides of the user's device, e.g., a smartphone. This configuration is motivated by the fact that conventional structures exhibit poor performance in the presence of random device orientation and blockage. We tested the performance of the proposed design in an indoor environment using measurement-based channel models. In addition, we have adopted spatial modulation (SM) as a modulation scheme and we showed that MDR outperforms the benchmark structure by over 10 dB at bit-error ratio (BER) of 3.8×10^{-3}. Moreover, an adaptive access point (AP) selection scheme for SM is considered where the number of APs are chosen adaptively in an effort to achieve the lowest energy requirement for a target BER and spectral efficiency. The user performance with random orientation and blockage in the entire indoor environment is evaluated for sitting and walking activities, for which the orientation-based random waypoint (ORWP) mobility model is invoked. We further demonstrated that the proposed adaptive technique with SM outperforms the conventional spatial multiplexing system. Our findings for this aim were published in [35] and [36].

4. **Position and Orientation Estimation**: In Chapter 5, the joint estimation of user's 3D position and orientation in indoor LiFi systems with unknown emission power is investigated. Existing solutions for this problem assume either ideal LiFi system settings or perfect knowledge of the user states, rendering them unsuitable for realistic LiFi systems. In addition, these solutions consider the non-line-of-sight (NLOS) links of the LiFi channel gain as a source of deterioration for the estimation performance instead of harnessing these components in improving the position and the orientation estimation performance. This is mainly due to the lack of appropriate estimation techniques that can extract the position and orientation information hidden in these components. Against the above limitations, we have adopted fingerprinting as an estimation technique and the received signal-to-noise ratio (SNR) as an estimation metric, where all components of the LiFi channel are considered. Motivated by the success of deep learning (DL) techniques in solving several complex estimation and prediction problems, we have employed two deep artificial neural network (ANN) models that can map efficiently the instantaneous received SNR with the user 3D position and the UE orientation. The first model is based on the multilayer perceptron (MLP) and the second model is based on the

convolutional neural network (CNN). Through numerous examples, we have investigated the performance of the proposed models in terms of the average estimation error, precision, computational time, and the BER. We have also compared this performance to that of the k-nearest neighbours (KNN) technique, which is widely used in solving wireless localization problems. It is demonstrated that the proposed models achieve significant gains and are superior to the KNN scheme. Our findings for this aim were published in [37].

5. **Proactive Optimization**: In Chapter 6, we have investigated the channel aging problem of LiFi systems. In the LiFi physical layer, the majority of the optimization problems for mobile users are non-convex and require the use of dual decomposition or heuristics techniques. Such techniques are based on iterative algorithms, and often, cause a high processing time at the physical layer. Hence, the obtained solutions are no longer optimal since the LiFi channels are evolving. Alternatively, a proactive optimization approach that can alleviate the LiFi channel aging problem is proposed. The core idea is designing a long-short-term-memory (LSTM) network that is capable of predicting posterior positions and orientations of mobile users, which can be then used to predict their posterior channel coefficients. Consequently, the obtained channel coefficients can be exploited for deriving near-optimal transmission schemes prior to the intended service time, which enables real time service. Through various simulations, the performance of the designed LSTM model is evaluated in terms of the prediction accuracy and time. Finally, the performance of the proposed approach is investigated in the sum rate maximization problem of multi-user LiFi systems with QoS constraints, where a performance gap of less than 7% is achieved, while maintaining a real time service. Our findings for this aim were published in [38] and submitted for possible publication in [39].

6. **Next Generation Multiple Access Techniques**: In Chapter 7, we have investigated the dynamic power allocation for a LiFi cellular system consisting of two coordinating attocells, each equipped with one AP. The coordinated multipoint (CoMP) between the two cells is introduced to assist users experiencing high inter-cell-interference (ICI). Specifically, the coordinated zero-forcing (ZF) precoding is used to cancel the ICI at the users located near the centers of the cells, whereas the joint transmission (JT) is employed to eliminate the ICI at the users located at the

edge of both cells and to improve their receptions as well. Furthermore, two multiple access techniques are invoked within each cell, namely, NOMA and cooperative NOMA (C-NOMA). Hence, two multiple access techniques are proposed for the considered multi-user multi-cell system, namely, the CoMP-assisted NOMA scheme and the CoMP-assisted C-NOMA scheme. For each scheme, two power allocation frameworks are formulated each as an optimization problem, where the objective of the former is maximizing the network sum data rate while guaranteeing a certain QoS for each user, whereas the goal of the latter is to maximize the minimum data rate among all coexisting users. The formulated optimization problems are not convex, and hence, difficult to be solved directly unless using some heuristic methods, which comes at the expense of high computational complexity. To overcome this issue, optimal and low complexity power allocation schemes are derived. In the simulation results, the performance of the proposed CoMP-assisted NOMA and CoMP-assisted C-NOMA schemes are compared with those of the CoMP-assisted orthogonal-multiple-access (OMA) scheme, the C-NOMA scheme, and the NOMA scheme, where the superiority of the proposed schemes are demonstrated. Finally, the performance of the proposed schemes and the considered baselines is evaluated while varying various system parameters. Our findings for this aim were published in [40].

1.6   Thesis Organization

The rest of the thesis is organized as follows. Chapter 2 provides a comprehensive introduction to LiFi technology, including the communication model, the propagation model, and the orientation model of LiFi devices. In Chapter 3, the proposed measurements-based LiFi channel models are presented. Chapter 4 presents the proposed MDR design for LiFi devices. In Chapter 5, the proposed joint 3D position and orientation estimation techniques for indoor LiFi users are presented. Chapter 6 presents the proposed proactive optimization technique for LiFi systems. In Chapter 7, the proposed advanced multiple access technique are presented. Chapter 8 provides a summary of the thesis along with some future research directions.

1.7 List of Publications

This dissertation has led to the key publications enumerated in Section 1.7.1. Moreover, during the doctorate studies, and in collaboration with our colleagues within our research lab in Gina Cody School of Engineering and Computer Science in Concordia University, we were able to publish an outstanding number of scientific articles related to various topics of next generations wireless networks. These publications are enumerated in Section 1.7.2 and focus mainly on RF cellular networks, NOMA, cooperative communication, device to device (D2D) communication, CoMP, RIS, traffic multiplexing of 6G services, IoT networks, IoT and time-sensitive applications, and vehicular networks. Overall, through our doctorate studies, we were able to produce and publish **33** research papers (**24** journal papers and **9** conference papers) in the top venues of the IEEE Communication Society (ComSoc) and the IEEE vehicular technology society (VTS).

1.7.1 Publications Related to the Dissertation

Journal Papers

[**J1**] **M. A. Arfaoui**, M. D. Soltani, I. Tavakkolnia, A. Ghrayeb, M. Safari, C. Assi, and H. Haas, "Physical Layer Security for Visible Light Communication Systems: A Survey," IEEE Commun. Surveys & Tutorials, vol. 22, no. 3, pp. 887 – 1908, Apr. 2020.

[**J2**] **M. A. Arfaoui**, M. D. Soltani, I. Tavakkolnia, A. Ghrayeb, C. Assi, M. Safari, and H. Haas, "Measurements-Based Channel Models for Indoor LiFi Systems," IEEE Trans. Wireless Commun., vol. 20, no. 2, pp. 827 – 842, Oct. 2020.

[**J3**] M. D. Soltani, **M. A. Arfaoui**, I. Tavakkolnia, A. Ghrayeb, M. Safari, C. M. Assi, M. O. Hasna, and H. Haas, "Bidirectional Optical Spatial Modulation for Mobile Users: Towards a Practical Design for LiFi Systems," IEEE JSAC SI Spatial Modulation in Emerging Wireless Systems, vol. 37, no. 9, pp. 2069 – 2086, Aug. 2019.

[**J4**] **M. A. Arfaoui**, M. D. Soltani, I. Tavakkolnia, A. Ghrayeb, C. Assi, M. Safari, and H. Haas, "Invoking Deep Learning for Joint Estimation of Indoor LiFi User Position

and Orientation," IEEE Journal on Selected Areas in Communications, vol. 39, no. 9, pp. 2890-2905, Sept. 2021.

[**J5**] **M. A. Arfaoui**, A. Ghrayeb, and C. Assi, "Deep Learning Based Proactive Optimization for Indoor LiFi Systems with Channel Aging," IEEE Trans. on Wireless Commun., Apr. 2021 (first round revision).

[**J6**] **M. A. Arfaoui**, A. Ghrayeb, C. Assi, amd M. Qaraqe "CoMP-Assisted NOMA and Cooperative NOMA in Indoor VLC Cellular Systems," IEEE Trans. Commun., Jul. 2021 (third round revision).

Conference Papers

[**C1**] **M. A. Arfaoui**, M. D. Soltani, I. Tavakkolnia, A. Ghrayeb, C. Assi, H. Haas, and M. Safari, "SNR Statistics of Indoor Mobile VLC Users with Random Device Orientation," in Proc. IEEE ICC, Shanghai, China, May 2019.

[**C2**] I. Tavakkolnia, M. D. Soltani, **M. A. Arfaoui**, A. Ghrayeb, C. Assi, M. Safari, and H. Haas, "MIMO System with Multi-Directional Receiver in Optical Wireless Communications," in Proc. IEEE ICC, Shanghai, China, May. 2019.

[**C3**] **M. A. Arfaoui**, A. Ghrayeb, and C. Assi, "Cascaded Artificial Neural Networks for Proactive Power Allocation in Indoor LiFi Systems," in Proc. IEEE ICC, Montreal, QC, Canada, Jun. 2021.

1.7.2 Publications Not related to the Dissertation

Journal Papers

[**J7**] P. Dinh, **M. A. Arfaoui**, S. Sharafeddine, C. Assi and A. Ghrayeb, "A Low-Complexity Framework for Joint User Pairing and Power Control for Cooperative NOMA in 5G and Beyond Cellular Networks," IEEE Trans. Commun, vol. 68, no. 11, pp. 6737-6749, Nov. 2020.

[**J8**] P. Dinh, **M. A. Arfaoui**, C. Assi and A. Ghrayeb, "Exploiting Antenna Diversity to Enhance Hybrid Cooperative Non-Orthogonal Multiple Access," IEEE Commun. Letters, vol. 24, no. 12, pp. 2936-2940, Dec. 2020.

[J9] M. Elhattab, **M. A. Arfaoui** and C. Assi, "A Joint CoMP C-NOMA for Enhanced Cellular System Performance," IEEE Commun. Letters, vol. 24, no. 9, pp. 1919-1923, Sept. 2020.

[J10] M. Elhattab, **M. A. Arfaoui** and C. Assi, "CoMP Transmission in Downlink NOMA-Based Heterogeneous Cloud Radio Access Networks," IEEE Trans. Commun., vol. 68, no. 12, pp. 7779-7794, Dec. 2020.

[J11] M. Elhattab, **M. A. Arfaoui**, C. Assi and A. Ghrayeb, "Reconfigurable Intelligent Surface Assisted Coordinated Multipoint in Downlink NOMA Networks," IEEE Commun. Letters, vol. 25, no. 2, pp. 632-636, Feb. 2021.

[J12] M. Elhattab, **M. A. Arfaoui** and C. Assi, "Power Allocation in CoMP-Empowered C-NOMA Networks," IEEE Networking Letters, vol. 3, no. 1, pp. 10-14, March 2021.

[J13] M. Elhattab, **M. A. Arfaoui**, C. Assi and A. Ghrayeb, "Reconfigurable Intelligent Surface Enabled Full-Duplex/Half-Duplex Cooperative Non-Orthogonal Multiple Access," IEEE Trans. Wireless Commun., vol. 21, no. 5, pp. 3349-3364, May 2022.

[J14] M. Elhattab, **M. A. Arfaoui**, C. Assi and A. Ghrayeb, "RIS-Assisted Joint Transmission in a Two-Cell Downlink NOMA Cellular System," IEEE JSAC, vol. 40, no. 4, pp. 1270-1286, April 2022.

[J15] M. Elhattab, **M. A. Arfaoui** and C. Assi, "Joint Clustering and Power Allocation in Coordinated Multipoint Assisted C-NOMA Cellular Networks," IEEE Trans. Commun., vol. 70, no. 5, pp. 3483-3498, May 2022.

[J16] M. Elhattab, **M. A. Arfaoui**, C. Assi and A. Ghrayeb, M Qaraqe, "On Optimizing the Power Allocation and the Decoding Order in Uplink Cooperative NOMA," in IEEE Commun. Letters, Apr. 2022 (first round revision).

[J17] M. Almekhlafi, M. Chraiti, **M. A. Arfaoui**, C. Assi, A. Ghrayeb and A. Alloum, "A Downlink Puncturing Scheme for Simultaneous Transmission of URLLC and eMBB Traffic by Exploiting Data Similarity," IEEE Trans. Vehicular Tech., vol. 70, no. 12, pp. 13087-13100, Dec. 2021.

[**J18**] M. Almekhlafi, **M. A. Arfaoui**, C. Assi and A. Ghrayeb, "Superposition-Based URLLC Traffic Scheduling in 5G and Beyond Wireless Networks," IEEE Trans. Commun., Jul. 2021 (third round revision).

[**J19**] M. Almekhlafi, **M. A. Arfaoui**, M. Elhattab, C. Assi and A. Ghrayeb, "Joint Resource Allocation and Phase Shift Optimization for RIS-Aided eMBB/URLLC Traffic Multiplexing," IEEE Trans. Commun, vol. 70, no. 2, pp. 1304-1319, Feb. 2022.

[**J20**] M. Almekhlafi, **M. A. Arfaoui**, C. Assi and A. Ghrayeb, "Enabling URLLC Applications Through Reconfigurable Intelligent Surfaces: Challenges and Potential," IEEE Internet of Things Magazine, vol. 5, no. 1, pp. 130-135, March 2022.

[**J21**] M. Almekhlafi, **M. A. Arfaoui**, C. Assi and A. Ghrayeb, "A Low Complexity Passive Beamforming Design for Reconfigurable Intelligent Surface (RIS) in 6G Networks," IEEE Trans. Vehicular Tech., Feb. 2022 (second round revision).

[**J22**] A. Muhammad, M. Elhattab, **M. A. Arfaoui**, C. Assi, "Optimizing Information Freshness in RIS-assisted NOMA-based IoT Networks," IEEE Trans. Vehicular Tech, Jan. 2022 (second round revision).

[**J23**] A. Muhammad, M. Elhattab, **M. A. Arfaoui**, C. Assi, "RIS-Empowered Uplink Cooperative NOMA For Real-Time Applications", IEEE Commun. Letters, Mar. 2022 (second round revision).

[**J24**] A. Muhammad, M. Elhattab, **M. A. Arfaoui**, A. Al-Hilo, C. Assi, "Age of Information Optimization in RIS-Assisted Wireless Networks," IEEE Trans. on Network and Service Management, Jun 2022 (first round revision).

Conference Papers

[**C4**] P. Dinh, **M. A. Arfaoui**, S. Sharafeddine, C. Assi and A. Ghrayeb, "Joint User Pairing and Power Control for C-NOMA with Full-Duplex Device-to-Device Relaying," in Proc. IEEE GLOBECOM, Dec. 2019, Waikoloa, HI, USA.

[**C5**] P. Dinh, **M. A. Arfaoui**, S. Sharafeddine, C. Assi and A. Ghrayeb, "A Low-Complexity Approach for Sum-Rate Maximization in Cooperative NOMA Enhanced Cellular Networks," in Proc IEEE ICC, Jun. 2020, Dublin, Ireland.

[**C6**] M. Almekhlafi, **M. A. Arfaoui**, M. Elhattab, C. Assi and A. Ghrayeb, "Joint Scheduling of eMBB and URLLC Services in RIS-Aided Downlink Cellular Networks," in Proc. IEEE ICCCN, Athens, Greece, Aug. 2021,

[**C7**] M. Almekhlafi, **M. A. Arfaoui**, C. Assi and, A. Ghrayeb, "Joint resource and power allocation for URLLC-eMBB traffics multiplexing in 6G Wireless networks," in Proc. IEEE ICC, Montreal, QC, Canada, Jun. 2021.

[**C8**] I. Sorkhoh, **M. A. Arfaoui**, M. Khabbaz, C. Assi, " Optimizing Information Freshness in RIS-Assisted Cooperative Autonomous Driving," in Proc. IEEE ICC, Seoul, South Korea, May 2022.

[**C9**] A. Muhammad, M. Elhattab, **M. A. Arfaoui**, C. Assi, "Optimizing Information Freshness Leveraging Multi-RISs in NOMA-based IoT Networks, in Proc. IEEE GLOBECOM, Rio De Janeiro, Brazil, Dec. 2022.

Chapter 2

Background

In this section, we build the theoretical background for the LiFi technology. In Sections 2.1 and 2.2, the communication model and the propagation model of LiFi systems are presented, respectively, whereas in Section 2.3, the orientation model of LiFi devices is detailed, with emphasis on mobile devices, such as smartphones.

2.1 Communication Model
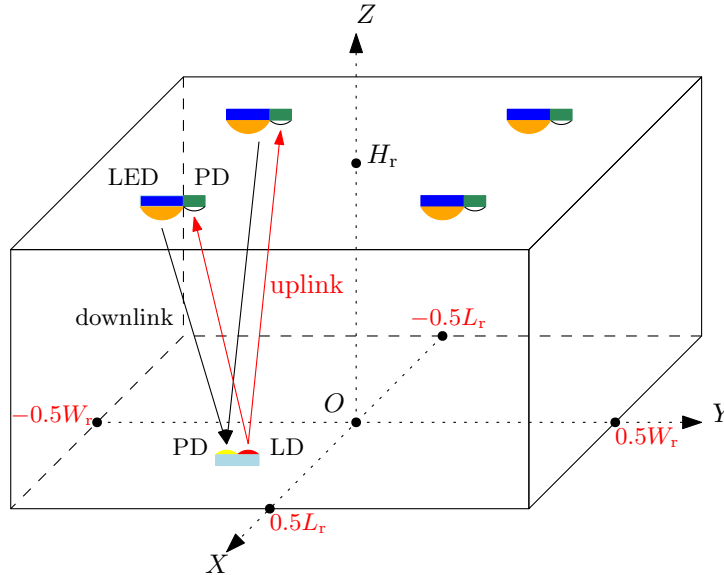
Figure 2.1: A typical indoor LiFi system.

Consider the indoor LiFi system shown in Figure 2.1, which consists of a room with size $L_r \times W_r \times H_r$, where L_r, W_r, and H_r denote the length, the width and the height of the room, respectively. The LiFi system is equipped with a set of APs installed at the ceiling of the room. Each AP is down facing and is equipped with a set of LEDs and
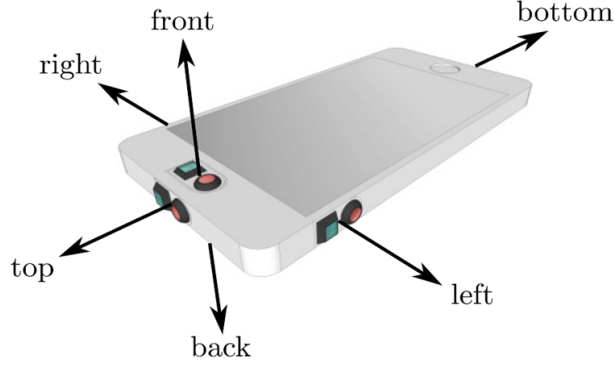
Figure 2.2: A typical LiFi UE equipped with a number of LDs and PDs, where each LD is adjacent to one PD.

PDs adjacent to each other, where the LEDs are used for illumination and downlink data transmission simultaneously and the PDs are used for uplink data reception. On the other hand, we denote a LiFi user by one that is capable of communicating with an indoor LiFi system. Precisely, as shown in Figure 2.2, the user equipment (UE) is equipped with a set of LDs and PDs, and hence, can transmit and receive data signals from the LiFi access point (AP). As shown in Figure 2.1, the communication between the APs and the UE is bidirectional. Specifically, in the downlink, the APs employ the visible light spectrum for transmitting the information and the LiFi UE receives this information through its PDs, whereas in the uplink, the LDs of the UE transmit the information using the IR spectrum and the APs detect the transmitted signals through their associated PDs. In this mechanism, there is no interference between the downlink and the uplink transmissions and the two phases can occur simultaneously.

Let N_t denotes the number of transmit elements of a LiFi transmitter and N_r denotes the number of receiving elements of a LiFi receiver. Accordingly, for the case of downlink transmission, N_t is the number of APs and N_r is the number of PDs of the UEs, whereas for the case of uplink transmission, N_t is the number of LDs of the UEs and N_r is the number of APs. Now, let us focus on the downlink transmission, where the intensity modulation direct detection (IM/DD) is considered. Figure 2.3 presents the main building blocks of a typical LiFi system. At the transmitter side, the information data bits are modulated and then converted into electrical analog signals using a digital-to-analog converter (DAC). The electrical signals are then used to modulate the LED's output light. The transmit elements are the LEDs of the N_t APs that are driven by a fixed bias direct current (DC) $I_{DC} \in \mathbb{R}_+$, which sets the average radiated optical power from the LEDs. The
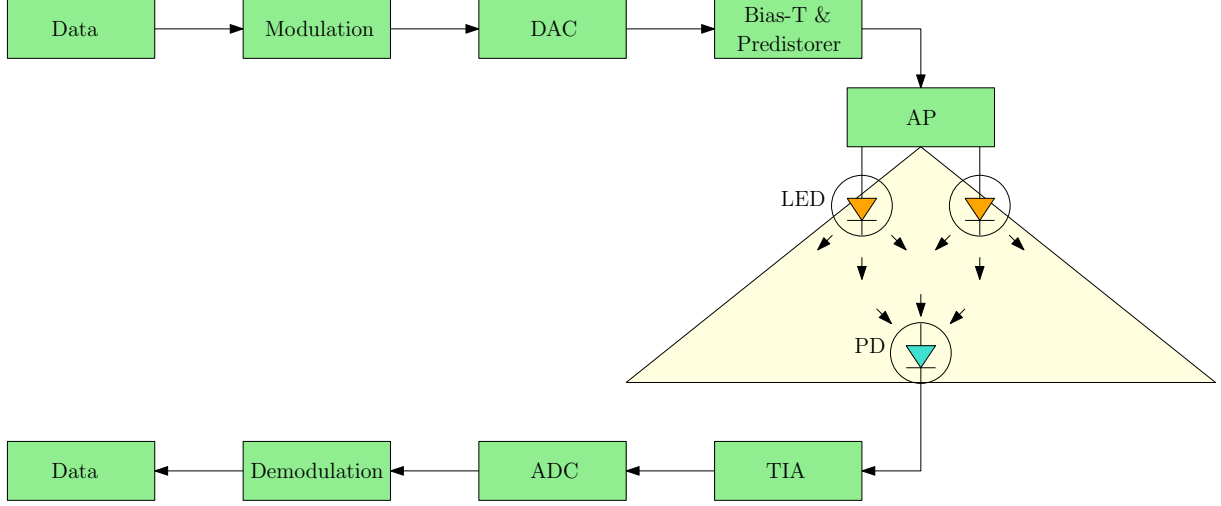
Figure 2.3: A simplified block diagram of a LiFi system.

data signals are grouped into an $N_{\mathrm{t}} \times 1$ zero-mean vector of current signals $\mathbf{s}$, which is then superimposed on I_{DC}, via, e.g., a bias-T circuit, to produce a positive-valued current $\mathbf{x} = \mathbf{s} + I_{\mathrm{DC}}\mathbf{1}_{N_{\mathrm{t}}}$ and to imperceptibly modulate the instantaneous optical power $\mathbf{p}_{\mathrm{t}}$ emitted from the LEDs of the APs. Then, using an appropriate pre-distorter [41], the electro-optical conversion can be modeled as $\mathbf{p}_{\mathrm{t}} = \eta N_{\mathrm{LEDs}}\left(\mathbf{s} + I_{\mathrm{DC}}\mathbf{1}_{N_{\mathrm{t}}}\right)$, where η (W/A) is the current-to-power conversion efficiency of the LEDs and N_{LEDs} is the number of LEDs per AP. Since $\mathbb{E}\left(\mathbf{s}\right) = 0$, the data signals do not contribute to the average optical power. At the receiver side, the optical power collected by the PDs of the UE is given by $\mathbf{p}_{\mathrm{r}} = \mathbf{H}\mathbf{p}_{\mathrm{t}}$, in which $\mathbf{H}$ is the $N_{\mathrm{r}} \times N_{\mathrm{t}}$ downlink channel matrix between the N_{t} LEDs of the APs and the N_{r} PDs of the UE, whose expression is detailed in the following section. Afterwards, the PDs of the UE, each with a responsivity R_{p} (A/W), convert the incident optical power into a proportional current $R_{\mathrm{p}}\mathbf{p}_{\mathrm{r}}$. Then, the DC bias is removed, and the signals are amplified via a transimpedance amplifier (TIA) of gain T (V/A) to produce an $N_{\mathrm{r}} \times 1$ voltage signal vector $\mathbf{y}$, which is a scaled, but noisy, version of the information-bearing signal $\mathbf{s}$.

Based on the above, the resulting downlink signal model is described as

$$\mathbf{y} = \lambda\mathbf{H}\mathbf{s} + \mathbf{n}, \tag{2.1}$$

where $\lambda = TR_{\mathrm{p}}\eta N_{\mathrm{LEDs}}$ and $\mathbf{n} = [n_1, n_2, ..., n_{N_{\mathrm{r}}}]^T$ is the $N_{\mathrm{r}} \times 1$ noise vector at the PDs of the UE, such that for all $i \in [\![1, N_{\mathrm{r}}]\!]$, n_i is the noise experienced at the ith PD of the UE. The noise here includes all possible noises, such as the shot noise and the thermal noise, and is assumed to be real valued additive white Gaussian noise (AWGN) that is

$\mathcal{N}(\mathbf{0}_{N_\mathrm{r}}, \sigma_\mathrm{VL}^2 \mathbf{I}_{N_\mathrm{r}})$ distributed and independent of the transmitted signal [42]. The variance of the noise is equal to $\sigma_\mathrm{VL}^2 = N_\mathrm{VL} B_\mathrm{VL}$, where N_VL is the noise single sided power spectral density and B_VL is the visible light bandwidth available at the APs. Finally, an analog-to-digital converter (ADC) is used to sample the signal $\mathbf{y}$. Following the demodulation of the signal, the information bits are recovered. It is important to mention here that the same communication model applies to the uplink transmission as well, but it is omitted here for brevity.

2.2   Propagation Model

In this section, the objective is to explain the downlink propagation model of indoor LiFi systems. For all $i \in [\![1, N_\mathrm{r}]\!]$ and $j \in [\![1, N_\mathrm{t}]\!]$, $h_{i,j}$ denotes the (i,j)th element of the downlink channel matrix $\mathbf{H}$, which corresponds to the downlink channel gain between the jth AP and the ith PD of the UE. In this context, for all $i \in [\![1, N_\mathrm{r}]\!]$ and $j \in [\![1, N_\mathrm{r}]\!]$, Figure 2.4 presents the link geometry between the jth AP and the ith PD of the UE. Based on this figure, and for all $i \in [\![1, N_\mathrm{r}]\!]$ and $j \in [\![1, N_\mathrm{r}]\!]$, the downlink channel gain of the wireless link between the jth AP and the ith PD of the UE is expressed as

$$h_{i,j} = h_{i,j}^{\mathrm{LOS}} + h_{i,j}^{\mathrm{NLOS}}, \tag{2.2}$$

where $h_{i,j}^{\mathrm{LOS}}$ and $h_{i,j}^{\mathrm{NLOS}}$ denote the line-of-sight (LOS) and the NLOS channel gains of this link, respectively. Both LOS and NLOS components depend on the position of the corresponding AP, as well as the position and the orientation of the corresponding PD of the UE. First, for all $i \in [\![1, N_\mathrm{r}]\!]$ and $j \in [\![1, N_\mathrm{t}]\!]$, the LOS channel gain $h_{i,j}^{\mathrm{LOS}}$ is expressed as [43]

$$h_{i,j}^{\mathrm{LOS}} = \frac{H_0}{d_{i,j}^2} \cos^m(\phi_{i,j}) \mathrm{rect}\left(\frac{\phi_{i,j}}{\Phi}\right) \cos(\psi_{i,j}) \mathrm{rect}\left(\frac{\psi_{i,j}}{\Psi}\right), \tag{2.3}$$

where, as shown in Figure 2.4, $\phi_{i,j}$ is the radiance angle, Φ is the divergence angle of the LEDs of the jth AP, $\psi_{i,j}$ is the incidence angle, Ψ is the field-of-view (FOV) of the ith PD of the UE, and $d_{i,j}$ is the distance between the jth AP and the ith PD of the UE. Moreover, the multiplicative coefficient $H_0 = \frac{(m+1)n_c^2 A_\mathrm{PD}}{2\pi \sin(\Psi)^2}$, in which $m = -1/\log_2(\cos(\Phi_{1/2}))$ is the Lambertian emission order of the LED of the jth AP, such that $\Phi_{1/2}$ is the associated half-power semi-angle of the LEDs, n_c is the refractive index of the PD's optical concentrator, and A_PD is the geometric area of the PD of the UE.

For all $i \in [\![1, N_\mathrm{r}]\!]$, let $\mathbf{n}_i^\mathrm{u}$ and $\mathbf{p}_i^\mathrm{u} = [x_i^\mathrm{u}, y_i^\mathrm{u}, z_i^\mathrm{u}]$ denote the normal vector and the 3D position of the ith PD of the UE in a Cartesian coordinate system (X, Y, Z). In addition,
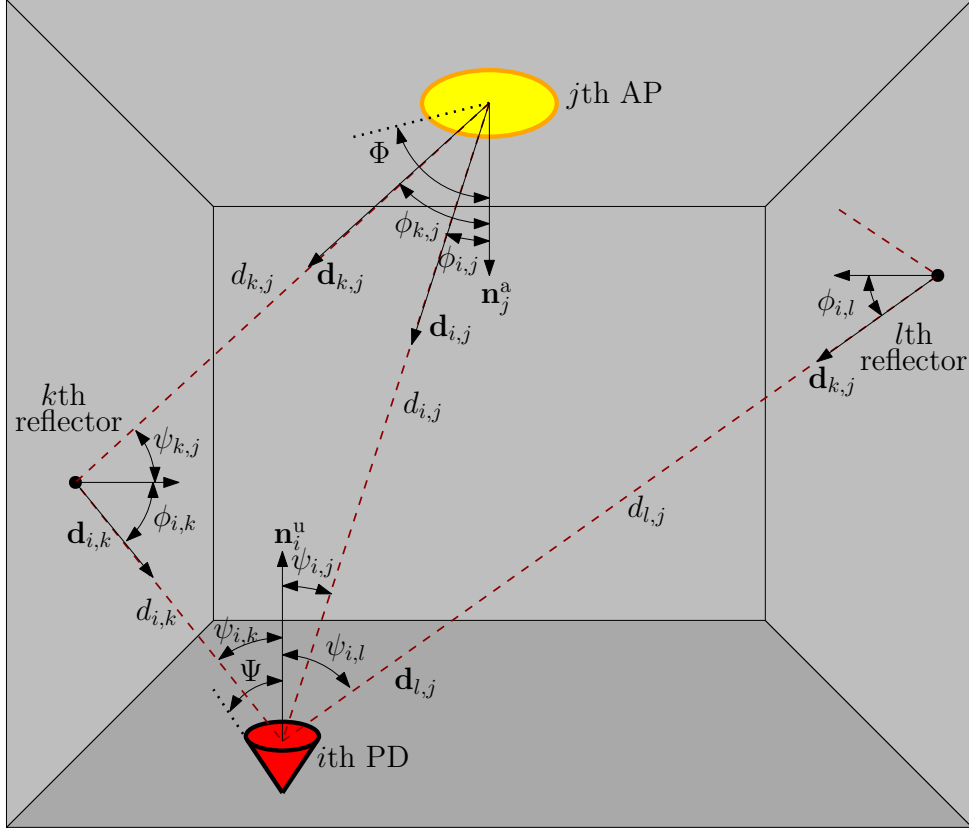
Figure 2.4: The downlink geometry of a point-to-point LiFi link.

for all $j \in [\![1, N_{\mathrm{t}}]\!]$, let $\mathbf{n}_j^{\mathrm{a}}$ and $\mathbf{p}_j^{\mathrm{a}} = \left[x_j^{\mathrm{a}}, y_j^{\mathrm{a}}, z_j^{\mathrm{a}}\right]$ denote the normal vector and the 3D position of the LEDs of the jth AP in the same Cartesian coordinate system. Moreover, for all $i \in [\![1, N_{\mathrm{r}}]\!]$ and $j \in [\![1, N_{\mathrm{t}}]\!]$, and as shown in Figure 2.4, let $\mathbf{d}_{i,j} = \frac{\mathbf{p}_i^{\mathrm{u}} - \mathbf{p}_j^{\mathrm{a}}}{||\mathbf{p}_i^{\mathrm{u}} - \mathbf{p}_j^{\mathrm{a}}||_2}$ denotes the unit vector or the direction vector between the LEDs of the jth AP and the ith PD of the UE. In this case, for all $i \in [\![1, N_{\mathrm{r}}]\!]$ and $j \in [\![1, N_{\mathrm{t}}]\!]$, the cosine of the radiance and the incidence angles in (2.3) are given by $\cos(\phi_{i,j}) = \mathbf{d}_{i,j}^T \mathbf{n}_j^{\mathrm{a}}$ and $\cos(\psi_{i,j}) = -\mathbf{d}_{i,j}^T \mathbf{n}_i^{\mathrm{u}}$, respectively.

Considering the NLOS components of the LiFi channel gain, they can be calculated based on the method described in [44]. Using the frequency domain instead of the time domain analysis, one is able to consider an infinite number of reflections to have an accurate value of the diffuse link. The environment is segmented into a number of surface elements that reflect the light beams. These surface elements are modeled as Lambertian radiators described by (2.3) with $m = 1$, a divergence of 90°, and a FOV of 90°. Assuming that the entire room can be decomposed into ξ surface elements, the NLOS channel gain $h_{i,j}^{\mathrm{NLOS}}$, including an infinite number of reflections between the LEDs of the jth AP and

21

the ith PD of the UE, for all $i \in [\![1, N_{\mathrm{r}}]\!]$ and $j \in [\![1, N_{\mathrm{t}}]\!]$, can be expressed as

$$h_{i,j}^{\mathrm{NLOS}} = \mathbf{r}_{i,j}^{\mathrm{T}} \mathbf{G}_\xi (\mathbf{I}_\xi - \mathbf{E}_\xi \mathbf{G}_\xi)^{-1} \mathbf{t}_{i,j}, \tag{2.4}$$

where the vectors $\mathbf{t}_{i,j}$ and $\mathbf{r}_{i,j}$ respectively represent the LOS link between the LEDs of the jth AP and all the surface elements of the room and from all the surface elements of the room to the ith PD of the UE [44]. The matrix $\mathbf{G}_\xi = \mathrm{diag}(\rho_1, ..., \rho_\xi)$ is the reflectivity matrix of all ξ reflectors, $\mathbf{E}_\xi$ is the LOS transfer function of size $\xi \times \xi$ for the links between all surface elements, and $\mathbf{I}_\xi$ is the unity matrix of order ξ. The elements of $\mathbf{E}_\xi$ as well as those of $\mathbf{r}_{i,j}$ and $\mathbf{t}_{i,j}$, for all $i \in [\![1, N_{\mathrm{r}}]\!]$ and $j \in [\![1, N_{\mathrm{t}}]\!]$, are found according to (2.3) between the LED of the jth AP, the surface elements and the ith PD of the UE.

Finally, it is important to mention here that the same propagation model applies to the uplink transmission as well, but it is omitted here for brevity.

2.3 Device Orientation Model

The performance of the considered LiFi system depends mainly on the channel gain between the transmitter and the receiver, which can be fully described by the channel matrix $\mathbf{H}$ described in the previous section for the case of downlink transmission for example. The channel gain depends in turn on the position and orientation of the UE. Devices such as laptops are usually placed on a flat surface and the associated LDs and PDs can be assumed to retain their orientation during each communication session whether upward or not [28]. However, hand-held devices, such as smartphones and wearables, are prone to random changes in orientation due to hand motion. In this dissertation, we focus on these types of devices and incorporate the random orientation in our analysis.

Current smartphones and wearables are equipped with a gyroscope, an accelerometer, and a compass that enable them to obtain the orientation in three dimensions by measuring the elemental rotation angles yaw, α, pitch, β, and roll, γ [28, 45]. As shown in Figure 2.5, the angles α, β and γ denote the rotations about the z-axis, the x-axis, and the y-axis, respectively. According to the Euler's rotation theorem, any rotation matrix can be expressed by $\mathbf{R} = \mathbf{R}_\alpha \mathbf{R}_\beta \mathbf{R}_\gamma$, where

$$\mathbf{R}_\alpha = \begin{bmatrix} \cos\alpha & -\sin\alpha & 0 \\ \sin\alpha & \cos\alpha & 0 \\ 0 & 0 & 1 \end{bmatrix}, \mathbf{R}_\beta = \begin{bmatrix} 1 & 0 & 0 \\ 0 & \cos\beta & -\sin\beta \\ 0 & \sin\beta & \cos\beta \end{bmatrix}, \mathbf{R}_\gamma = \begin{bmatrix} \cos\gamma & 0 & \sin\gamma \\ 0 & 1 & 0 \\ -\sin\gamma & 0 & \cos\gamma \end{bmatrix}.$$

$$\tag{2.5}$$
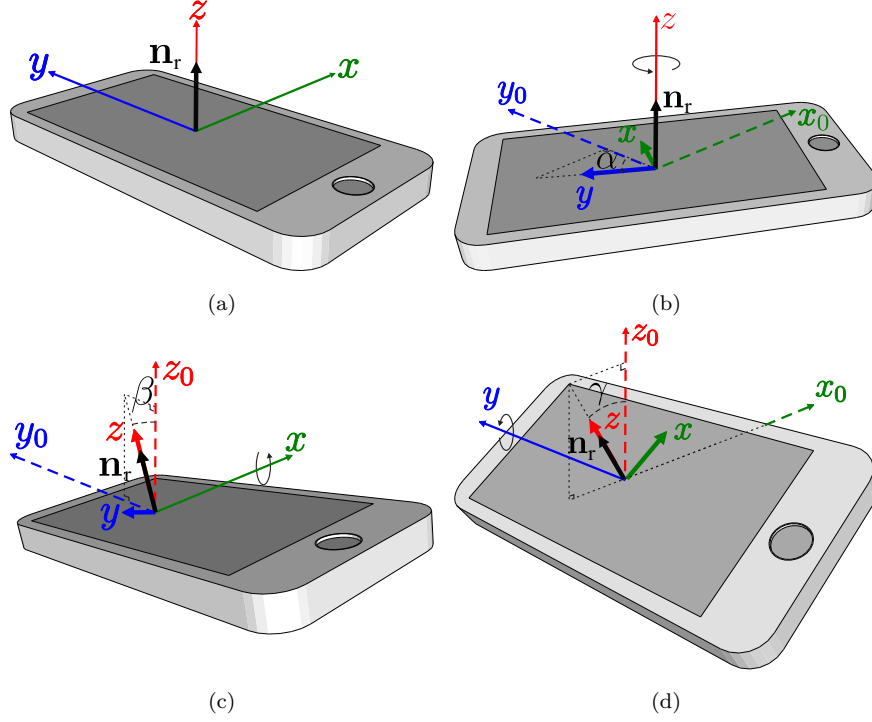
Figure 2.5: Orientations of a mobile device: (a) normal position, (b) yaw rotation with angle α about the z-axis, (c) pitch rotation with angle β about the x-axis, and (d) roll rotation with angle γ about the y-axis.

Accordingly. the normal vector of a PD can be described by $\mathbf{n}_{\mathrm{r}} = \mathbf{R}\mathbf{n}_0$, where $\mathbf{n}_0$ is the orientation vector for the vertically upward case. Furthermore, the rotated normal vector $\mathbf{n}_{\mathrm{r}}$ can be also represented in the spherical coordinate system corresponding to (X, Y, Z), with the polar angle θ, and the azimuth angle ω. As shown in Figure 2.6, θ is the angle between the rotated normal vector $\mathbf{n}_{\mathrm{r}}$ and the positive direction of the Z-axis, while ω denotes the angle between the projection of $\mathbf{n}_{\mathrm{r}}$ in the XY-plane and the positive direction of the X-axis. Then, from (2.5), the elevation angle θ, and the azimuth angle ω, can be obtained as

$$\theta = \cos^{-1}\left(\cos\left(\beta\right)\cos\left(\gamma\right)\right), \tag{2.6a}$$

$$\omega = \tan^{-1}\left(\frac{\sin(\alpha)\sin(\gamma) - \cos(\alpha)\cos(\gamma)\sin(\beta)}{\cos(\gamma)\sin(\alpha)\sin(\beta) + \cos(\alpha)\sin(\beta)}\right). \tag{2.6b}$$

In order to have a complete and concrete analysis of the performance of LiFi systems from which optimal transceiver designs can be obtained, the orientation models of LiFi devices should be carefully studied. Toward this goal, a set of experiments was conducted in [28] in order to derive measurements-based statistical models for the device orientation angles, namely, yaw, α, pitch, β, roll, γ, azimuth ω, and elevation θ. For collecting the measurements, 40 participants were asked to take part in the experiment while they were
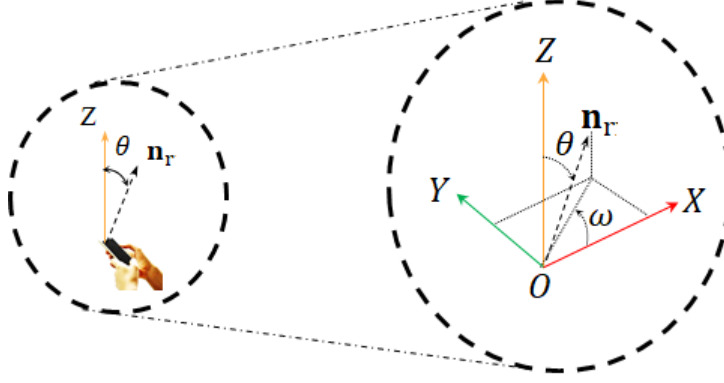
Figure 2.6: Elevation and azimuth angles.

Table 2.1: Statistics of orientation measurement.

	Sitting				Walking			
	α	β	γ	θ	α	β	γ	θ
Mean	Ω-90	40.78	-0.84	41.39	Ω-90	28.81	-1.35	29.67
Standard deviation	3.67	2.39	2.21	7.68	10	3.26	5.42	7.78
Gaussian KSD	0.07	0.09	0.13	0.04	0.02	0.03	0.02	0.02
Laplace KSD	0.01	0.01	0.04	0.04	0.04	0.06	0.05	0.05

working with their cellphones. The application `physics toolbox sensor suite` [46] was used to record the orientation data of yaw, pitch and roll while users were doing normal activities like browsing or watching a video stream. Measurements were recorded for static (sitting activity) and mobile users (walking activity). More details about the data measurement can be found in [28, 47, 48]. Laplace and Gaussian distributions were employed to fit the measured data, taking into account the first and second laws of error [49]. According to these laws, the frequency of error, which is defined as the difference between the measured data and the actual one, can be modeled as Laplace (first law) and Gaussian (second law) distributions.

The results of the measurements campaign performed in [28] demonstrate that the distributions of the yaw, α, pitch, β, roll, γ, and elevation θ are well fitted with a Laplace distribution for sitting activities, and more close to a Gaussian distribution for walking activities. The mean and variance for each case is noted in Table 2.1. The Kolmogorov-Smirnov distance (KSD) and kurtosis was used to evaluate the similarity of the collected measurements with the considered distributions [50]. The two-sample KSD is the maximum absolute distance between the cumulative distribution functions (CDFs), F_1 and F_2, of two distributions [51], i.e.,

$$\text{KSD} = \max_{x} |F_1(x) - F_2(x)|. \tag{2.7}$$
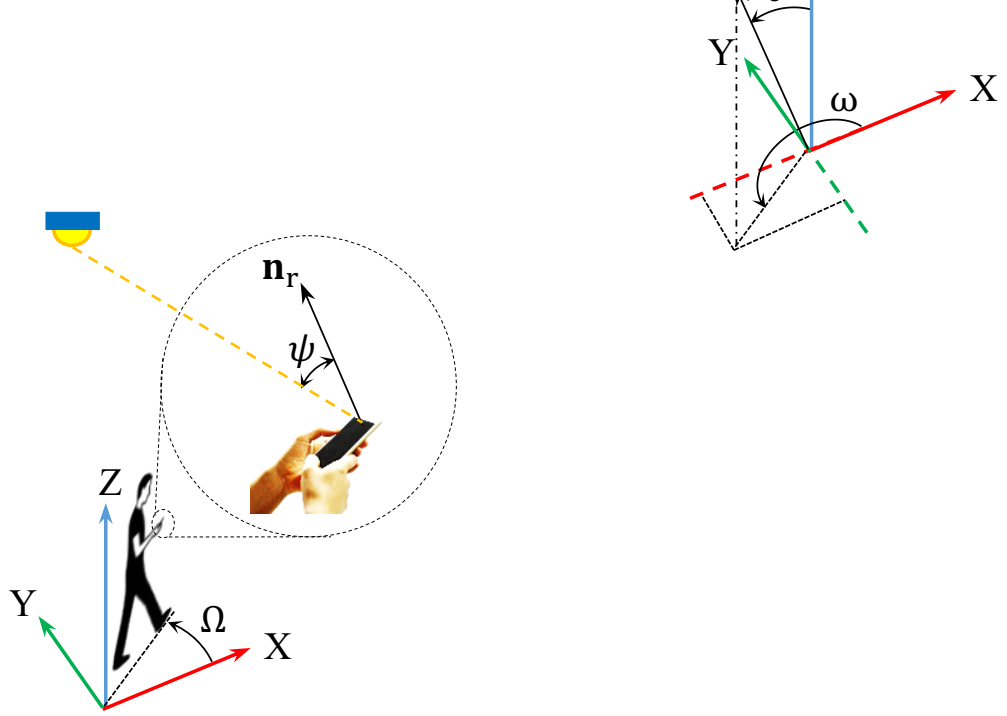
Figure 2.7: User direction.

Obviously, Small values of KSD (close to zero) correspond to more similarity between distributions, which is the case for the angles α, β, γ, and θ as shown in Table 2.1. Finally, the experiments conducted in [28] shows that the azimuth angle ω is well fitted with a uniform distribution within $[-\pi, \pi]$ for both cases of sitting and walking activities. The KSD of the sitting and walking activities are 0.034 and 0.019, respectively, which demonstrates the accuracy of the model.

The statistics given in Table 2.1 can be used to model the device random orientation. The parameter Ω shows the user direction. Precisely, $\Omega = \omega + \pi$ denotes the facing or movement direction of a user while sitting or walking, which is measured from the East direction in the Earth coordinate system as shown in Figure 2.7. From a statistical point of view, since $\omega \sim \mathcal{U}[-\pi, \pi]$, then $\Omega \sim \mathcal{U}[0, 2\pi]$

Chapter 3

Measurements-Based LiFi Channel Models

3.1 Motivation and Related Works

Some statistical channel models for stationary and uniformly distributed users were proposed in [52–55], where a fixed incidence angle was assumed in [52–54] and a random incidence angle was assumed in [55]. However, accounting for mobility, which is an inherent feature of wireless networks, requires a more realistic and non-uniform model for users' spatial distribution. Several mobility models, such as the random waypoint (RWP) model, have been proposed in the literature to characterize the spatial distribution of mobile users for indoor RF systems [56, 57]. However, these studies were limited to RF spectrum where statistical fading channel models were used. Recently, [33, 58] employed the RWP mobility model to characterize the SNR for indoor LiFi systems. In [58], the device orientation was assumed constant over time, which is not a realistic scenario, whereas in [33], the incidence angle of optical signals was assumed to be uniformly distributed, which is not a proper model for the incidence angle, since it does not account for the actual statistics of device orientation.

The majority of studies on optical wireless communication (OWC) assume that the device always faces vertically upward. This assumption may have been driven by the lack of having a proper model for orientation, and/or to make the analysis tractable. Such an assumption is only accurate for a limited number of devices (e.g., laptops with a LiFi dongle), while the majority of users use devices such as smartphones and wearables, and in real-life scenarios, users tend to hold their devices in a way that feels most comfort-

able. This random orientation can affect the users' throughput remarkably and it should be analyzed carefully. Even though a number of studies have considered the impact of random orientation in their analysis [33, 45, 59–65], all these studies assume a predefined model for the random orientation of the receiver. However, little or no evidence is presented to justify the assumed models. Nevertheless, none of these studies have considered the actual statistics of device orientation and have mainly assumed uniform or Gaussian distribution with hypothetical moments for device orientation. Recently, and for the first time, experimental measurements were carried out to model the polar and azimuth angles of the user's device in [28, 66–68]. It is shown that the polar angle can be modeled by either a truncated Laplace distribution for the case of stationary users or a truncated Gaussian distribution for the case of mobile LiFi users, while the azimuth angle follows a uniform distribution for both cases. Motivated by these results, the impact of the random receiver orientation on the SNR and the bit error rate (BER) was studied for indoor stationary users in [69]. However, proper statistical channel models for indoor LiFi systems that encompass both the random spatial distribution and the random device orientation of users were not derived in the literature, which is the focus of this chapter.

3.2 Contributions and Outcomes

Against the above background, we investigate in this chapter the channel statistics of indoor LiFi systems. Novel realistic and measurement-based channel models for indoor LiFi systems are proposed, and the proposed models encompass the random motion and device orientation of users. Precisely, the statistics of the LOS channel gain are derived for stationary and mobile users with random device orientation, using the measurements-based models of device orientation derived in [28]. For stationary users, the model of randomly located user is employed to characterize the spatial distribution of users, and the truncated Laplace distribution is used to model the device orientation. For mobile users, the RWP mobility model is used to characterize the spatial distribution of users and the truncated Gaussian distribution is used to model the device orientation. In light of the above discussion, we may summarize the contributions of this chapter as follows.

- For stationary users, two channel models are proposed, namely, the modified truncated Laplace (MTL) model and the modified Beta (MB) model. For mobile users,

also two channel models are proposed, namely, the sum of modified truncated Gaussian (SMTG) model and the sum of modified Beta (SMB) model. The accuracy of the derived models is then validated using the KSD criterion.

- The BER performance of LiFi systems is investigated for both cases of stationary and mobile users using the derived statistical channel models. We show that the random orientation and the random spatial distribution of users could have strong effect on the error performance of LiFi systems.

- We propose a novel design of indoor LiFi systems that can alleviate the effects of random device orientation and random spatial distribution of users. We show that the proposed design is able to guarantee good error performance for LiFi systems under the realistic behaviour of users.

The rest of the chapter is organized as follows. The system model is presented in Section 3.3. Section 3.4 presents the exact statistics of the LOS channel gain. In Sections 3.5, approximate statistical channel models for stationary and mobile users are proposed. The simulation results are presented in Section 3.6. Finally, the chapter is concluded in Section 3.7.

3.3 System Model

Consider the indoor LiFi system shown in Figure 3.1, which consists of a LiFi attocell with a radius R_{e} (green attocell) that is equipped with a single AP installed at height h_{a} from the ground. The LiFi attocell is concentric with a larger circular area with a radius R_{o} ($R_{\mathrm{e}} \leq R_{\mathrm{o}}$), within which a user may be located. The UE is equipped with a single PD that is used for communication with the AP. Assuming that the global coordinate system (X, Y, Z) is cylindrical, the coordinates of the UE are given by $(R_{\mathrm{e}}, \chi, h_{\mathrm{u}})$, where $r \in [0, R_{\mathrm{o}}]$ is the polar distance, $\chi \in [0, 2\pi]$ is the polar angle, and $h_{\mathrm{u}} \in [0, h_{\mathrm{a}}]$ is the height of the LiFi receiver. The user is assumed to hold the UE within a close distance of the body. Therefore, the polar coordinates (r, χ) of the UE are assumed to be exactly the same as those of the user. However, this is not the case for the height h_{u}, since it depends mainly on the activity of the user, i.e., either stationary (sitting activity) or mobile (walking activity). Furthermore, in this communication model, the UE is connected to the AP if it is located inside the LiFi attocell, i.e., when $r \leq R$.

28

(a) Front view

(b) Top view.
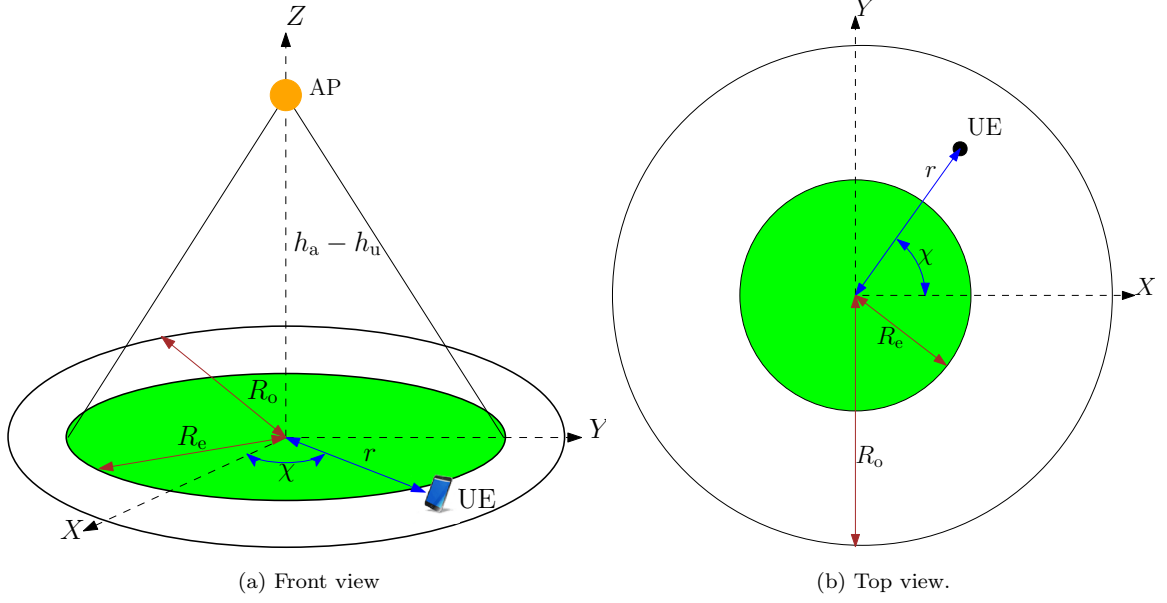
Figure 3.1: A LiFi attocell concentric with a larger circular area.

As presented in Section 2.2, the channel gain between the AP and the UE is the sum of a LOS and the NLOS components resulting from reflections off walls. Concerning the NLOS components, it was observed in [70,71] that, when the LiFi AP is far from the walls, those components are insignificant as compared to the LOS component, except when the receiver is very close to a corner in the indoor environment. In the system setup considered in this chapter, which is shown in Figure. 3.1, we assume that the LiFi AP is relatively far from the walls of the indoor environment and we are interested in investigating the channel statistics of the LiFi attocell when the user is within its coverage area (the green area with radius R_{e}). In this case, the contribution of the NLOS components is negligible compared to that of the LOS component, and hence, only the LOS component is considered in our analysis. Hence, the received signal at the receiver at each channel use is expressed as

$$y = \lambda h_{\mathrm{LOS}} x + n, \tag{3.1}$$

where h_{LOS} is the LOS downlink channel gain, x is the transmitted signal and n is an AWGN that is $\mathcal{N}(0, \sigma_{\mathrm{VL}}^2)$ distributed, such that $\sigma_{\mathrm{VL}}^2 = N_{\mathrm{VL}} B_{\mathrm{VL}}$, where N_{VL} is the noise single sided power spectral density and B_{VL} is the visible light bandwidth available at the AP. In addition, as was explained in Section 2.1, $\lambda = T R_{\mathrm{p}} \eta N_{\mathrm{LEDs}}$, in which T is the TIA gain at the receiver, R_{p} is the responsivity of the receiver's PD, η is the current-to-power conversion efficiency of the LEDs, and N_{LEDs} is the number of LEDs per AP. Based on the propagation model presented in Section 2.2, the channel gain h_{LOS} is expressed as

$$h_{\mathrm{LOS}} = H_0 \frac{\cos(\phi)^m \cos(\psi)}{d^2} \times \mathcal{U}_{[0,\Psi]}(\psi), \tag{3.2}$$

29

where H_0 is expressed as shown in Section 2.2 and $d = \sqrt{r^2 + (h_\mathrm{a} - h_\mathrm{u})^2}$ is the distance between the AP and the UE.

Based on the results of [28], $\cos(\phi)$ and $\cos(\psi)$ are expressed, respectively, as

$$\cos(\phi) = \frac{h_\mathrm{a} - h_\mathrm{u}}{d}, \tag{3.3a}$$

$$\cos(\psi) = \frac{(z_\mathrm{a} - z_\mathrm{u})}{d} \cos(\theta) - \frac{(x_\mathrm{a} - x_\mathrm{u})}{d} \cos(\Omega) \sin(\theta) - \frac{(y_\mathrm{a} - y_\mathrm{u})}{d} \sin(\Omega) \sin(\theta),$$

where $(x_\mathrm{a}, y_\mathrm{a}, z_\mathrm{a})$ and $(x_\mathrm{u}, y_\mathrm{u}, z_\mathrm{u})$ are the Cartesian coordinates of the AP and the UE, respectively, and as shown in Figures 2.6 and 2.7 in Section 2.3, Ω and θ are the angle of direction and the elevation angle of the UE, respectively. The angle of direction Ω represents the angle between the direction the user is facing and the X-axis, whereas the elevation angle θ is the angle between the normal vector of PD n_rx and the Z-axis. Based on this, we have $(x_\mathrm{a}, y_\mathrm{a}, z_\mathrm{a}) = (0, 0, h_\mathrm{a})$ and $(x_\mathrm{u}, y_\mathrm{u}, z_\mathrm{u}) = (r \cos(\chi), r \sin(\chi), h_\mathrm{u})$. Therefore, $\cos(\psi)$ can be expressed as

$$\cos(\psi) = \frac{r \cos(\Omega - \chi) \sin(\theta) + (h_\mathrm{a} - h_\mathrm{u}) \cos(\theta)}{d}, \tag{3.4}$$

and consequently, the LOS channel gain h_LOS is expressed as

$$h_\mathrm{LOS} = \left(\frac{a(\theta)r}{d^{m+3}} \cos(\Omega - \chi) + \frac{b(\theta)}{d^{m+3}} \right) \times \mathcal{U}_{[\cos(\Psi), 0]} \left(\cos(\psi) \right), \tag{3.5}$$

where $a(\theta) = H_0(h_a - h_u)^m \sin(\theta)$ and $b(\theta) = H_0(h_a - h_u)^{m+1} \cos(\theta)$.

Based on the above, we conclude that the random behaviour of the channel gain h_LOS depends mainly on the four random variables r, χ, Ω, and θ. Precisely, the variables r and χ model the randomness of the instantaneous location of the user, whereas the variables Ω and θ model the randomness of the instantaneous UE's orientation. Additionally, the statistics of the polar distance r and the the elevation angle θ depend on the motion of the user, either stationary or mobile. Consequently, the statistics of the LOS channel gain h_LOS inducibly depend on the user's activity. In the following section, the exact statistics of the channel gain h_LOS are derived for the case of stationary and mobile users.

3.4 Channel Statistics of Stationary and Mobile Users with Random Device orientation

The objective of this section is deriving the exact statistics of the LOS channel gain h_LOS for the case of stationary and mobile users. In subsection 3.4.1, we present the statistics of the four main factors r, χ, Ω and θ for each case, from which we derive in subsection 3.4.2 the exact statistics of h_LOS.

3.4.1 Parameters Statistics

From a statistical point of view, the instantaneous location and the instantaneous orientation of the UE are independent. Thus, the couples of random variables (R_e, χ) and (Ω, θ) are independent. In addition, based on the results of [58, 72], the random variables r and χ are independent, since r defines the polar distance and χ defines the polar angle. On the other hand, based on the results of [28], the angle of direction Ω and the elevation angle θ are also statistically independent. Therefore, the random variables r, χ, Ω and θ are independent. In addition, for both cases of stationary and mobile users, the random variables χ and Ω are uniformly distributed within $[0, 2\pi]$ [28, 58, 72]. However, this is not the case for the polar distance r and the elevation angle θ. In fact, as we will show in the following, the statistics of r and θ depend on whether the user is stationary or mobile.

When the user is stationary, its location is fixed. However, the user is randomly located, i.e., its instantaneous location is uniformly distributed within the circular area of radius R_o. In this case, the probability density function (PDF) of the polar distance r is expressed as

$$f_r(r) = \frac{2r}{R_o^2} \mathcal{U}_{[0,R_o]}(r). \tag{3.6}$$

On the other hand, as presented in subsection 2.3, the elevation angle θ follows a truncated Laplace distribution for the case of stationary users. For a mobile user, and especially in indoor environments, the UE motion represents the user's walk, which is equivalent to a 2-D topology of the RWP mobility model, where the direction, velocity and destination points (waypoints) are all selected randomly. Based on [56, 57], the spatial distribution of the UE within a circular area of radius R_o is polynomial in terms of the polar distance r and its PDF is expressed as

$$f_r(r) = \sum_{i=1}^{3} a_i \frac{r^{b_i}}{R_o^{b_i+1}} \mathcal{U}_{[0,R_o]}(r), \tag{3.7}$$

where $[a_1, a_2, a_3] = \frac{1}{75}[324, -420, 96]$ and $[b_1, b_2, b_3] = [1, 3, 5]$. Moreover, as presented in subsection 2.3, the elevation angle θ follows a truncated Gaussian distribution for the case of mobile users.

3.4.2 Channel Statistics

As stated in Section 3.3, the user can be located anywhere inside the outer circular area with radius R_o. However, it is connected to the desired AP if it is located inside the LiFi

attocell, i.e., if $r \in [0, R]$. In other words, in order to establish a communication link between the user and the desired AP, the only admitted values of the polar distance r should be within the range $[0, R_e]$. Due to this, we constrain the range of r to be $[0, R_e]$, and therefore, the exact PDF of the polar distance r becomes $\tilde{f}_r(r) = \frac{f_r(r)}{F_r(R_e) - F_r(0)} \mathcal{U}_{[0, R_e]}(r)$, where F_r denotes the CDF of r. Consequently, the PDF of the distance $d = \sqrt{r^2 + (h_a - h_u)^2}$ between the AP and the user is given by

$$f_d(l) = \frac{l \times \tilde{f}_r\left(\sqrt{d^2 - (h_a - h_u)^2}\right)}{\sqrt{l^2 - (h_a - h_u)^2}} \mathcal{U}_{[d_{\min}, d_{\max}]}(l), \tag{3.8}$$

where $d_{\min} = h_a - h_u$ and $d_{\max} = \sqrt{R_e^2 + (h_a - h_u)^2}$.

Now, consider the random variable $\cos(\Omega - \chi)$ appearing in the expression of h_{LOS} in (3.5). Since Ω and χ are independent and uniformly distribution within $[0, 2\pi]$, and using the PDF transformation of random variables, $\cos(\Omega - \chi)$ follows the arcsine distribution within the range $[-1, 1]$. Thus, the PDF and the CDF of $\cos(\Omega - \chi)$ are expressed, respectively, as

$$f_{\cos(\Omega - \chi)}(z) = \frac{1}{\pi\sqrt{1 - z^2}} \mathcal{U}_{[-1,1]}(z), \tag{3.9}$$

$$F_{\cos(\Omega - \chi)}(z) = \left(\frac{\arcsin(z)}{\pi} + \frac{1}{2}\right) \mathcal{U}_{[-1,1]}(z) + \mathcal{U}_{[1,+\infty]}(z). \tag{3.10}$$

Based on this, the exact PDF of the channel gain h_{LOS} is given in the following theorem.

Theorem 3.1. *The range of the LOS channel gain h_{LOS} is $[h_{\min}, h_{\max}]$, where $h_{\min} = 0$ and $h_{\max} = \frac{H_0}{(h_a - h_u)^2}$. In addition, for $h \in [h_{\min}, h_{\max}]$, the PDF of h_{LOS} is expressed as*

$$f_{h_{\mathrm{LOS}}}(h) = g_{h_{\mathrm{LOS}}}(h) \mathcal{U}_{[h_{\min}^*, h_{\max}]}(h) + F_{\cos(\psi)}(\cos(\Psi))\delta(h), \tag{3.11}$$

where $h_{\min}^* = \frac{H_0(h_a - h_u)^m \cos(\Psi)}{d_{\max}^{m+2}}$, $F_{\cos(\psi)}(\cos(\Psi))$ is given by

$$F_{\cos(\psi)}(\cos(\Psi)) = \int_{d_{\min}}^{d_{\max}} \int_0^{\frac{\pi}{2}} F_{\cos(\Omega - \chi)}\left(\frac{d\cos(\Psi) - (h_a - h_u)\cos\theta}{\sin(\theta)\sqrt{l^2 - (h_a - h_u)^2}}\right) f_\theta(\theta)\mathrm{d}\theta f_d(l)\mathrm{d}l, \tag{3.12}$$

in which $d_{\min}^*(h) = \max(d_0(h), d_{\min})$, such that

$$d_0(h) = \left(\frac{h_0(h_a - h_u)^m \cos(\Psi)}{h}\right)^{\frac{1}{m+2}}, \tag{3.13}$$

and the function $g_{h_{\mathrm{LOS}}}$ is expressed as

$$g_{h_{\mathrm{LOS}}}(h) = \int_{d_{\min}^*(h)}^{d_{\max}} \int_0^{\frac{\pi}{2}} \frac{l^{m+3}}{a(\theta)\sqrt{l^2 - (h_a - h_u)^2}} f_{\cos(\Omega - \chi)}\left(\frac{l^{m+3}h - b(\theta)}{a(\theta)\sqrt{l^2 - (h_a - h_u)^2}}\right) f_\theta(\theta) f_l(l)\mathrm{d}\theta\mathrm{d}l$$

$$+ v(h) \int_0^{\frac{\pi}{2}} J_{h_{\mathrm{LOS}}}(\theta, l) f_\theta(\theta) f_l(l)\mathrm{d}\theta\mathrm{d}l, \tag{3.14}$$

in which the function v is expressed as $v(h) = \frac{-(h_0(h_a - h_u)^m \cos(\Psi))^{\frac{1}{m+2}}}{(m+2)h^{\frac{m+3}{m+2}}} \mathcal{U}_{[h_{\min}^*, h_{\max}^*]}$, such that

32

$h^*_{\max} = \frac{H_0(h_a - h_u)^m \cos(\Psi)}{d^{m+2}_{\min}}$, and the function $J_{h_{\mathrm{LOS}}}$ is expressed as

$$J_{h_{\mathrm{LOS}}}(\theta, l) = F_{\cos(\Omega - \chi)}\left(\frac{l^*_{\min}\cos(\Psi) - (h_a - h_u)\cos(\theta)}{\sin(\theta)\sqrt{l^*_{\min}{}^2 - (h_a - h_u)^2}}\right)$$

$$- F_{\cos(\Omega - \chi)}\left(\frac{l^*_{\min}{}^{m+3}h - b(\theta)}{a(\theta)\sqrt{l^*_{\min}{}^2 - (h_a - h_u)^2}}\right). \qquad (3.15)$$

Proof. See Appendix A.1. The exact CDF of the LOS channel gain h_{LOS} is also provided in Appendix A.1. ∎

As it can be seen in **Theorem 3.1**, the closed-form expression of the exact PDF of the LOS channel gain h_{LOS} in (3.11) is neither straightforward nor tractable, since it involves some complex and atypical integrals. Due to this, in order to provide simple and tractable channel models for indoor LiFi systems, we propose in the following section some approximations for the PDF of h_{LOS} in (3.11), for both cases of stationary and mobile users.

3.5 Approximate PDFs of the LOS Channel Gain

In this section, our objective is to derive some approximations for the PDF of h_{LOS}, starting from the results of **Theorem 3.1**. The cases of stationary and mobile users are investigated separately in subsections 3.5.1 and 3.5.2, respectively.

3.5.1 Stationary Users

An approximate expression of the PDF of the LOS channel gain h_{LOS} for the case of a stationary user is given in the following theorem.

Theorem 3.2. *For the case of a stationary user, an approximate expression of the PDF of the channel gain h_{LOS} is given by*

$$f_{h_{\mathrm{LOS}}}(h) \approx \frac{1}{h^\nu}g(h) + F_{\cos(\psi)}(\cos(\Psi))\delta(h), \qquad (3.16)$$

where $\nu > 0$ and g is a function with range $[h^*_{\min}, h_{\max}]$.

Proof. See Appendix A.2. ∎

The approximation of the PDF of the LOS channel gain h_{LOS} provided in **Theorem 3.2** expresses two main factors, which are the random location of the user and the random orientation of the UE. The functions $h \mapsto \frac{1}{h^\nu}$ and $h \mapsto g(h)$ express respectively the effects

of the random location of the user and the random orientation of the UE on the LOS channel gain h_{LOS}. At this point, the missing part is the function g that provides the best approximation for the PDF of the LOS channel gain $f_{h_{\mathrm{LOS}}}$. In the following, we provide two approximate expressions for the function g.

1) The Modified Truncated Laplace (MTL) Model

Since the function $h \mapsto g(h)$ expresses the effect of the random orientation of the UE on the LOS channel gain h_{LOS}, and motivated by the fact that the elevation angle θ follows a truncated Laplace distribution for the case of stationary users, one reasonable choice for g is the truncated Laplace distribution. Consequently, an approximate expression of the PDF of the LOS channel gain h_{LOS} can be given by

$$f_{h_{\mathrm{LOS}}}(h) \approx \frac{h^{-\nu} \exp\left(-\frac{|h-\mu_H|}{b_H}\right)}{M_1\left(-\nu, \mu_H, b_H\right)} \mathcal{U}_{\left[h^*_{\min}, h_{\max}\right]}(h) + F_{\cos(\psi)}(\cos(\Psi))\delta(h), \qquad (3.17)$$

where $\mu_H \in [h^*_{\min}, h_{\max}]$, $b_H > 0$ and $M_1\left(-\nu, \mu_H, b_H\right)$ is a normalization factor given by

$$M_1\left(-\nu, \mu_H, b_H\right) = \frac{G_1\left(-\nu, \mu_H, b_H\right)}{\left[1 - F_{\cos(\psi)}(\cos(\Psi))\right]}, \qquad (3.18)$$

in which G_1 is given by

$$\begin{aligned} G_1\left(\gamma, \mu_H, b_H\right) = -b_H^{1+\gamma} e^{\frac{-\mu_H}{b_H}} &\left[\Gamma\left(1+\gamma, \frac{h_{\max}}{b_H}\right) - \Gamma\left(1+\gamma, \frac{\mu_H}{b_H}\right)\right. \\ &\left. +(-1)^{1-\gamma}\left(\Gamma\left(1+\gamma, -\frac{\mu_H}{b_H}\right) - \Gamma\left(1+\gamma, -\frac{h^*_{\min}}{b_H}\right)\right)\right], \end{aligned} \qquad (3.19)$$

such that Γ denotes the upper incomplete Gamma function. At this stage, we need to determine the parameters (ν, μ_H, b_H) of f_H. One approach to do this is through moments matching. Using the exact PDF of h_{LOS} in (3.11), the non-centered moments of the LOS channel gain h_{LOS} are given by

$$m_i^e = \int_{h^*_{\min}}^{h_{\max}} h^i g_H(h)\mathrm{d}h + F_{\cos(\psi)}(\cos(\Psi)), \quad i \in \mathbb{N}, \qquad (3.20)$$

whereas by using the approximate PDF of h_{LOS} in (3.17), the non-centered moments of the LOS channel gain h_{LOS} are given by

$$m_i^a\left(\nu, \mu_H, b_H\right) = \frac{M_1\left(i - \nu, \mu_H, b_H\right)}{M_1\left(-\nu, \mu_H, b_H\right)}, \quad i \in \mathbb{N}. \qquad (3.21)$$

Therefore, since only three parameters need to be determined, which are (ν, μ_H, b_H), they can be obtained by solving the following system of equations

$$m_i^a\left(\nu, \mu_H, b_H\right) = m_i^e, \quad \text{for } i = 1, 2, 3. \qquad (3.22)$$

2) The Modified Beta (MB) Model

The exact PDF of the LOS channel gain h_{LOS} involves the integral of a function that has the form $(x, y) \mapsto f_{\cos(\Omega-\chi)}(g(x, y))$. Since $\cos(\Omega - \chi)$ follows the arcsine distribution

and based on the fact that the arcsine distribution is a special case of the Beta distribution, we approximate the function g with a Beta distribution. Consequently, an approximate expression of the PDF of the LOS channel gain h_{LOS} can be given by

$$f_{h_{\text{LOS}}}(h) \approx \frac{h^{-\nu}\left(\frac{h-h_{\min}^*}{h_{\max}-h_{\min}^*}\right)^{\chi_H-1}\left(\frac{h_{\max}-h}{h_{\max}-h_{\min}^*}\right)^{\beta_H-1}}{M_2\left(-\nu,\chi_H,\beta_H\right)}\mathcal{U}_{\left[h_{\min}^*,h_{\max}\right]}(h) + F_{\cos(\psi)}(\cos(\Psi))\delta(h),$$
(3.23)

where $\chi_H > 0$, $\beta_{h_{\text{LOS}}} > 0$ and $M_2\left(-\nu,\chi_H,\beta_H\right)$ is a normalization factor given by

$$M_2\left(-\nu,\chi_H,\beta_H\right) = \frac{G_2\left(-\nu,\chi_H,\beta_H\right)}{\left[1 - F_{\cos(\psi)}(\cos(\Psi))\right]},$$
(3.24)

such that G_2 is given by

$$G_2\left(\gamma,\chi_H,\beta_H\right) = \left[\Gamma(\beta_H)\Gamma(-\gamma)h_{\max}^{\chi_H+\gamma}{_2\tilde{F}_1}\left(1-\chi_H,-\chi_H-\beta_H-\gamma+1;-\chi_H-v+1;\frac{h_{\min}^*}{h_{\max}}\right)\right.$$
$$\left.-\Gamma(\chi_H)h_{\min}^{*\chi_H+\gamma}\Gamma(\chi_H+\beta_H+\gamma){_2\tilde{F}_1}\left(1-\beta_H,\gamma+1;\beta_H+\gamma+1;\frac{h_{\min}^*}{h_{\max}}\right)\right] \times B(\gamma,\chi_H,\beta_H),$$
(3.25)

in which ${_2\tilde{F}_1}$ denotes the regularized hyper-geometric function and

$$B(\gamma,\chi_H,\beta_H) = \frac{\pi h_{\max}^{\beta_H-1}(h_{\max}-h_{\min}^*)^{-\chi_H-\beta_H+2}}{\sin(\pi(\chi_H+\gamma))\Gamma(-\gamma)\Gamma(\chi_H+\beta_H+\gamma)}.$$
(3.26)

Based on the above, it remains to derive the parameters (ν,χ_H,β_H) of f_H. Similar to the case of the MTL model, one approach to do this is through moments matching. Specifically, (ν,χ_H,β_H) can be obtained by solving the system of equations in (3.22), where for $i = 1,2,3$, m_i^a is expressed in this case as

$$m_i^a\left(\nu,\mu_H,b_H\right) = \frac{M_2\left(i-\nu,\chi_H,\beta_H\right)}{M_2\left(-\nu,\chi_H,\beta_H\right)}, \quad i \in \mathbb{N}.$$
(3.27)

3.5.2 Mobile Users

An approximate expression of the PDF of the LOS channel gain h_{LOS} for the case of a mobile user is given in the following theorem.

Theorem 3.3. *For the case of a mobile user, an approximate expression of the PDF of the channel gain h_{LOS} is given by*

$$f_{h_{\text{LOS}}}(h) \approx \sum_{j=1}^{3}\frac{1}{h^{\nu_i}}g_j(h) + F_{\cos(\psi)}(\cos(\Psi))\delta(h),$$
(3.28)

where, for $j = 1,2,3$, $\nu_j > 0$ and g_j is a function with range $[h_{\min}^*, h_{\max}]$.

Proof. See Appendix A.3. ∎

It is important to highlight here that, for $j = 1,2,3$, the functions $h \mapsto \frac{1}{h^{\nu_j}}$ and $h \mapsto g_j(h)$ express respectively the effects of the user mobility and the random orientation of the UE on the LOS channel gain h_{LOS}. At this point, the missing part is the functions

g_j, for $j = 1, 2, 3$, that provide the best approximation for the PDF of the LOS channel gain $f_{h_{\text{LOS}}}$. In the following, we provide two expressions for each function g_j for $j = 1, 2, 3$.

1) The Sum of Modified Truncated Gaussian (SMTG) Model

Since for $j = 1, 2, 3$, the functions $h \mapsto g_j(h)$ express the effect of the random orientation of the UE on the channel gain h_{LOS} and motivated by the fact that, for the case of mobile users, the elevation angle θ follows a truncated Gaussian distribution, one reasonable choice for the functions g_j is the truncated Gaussian distribution. Consequently, an approximate expression of the PDF of the LOS channel gain h_{LOS} can be given by

$$f_{h_{\text{LOS}}}(h) \approx \frac{\sum_{j=1}^{3} h^{-\nu_j} \exp\left(-\frac{(h - \mu_{H,j})^2}{2\sigma_{H,j}^2}\right)}{\sum_{j=1}^{3} M_3\left(-\nu_j, \mu_{H,j}, \sigma_{H,j}\right)} \mathcal{U}_{[h_{\min}^*, h_{\max}]}(h) + F_{\cos(\psi)}(\cos(\Psi))\delta(h), \quad (3.29)$$

where for $j = 1, 2, 3$, $\mu_{H,j} \in [h_{\min}^*, h_{\max}]$, $\sigma_{H,j} > 0$ and $M_3\left(-\nu_j, \mu_{H,j}, \sigma_{H,j}\right)$ is a normalization factor that is given by

$$M_3\left(-\nu_j, \mu_{H,j}, \sigma_{H,j}\right) = \frac{\int_{h_{\min}^*}^{h_{\max}} h^{-\nu_j} \exp\left(-\frac{(h - \mu_{H,j})^2}{2\sigma_{H,j}^2}\right) \mathrm{d}h}{\left[1 - F_{\cos(\psi)}(\cos(\Psi))\right]}. \quad (3.30)$$

Now, in order to to have the complete closed-form expression of f_H, we have to determine the parameters $\{(\nu_j, \mu_{H,j}, b_{H,j}) \mid \forall j = 1, 2, 3\}$. Similar to the one of the stationary users case, one approach to determine these parameters is through moments matching. Specifically, since only nine parameters need to be determined, which are $\{(\nu_j, \mu_{H,j}, \sigma_{H,j}) \mid \forall j = 1, 2, 3\}$, they can be obtained by solving the following system of equations

$$m_i^a = m_i^e, \quad \text{for } i = 1, 2, .., 9, \quad (3.31)$$

where, for $i = 1, 2, ..., 9$, m_i^a is expressed in this case as

$$m_i^a = \frac{\sum_{j=1}^{3} M_3\left(i - \nu_j, \mu_{H,j}, b_{H,j}\right)}{\sum_{j=1}^{3} M_3\left(-\nu_j, \mu_{H,j}, \sigma_{H,j}\right)}. \quad (3.32)$$

2) The Sum of Modified Beta (SMB) Model

Motivated by the same reasons as for the MB model in Section 3.5.1, we approximate each function g_j, for $j = 1, 2, 3$, with a Beta distribution. Consequently, an approximate expression of the PDF of the LOS channel gain h_{LOS} is given by

$$f_{h_{\text{LOS}}}(h) \approx \frac{\sum_{j=1}^{3} h^{-\nu_j} \left(\frac{h - h_{\min}^*}{h_{\max} - h_{\min}^*}\right)^{\chi_{H,j} - 1} \left(\frac{h_{\max} - h}{h_{\max} - h_{\min}^*}\right)^{\beta_{H,j} - 1} \mathcal{U}_{[h_{\min}^*, h_{\max}]}(h)}{\sum_{j=1}^{3} M_2\left(-\nu_j, \chi_{H,j}, \beta_{H,j}\right)}$$
$$+ F_{\cos(\psi)}(\cos(\Psi))\delta(h), \quad (3.33)$$

Table 3.1: Simulation Parameters

Parameter	Symbol	Value	Parameter	Symbol	Value
Ceiling height	h_a	2.4 m	LED half-power semiangle	$\Phi_{1/2}$	60°
LED conversion factor	η	0.7 W/A	PD responsivity	R_p	0.6 A/W
PD geometric area	A_{PD}	1 cm^2	Refractive index	n_c	1
UE's height (stationary)	h_u	0.9 m	UE's height (mobile)	h_u	1.4 m
VL bandwidth	B_{VL}	20 MHz	VL Noise power spectral density	N_{VL}	10^{-21} W/Hz

where $\chi_{H,j} > 0$, $\beta_{H,j} > 0$ and $M_2\left(-\nu_j, \chi_{H,j}, \beta_{H,j}\right)$ is given in (3.24). Finally, it remains now to derive the parameters $\{(\nu_j, \chi_{H,j}, \beta_{H,j}) \,|\, j = 1, 2, 3\}$ of f_H. Similar to the STMG model, these parameters can be obtained by solving the system of equations in (3.31), where for $i = 1, 2, ..., 9$, m_i^a is expressed in this case as

$$m_i^a = \frac{\sum_{j=1}^3 M_2\left(i - \nu_j, \chi_{H,j}, \beta_{H,j}\right)}{\sum_{j=1}^3 M_2\left(-\nu, \chi_H, \beta_H\right)}. \tag{3.34}$$

3.6 Simulation Results and Discussions

We consider a typical indoor LiFi attocell [33, 58]. Parameters used throughout the chapter are shown in Table 3.1. In Subsection 3.6.1, we present the PDF and CDF of the LOS channel gain h_{LOS} for the case of stationary and mobile users. In Subsection 3.6.2, we investigate the error performance of indoor LiFi systems using the derived statistics of the LOS channel gain h_{LOS}. Finally, based on the error performance presented in 3.6.2, we propose in subsection 3.6.3 an optimized design for indoor LiFi cellular systems that can enhance the error performance.

3.6.1 Channel Statistics

For stationary users, Figures 3.2 and 3.3 present the exact, simulated and approximated PDF and CDF of the LOS channel gain h_{LOS}, when the radius of the attocell $R_e = 1$ m and $R_e = 2.5$ m, respectively. For both cases, two different values for the FOV of the UE were considered, which are $\Psi = 90°$ and $60°$. These figures show that the proposed MTL and MB models offer good approximation for the distribution of the LOS channel gain h_{LOS}. Analytically, in order to evaluate the goodness of the proposed MTL and MB models, we use the well-known KSD [51]. In our case, the KSD of the MTL and MB models are shown in Table 3.2. As it can be seen in this table, the maximum KSD

(a) PDF: $\Psi = 90°$.   (b) CDF: $\Psi = 90°$.   (a) PDF: $\Psi = 90°$.   (b) CDF: $\Psi = 90°$.

(c) PDF: $\Psi = 60°$.   (d) CDF: $\Psi = 60°$.   (c) PDF: $\Psi = 60°$.   (d) CDF: $\Psi = 60°$.
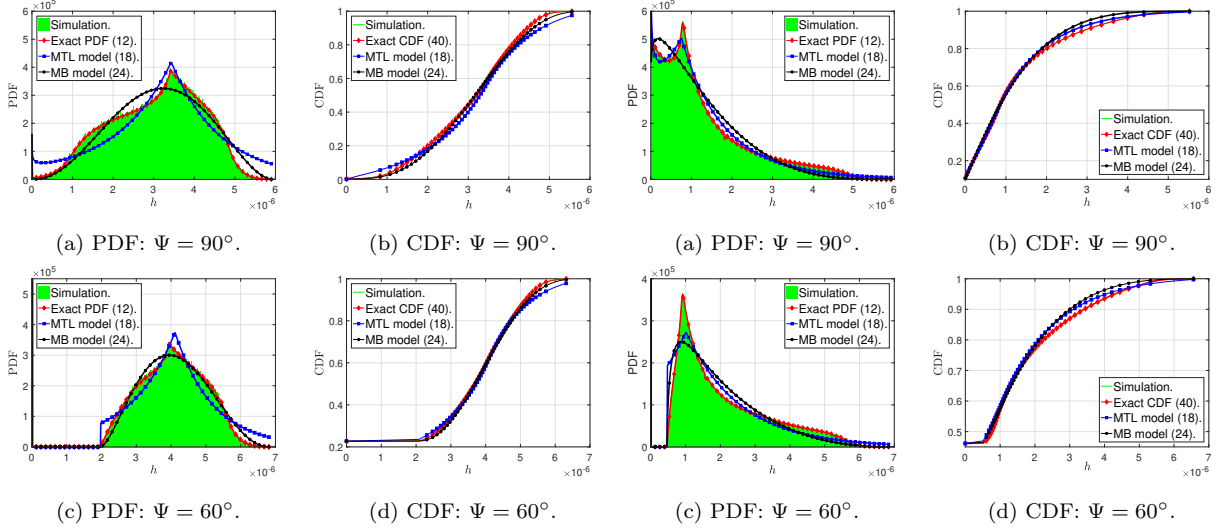
Figure 3.2: Comparison between the simulation, theoretical and approximation results of the PDF and the CDF of the LOS channel gain h_{LOS} for the case of stationary users when $R_{\mathrm{e}} = 1$ m.

Figure 3.3: Comparison between the simulation, theoretical and approximation results of the PDF and the CDF of the LOS channel gain h_{LOS} for the case of stationary users when $R_{\mathrm{e}} = 2.5$ m.

Table 3.2: KSD of the MTL and the MB models

	MTL model		MB model	
	$\Psi = 90°$	$\Psi = 60°$	$\Psi = 90°$	$\Psi = 60°$
$R_{\mathrm{e}} = 1$ m	0.0669	0.0448	0.0336	0.0197
$R_{\mathrm{e}} = 2.5$ m	0.0239	0.0241	0.0444	0.0316

value for the MTL and MB models are 0.0669 and 0.0444, respectively, which demonstrates the good approximation offered by the MTL and MB models.

For mobile users, Figures. 3.4 and 3.5 present the exact, simulated and approximated PDF and CDF of the LOS channel gain h_{LOS}, when the radius of the attocell is $R_{\mathrm{e}} = 1$ m and $R_{\mathrm{e}} = 2.5$ m, respectively. For both cases, two different values for the FOV of the UE were considered, which are $\Psi = 90°$ and $60°$. These figures show that the proposed SMTG and SMB models offer good approximation for the distribution of the LOS channel gain h_{LOS}. Nevertheless, Table 3.3 presents the KSD of the SMTG and the SMB models, where it shows that their maximum KSD values are 0.0238 and 0.0054, respectively. These results demonstrate the good approximation offered by the SMTG and SMB models.

As it can be seen in Figures 3.2-3.5, one can remark that the accuracy of the SMTG and SMB models, relative to the case of mobile users, provide better accuracy than the

(a) PDF: $\Psi = 90°$.   (b) CDF: $\Psi = 90°$.   (a) PDF: $\Psi = 90°$.   (b) CDF: $\Psi = 90°$.

(c) PDF: $\Psi = 60°$.   (d) CDF: $\Psi = 60°$.   (c) PDF: $\Psi = 60°$.   (d) CDF: $\Psi = 60°$.
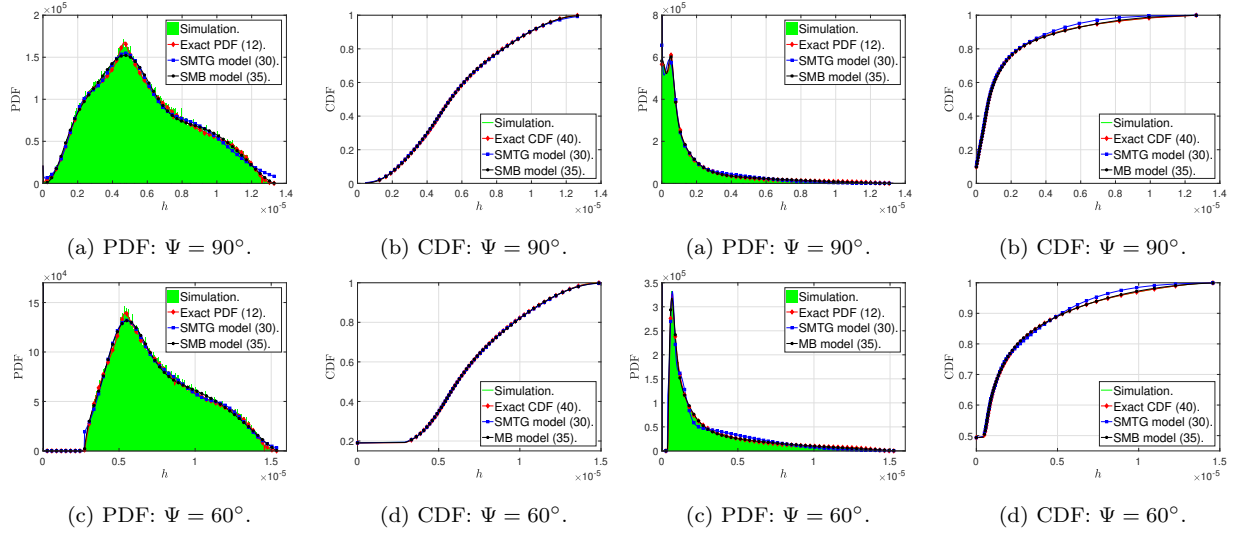
Figure 3.4: Comparison between the simulation, theoretical and approximation results of the PDF and the CDF of the LOS channel gain h_{LOS} for the case of mobile users when $R_{\mathrm{e}} = 1$ m.

Figure 3.5: Comparison between the simulation, theoretical and approximation results of the PDF and the CDF of the LOS channel gain h_{LOS} for the case of mobile users when $R_{\mathrm{e}} = 2.5$ m.

Table 3.3: KSD of SMTG and SMB models

	SMTG model		SMB model	
	$\Psi = 90°$	$\Psi = 60°$	$\Psi = 90°$	$\Psi = 60°$
$R_{\mathrm{e}} = 1$ m	0.0082	0.0037	0.0048	0.0030
$R_{\mathrm{e}} = 2.5$ m	0.0238	0.0156	0.0054	0.0047

MTL and MB models, which are associated with the case of stationary users. This can be also observed from the KSD values presented in Tables 3.2 and 3.3. This occurs mainly because for mobile users, the approximated PDF given in (3.28) is a mixture of three PDFs with nine parameters in total, whereas for the case of stationary users, the approximated PDF given in (3.17) is a single PDF expression with only three parameters in total. However, this better accuracy comes with a higher complexity, since for the MTL and MB models, we only need to estimate three parameters, whereas for the SMTG and SMB models, we need to estimate nine parameters.

3.6.2 Error Performance

Figures 3.6a and 3.6b present the average BER performance of the on-off keying (OOK) modulation versus the transmitted optical power P_{opt} for stationary users, when the radius

Figure 3.6: BER performance of OOK modulation versus the transmitted optical power for stationary and mobile users.

of the attocell $R_\mathrm{e} = 1$ m and 2.5 m and when the FOV of the UE $\Psi = 90°$ and $60°$. These figures shows that the BER results of the MTL and MB models match perfectly the simulated BER for both cases when $(R_\mathrm{e}, \Psi) = (2.5\,\mathrm{m}, 90°)$ and when $\Psi = 60°$. However, for the case when $(R_\mathrm{e}, \Psi) = (1\,\mathrm{m}, 90°)$, we remark that the average BER results of the MB model match the simulated BER better than the ones of the MTL model. This can be also seen from the values of the KSD in Table 3.2, where we can see that the KSD of the MB model is lower than the one of the MTL model when $(R_\mathrm{e}, \Psi) = (1\,\mathrm{m}, 90°)$. In other words, when $(R_\mathrm{e}, \Psi) = (1\,\mathrm{m}, 90°)$, the MB model offers a better accuracy than the MTL model. This is mainly due to the assumptions made for both models. In fact, when the radius of the attocell R_e is small and by referring to (3.4), the random variable $\cos(\Omega - \chi)$ is dominant in $\cos(\psi)$. Hence, assuming that the distribution of the random orientation of the UE can be approximated by a Beta distribution makes more sense.

Figures 3.6c and 3.6d present the average BER performance of the OOK modulation versus the transmitted optical power P_{opt} for mobile users, when the radius of the attocell $R_{\text{e}} = 1$ m and 2.5 m and when the FOV of the UE $\Psi = 90°$ and $60°$. These figures show that the BER results of the SMTG and the SMB models match perfectly the simulated BER for both cases when $(R_{\text{e}}, \Psi) = (2.5\,\text{m}, 90°)$ and when $\Psi = 60°$. However, for the case when $(R_{\text{e}}, \Psi) = (1\,\text{m}, 90°)$, we remark that the BER results of the SMB model matches the simulated BER better than the ones of the SMTG model. Similar to the case of stationary users, the SMB model offers better accuracy than the SMTG model when $(R_{\text{e}}, \Psi) = (1\,\text{m}, 90°)$ due to the assumptions made for both models.

In order to give insights about the different factors that affects the error performance of LiFi systems, we consider for comparison purposes the following three baseline scenarios.

- *Baseline 1:* A fixed orientation with an elevation angle $\theta = 0°$. This benchmark was considered in [54] for stationary users and in [58] for mobile users.

- *Baseline 2:* A fixed radial location with a polar distance $r = 0$ m.

- *Baseline 3:* A fixed radial location with polar distance $r = R$.

Figure 3.7 presents the BER of the OOK modulation of our proposed channel models and of the aforementioned baselines versus the transmitted optical power for a UE with a FOV $\Psi = 90°$ in a LiFi attocell with a radius $R_{\text{e}} = 1$ m. This figure demonstrates the effects of the random motion of the user and the random orientation of the UE in the error performance of LiFi systems. In fact, for the considered simulation setup, and for both cases of stationary and mobile users, Figure 3.7 shows that a target bit-error-rate of 10^{-4} can not be achieved due to these two factors. Hence, while designing indoor LiFi systems, these effects should be compensated.

Figures 3.6 and 3.7 show also two important facts about the BER performance of users. First, it can be seen that the BER performance degrades heavily when either the radius of the attocell R_{e} increases or the FOV of the UE decreases. Second, the BER saturates as the transmitted optical power increases. These two facts can be explained by the following corollary.

Corollary 3.1. *At high transmitted optical power, the average probability of error of the M-ary pulse amplitude modulation (PAM) for the considered LiFi system is given by*

$$\lim_{P_{\text{opt}} \to \infty} P_e\left(P_{\text{opt}}\right) = \frac{F_{\cos(\psi)}(\cos(\Psi))}{2}. \tag{3.35}$$

41
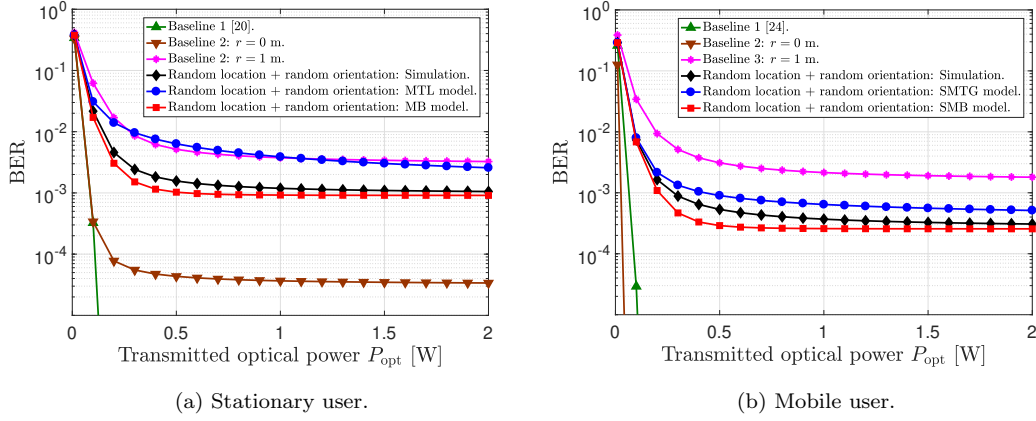
Figure 3.7: BER performance of the OOK modulation, versus the transmitted optical power, of our proposed channel models and of the aforementioned baselines. The FOV $\Psi = 90°$ the radius of the LiFi attocell $R_{\mathrm{e}} = 1$ m.

Proof. See Appendix A.4. ∎

The result of **Corollary 3.1** shows that, even when the transmitted optical power P_{opt} is high, the BER is stagnating at $\frac{F_{\cos(\psi)}(\cos(\Psi))}{2}$. This result is directly related to the case when the AP is out of the FOV of the UE. On the other hand, based on its expression in (3.12), $F_{\cos(\psi)}(\cos(\Psi))$ is a function of the attocell radius R_{e} and the FOV of the receiver Ψ. Therefore, since $d_{\max}$ increases as R_{e} increases, then $F_{\cos(\psi)}(\cos(\Psi))$ is an increasing function in R_{e}. In addition, since $x \mapsto F_{\cos(\psi)}(x)$ is a CDF, it is an increasing function, and due to the fact that $x \mapsto \cos(x)$ is a decreasing function within $[0, \pi/2]$, then $F_{\cos(\psi)}(\cos(\Psi))$ increases as the FOV Ψ decreases. The aforementioned reasons explain the poor BER performance of the LiFi system when either the radius of the attocell R_{e} increases or the FOV Ψ decreases.

From a practical point of view, the above observation can be explained as follows. Recall that

$$F_{\cos(\psi)}(\cos(\Psi)) = \Pr\left(\cos(\psi) \leq \cos(\Psi)\right) = \Pr\left(H \leq 0\right), \qquad (3.36)$$

which is literally the outage probability of the LiFi system, i.e., the probability that the UE is not connected to the AP even when it is inside the attocell. Obviously, for large values of R_{e} or small values of Ψ, the probability that the UE is not connected to the AP increases. This is mainly due to the effects the random location of the user along with the random orientation of the UE and it explains the poor BER performance in this case.

The question that may come to mind here is how can one enhance the performance of the LiFi system under such a realistic environment? Recently, some practical solutions

have been proposed in the literature to alleviate the effects of the random behaviour of LiFi channels. These solutions include the use of MIMO LiFi systems along with transceiver designs that have high spatial diversity gains such as the omni-directional transceiver [73] and the angular diversity transceiver [74]. Alternatively, we propose in the following subsection a new design for indoor LiFi cellular systems that can alleviate the effects of the random location of the users and the random orientations of their UEs.

3.6.3   Design Considerations of Indoor LiFi Cellular Systems

The concept of indoor cellular systems has been introduced in practical LiFi systems, where multiple LiFi APs coordinate together and serve multiple users within the resulting illuminated area [74–80]. Each LiFi AP creates an optical attocell and the respective illumination areas of the adjacent attocells overlap with each other. Consider the indoor LiFi cellular system shown in Figure 3.8, which consists of five APs that correspond to small and adjacent attocells, where each has a radius R_c. The distance between the AP of the attocell in the middle (green attocell), which we refer to as the reference attocell, and the APs of the remaining adjacent attocells is D_c. Let us assume that a user is located within the reference attocell, where all five APs are cooperating and coordinating together to serve this user by transmitting the same signal. One way to reduce the outage probability of the user, i.e., the probability that it is not connected to at least one of the APs, is through a well designed attocells radius R_c and APs spacing D_c that guarantee a maximum target probability of error P_e^{th}.

In this context, Figure 3.9 presents the BER performance of a user that is located within the reference attocell, where the FOV of the UE is $\Psi = 60°$. Both stationary and mobile cases are considered and different values of R_c and D_c are evaluated. By comparing the results of this figure and those of Figure 3.6, for the case when $R_e = 1$ m for example, we can see how the coexisting APs can significantly improve the BER performance of the system. In addition, we remark from Figure 3.9 that the choice of (R_c, D_c) has also a big impact on the BER performance. For example, for the case of a stationary user, the best choice among the considered values is $(R_c, D_c) = (1\,\text{m}, 1.5\,\text{m})$, whereas for the case of a mobile user, the best choice is $(R_c, D_c) = (1\,\text{m}, 1\,\text{m})$. Overall, for a target probability of error $P_e^{\text{th}} = 3.8 \times 10^{-3}$, we conclude that the choice $(R_c, D_c) = (1\,\text{m}, 1\,\text{m})$ is the best choice that guarantees the target performance jointly for both stationary and

(a) Top view.

(b) Horizontal view.

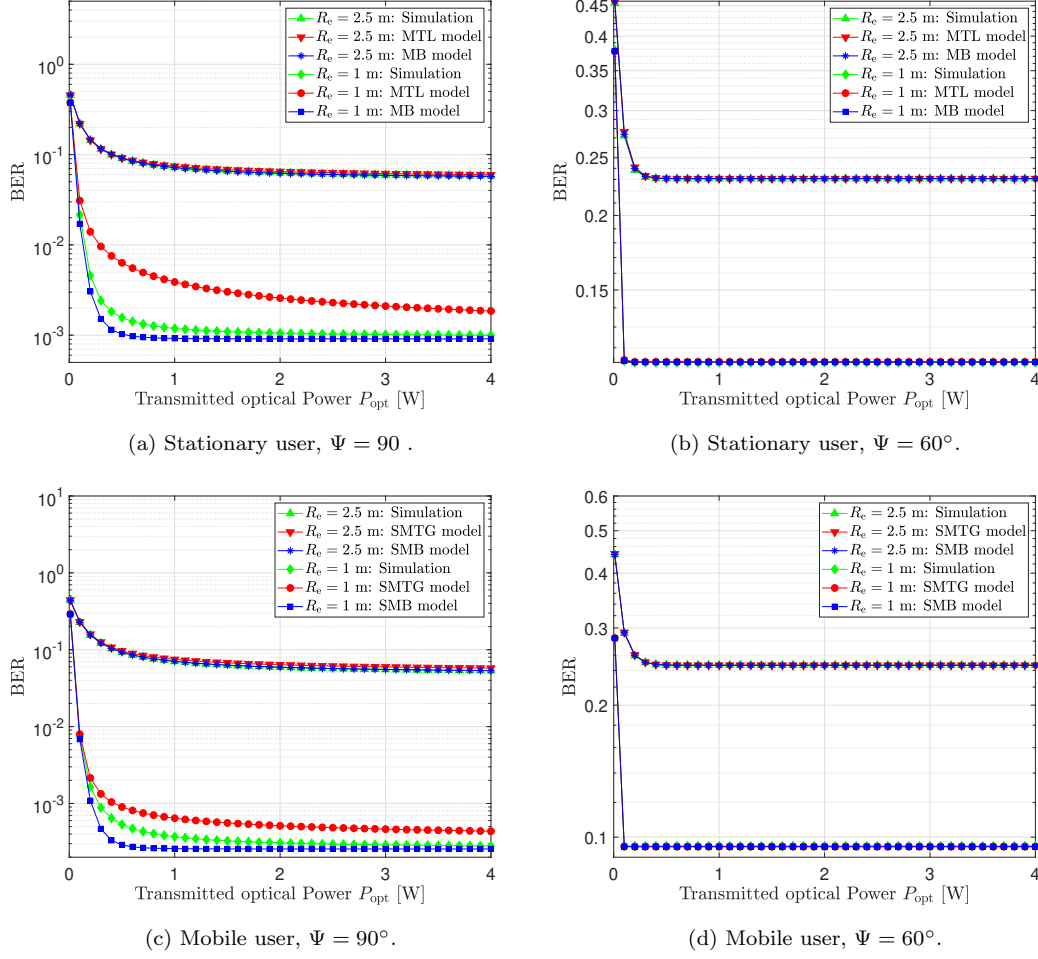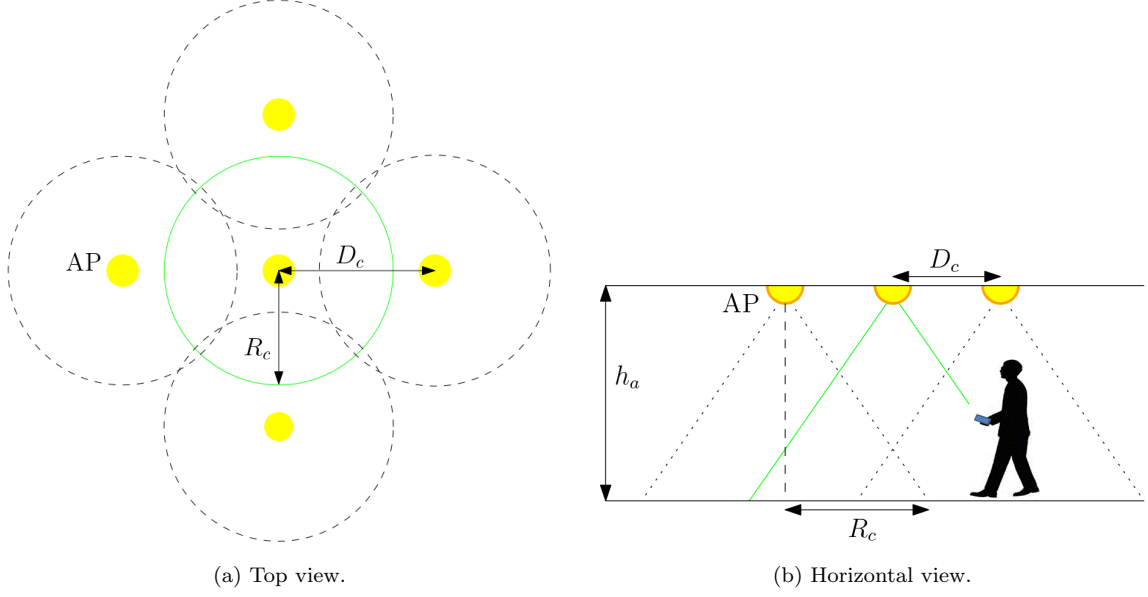Figure 3.8: An indoor multi-cell LiFi system.

(a) Stationary user.
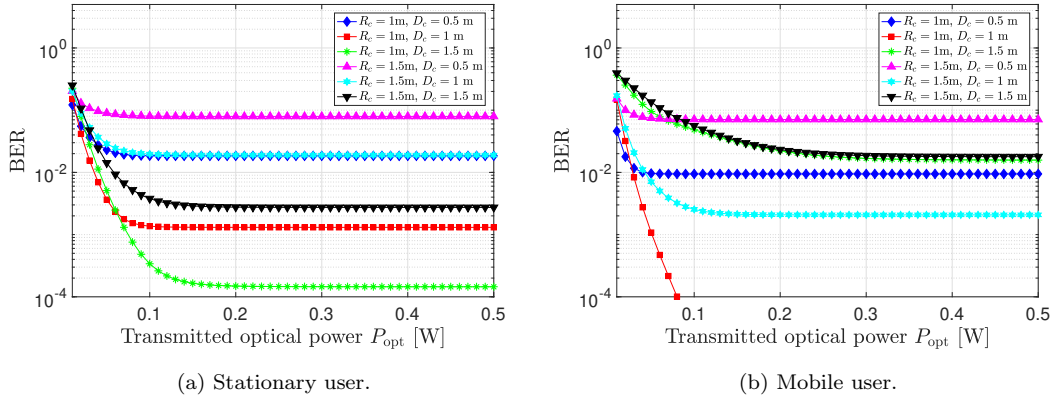
(b) Mobile user.

Figure 3.9: BER performance of OOK modulation versus the transmitted optical power for stationary and mobile users when the FOV $\Psi = 60°$.

mobile users. Obviously, the optimal (R_c, D_c) depends on the geometry of the attocells and the parameters of the UE as well, such as the height of the APs and the height of the UE.

3.7 Conclusion

In this chapter, novel, realistic, and measurement-based channel models for indoor LiFi systems have been proposed. The statistics of the LOS channel gain are derived for the case of stationary and mobile users, where the LiFi receiver is assumed to be randomly oriented. For stationary users, the MTL and the MB models were proposed, whereas for the case of mobile users, the SMTG and SMB models were proposed. The accuracy of

each model was evaluated using the KSD. In addition, the effect of random orientation and spatial distribution of users on the error performance of users was investigated based on the derived models. Our results showed that the random behaviour and motion of users has strong effect on the LOS channel gain. Therefore, we proposed a novel design of indoor LiFi cellular systems in order to guarantee the required reliability performance for LiFi communication links.

Since a competent transceiver requires developing not only capable transmitter structures but also efficient receiver designs, we aim in the next chapter to provide an efficient design for LiFi devices that are able to alleviate the effects of the user mobility, random orientation, and the impurities of indoor environment, such as blockage.

Chapter 4

Multi-Directional Receiver (MDR) for Indoor LiFi Systems

4.1 Motivation and Related Works

Different data transmission techniques, which originate from RF wireless communication, are modified and adopted for OWC. Many of the developed communication techniques are validated by experiments and are even standardized [16, 81]. For instance, the single-carrier modulation format OOK is used in IEEE 802.15.7 [81] as a simple technique which could also provide dimming. However, high data rates cannot be achieved using OOK. Therefore, parallel transmission techniques are proposed to increase the spectral efficiency. Multi-carrier modulation techniques, such as orthogonal frequency division multiplexing (OFDM) [82], wavelength division multiplexing (WDM) [83], and MIMO techniques [42], are among the most common realizations of parallel data transmission. Each of these techniques has several variants which make them favorable in various conditions [18].

Spatial modulation (SM) is a type of MIMO structure that offers enhanced spectral efficiency compared to non-MIMO systems, and is more energy efficient with lower complexity as compared to full MIMO (i.e., spatial multiplexing while using all available transmitters) [84]. In SM, part of the information is mapped on the degrees of freedom in the spatial domain, and the remaining part is mapped on the signal domain [85]. In optical SM, the selection of one or more APs forms the *spatial information*. A modulation format is also used to map the *signal information* for each selection of APs. Usually, PAM is used for modulating the signal information [86]. Space shift keying (SSK) and

generalized space shift keying (GSSK) are two modulation schemes that are used when OOK is chosen for signal modulation [87–89]. The performance of SM is well studied theoretically and experimentally, and its advantages and potential practical applications are highlighted [90]. An important benefit of SM is the absence of interference from other transmitter units in single user scenarios. However, as expected for any MIMO system, the performance of SM also heavily depends on the channel conditions [88]. This problem is more severe in OWC where the transmitter and/or receiver units are usually placed close to each other, and thus, the channel matrix may become ill-conditioned [42, 86]. Moreover, the performance of the system significantly changes for different environments, activities, user positions, and device orientations. Only a few studies have considered the impact of random orientation in their analysis, see for instance [28, 33, 91–96] and references therein. All these works signify the importance of incorporating device orientation. The other important metric that can influence the system performance is the blockage of the optical channel by the user itself, known as self-blockage, or by other users or objects, and this consequently can interrupt the communication link. Blockage has been modeled in both millimeter wave and LiFi systems [97–99].

4.2 Contributions and Outcomes

Against the above background, we present in this chapter a bidirectional communication framework for an indoor LiFi environment. We adopt downlink channel models derived from real-life measurements, which makes the proposed framework relevant to the deployment efforts of LiFi networks. The adopted models encompass the combined effect of user mobility, random orientation, and blockage. We note that this is the first time that such factors are incorporated into the design and analysis of LiFi networks when SM is employed. Among the considered performance measures are the BER and the spectral efficiency. Motivated by the fact that SM is highly energy efficient, we adopt a variation of it to ensure that the least amount of energy is needed to achieve a target BER and spectral efficiency.

It has been now well established that correlation among the channel gains between the transmit and receive elements affects the performance of SM. To this end, we consider two representative configurations of PD placements. In the first configuration, we assume that the PDs are placed uniformly at one end of the UE, and in the second configuration,

the PDs are placed on different edges of the UE. We refer to the first configuration as screen receiver (SR), and multi-directional receiver (MDR) for the second configuration. The motivation behind introducing the latter configuration is twofold. First, SM performs best when the channel gains are uncorrelated, i.e., the performance degrades with correlation. Second, the random orientation may give rise to the problem of ill-conditioned channel matrices for the SR configuration, suggesting that a few sub-channels become inadequate to support reliable transmission.

The random orientation of the UE is modeled based on the experimental measurements reported in [28] and presented in Section 2.3 to obtain the instantaneous orientation of PDs. Furthermore, not only is LOS considered but also NLOS channel gains are included to have an accurate channel model. Also, the blockage of the optical channel by human users and other random objects is considered. Therefore, a channel model that is close to realistic scenarios is incorporated which makes the methods and results presented in this chapter reliable for future system design.

We study the robustness of MDR in conjunction with SM against random orientation and blockage and show the impact of the channel on the overall performance. To improve the performance further, we propose using an adaptive SM (ASM) scheme in which the order of SM (i.e., the number of active APs) is determined based on the strength of the channels between the APs and PDs. We examine the proposed ASM scheme for both sitting and walking activities. For sitting activities, about 10^4 locations in a 5 m $\times$ 5 m room are considered, while for the walking activities, an orientation-based RWP (ORWP) mobility model is applied. It is observed that such adaptive methods significantly improve the performance. As a benchmark, we compare the proposed adaptive method with a spatial multiplexing MIMO system for different spectral efficiencies. The results confirm that the proposed ASM is more efficient. Moreover, the proposed MDR method can achieve up to twice the spectral efficiency of SR for the same SNR and target BER.

In light of the above discussion, we may summarize the chapter contributions as follows.

- Based on real-life measurements, we adopt a practical channel model that incorporates LOS and NLOS channel gain components, user mobility, UE random orientation, and link blockage. The effect of each of these phenomena on the performance of SM is studied.

- We investigate the impact of different component placement configurations on the system performance. We show that placing the PDs on different sides of the UE (i.e. MDR) makes the system robust against blockage and random orientation.

- We propose an ASM scheme in an effort to optimize the system performance. We propose algorithms for selecting the optimal number of used APs for a given target spectral efficiency and reliability.

- The performance of the downlink is investigated over the whole area of a typical indoor environment for walking and sitting activities. It is demonstrated that the MDR structure along with ASM improves the performance significantly. Furthermore, we show that the proposed framework is superior to spatial multiplexing MIMO systems.

The results presented in this chapter signify the importance of including different phenomena for modeling the communication channel such as NLOS channel gain, random orientation of UE, link blockage, and mobility. Moreover, it is demonstrated that a robust energy efficient bidirectional communication channel can be established by a simple practical MDR as well adaptive spatial modulation scheme which can outperform spatial multiplexing MIMO systems.

The rest of the chapter is organized as follows. The system model is presented in Section 4.3. Section 4.4 presents the link blockage modeling. In Section 4.5, the downlink performance is studied. Finally, the chapter is concluded in Section 4.6.

4.3   System Model

In this section, the channel model is described, and the basics of SM are explained. The system model can be used for both downlink and uplink transmissions.

4.3.1   Channel Model

The IM/DD optical wireless MIMO channel is considered, where N_t APs can transmit the signal and one UE receives the signal with N_r PDs. The resulting channel is described as:

$$\mathbf{y} = \lambda \mathbf{H} \mathbf{x} + \mathbf{n}, \tag{4.1}$$

where $\mathbf{x}$ is the transmitted signal vector of size $N_\mathrm{t} \times 1$, and $\mathbf{y}$ and $\mathbf{n}$ are $N_\mathrm{r} \times 1$ vectors respectively representing the received signal and noise at each PD. The noise is assumed to be real valued additive white Gaussian $\mathcal{N}\left(\mathbf{0}_{N_\mathrm{r}}, \sigma_\mathrm{VL}^2 \mathbf{I}_{N_\mathrm{r}}\right)$ and independent of the transmitted signal [42]. The variance of the noise is equal to $\sigma_\mathrm{VL}^2 = N_\mathrm{VL} B_\mathrm{VL}$, where N_VL is the noise single sided power spectral density and B_VL is the visible light bandwidth available at the APs. In addition, as was explained in Section 2.1, $\lambda = T R_\mathrm{p} \eta N_\mathrm{LEDs}$, in which T is the TIA amplifier gain at the receiver, R_p is the responsivity of the receiver's PD, η is the current-to-power conversion efficiency of the LEDs, and N_LEDs is the number of LEDs per AP. Moreover, as was presented in Section 2.2, the channel matrix $\mathbf{H}$ is given by:

$$\mathbf{H} = \begin{pmatrix} h_{1,1} & \cdots & h_{1,N_\mathrm{t}} \\ \vdots & \ddots & \vdots \\ h_{N_\mathrm{r},1} & \cdots & h_{N_\mathrm{r},N_\mathrm{t}} \end{pmatrix}, \tag{4.2}$$

where the entity $h_{i,j}$, for all $(i,j) \in [\![1, N_\mathrm{r}]\!] \times [\![1, N_\mathrm{t}]\!]$ is the channel gain of the link between the jth transmitter and the ith PD, which can be expressed as $h_{i,j} = h_{i,j}^\mathrm{LOS} + h_{i,j}^\mathrm{NLOS}$, where $h_{i,j}^\mathrm{LOS}$ is the LOS and $h_{i,j}^\mathrm{NLOS}$ is the NLOS channel gain.

The performance of a MIMO system depends heavily on the channel matrix. In this chapter, we include the random device orientation in our analysis. Moreover, objects and people may be placed close to the UE and block all or part of the light reaching one or more PDs. The details blockage modeling will be presented in Section 4.4.

4.3.2 Spatial Modulation

SM was first introduced in [84], which can provide the spectral and energy efficiency fulfillment of the next generation wireless communications. We review the basics of SM in this section and elaborate on how we adapt SM to the optical communication. More details can be found in [86–88, 100–103] and references therein.

Following the basic principles of SM, the spatially distributed APs are utilized to carry data along with the transmitted signal. In the original SM format [86], only one AP is turned on at each time instant. Let $N_\mathrm{a} \leq N_\mathrm{t}$ be the number of used APs, chosen out of N_t APs. Thus, by activating only one AP at each channel use, $\log_2(N_\mathrm{a})$ bits (the spatial information) are transmitted by SM. The transmitted symbol by an individual AP is also encoded by an M-ary PAM constellation. Hence, the spectral efficiency is $R = \log_2(M) + \log_2(N_\mathrm{a})$ bit/sec/Hz. Note that, unlike spatial multiplexing (i.e., full MIMO),

even one PD can be sufficient for signal detection because only the differences between all possible received symbols determine the system performance. This highlights the benefit of SM which is simple and is capable of potentially satisfying communication requirements when some PDs are blocked and not available. If only the spatial dimension is used to encode data, the system is referred to as space shift keying (SSK) with spectral efficiency of $\log_2(N_a)$. Moreover, the system is called generalized space shift keying (GSSK) if information bits are assigned to all combinations of APs with a single level modulation.

In this chapter, we consider activating one of the available N_a APs with an M-PAM modulation format, which results in a total of MN_a symbols. The intensity levels of the M-PAM are given by

$$I_m = \frac{2I_{\mathrm{DC}}}{M+1}m, \quad \text{for } m = 1, \dots, M, \tag{4.3}$$

where I_{DC} is the DC bias. Therefore, one of the available N_a APs transmits one of the M levels at each channel use, and the input vector $\mathbf{x} = \mathbf{x}_k$, $k = 1, \dots, MN_a$, is chosen from the columns of the $N_a \times MN_a$ matrix $\mathbf{X} = [I_1\mathbf{I}_{N_a} \ I_2\mathbf{I}_{N_a} \ \cdots I_M\mathbf{I}_{N_a}]$, where $\mathbf{I}_{N_a}$ is the square unity matrix of size N_a. At the Rx, the maximum-likelihood detection is performed. An error occurs whenever a transmitted vector $\mathbf{x}_p$ is detected mistakenly as another vector $\mathbf{x}_q$, with $(p,q) \in [\![1, MN_a]\!]^2$. As such, the upper bound on the BER can be derived using the union bound method as

$$\begin{aligned}
\mathrm{BER}\,(M, E_x, \mathbf{H}) \simeq &\frac{1}{MN_a\log_2(MN_a)}\sum_{k_1=1}^{MN_a}\sum_{k_2=1}^{MN_a}\mathrm{d_H}(b_{k_1}, b_{k_2}) \\
&\times Q\left(\sqrt{\frac{\lambda^2\gamma_{\mathrm{Tx}}}{4I_{\mathrm{DC}}^2}||\mathbf{H}(\mathbf{x}_{k_1} - \mathbf{x}_{k_2})||^2}\right),
\end{aligned} \tag{4.4}$$

where $\gamma_{\mathrm{Tx}} = \frac{E_s}{N_{\mathrm{VL}}}$ is the average transmit SNR, in which E_s is the mean emitted electrical energy, $Q(\cdot)$ is the Q-function, and for all $(p,q) \in [\![1, MN_a]\!]^2$, $\mathrm{d_H}(b_{k_1}, b_{k_2})$ is the Hamming distance between the two bit allocations of b_{k_1} and b_{k_2} corresponding to signal vectors $\mathbf{x}_{k_1}$ and $\mathbf{x}_{k_1}$, respectively. It has been shown in the literature [42] and later in the chapter that (4.4) is a tight bound at a high SNR. We define the received SNR γ_{Rx} by considering the received signal energy as the total received signal energies at all N_r PDs. Therefore, the received SNR can be expressed as [42]:

$$\gamma_{\mathrm{Rx}} = \frac{\lambda^2\gamma_{\mathrm{Tx}}}{N_a^2}\sum_{i=1}^{N_r}\left(\sum_{j=1}^{N_a}h_{i,j}\right)^2. \tag{4.5}$$

It can be seen from (4.4) that the error performance of SM directly depends on the channel matrix which determines the differentiability between signal vectors. We can assume that all PDs are placed on the screen of a smartphone, as shown in Figure

51
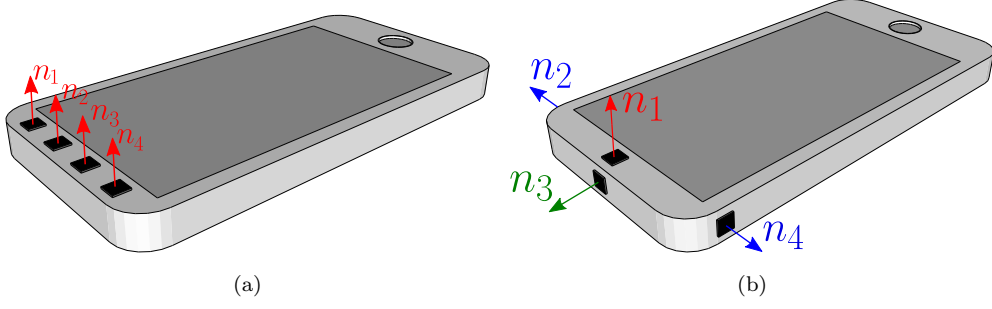
Figure 4.1: The SR and MDR structures for a hand-held smartphone

4.1a. However, this results in poor performance due to two issues. First, the resulting channel matrix is likely to be highly ill-conditioned because PDs are placed close to each other and this gives rise to correlation [35]. Second, it is highly likely that some of the transmitters are out of the FOV of all PDs since usually the smart phone is held with an orientation other than upward. Therefore, we propose another structure by placing the PDs on the screen and three other sides of the mobile device, as shown in Figure 4.1b. Note that another PD can be placed at the back, which can be activated instead of the one on the screen for situations where the user is lying on a horizontal surface. We call this structure the "multi-directional receiver" (MDR), which solves both above-mentioned problems. We investigate the performance of both structures later in the chapter. We refer to the structure in Figure 4.1a as the screen receiver (SR). It should be noted that, in either structure, since the PDs are located at the top of the cellphone, there is a very low probability that they will be covered by the user's hand when the cellphone is being used.

4.4 Link Blockage

Due to the nature of OWC, the link between a pair of Txs and Rxs can be blocked by an opaque object. In this study, we consider the blockage due to a human body and other similar objects, which can be modeled as rectangular prisms. It is shown in [97] that MIMO can help the optical wireless networks to be robust against blockage because the transmit or receive diversity is exploited. Here the model for link blockage is introduced, which is used throughout the chapter. In this study, we model a human body as a rectangular prism of length L_{b}, width W_{b}, and height H_{b}. Two types of blockers are assumed, non-user blockers and user-blockers. The former is due to the other
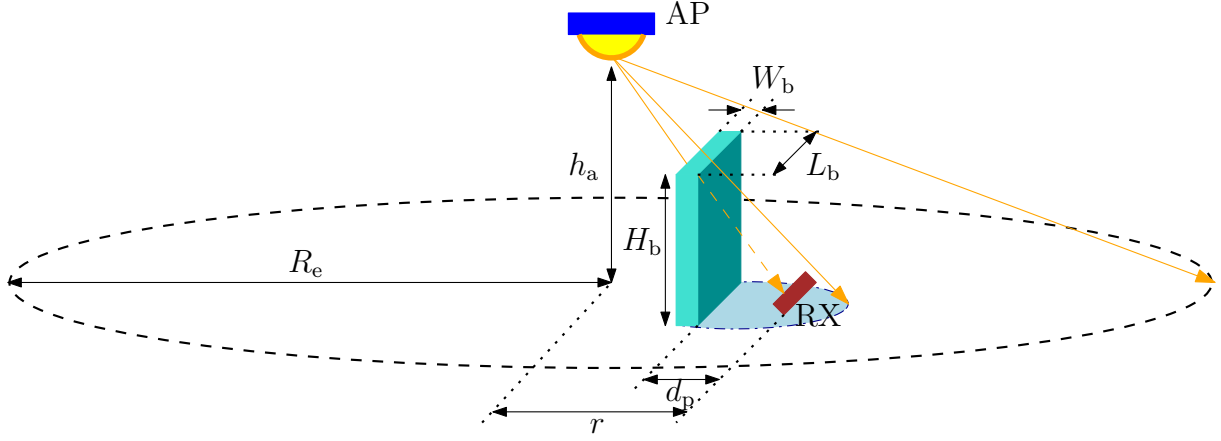
Figure 4.2: Geometry of link blockage.

people or objects in the indoor environment while the latter is due to the user who is using the actual UE, also known as self-blockage. Thus, one user-blocker is considered in the direction that the user is facing, and other non-user blockers' directions are chosen from a uniform distribution of $\mathcal{U}[0°, 360°]$. Figure 4.2 shows the blockage model and the parameters that are considered in this study. The density of a non-user blocker is denoted by κ_b, which is the number of non-user blockers per area. It is assumed that non-user blockers are uniformly distributed in the indoor environment. The direction and location of the self-blocker are obtained based on the direction and location of the UE. It is assumed that the users keep the UE at a distance of d_p away from themselves.

The availability of the CSI is essential for the implementation of SM, as explained in Section 4.3.2. The measurement results reported in [28] show that the coherence time for the orientation angles are in the order of several hundred milliseconds, and we assume that the coherence time for the channel matrix is also similar. Therefore, it can be assumed that the channel gains are known for each transmitted data block of a length smaller than the channel coherence time. However, there can be errors in the estimation of the LiFi channel gains, which could be independent of the channel gains themselves [104–106]. An estimation error causes additional errors depending on the estimation method used. However, we assume that the estimation error can be ignored throughout this chapter. An individual study can be carried out in the future to investigate the effect of the channel estimation error in different conditions and for various estimation methods.
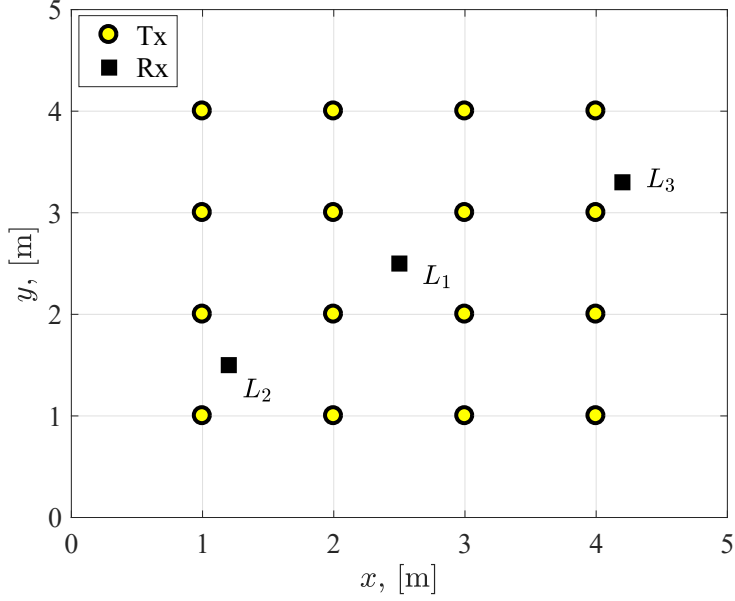
Figure 4.3: Room geometry and transmitters arrangement.

4.5 Performance Evaluation

4.5.1 System Configuration

In this chapter, we consider a typical indoor environment. Although the results may change slightly in other scenarios, it is expected that the same behavior will be observed provided that the main characteristics of the environment, such as transmitter separation, the room dimensions and the ceiling height, etc., do not vary dramatically. Figure 4.3 shows the geometric configuration of the transmitters which are arranged on the vertexes of a square lattice over the ceiling of a room. This configuration is used throughout the chapter, where $N_\mathrm{t} = 16$ APs are considered in a room of $5 \times 5 \times 3$ m^3. The APs are oriented vertically downward, while the receivers may have a random orientation as depicted in Section 2.3.

The parameters used throughout the chapter are shown in Table 4.1. The dimensions of the smartphone are $14 \times 7 \times 1$ cm^3. As shown in Figure 4.1, the PDs on the screen are placed 1 cm from the top edge. One PD for MDR is considered at the center of the screen side, and 4 PDs for SR are uniformly distributed. For MDR, the PD associated with $\mathbf{n}_3$ is placed at the center of the corresponding side, and PDs shown by $\mathbf{n}_2$ and $\mathbf{n}_4$ are placed 1.5 cm from the top edge.

Table 4.1: Simulation Parameters

Parameter	Symbol	Value
Room dimensions	$L_{\mathrm{r}} \times W_{\mathrm{r}} \times H_{\mathrm{r}}$	5 m×5 m ×3 m
AP height	h_{a}	2.95 m
UE height (sitting)	h_{u}	0.8m
UE height (walking)	h_{u}	1.4m
Receiver FOV	Ψ	60°
LED half-power semiangle	$\Phi_{1/2}$	60°
PD responsivity	R_{p}	1 A/W
Physical area of a PD	A_{PD}	0.25 cm^2
LED conversion factor	η	0.7 W/A
Reflectivity factor of walls	ξ_{w}	0.6
Reflectivity factor of the floor	ξ_{f}	0.2
Reflectivity factor of the ceiling	ξ_{c}	0.8
Length of the blockers	L_{b}	0.7 m
Width of the blockers	W_{b}	0.2 m
Height of the blockers	H_{b}	1.75 m
UE distance from user	d_{p}	0.3m
VL bandwidth	B_{VL}	20 MHz
VL Noise power spectral density	N_{VL}	10^{-21} W/Hz

4.5.2 The Effect of Blockage and Random Orientation

In this section, we investigate the effect of low and high density receiver blockage, random orientation, and the NLOS channel component. First, an example scenario is considered at the middle of the room (i.e., location L_1 in Figure 4.3) with a fixed AP allocation with $N_{\mathrm{a}} = 4$ and a spectral efficiency $R = 5$ bit/sec/Hz. The user direction is $\Omega = 90°$. The APs are determined by measuring the received power from each AP, and the strongest $N_{\mathrm{a}} = 4$ APs, i.e., the ones corresponding to the highest received power at the user position, are selected. The results are shown in Figure 4.4a for both BER approximation in (4.4) (solid lines) and Monte-Carlo simulations (markers). Note that the statistics of the random orientation for sitting activities are used according to Table 2.1 in Section 2.3 for Laplace distribution.

It is observed in Figure 4.4a that the simulation results match the BER approximation at around BER $\geq 10^{-2}$ for both cases. The performance of both SR and MDR are significantly degraded when the NLOS channel gains are ignored because it is highly likely that the channel gains for some of the APs are zero due to blockage or limited FOV. In such a case, the information will be lost, and the BER saturates at a high SNR.
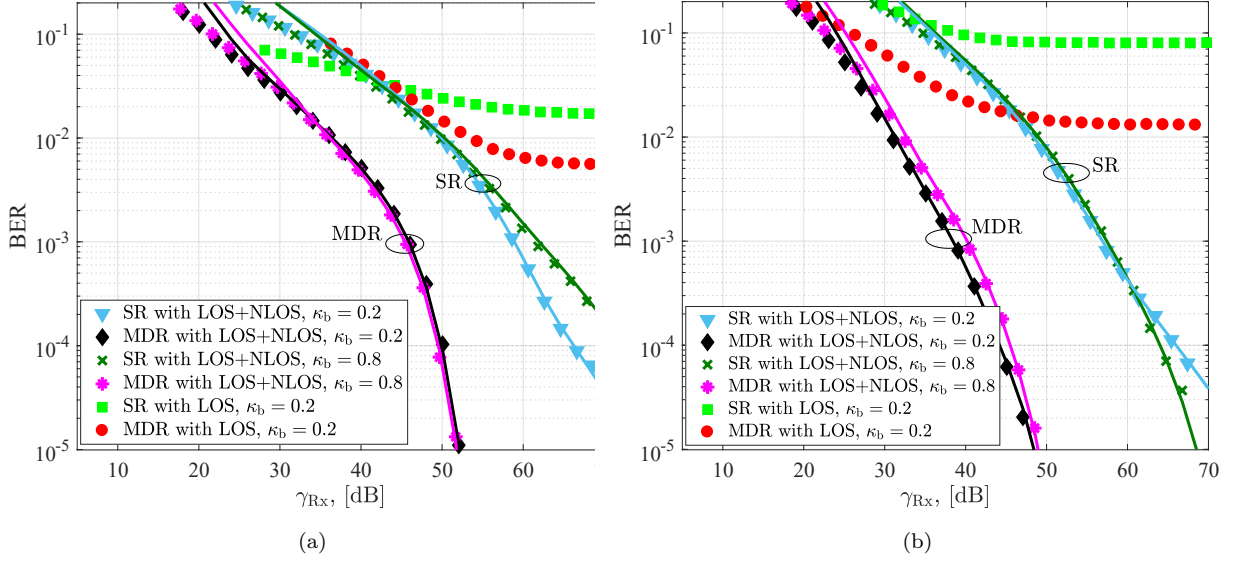
Figure 4.4: Performance comparison of SR and MDR for UE's location of a) L_1 and direction of $\Omega = 90°$ b) L_3 and direction of $\Omega = 180°$. Marks denote Monte-Carlo simulation results and solid lines are based on the BER upper bound given in (4.4).

The BER approximation (4.4) is not valid in this case and is not shown in Figure 4.4a. When the NLOS gain is included, the performance of MDR is always better than SR with SNR gains up to 12 dB at target BER 3.8×10^{-3}. For SR, when the blockage parameter is increased, the BER increases because the probability of blocking all PDs and having an ill-conditioned channel matrix increases. On the other hand, an increased blockage is beneficial for MDR since the induced randomness increases the differentiability between spatial symbols, which consequently leads to better performance. Overall, it can be seen that the proposed MDR structure is robust against random orientation and blockage, and exhibits superior performance compared to the conventional SR.

Another location, L_3 in Figure 4.3, is also considered with user direction $\Omega = 180°$. In this case the user is facing the room and the UE screen is facing the wall. The results are shown in Figure 4.4b. In this scenario the effect of the NLOS channel gain is much more significant. Note that, unlike L_1, the channel matrix is non-symmetric at L_3, which generally leads to better performance compared to L_1. Again, MDR outperforms SR in all conditions, and demonstrates a robust performance against random orientation and blockage. In Figure 4.4b, the link blockage adversely affects the BER performance because the channel matrix is already non-symmetric, and blockage slightly worsens the channel matrix. The results shown in Figures 4.4a and 4.4b confirm that the proposed MDR outperforms SR and is robust against random orientation and blockage. However, the

56

exact performance depends on the user location. This will be investigated later in this section, but first the effect of AP selection is studied.

4.5.3   AP Selection

In the previous subsection, the number of selected APs was fixed and the APs were selected based on the received power at the UE location, direction and orientation. It is expected that the choice of parameter N_a can affect the performance of the system with fixed target BER and spectral efficiency. Therefore, the BER performance of MDR and SR are shown in Figure 4.5 for position L_2 (see Figure 4.3) with $\Omega = 0°$ and for $R = 5$ bit/sec/Hz and $N_a = 1, 4, 16$. It is observed that the BER varies for each choice of N_a. Note that, according to the definition of SM in Section 4.3.2, the modulation order M varies for each selection to keep the spectral efficiency equal to $R = 5$ bit/sec/Hz. For MDR, $N_a = 16$ achieves the best performance while $N_a = 1$ is the best choice for SR in this specific scenario. It is also observed that $N_a = 4$ leads to lower BER compared to $N_a = 16$ and $N_a = 1$, respectively for SR and MDR, at low SNRs. It should be emphasized here that the results may be different for other locations. Therefore, it is beneficial to define an adaptive AP selection, which determines the best choice of N_a for each scenario.

Figure 4.5 is an example which highlights the importance of AP selection. A simple method can be defined based on this observation, and an adaptive SM (ASM) is defined. The parameter N_a is determined at each user position, direction, and UE orientation in order to select the one associated with the minimum energy requirement at the target BER 3.8×10^{-3}. This simple method is performed by calculating the required γ_{RX} based on BER approximation (4.4) which is a tight approximation for the target BER.

In order to evaluate the performance of the proposed adaptive SM, the room area is divided into uniformly distributed points that are 25 cm apart in x and y directions. At each point, 24 user directions (every $15°$) are used, and 500 random orientation angles are generated for each user position and direction. The CDF of the required received SNR over the room is demonstrated in Figure 4.6 for MDR and SR structures. Fixed APs numbers of $N_a = 1$ and 16 are depicted along with the adaptive method, in which the optimum number is determined from $N_a \in \{1, 2, 4, 8, 16\}$ for each user position, direction, and UE orientation. As expected, the minimum energy consumption is achieved by using this simple adaptive method, and MDR significantly outperforms SR. However, it can be
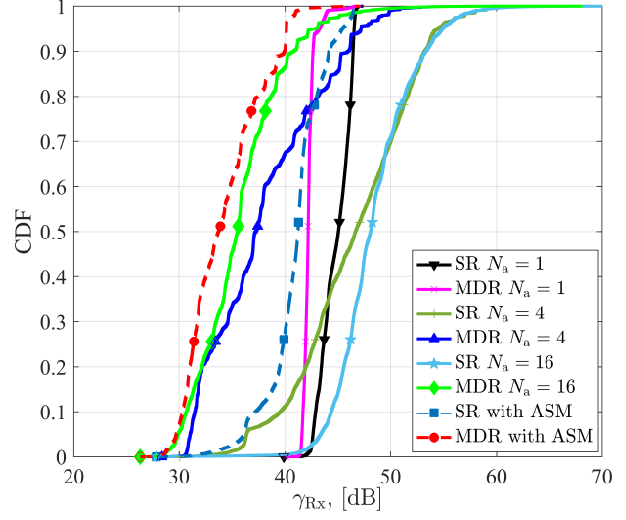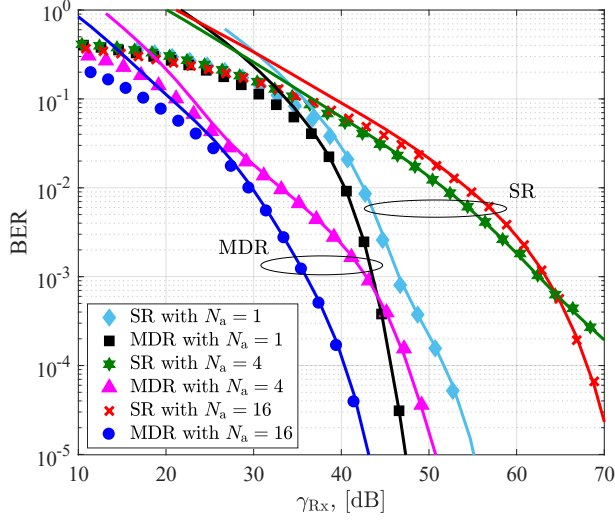
Figure 4.5: Performance comparison of SR and MDR for UE's location of L_2 and direction of $\Omega = 0°$. Markers denote Monte-Carlo simulation and solid lines are based on the BER approximation given in (4.4).

Figure 4.6: Performance comparison of SR and MDR for all UE's locations and directions in the room.

seen that the CDF of the received SNR for ASM with the MDR method is similar to the fixed AP selection with $N_a = 16$. This indicates that whenever the complexity is a limiting factor, fixing $N_a = 16$ can be used for MDR. However, a similar statement is not applicable to SR.

4.5.4 Mobility

Performance analysis with consideration of user mobility is crucial in the design of wireless communication networks. The simple adaptive algorithm used for the sitting scenario is also incorporated here in conjunction with the ORWP model. About 500 random waypoints are generated and the user walks between these points with a constant speed of 1 m/s. The required received SNRs are calculated along the user's route for $N_a \in \{1, 2, 4, 8, 16\}$ and the adaptive scheme for a target BER of 3.8×10^{-3} and spectral efficiency of $R = 5$ bit/sec/Hz. The results are shown in Figure 4.7 for $N_a = 1, 4, 16$ and ASM. Note that ASM is carried out with the choice of $N_a \in \{1, 2, 4, 8, 16\}$ for each channel realization. Comparing Figures 4.7a and 4.7b, it is observed once again that the MDR method requires lower received SNR around the environment. By using ASM, more than 10 dB reduction in the required SNR is achieved for MDR compared to SR. The ASM for SR does not change the required SNR value compared to $N_a = 1$, and therefore, $N_a = 1$
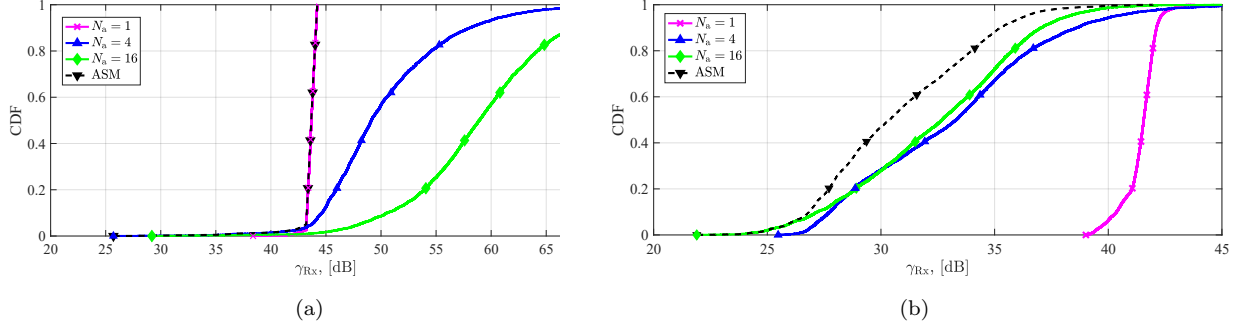
Figure 4.7: Performance comparison of (a) SR and (b) MDR for mobile users based on RWP mobility model for different number of active APa and ASM.

is almost optimal for SR in the walking scenario. However, MDR with ASM improves the performance by about 2 dB compared to the best fixed allocation $N_{\mathrm{a}} = 16$.

In Figure 4.8, the CDF of the required received SNR is simulated for ASM with MDR and SR. Two different spectral efficiency values, namely, $R = 4$ and 8 bit/sec/Hz, are chosen. Moreover, a 4×4 full MIMO (i.e., spatial multiplexing) is also considered with both structures. For full MIMO, the strongest 4 APs are selected for each channel realization, and the required received SNR is calculated using the union bound method for the BER approximation [42]. Since only four PDs are available, a 4×4 MIMO is the highest MIMO order that can be realized. However, SM does not require an equal number of transmitters and receivers, and therefore it benefits from a larger number of available APs. Interestingly, it is observed that the proposed ASM method outperforms the full MIMO system by demanding a lower received SNR at the target BER. As expected, a higher spectral efficiency requires more received SNR in any case. Note that the full MIMO system also benefits from the improved channel condition with MDR. As a result, its performance is close to that of ASM at $R = 8$ bit/sec/Hz because the full MIMO utilizes all available spatial degrees of freedom [18].

4.6 Conclusion

In this chapter, the effects of mobility, random orientation, and blockage, on indoor optical SM were investigated while adopting a channel model derived from real-life measurements. A new user device configuration, called MDR, was proposed to overcome the problem of high channel correlation. In addition, an adaptive SM scheme based on AP selection for downlink was proposed to overcome the effect of random orientation and
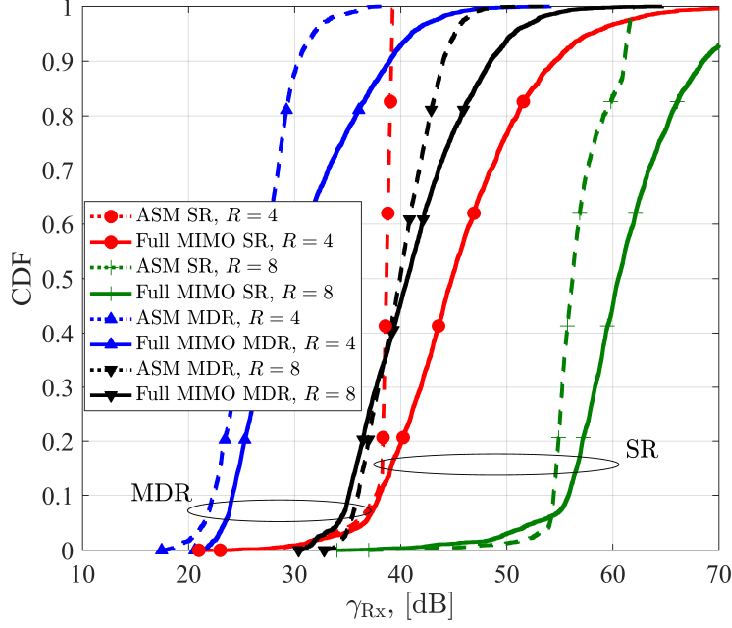
Figure 4.8: Performance comparison of SR and MDR for mobile users with ASM and full MIMO utilization.

blockage and to reduce the power consumption. It was shown that MDR provides a superior performance in terms of SNR and BER and significantly outperform its counterpart SR configuration.

As was mentioned in Chapter 3 and in this chapter, an important component in the optimization of LiFi systems is the channel gain between the transmitter and the receiver. Hence, one crucial factor in the optimization of LiFi systems is the acquisition of the CSI between different LiFi nodes. Nevertheless, as was presented in Section 2.2, the LiFi channel gain depends mainly on the position and orientation of LiFi receivers. Motivated by this, the next chapter focuses on the joint estimation of LiFi user's position and orientation, which are needed not only for indoor LiFi-based and localization services and applications, but also for the CSI acquisition.

Chapter 5

Estimation of Indoor LiFi User Position and Orientation

5.1 Motivation and Related Works

Nowadays, the availability of location and data of mobile terminals at the communications stations (APs and base stations (BSs)), i.e., their knowledge by the telecommunications operators, has become a key factor in enabling next generation communication systems. Such information enables better estimation of the quality of the wireless links, which can improve the resource management and provide new location-based services [107]. Nevertheless, the knowledge of UE's position and orientation is a crucial factor for indoor location-based applications such as robotic navigation [108] and autonomous parcel sorting [109]. Although Wireless Fidelity (WiFi) and Bluetooth are the most utilized positioning systems, which have already been widely deployed in current smart devices, they cannot satisfy the requirements of the above applications (joint UE position and orientation estimation) and their localization performance suffers from the limited number of available APs in their local area [110]. Due to this issue, novel and accurate LiFi-based position and orientation estimation solutions are highly demanded.

Over the past few years, many algorithms for LiFi-based indoor positioning have been proposed and verified by experiments. LiFi-based indoor positioning systems have shown to be more accurate (0.1-0.35 m positioning error) when compared to WiFi (1-7 m), Bluetooth (2-5 m), and other technologies [111]. RF-based positioning metrics and algorithms have been developed for indoor positioning systems and these are also applicable to LiFi-based positioning systems. In fact, we distinguish between three main positioning metrics,

namely, the received signal strength (RSS), the time of arrival (TOA), and the angle of arrival (AOA) [107]. The RSS measures the power of the received signals, which follows the channel model in general, and hence the position estimation can be obtained. The TOA measures the travel time of the signal from the transmitter to the receiver, which is a function of the distance as well. Finally, the AOA measures the angle from which the signal arrives at the receiver, and such information can be also exploited in estimating the location of the transmitter [107].

Several LiFi-based indoor positioning solutions have been proposed in the literature [112–117]. An AOA-based technique is proposed in [112], which uses a receiver array with known orientation angle differences between receivers. In [113–115] both the LED transmitters and the UE receiver are assumed to have perpendicular orientations to the room ceiling, and the height of the UE is assumed to be known. However, the assumption of having a perfect alignment between the orientations of the UE and the LED transmitter is not valid since as discussed throughout the previous chapters, most LiFi devices have random orientation in real-life scenarios. Due to this, an inertial measurement unit (IMU) was required in [116] to measure the UE tilt angle for position estimation. However, the IMU may not be available in some real-life scenarios and the accuracy of the IMU in estimating the UE tilt angle is not also guaranteed.

Based on the above discussion, there are a number of limitations in the aforementioned approaches. In fact, only the estimate of the UE's location was considered, and hence, the estimate of the UE's orientation remains unresolved. This is mainly due to the fact that the position and orientation estimation metrics of LiFi systems, such as the RSS, are non-linear functions with respect to the UE position and orientation [28], which leads to a non-convex optimization problem with a lot of local optima. In addition, the imperfect estimation of these uncertain parameters will result in a serious estimation performance loss. Despite this, the orientation estimation in LiFi systems should not be ignored. In fact, unlike conventional RF wireless systems, the LiFi channel is not isotropic, i.e., the device orientation affects the channel gain significantly. This makes the orientation estimation a crucial factor, since as was depicted throughout the previous chapters, it can affect the users' BER and throughput remarkably and it should be estimated carefully [28].

In [118], a simultaneous position and orientation algorithm for indoor LiFi users with unknown LED emission power is proposed. This approach is based on the RSS where an

iterative algorithm for jointly estimating the UE position and orientation is developed. Although the proposed approach considers estimating the UE orientation, it does require that the UE should be connected to at least six APs, which is equal to the number of unknown parameters (three parameters for the UE position and three others for the UE orientation). However, such an assumption on the system setting is not valid in realistic LiFi systems due to the random orientation of LiFi UEs. Against the above background, an accurate LiFi-based indoor position and orientation estimation solution without any requirement regarding the LiFi system settings or perfect knowledge of the UE states is highly desirable.

The existing position and orientation estimation solutions discussed above considered only the LOS component in estimating the UE position and orientation and treated the NLOS component as a source of noise that deteriorates the estimation performance. This is mainly due to the fact that the expression of the NLOS channel gain with respect to the UE location and orientation is complex, and hence, it could not be handled straightforwardly in an optimization fashion. However, it was shown recently in [119] that LiFi systems can gain additional UE position and orientation information from the NLOS links via leveraging the NLOS propagation knowledge. Specifically, the closed-form Cramer-Raw lower bounds on the estimation errors of the UE location and orientation, are derived. In addition, the information contribution of NLOS links was quantified to gain insights into the effect of NLOS propagation on the LiFi-based indoor position and orientation estimation performance. It was shown that the NLOS channel, in addition to the LOS channel, can be exploited to improve the LiFi-based indoor position and orientation estimation performance. However, due to the fact that the channel gain expression of the NLOS components is very complex with respect to the UE position and orientation, including the NLOS components in the estimation process is not straightforward from an optimization point of view. Therefore, this gives rise to the following question: *"How can the NLOS components be exploited in estimating the UE location and orientation in LiFi-based indoor environments?"* The answer is in fact using deep learning (DL) techniques.

As a prevailing approach to artificial intelligence, machine learning (ML) has drawn much attention in recent years due to its great successes in computer vision and natural language processing [120]. ML is capable of solving complex problems that are lacking explicit models or straightforward programming. Motivated by its successful applications

to many practical tasks, both industry and research communities have advocated the applications of ML in wireless communication, with emphasis on resource management, networking, mobility management and localization [121, 122]. Recently, some works have investigated the use of ML techniques in indoor positioning using LiFi technology, such as K-Nearest Neighbor (KNN) [123], support vector machine (SVM) and extreme learning machine (ELM) [124].

DL is a particular ML technique that implements the learning process elaborating the data through ANNs. The use of ANNs is a key factor that makes DL outperform other machine learning schemes, especially when a large amount of data is available [125]. This has made DL the leading ML technique in many scientific fields such as image classification, text recognition, speech recognition, audio and language processing, and robotics [125]. The potential application of DL to wireless communication has also been increasingly recognized because of the new features for future communications, such as complex scenarios with unknown channel models, high speed and accurate processing requirements, which present big challenges to 6G wireless networks [120]. Motivated by this, DL has been applied to wireless communications, such as physical layer communications [120, 126], resource allocation [127, 128], and intelligent traffic control [129]. Motivated by the above discussion, DL techniques are auspicious candidates for LiFi-based indoor position and orientation estimation. Therefore, the use of ANNs is a promising solution for this problem, which is the focus of this chapter.

5.2   Contributions and Outcomes

In this section, the joint estimation of UE's 3D position and orientation in indoor LiFi systems is investigated. Existing solutions for this problem assume either ideal LiFi system settings or perfect knowledge of the UE states, rendering them unsuitable for realistic LiFi systems [112–118]. In addition, these solutions consider the NLOS links of the LiFi channel gain as a source of deterioration for the estimation performance instead of harnessing these components in improving the position and the orientation estimation accuracy. This is mainly due to the lack of appropriate estimation techniques that can extract the position and orientation information hidden in these components. Against the above limitations, the UE is assumed to be connected with at least one AP, i.e., at least one active LiFi link. Fingerprinting is employed as an estimation technique and the

received SNR is used as an estimation metric, where both the LOS and NLOS components of the LiFi channel are considered. Motivated by the success of DL techniques in solving several complex estimation and prediction problems, we employ two deep ANN models, one based on the multilayer perceptron (MLP) and the second on the convolution neural network (CNN), that can map efficiently the instantaneous received SNR with the user 3D position and the UE orientation. Through numerous examples, we investigate the performance of the proposed schemes in terms of the average estimation error, precision, computational time, and BER. We also compare this performance to that of the KNN scheme, which is widely used in solving wireless localization problems. It is demonstrated that the proposed schemes achieve significant gains and are superior to the KNN scheme.

5.3 RSS-Based Fingerprinting for Position and Orientation Estimation

5.3.1 System Model, Objective and RSS Analysis

We consider the indoor LiFi system presented in Section 2.1 and shown in Figure 2.1. The objective is estimating the 3D position and orientation of a UE communicating in the uplink phase with the APs. In this setup, the transmitter is the UE which is equipped with N_t LDs and the receiver is the N_r LiFi APs. The UE is randomly located within the indoor environment shown in Figure 2.1 and its orientation is also varying randomly. In the joint position and orientation estimation process, the UE needs to transmit a reference signal to the APs in a one time/frequency resource block. Assuming that the DC-biased PAM with order M is used, the UE broadcasts through its N_t LDs a scalar signal x that is equal to one of the M-PAM intensity levels, which are given by $I_m = \frac{2m}{M+1}I_{\text{DC}}$, for $m \in [\![1, M]\!]$. Hence, the transmitted vector of signals is given by $\mathbf{x} = x\mathbf{1}_t$, and for $i \in [\![1, N_r]\!]$, the received signal at the ith AP is given by

$$z_i = \left(\lambda \sum_{j=1}^{N_t} g_{i,j} \right) x + n_i, \tag{5.1}$$

where, for all $i \in [\![1, N_r]\!]$ and $j \in [\![1, N_t]\!]$, $g_{i,j}$ is the uplink channel gain between the jth LD of the UE and the PD ith AP, and n_i is an AWGN experienced at the PD of the ith AP that is $\mathcal{N}(0, \sigma_{\text{IR}}^2)$ distributed, such that $\sigma_{\text{IR}}^2 = N_{\text{IR}}B_{\text{IR}}$ is the noise power, in which N_{IR} is the IR noise power spectral density at the optical receivers and B_{IR} is the

IR bandwidth. In addition, as was explained in Section 2.1, $\lambda = TR_{\mathrm{p}}\eta$, in which T is the TIA gain at the AP, R_{p} is the responsivity of the AP's PD, and η is the current-to-power conversion efficiency of the LDs. Consequently, for all $i \in [\![1, N_{\mathrm{r}}]\!]$, the received SNR at the ith AP is given by

$$r_i = \frac{\left(\lambda \sum_{j=1}^{N_{\mathrm{t}}} g_{i,j}\right)^2 P_{\mathrm{elec}}}{\sigma_{\mathrm{IR}}^2}, \tag{5.2}$$

where $P_{\mathrm{elec}} = \frac{I_{\mathrm{DC}}^2}{3} \frac{M-1}{M+1}$ is the electrical power of the transmitted signal x. Based on this, the $N_{\mathrm{t}} \times 1$ received SNR vector at the APs, defined as $\boldsymbol{r} \triangleq [r_1, r_2, ..., r_{N_{\mathrm{t}}}]$, is based on the $N_{\mathrm{r}} \times N_{\mathrm{t}}$ uplink channel matrix $\mathbf{G}$, which in turn depends mainly on six random variables, which are $(x, y, z, \alpha, \beta, \gamma)$. Precisely, the variables (x, y, z) model the randomness of the instantaneous position of the UE, whereas the variables (α, β, γ) model the randomness of its instantaneous orientation. Such correlation can be exploited in estimating the instantaneous UE position and orientation.

5.3.2 Proposed Approach

In this section, we present the proposed joint 3D position and orientation estimation approach, which is based on the use of DL through some sophisticated deep ANNs. First, we explain the details of the approach. Second, we present the steps followed for generating the data set. Second, we investigate the structure of the ANN models employed in the proposed approach. Then, we discuss how the training and the testing of the deep ANNs is performed. Finally, we demonstrate how the proposed models estimate the 3D position and the orientation of LiFi-enables UEs in real time.

Let us consider the indoor LiFi system presented in the previous section. Assuming that the UE is communicating with the APs installed at the ceiling of the room, the objective of here is estimating the instantaneous 3D position and orientation of the UE based on the instantaneous received SNRs at the APs. Unlike the different positioning methods reported in the literature, there are no requirements or prior knowledge neither on the UE position and orientation nor on the emitting power of the positioning signals transmitted by the UE. In other words, the variables $(x, y, z, \alpha, \beta, \gamma)$ along with the UE transmit power P_{elec} are totally unknown without any prior information on them. The adopted estimation technique is fingerprinting and the estimation metric is the received SNR, $\boldsymbol{r}$, at the APs. The details of the proposed approach are explained in the following.

The proposed joint position and orientation estimation approach is divided into two phases: 1) an offline survey (offline phase) and 2) an online testing (online phase). In the offline survey, the received SNRs at the APs for a large number of possible 3D positions (x, y, z) and orientation angles (α, β, γ) are collected, processed, and recorded into a data set. Then, based on the obtained measurements-based data set, optimal learning models that provide the best mappings between the instantaneous received SNR and the 3D position and orientation are built. In the online testing, the obtained models are tested against the real 3D position and orientation angles of the UE to evaluate the accuracy of the derived models. In the following, we will present first the steps of the offline phase and then we will discuss the deployment of the obtained models in the online phase.

5.3.3 Data Set Generation

Each UE is assumed to be stationary within the indoor environment. In this case, and as shown in [34], the user is uniformly located within the indoor environment, and therefore, the PDFs of the UE 3D position are given by:

$$f_x(x) = \frac{1}{L}\mathcal{U}_{[-\frac{L}{2},\frac{L}{2}]}(x), \qquad f_y(y) = \frac{1}{W}\mathcal{U}_{[-\frac{W}{2},\frac{W}{2}]}(y), \quad \text{and} \quad f_z(z) = \frac{1}{h_{\text{device}}}\mathcal{U}_{[0,h_{\text{device}}]}(z),$$
(5.3)

where $0 \leq h_{\text{device}} \leq H$ is the maximum height of any UE within the indoor environment. On the other hand, based on the device orientation model presented in Section 2.3, the rotation angles α, β, and γ follow each a truncated Laplace distribution with mean and standard deviation $(\mu_\alpha, \sigma_\alpha) = (\Omega - 90°, 3.67°)$, $(\mu_\beta, \sigma_\beta) = (40.78°, 2.39°)$, and $(\mu_\gamma, \sigma_\gamma) = (-0.84°, 2.21°)$, respectively, where Ω denotes the movement direction, where Ω denotes the facing or movement direction of a user while sitting, which follows a uniform distribution within $[0°, 360°]$.

Based on the above, assuming that the target data set contains Q_{d} data points, the procedure of generating the nth measurement-based data point, for $n \in [\![1, Q_{\text{d}}]\!]$, are detailed as follows.

1. A sample of 3D position (x, y, z) is generated using the statistics in (5.3).

2. A sample of movement direction angle Ω is generated uniformly from $[0°, 360°]$.

3. The three orientation angles (α, β, γ) are generated using the truncated Laplace distribution and their statistics specifications.
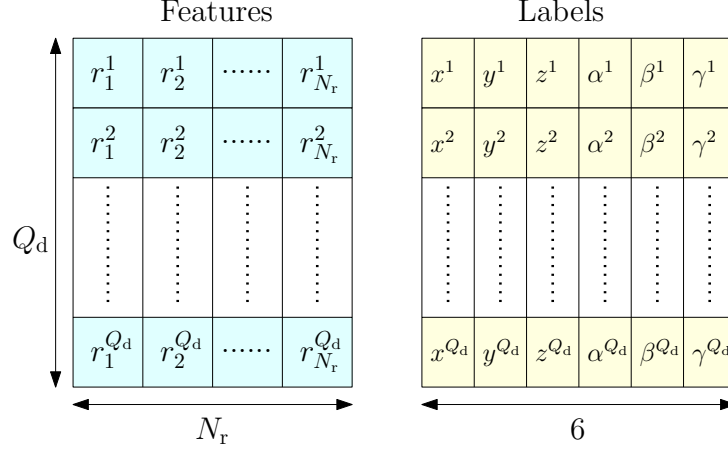
Figure 5.1: Data set structure

4. The resulting channel matrix $\mathbf{H}$ is then calculated as explained in Section 2.2.

5. A random electrical emission power P_{elec} is generated uniformly from $[0, P_{\text{elec}}^{\max}]$, where $P_{\text{elec}}^{\max}$ is the highest possible electrical emission power from the UE.

6. The corresponding SNR vector $\boldsymbol{r}$ is calculated as shown in (5.2).

7. Finally, the resulting SNR vector $\boldsymbol{r}$ is stored into the data set as a feature vector and the corresponding 3D-position and orientation angles $(x, y, z, \alpha, \beta, \gamma)$ are stored as a label vector as shown in Figure 5.1.

Once the data set is obtained, the goal now is how to obtain "good" mappings between the feature vector that contains the received SNR and the label vector that contains the 3D position and the orientation angles of the UE. For such a goal, several learning methods can be applied such as KNN [123], SVM and ELM [124]. To the best of our knowledge, this work is the first that employs deep ANNs for the joint position and orientation estimation of LiFi UEs. This will be presented in details in the following part.

5.3.4 Learning Models: Deep ANNs

ANNs have been widely applied in various fields to overcome the problem of complex and nonlinear mappings. Recently, different kinds of ANNs have been applied in a wide range of applications in wireless communications, especially in the physical layer, such as modulation recognition, channel modeling, signal processing and data decoding [130]. In our context, and as it can be seen in Figure 5.2, our objective is to find a parametric mapping $J(\mathcal{P}; \cdot)$, where $\mathcal{P}$ represents a set of parameters, that can link between the

68
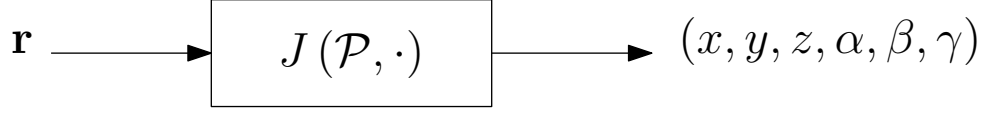
Figure 5.2: Estimation mapping.

instantaneous received SNR vector $\boldsymbol{r}$ in one hand and the 3D position and the orientation angles of the UE $(x, y, z, \alpha, \beta, \gamma)$ in the other hand. Using ANNs, $J(\mathcal{P}; \cdot)$ is indeed a neural network and such mapping can be obtained by determining the optimal set of parameters $\mathcal{P}^*$ that produce the best mapping with respect to a given estimation error metric, i.e.,

$$(x, y, z, \alpha, \beta, \gamma) = J\left(\mathcal{P}^*, \boldsymbol{r}\right). \tag{5.4}$$

For this mission, two different models of ANNs are considered for this problem, which are the MLP and the CNN. In the following, we present the architectures of MLP and CNN models. The optimal set of parameters for each model is obtained by training each model over the whole data set by minimizing a certain loss function, in a way that captures the patterns between the instantaneous received SNR vector $\boldsymbol{r}$ and the 3D position and the 3D orientation angles of the UE $(x, y, z, \alpha, \beta, \gamma)$ over the whole data set.

An ANN is a series of layers, where each layer is composed of multiple artificial neurons and their connections. Specifically, as shown in Figure 5.3, an ANN is composed of an input layer, D hidden layers, and an output layer, where D denotes the depth of the neural network. First, at the input layer, the SNR feature vector $\boldsymbol{r}$ with a bias $\mathbf{b}_1$ is fed into the neural network. Second, for $d = 1, 2, ..., D$, the dth hidden layer consists of M_d artificial neurons and their connection. Each artificial neuron has the ability to calculate a mathematical operation of its inputs and then applies an activation function to obtain a signal that will be forwarded to the next layer. Finally, the output layer consists of six artificial neurons, where each neuron is responsible for estimating one parameter in $(x, y, z, \alpha, \beta, \gamma)$. As shown in Figure 5.3, the propagation rules within the hidden layers are expressed as follows. For $j \in [\![1, D]\!]$ and $i \in [\![1, M_j]\!]$, the output of the ith neuron in the jth hidden layer is expressed as

$$v_{i,j} = a_{i,j}\left[\mathrm{t}\left(\mathbf{u}_{j-1}, \mathbf{w}_{i,j}, b_{i,j}\right)\right], \tag{5.5}$$

where $a_{i,j}[\cdot]$, $\mathbf{u}_{j-1}$ and $\mathbf{w}_{i,j}$ denote the activation function, the input, and the weights vector of the ith neuron of the jth hidden layer, respectively, $\mathrm{t}(\cdot, \cdot, \cdot)$ is a linear transformation that depends on the type of the ANN, and $b_{i,j}$ is a scalar bias. Assuming that the output layer is referred to as the $(D+1)$th layer, note that for $j \in [\![0, D]\!]$, the input vector $\mathbf{u}_j$ of
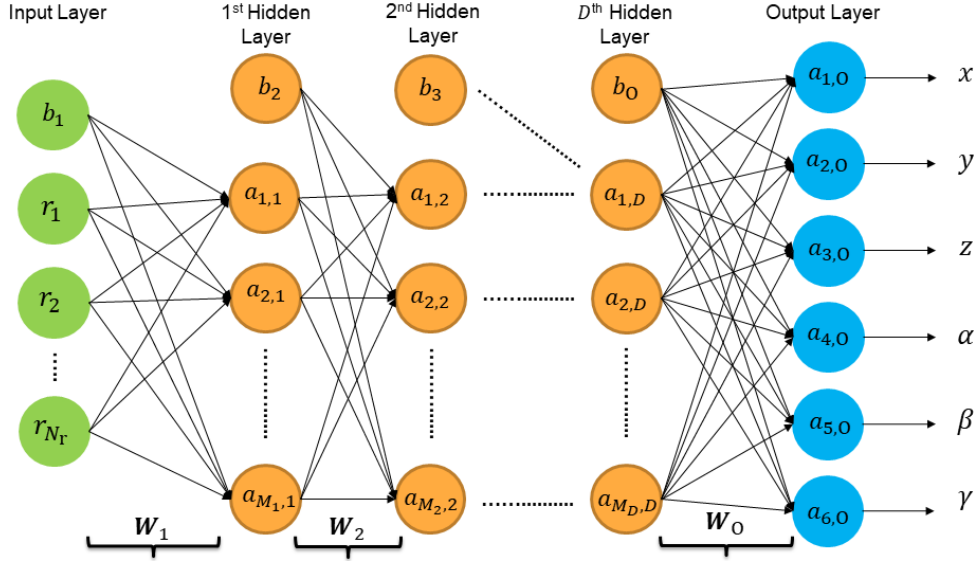
Figure 5.3: ANN architecture for joint 3D position and orientation estimation.

the $(j+1)$th layer is exactly the output vector $\mathbf{v}_j$ of jth layer, i.e.,

$$\mathbf{u}_j = \mathbf{v}_j = \left[v_{1,j}, v_{2,j}, ..., v_{M_j,j}\right]^T, \tag{5.6}$$

with the convention $\mathbf{u}_0 = \mathbf{v}_0 = \boldsymbol{r}$, which is the SNR feature vector. On the other hand, the propagation rules in the output layer are given by

$$x = a_{1,\text{o}}\left[\text{t}\left(\mathbf{u}_D, \mathbf{w}_{1,\text{o}}, b_{i,\text{O}}\right)\right], \quad \alpha = a_{4,\text{o}}\left[\text{t}\left(\mathbf{u}_D, \mathbf{w}_{4,\text{o}}, b_{i,\text{O}}\right)\right],$$

$$y = a_{2,\text{o}}\left[\text{t}\left(\mathbf{u}_D, \mathbf{w}_{2,\text{o}}, b_{i,\text{O}}\right)\right], \quad \beta = a_{5,\text{o}}\left[\text{t}\left(\mathbf{u}_D, \mathbf{w}_{5,\text{o}}, b_{i,\text{O}}\right)\right], \tag{5.7}$$

$$z = a_{3,\text{o}}\left[\text{t}\left(\mathbf{u}_D, \mathbf{w}_{3,\text{o}}, b_{i,\text{O}}\right)\right], \quad \gamma = a_{6,\text{o}}\left[\text{t}\left(\mathbf{u}_D, \mathbf{w}_{6,\text{o}}, b_{i,\text{O}}\right)\right],$$

where for $k \in [\![1, 6]\!]$, $a_{k,\text{O}}(\cdot, \cdot, \cdot)$ and $\mathbf{w}_{k,\text{o}}$, denote the activation function and the weights vector of the kth neuron of the output layer, and $b_{i,\text{O}}$ is a scalar bias.

The set of parameters P that defines the ANN is given by $\mathcal{P} = \mathcal{W} \cup \mathcal{B}$, where $\mathcal{W} = \{\mathbf{W}_\text{O}, \mathbf{W}_j | j \in [\![1, D]\!]\}$, such that $\mathbf{W}_\text{O} = [\mathbf{w}_{j,\text{O}}, \mathbf{w}_{2,\text{O}}, ..., \mathbf{w}_{M_\text{O},\text{O}}]$, and for all $j \in [\![1, D]\!]$, $\mathbf{W}_j = \left[\mathbf{w}_{1,j}, \mathbf{w}_{2,j}, ..., \mathbf{w}_{M_j,j}\right]$, and $\mathcal{B} = \{\mathbf{b}_\text{O}, \mathbf{b}_j | j \in [\![1, D]\!]\}$, such that $\mathbf{b}_\text{O} = [\mathbf{b}_{j,\text{O}}, \mathbf{b}_{2,\text{O}}, ..., \mathbf{b}_{M_\text{O},\text{O}}]^T$, and for all $j \in [\![1, D]\!]$, $\mathbf{b}_j = \left[\mathbf{b}_{1,j}, \mathbf{b}_{2,j}, ..., \mathbf{b}_{M_j,j}\right]^T$. As was mentioned above, the linear transformation $\text{t}(\cdot, \cdot, \cdot)$ depends on the type of the ANN used. In our approach, we distinguish between two main linear transformations, which are the weighted sum and the 1D convolution. The ANN that employs the weighted sum as a linear transformation is the MLP. In this case, for $j \in [\![1, D]\!]$, $i \in [\![1, M_j]\!]$ and $k \in [\![1, 3]\!]$, the linear transformation $\text{t}(\cdot, \cdot, \cdot)$ is expressed as

$$\begin{cases} \text{t}\left(\mathbf{u}_{j-1}, \mathbf{w}_{i,j}, b_{i,j}\right) = \mathbf{w}_{i,j}^T \mathbf{u}_{j-1} + b_{i,j}, \\ \text{t}\left(\mathbf{u}_D, \mathbf{w}_{k,\text{o}}, b_{i,\text{O}}\right) = \mathbf{w}_{k,\text{o}}^T \mathbf{u}_D + b_{i,\text{O}}. \end{cases} \tag{5.8}$$

On the other hand, the ANN that employs the 1D convolution as a linear transformation is the CNN. In this case, for $j \in [\![1, D]\!]$, $i \in [\![1, M_j]\!]$ and $k \in [\![1, 3]\!]$, the linear transformation $\mathrm{t}(\cdot, \cdot, \cdot)$ is defined as

$$
\begin{cases}
\mathrm{t}\left(\mathbf{u}_{j-1}, \mathbf{w}_{i,j}, b_j\right) = \mathbf{w}_{i,j} \circledast \mathbf{u}_{j-1} + b_{i,j}, \\
\mathrm{t}\left(\mathbf{u}_D, \mathbf{w}_{k,\mathrm{o}}, b_{\mathrm{O}}\right) = \mathbf{w}_{k,\mathrm{o}} \circledast \mathbf{u}_D + b_{i,\mathrm{O}}.
\end{cases}
\tag{5.9}
$$

where $\circledast$ denotes the convolution operator.

The activation function, also known as the threshold function or the transfer function, is a scalar-to-scalar function that determines the output of each neuron in a neural network. The function is attached to each neuron in the network, and determines whether it should be activated or not, based on whether each neuron's input is relevant for the model's estimation or not. Some of the most commonly used activation functions for solving non-linear problems include linear function, rectified linear unit (Relu) function, sigmoid function, Hyperbolic tangent (tanh), etc [131].

At this stage, the architecture of the ANN model, either MLP or CNN, is set up. The next step is how the ANN model should be trained in a way that provides the best estimation accuracy for the 3D position and the orientation angles of the UE. This is detailed in the following paragraphs.

5.3.5   Offline Phase: Models Training

Once the ANN model is selected, i.e., either MLP or CNN, the goal now is how to obtain the optimal sets of weights $\mathcal{P}^*$ that can map between the instantaneous received SNR vector $\boldsymbol{r}$ and the 3D position and the orientation angles of the UE $(x, y, z, \alpha, \beta, \gamma)$. This can be obtained by training the selected model as explained in the following. In the estimation (or regression) problem in hands, obtaining the optimal sets of weights is performed by minimizing a certain loss function. In a typical regression problem, several loss functions can be considered, such as the mean-square-error (MSE) or the mean-absolute-error (MAE) [132]. In our analysis, we consider the MSE loss, also known as the L_2 loss. Hence, obtaining the optimal sets of weights $\mathcal{P}$ can be obtained as

$$
\mathcal{P}^* = \underset{\mathcal{P}}{\operatorname{argmin}} \ \mathrm{L}_2(\mathcal{P}) = \underset{\mathcal{P}}{\operatorname{argmin}} \ \frac{1}{Q_{\mathrm{train}}} \sum_{l=1}^{Q_{\mathrm{train}}} ||\mathbf{P}^l - \widehat{\mathbf{P}}^l\left(\mathcal{P}, \boldsymbol{r}_l\right)||_2^2,
\tag{5.10}
$$

where $Q_{\mathrm{train}} \in [\![1, Q_{\mathrm{d}}]\!]$ is the number of data points used for training the models, and for $l \in [\![1, Q_{\mathrm{train}}]\!]$, $\mathbf{P}^l = [x^l, y^l, z^l, \alpha^l, \beta^l, \gamma^l]^T$ and $\widehat{\mathbf{P}}^l = \left[\widehat{x}^l, \widehat{y}^l, \widehat{z}^l, \widehat{\alpha}^l, \widehat{\beta}^l, \widehat{\gamma}^l\right]^T$ are the true and estimated label vectors associated to the lth feature vector $\mathbf{r}^l$ of the data set, respectively,

such that $\widehat{\mathbf{P}}^l$ is obtained from the selected ANN with respect to the set of parameters $\mathcal{P}$.

Solving the optimization problem in (5.10) can be performed using the gradient descent algorithm. In fact, gradient descent can be used to minimize the loss function L_2 by iteratively moving in the direction of steepest descent as defined by the negative of the gradient [133]. A variety of the gradient descent method is the stochastic gradient descent (SGD), which updates the weight parameters after evaluation of the loss function L_2 after each sample. That is, rather than summing up the loss function results for all the samples then taking the mean, SGD updates the weights after every training sample is analysed [133]. Moreover, several adaptive varieties of the SGD have been proposed in the literature of learning neural networks aiming at either increasing the convergence speed and/or the convergence accuracy, such as Adagrad, Adadelta, RMSprop and Adam, with Adam being the de facto standard in DL [133].

5.3.6 Online Phase: Models Deployment

Once the selected ANN model is trained and the optimal parameters $\mathcal{P}^*$ are obtained, the model will be deployed in the online phase. A UE with a random 3D position (x, y, z) and 3D orientation angles (α, β, γ) communicates with the APs through IR links. The APs measure the received SNR values $\boldsymbol{r}$ and inject them into the trained ANN model, which in turn will produce an estimate of the 3D position $(\widehat{x}, \widehat{y}, \widehat{z})$ and the 3D orientation angles $(\widehat{\alpha}, \widehat{\beta}, \widehat{\gamma})$ of the UE, i.e.,

$$(\widehat{x}, \widehat{y}, \widehat{z}, \widehat{\alpha}, \widehat{\beta}, \widehat{\gamma}) = J(\mathcal{P}^*, \boldsymbol{r}). \tag{5.11}$$

Consequently, whenever the UE is connected to the APs, i.e., at least there is one active communication link between the UE and the APs, the APs keep tracking if there is any change in the received SNR values. If this is the case, the new SNR values are injected into the trained ANN model and then a new position and orientation estimate is performed.

The performance of the ANN models will be tested over new unseen received SNR vectors. In this case, the performance of each ANN model can be evaluated in terms of the following performance metrics:

1. **The average estimation error**: it represents the average gap between the true label vectors and the estimated label vectors.

2. **Precision**: it represents the estimation error that is higher than 90% of the possible

Table 5.1: Simulation Parameters

Parameter	Symbol	Value
Room dimension	$L_r \times W_r \times H_r$	5 m×5 m×3 m
LED half-power semiangle	$\Phi_{1/2}$	60°
LED conversion factor	η	0.7 W/A
PD responsivity	R_p	0.6 A/W
PD geometric area	A_{PD}	1 cm^2
Optical concentrator refractive index	n_c	1
Maximum UE's height	h_{device}	1.5m
Maximum UE's power	P_{elec}^{max}	0.04 W
Reflection coefficient of the walls	ξ	0.7
Field of view of the LDs	Φ	90°
Field of view of the PDs	Ψ	90°
IR bandwidth	B_{IR}	10 MHz
IR noise power spectral density	N_{IR}	10^{-21} W/Hz

estimation errors. This can be depicted from the empirical CDF of the estimation error.

3. **The computational time**: it measures the average time needed to estimate the label vector of a given feature vector during one estimation session in the online phase.

.

5.4   Simulation Results

In this section, our objective is evaluating the performance of the proposed ANN-based joint user position and orientation estimation approach through extensive and various simulations.

5.4.1   Simulations Parameters

In this chapter, we consider a typical indoor environment with dimensions $L_r \times W_r \times H_r$ = $5 \times 5 \times 3$ m^3 [36]. Unless otherwise stated, the indoor environment is equipped with $N_r = 16$ APs which are arranged on the vertexes of a square lattice over the ceiling of the room, where each AP is oriented vertically downward. In addition, a LiFi UE, that is equipped with $N_t = 1$ LD, is randomly located within the room and its UE may have a random orientation. The UE is a typical smartphone with dimensions $14 \times 7 \times 1$ cm^3.

Table 5.2: ANNs Specifications

data set size	First data set: $Q_{\mathrm{d}} = 10^5$
	Second data set: $Q_{\mathrm{d}} = 10^6$
Depth of the ANN D	4
Number or neuron per hidden layer M_j	MLP: 256 CNN: 64
Kernel size for CNN neuron	16
Total number of trainable parameters	MLP: $207,36$ CNN: $205,062$
(Train, test) partition	$(0.9, 0.1) \times Q_{\mathrm{d}}$
Optimizer	Adam

The LD is placed at screen of the smartphone, exactly at 6 cm above the center. The parameters used throughout the chapter are shown in Table 5.1. The central processing unit (CPU) of the machine on which all the simulations were performed was an Intel Core i5 from the second generation that has a dual-core, a basic frequency of 2.40 GHz, and a maximum turbo frequency of 3.40 GHz.

5.4.2 ANNs Specifications

The architecture of the MLP and CNN Models are shown in Table 5.2. Each ANN consists of an input layer, an output layer, and $D = 4$ hidden layers, where each hidden layer is composed of $M_j = 256$ neurons for the MLP and $M_j = 64$ filters for the CNN. In addition, the kernel size of each convolution neuron is composed of 16 parameters. Two distinct data sets are used in training the models, where the first has a size of $Q_{\mathrm{d}} = 10^5$ data points and the second has a size of $Q_{\mathrm{d}} = 10^6$ data points. Moreover, for each data set size Q_{d}, $0.9 \times Q_{\mathrm{d}}$ data points are used for training the models in the offline phase and $0.1 \times Q_{\mathrm{d}}$ are used for testing the models in the online phase.

In our proposed ANNs, the structure of each neuron in each hidden layer are presented in Figure 5.4. For the MLP-based model, and as shown in Figure 5.4(a), each neuron consists of a dense layer, a Relu layer, a dropout layer, and a normalization layer. The dense layer is a fully connected linear layer in which every input is connected to every output by a weight. Then, the Relu layer applies the Relu activation function to the resulting output from the dense layer. After this, at each training stage, individual neurons are dropped out of the ANN with a certain probability, so that the complexity of the network is reducing. This layer is fundamental in order to prevent overfitting of the

Dense layer	Convolution layer	
Relu layer	Relu layer	
Dropout layer	Dropout layer	Dense layer
Normalization layer	Normalization layer	Linear layer
(a)	(b)	(c)
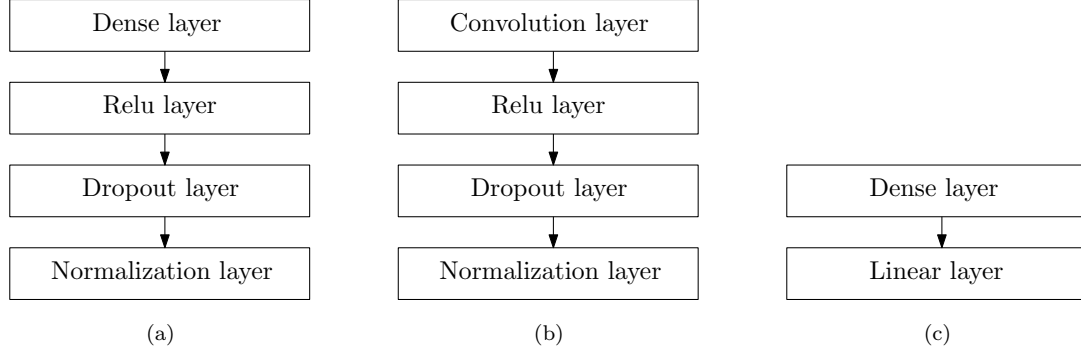
Figure 5.4: Neuron architecture: (a) in each hidden layer in the MLP-based model, (b) in each hidden layer in the CNN-based model, and (c) in the output layer.

ANNs [134]. Finally, The normalization layer scales the input so that the output has near to a zero mean and unit standard deviation, to allow a faster and a more resilient training. For the CNN-based model, and as shown in Figure 5.4(b), a similar neuron architecture can be observed but with replacing the dense layer with a convolution layer, which operates the convolution between the input of the neuron and its kernel. Concerning the neurons architecture at the output layer, and as shown in Figure 5.4(c), each one consists of a dense layer and a linear activation layer that establishes a link with each label at the output. The design of the ANNs is performed using the programming environment Python 3 and the Keras library developed by Google's TensorFlow team in 2017 [135].

5.4.3 Learning and Estimation Performance Evaluation

Figure 5.5 presents the training and validation losses of both the MLP and CNN models, measured in terms of the MSE, versus the epoch index, for the two considered data sets, and for the cases when only the LOS component of the channel gain is considered and when both the LOS and NLOS components are considered. In total, 30 epochs have been used for training and validating each model. Specifically, the portion of data advocated for training the ANN models is in fact divided into two subsets, one for training the models to obtain the weights $\mathcal{P}$ and one for validating the generalization error of the obtained weights on the unseen data. Hence, each epoch is a pass through the entire training set in one time. As shown in Figure 5.5, the training and validation losses are decreasing as the epoch index increases which demonstrates that the obtained ANN models are not overfitting and can generalize well over unseen data points in the online testing. Moreover, as it can be seen in Figure 5.5 that the training loss is higher than the validation loss.

(a) CNN, $Q_d = 10^5$.

(b) MLP, $Q_d = 10^5$.

(c) CNN, $Q_d = 10^6$.

(d) MLP, $Q_d = 10^6$.
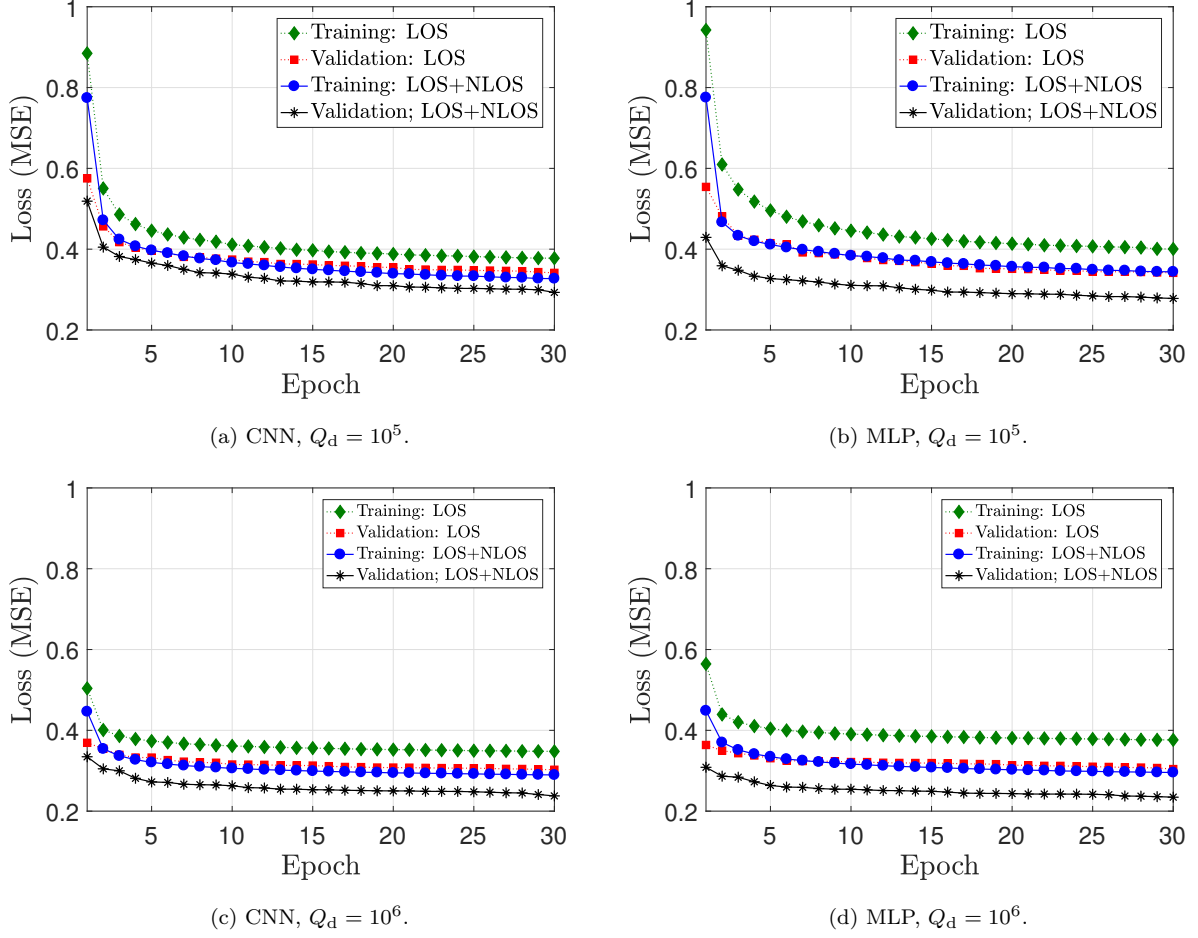
Figure 5.5: Training and validation losses of CNN and MLP models versus the epoch index.

This is mainly due to the use of dropout. In fact, similar to any regularization technique, dropout is applied during the training phase, but not during the validation phase [136]. In other words, regularization mechanisms, such as dropout, are turned off at the validation time, and this leads to having the training loss being higher than the validation loss [136].

Tables C.1, C.2, and C.3 present the average estimation error and the precision of the 3D position and the orientation angles of the UE in the online phase using the proposed CNN and the MLP models and the KNN technique, respectively, for the two considered data sets, and for the cases when only the LOS component of the channel gain is considered and when both the LOS and NLOS components are considered. The number of neighbours of the KNN technique is optimized for each setting. Specifically, the validation error is computed for each possible number of neighbors and the optimal value that produces the lowest validation error is then selected. For instance, for the case when only the LiFi LOS channel gain is considered, the optimal value of neighbors is 4. These tables shows that the CNN model outperforms both the MLP model and

(a) $Q_d = 10^5$.

(b) $Q_d = 10^6$.
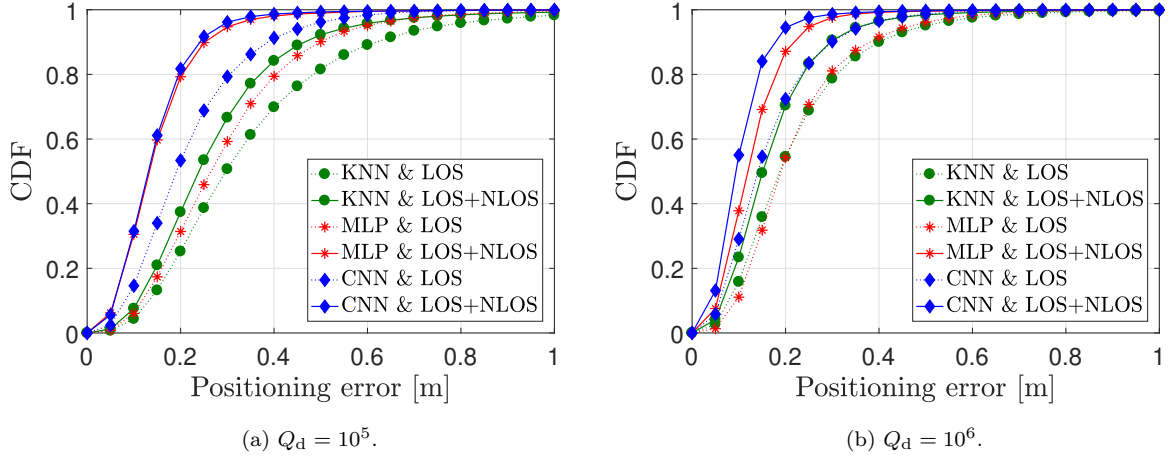
Figure 5.6: CDF of the positioning error for the proposed CNN and MLP models and the KNN technique.

(a) $Q_d = 10^5$..
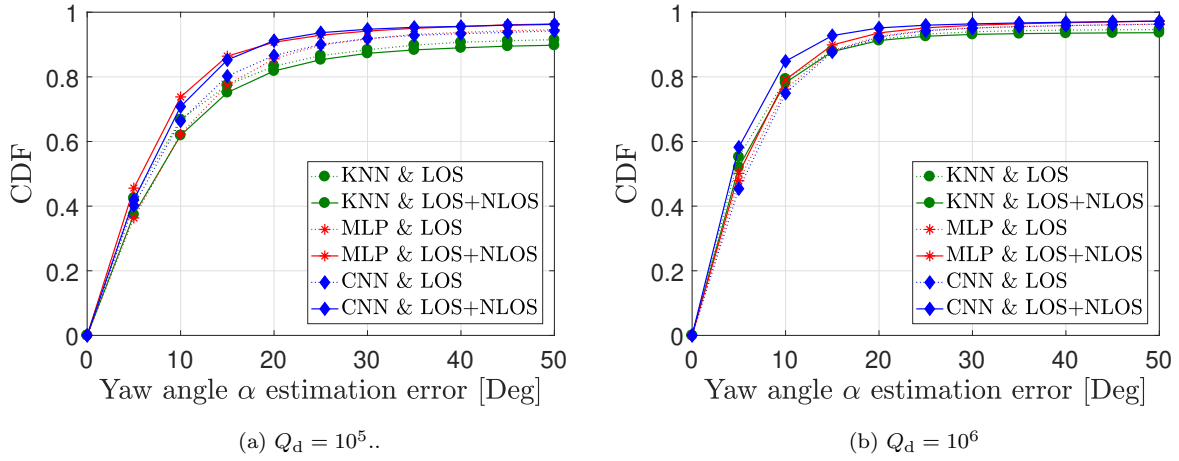
(b) $Q_d = 10^6$

Figure 5.7: CDF of the estimation error of the yaw angle α for the proposed CNN and MLP models and the KNN technique.

the KNN technique. In fact, when considering the total channel gain and a data set of size $Q_d = 10^6$, the proposed CNN model is able to achieve an average positioning error of 10.53 cm with 90% of the positioning errors below 17.15 cm (precision), without any prior knowledge on the UE position and orientation and any assumptions on the LiFi system. The same performance and observations can be seen in the average estimation error and the precision of the orientation angles.

Figures 5.6, 5.7, 5.8, and 5.9 present the CDF of the instantaneous positioning error and the instantaneous estimation error of the yaw angle α, the pitch angle β, and the roll angle γ, resulting from the proposed CNN and MLP models and from the KNN technique, for the two considered data sets and for the cases when only the LOS component of the channel gain is considered and when both the LOS and NLOS components are considered.

(a) Pitch angle $\beta, Q_\mathrm{d} = 10^5$.   (b) Pitch angle $\beta, Q_\mathrm{d} = 10^6$.
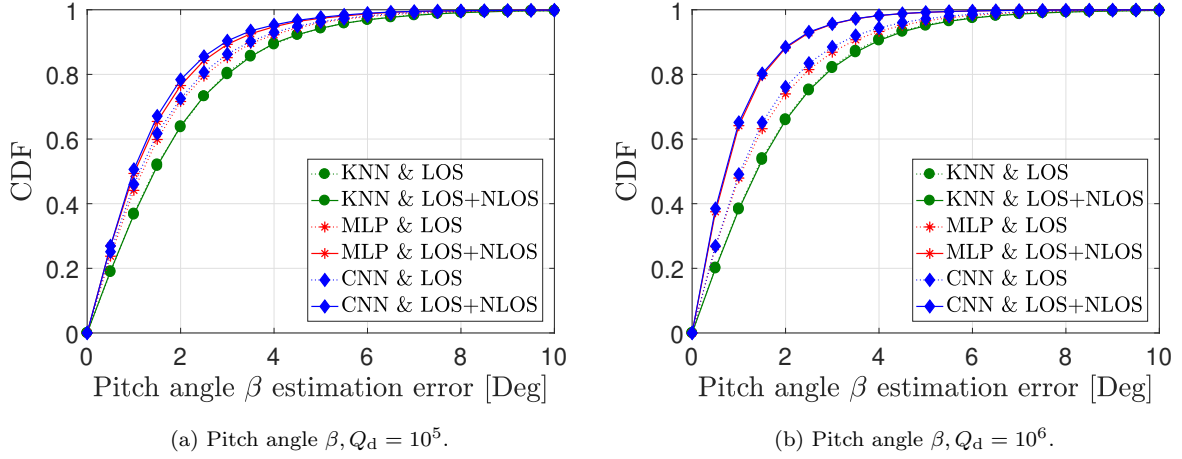
Figure 5.8: CDF of the estimation error of the pitch angle β for the proposed CNN and MLP models and the KNN technique.

(a) Roll angle $\gamma, Q_\mathrm{d} = 10^5$.   (b) Roll angle $\gamma, Q_\mathrm{d} = 10^6$.
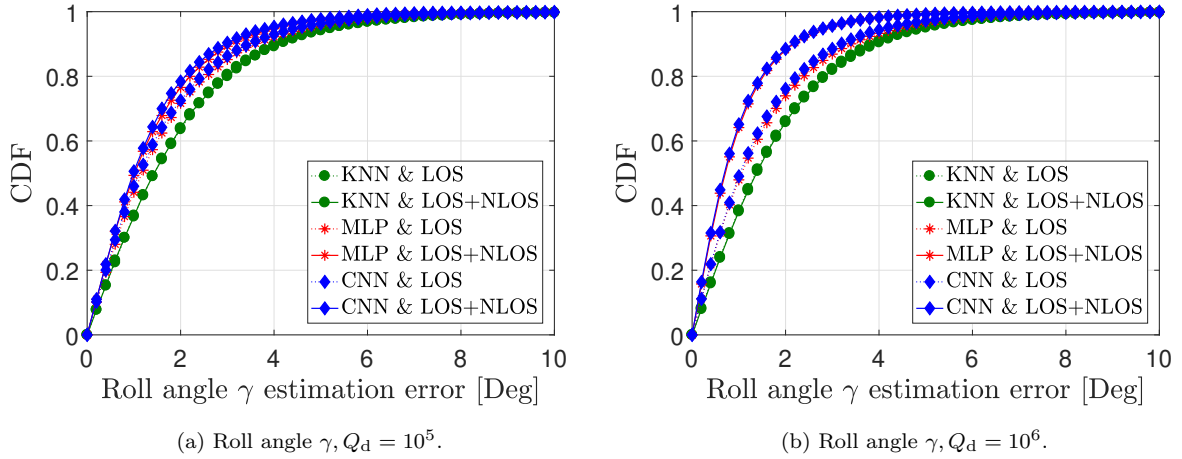
Figure 5.9: CDF of the estimation error of the roll angle γ for the proposed CNN and MLP models and the KNN technique.

These figures also confirm that the proposed CNN and MLP models outperform the KNN technique, with the CNN being the best model to adopt. Furthermore, jointly with Tables C.1, C.2, and C.3, Figures 5.6, 5.7, 5.8 and 5.9 show that increasing the data set size increases the learning efficiency of the ANN models. This is mainly due to the fact that having more data points will allow the ANNs to learn better the random behaviour of the environment, which is translated in terms of the effects of the random position and the random orientation of the UE on the instantaneous received SNR. In addition, it can be seen that the estimation performance of the ANN models increases when the total channel gain is considered instead of only the LOS components. This confirms that the NLOS components provide useful information that improves the estimation performance

of the 3D position and the orientation angles of the UE, rather than a source of noise as was considered in the literature [118]. In fact, including the NLOS components of a UE with random orientation leads to a non-symmetric SNR change within the room, which is not the case when only the LOS components and upward LD/PD are considered, in which many positions may have similar SNRs.

Another observation that can be seen is that the estimation performance of the CNN, the MLP and the KNN models are more accurate for some parameters than others. In fact, we can see that the estimation performance of the pitch angle β and the roll angle γ is way better than the one of the yaw angle α. This is mainly due to the statistics of these angles. Specifically, as presented in Section 2.3, the standard deviations of the pitch angle β and the roll angle γ are very small. Therefore, when generating the data set, the random realizations of these angles will fluctuate slightly over their individual means. However, the mean of the yaw angle α, which is $\Omega - 90°$, is also randomly changing, whereas the means of the pitch angle β and the roll angle γ are fixed. This explains why the estimation accuracy of the pitch and the roll angles is better than the one of the yaw angle.

5.4.4 Computational Complexity Evaluation

Considering the CNN model, and as shown in Table 5.3, the total training time for a data set of size $Q_{\mathrm{d}} = 10^5$ is approximately 30 minutes and the total training time for a data set of size $Q_{\mathrm{d}} = 10^6$ is approximately 4.7 hours. In addition, the required time for generating the data set of size $Q_{\mathrm{d}} = 10^5$ is approximately 1.5 hours and the required time for generating the data set of size $Q_{\mathrm{d}} = 10^6$ is approximately 15 hours. Although the time required for the data set generation and the models training is large, this high computational complexity is not an issue, since the data set generation and the models training is performed in the offline phase and only once prior to the deployment of the APs. Concerning the online complexity, and as it can be seen in Table 5.3, the computational time of the proposed CNN and MLP models in the online phase is extremely low. In fact, the maximum computational time in the online phase is 19 seconds for a data set with size $Q_{\mathrm{d}} = 10^5$ and 140 seconds for a data set with size $Q_{\mathrm{d}} = 10^6$. Therefore, the average estimation time in the online phase is $\frac{19}{0.1 \times 10^5} = 1.9$ ms per trial for a data set of size $Q_{\mathrm{d}} = 10^5$ and $\frac{140}{0.1 \times 10^6} = 1.4$ ms per trial for a data set of size $Q_{\mathrm{d}} = 10^6$, i.e., real-

Table 5.3: Total computational time [in seconds]

		CNN		MLP		KNN	
		$N = 10^5$	$N = 10^6$	$N = 10^5$	$N = 10^6$	$N = 10^5$	$N = 10^6$
LOS	Offline phase	1800	17000	250	2000	0.3	0.54
	Online phase	19	140	9	30	1	26
LOS+NLOS	Offline phase	1800	17000	220	2300	0.34	0.7
	Online phase	20	200	8	30	1	29

time estimation. Nevertheless, the best existing joint position and orientation estimation technique, which was proposed in [118], has an average online computational time of 0.5 s per trial, which demonstrates the potential of the proposed ANN models in providing highly accurate and real-time joint position and orientation estimation.

5.4.5 Effects of the Indoor Environment Geometry

Figure 5.10 presents the CDF of the positioning error for the proposed CNN and MLP models and the KNN technique for different room dimensions $L_{\mathrm{r}} \times W_{\mathrm{r}} \times H_{\mathrm{r}}$, where the number of APs $N_{\mathrm{r}} = 16$ and the total channel gain is considered. This figure shows that increasing the room dimension while keeping the number of APs fixed will decrease the estimation performance. This observation is expected, since increasing the room dimensions will enlarge the search space of the unknown position parameters, and therefore, the probability of wrong estimation will increase. On the other hand, Figure 5.11 presents the CDF of the positioning error for the proposed CNN and MLP models and the KNN technique for different number of APs N_{r}, where the room dimension is $L_{\mathrm{r}} \times W_{\mathrm{r}} \times H_{\mathrm{r}} = 5 \times 5 \times 3$ m^3 and the total channel gain is considered. This figure shows that decreasing the number of APs while keeping the room dimension fixed will decrease the estimation performance. This observation is also expected since decreasing the number of APs will decrease the size of the feature SNR vector, which reduces the amount of information that can be exploited for the estimation.

5.4.6 Reliability Performance Evaluation

The main objective behind estimating the UE position and orientation, other than the purpose of navigation-based or location-aware services, is estimating the indoor channel gain between the APs and the UE. In this context, although some navigation-based or location-aware services may tolerate a range of estimation errors, it is not the case when
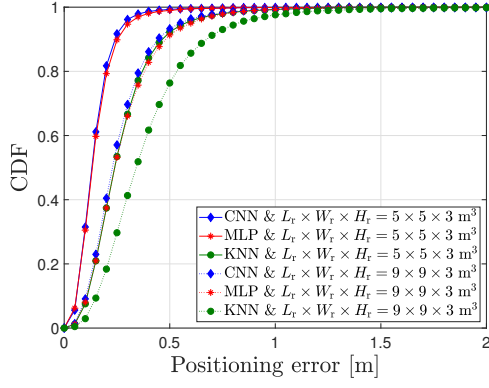
Figure 5.10: CDF of the positioning error for the proposed CNN and MLP models and the KNN technique for different room dimensions.
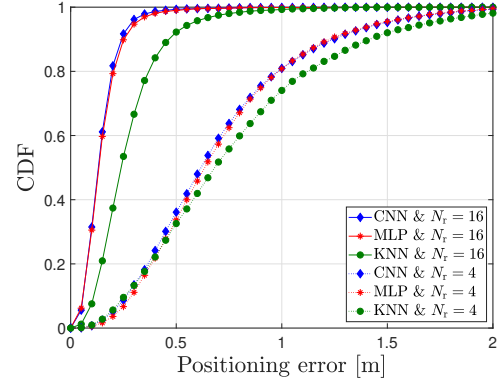
Figure 5.11: CDF of the positioning error for the proposed CNN and MLP models and the KNN technique for different number of APs N_{r}.
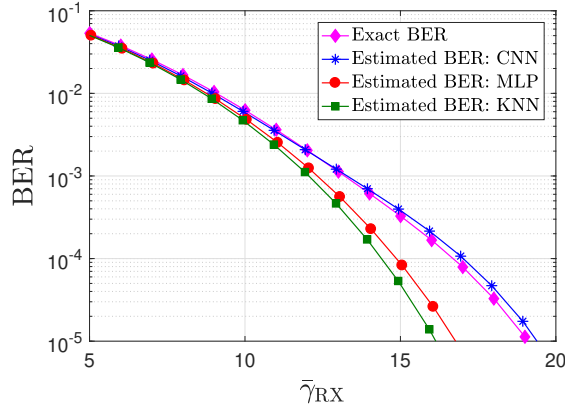
Figure 5.12: Downlink BER evaluation versus the average received SNR $\bar{\gamma}_{\mathrm{RX}}$, for an indoor environment with dimensions $L_{\mathrm{r}} \times W_{\mathrm{r}} \times H_{\mathrm{r}} = 5 \times 5 \times 3 \ m^3$ with the number of APs $N_{\mathrm{t}} = 16$ and a data set with size $Q_{\mathrm{d}} = 10^5$.

estimating the UE channel gain. In fact, the position and orientation estimation errors will affect the CSI estimation accuracy, which in turn will affect the performance of LiFi systems in terms of reliability and achievable rates. Due to this reason, the reliability performance of LiFi systems under the position and orientation estimation errors is investigates in this section.

Let us consider the downlink transmission between the APs and the UE. In this case, the transmitter is the LiFi APs and the receiver is the UE. Accordingly, let $\mathbf{h}$ denotes the $N_{\mathrm{t}} \times 1$ total downlink channel gain vector between the N_{t} APs and the UE and $P_{\mathrm{elec}}^{\mathrm{d}}$ denotes the electrical transmit power from the APs. In this case, the instantaneous received SNR at the UE is given by $\gamma_{\mathrm{RX}} = \frac{P_{\mathrm{elec}}^{\mathrm{d}} \|\mathbf{h}\|_1^2}{\sigma_{\mathrm{VL}}^2}$. Assuming that the OOK modulation is employed and that the APs broadcast the same signal to the UE, Figure 5.12 presents

the average exact and estimated BERs versus the average received SNR $\bar{\gamma}_{\mathrm{RX}} = \mathbb{E}\left[\gamma_{\mathrm{RX}}\right]$ for an indoor environment with dimensions $L_{\mathrm{r}} \times W_{\mathrm{r}} \times H_{\mathrm{r}} = 5 \times 5 \times 3 \mathrm{~m}^3$ and for the number of APs $N_{\mathrm{t}} = 16$. The average here is with respect to to all the realizations of the channel gain vector $\mathbf{h}$ induced by all the exact and the estimated positions and orientations.

From Figure 5.12, the following observations can be highlighted. First, the proposed CNN model provides the most accurate estimation of the BER compared to the proposed MLP model and the KNN technique. This is mainly due to the fact that, based on the results of the previous subsections, the CNN model was shown to be the best model in estimating the position and the orientation of the UE. Second, the proposed MLP model along with the KNN technique provide an underestimation of the BER. In fact, one might think that the estimated average BER by the MLP model and the KNN technique is better than the exact one but it is not what it looks like. In fact, this underestimation is mainly due to the position and orientation estimation errors. Specifically, the estimated position and orientation, although they produce better BER performance, but they don't reflect the realistic BER resulting from the exact position and orientation of the UE.

5.5   Conclusion

In this chapter, novel ANN models were proposed for the joint 3D position and orientation estimation of a LiFi UE with a random orientation and an unknown emitting power. Using RSS-based fingerprinting, the proposed approach consisted of generating a measurement-based data set that contains the instantaneous received SNR along with the corresponding 3D position and orientation angles. Then, an MLP and a CNN models were designed to map efficiently the SNR feature vectors with the corresponding positions and orientation angles. Although there were no prior knowledge on the UE position and orientation and any assumptions on the LiFi system, the proposed models were able to achieve centimeter level positioning error and high accurate orientation angles estimation. The performance of the proposed models were compared with the KNN technique, in terms of average estimation error, precision, BER, and computational time, where the superiority of the proposed ANN models was shown. These results have enlightened the potential of the proposed ANN models in providing highly accurate and real-time joint position and orientation estimation. In addition, the simulation results have demonstrated how including the NLOS components of the channel gain can improve significantly the position

and orientation estimation performance.

The analysis presented in the chapter considered the case when the user is stationary. Although the the same proposed techniques can be applied for the case of mobile users, the performance of LiFi systems is highly affected by the users mobility. In the next chapter, a novel approach is proposed to alleviate the effect of users mobility on the optimization of LiFi systems.

Chapter 6

Proactive Optimization for Indoor LiFi Systems with Channel Aging

6.1 Motivation, Related Works, and Contributions

A LiFi UE is mobile if its position and/or orientation are changing over consecutive time slots, such as the case of a user that is browsing or watching streaming video while walking [28]. However, at the LiFi physical layer, the majority of the invoked optimization problems are non-convex, e.g., maximizing throughput by means of power control, multi-user spectrum optimization in multi-carrier systems, optimal beamforming for sum rate maximization, to name only a few [72, 76, 137–140]. These problems may be solved using dual decomposition or heuristic techniques that require iterative algorithms, which induces a certain processing delay at the LiFi physical layer [130]. However, for the case of mobile LiFi users, such processing delay may exceed the maximum amount of time allocated to serve all the mobile users, and therefore, can not be tolerated. In fact, since users are mobile, they might change their instantaneous positions and/or orientation within the processing time. Consequently, their channel coefficients may evolve within the processing time and their previously estimated channel coefficients are no longer accurate, which makes the obtained solution no longer optimal after the processing time, and this can lead to performance degradation. This problem is known as *channel aging*, i.e., the LiFi channel coefficients are outdated after the optimization time, which is a very known problem in the wireless and mobile communication literature [141, 142].

In this chapter, a proactive optimization (PO) approach that can alleviate the LiFi *channel aging* problem is proposed. The core idea is to design a long-short-term-memory

(LSTM) network that is capable of predicting posterior positions and orientations of mobile users, which can be then used to predict their channel coefficients. Consequently, the obtained channel coefficients can be exploited for deriving near-optimal transmission schemes prior to the intended service time, which enables real-time service. Through various simulations, the performance of the designed LSTM model is evaluated in terms of prediction accuracy and time. Finally, the performance of the proposed PO approach is investigated in the sum rate maximization problem of multi-user LiFi systems with QoS constraints, where a performance gap of less than 7% is achieved and a real-time service is guaranteed.

6.2   System Model and Problem Statement

We consider the multi-user indoor LiFi system presented in Figure 6.1, where K mobile LiFi users are communicating simultaneously (within the same time/frequency resource block) with the APs. Each user is equipped with a LiFi-enabled UE and is moving following a certain trajectory. In addition, during the movements of users, each UE has a random orientation over time, i.e., at each point of the trajectory of each user, the orientation of its associated UE is random. Moreover, each UE is equipped with a single LD and a single PD that are used for data transmission and reception in the downlink and uplink phases, respectively.

Let us consider an optimization problem $\mathcal{P}\left[\mathbf{H}(t)\right]$, where $\mathbf{H}(t)$ is the instantaneous channel matrix of the mutli-user LiFi system at time slot t, that aims at enhancing the performance of the LiFi system at hand at each time slot t, with respect to a certain performance metric, such as sum-rate maximization, minimum rate maximization, age of information (AoI), latency, etc. In addition, let Δt denotes the processing time required to solve the optimization problem $\mathcal{P}\left[\mathbf{H}(t)\right]$ at each time slot t, which increases as the number of mobile users and/or APs increases. Within the time interval Δt, the channel matrix of $\mathbf{H}$ evolves from $\mathbf{H}(t)$ to $\mathbf{H}(t + \Delta t)$, since the users are mobile and may have changed their instantaneous positions and orientations during the time interval Δt. In this case, the obtained solution from solving problem $\mathcal{P}\left[\mathbf{H}(t)\right]$ at time slot t may no longer be optimal after the optimization time Δt. In other words, the obtained solution, which is optimal for $\mathbf{H}(t)$, may not optimal for $\mathbf{H}(t + \Delta)$ and can imply a performance loss to the system. This problem is known as *channel aging*, i.e., the channel matrix $\mathbf{H}(t)$ is outdated
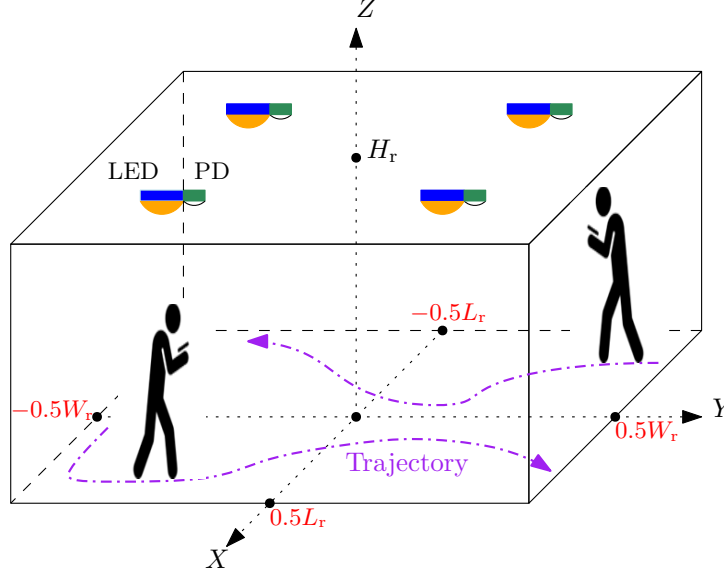
Figure 6.1: A typical multi-user indoor LiFi system.

at time slot $t + \Delta t$, and this is actually a very known problem in the wireless and mobile communication literature, especially for mobile massive MIMO systems [141, 142]. Based on the above discussion, a PO approach is proposed to overcome the aforementioned *channel aging* problem, which will be presented in the following section.

6.3 Proposed PO Approach

In this section, the proposed PO technique is presented. The basics of the proposed approach will be presented first. Then, its detailed implementation is investigated.

6.3.1 Proposed Approach

Let $L \in \mathbb{N} \backslash \{0\}$ denotes a posterior time slot index and let us consider an optimization problem $\mathcal{P} \left[\mathbf{H}(t + L) \right]$ that needs to be solved at each time slot $t + L$. In order to overcome the *channel aging* problem discussed in Section 6.2, an alternative approach is to solve problem $\mathcal{P} \left[\mathbf{H}(t + L) \right]$ prior to the occurring of the target time slot $t + L$. Precisely, the proposed PO approach consists first of predicting the channel matrix $\mathbf{H} \left(t + L \right)$ at time slot t, which is denoted by $\widehat{\mathbf{H}} \left(t + L \right)$. Then, the optimization problem $\mathcal{P} \left[\widehat{\mathbf{H}}(t + L) \right]$ is solved within the time interval $[t, t + L]$. In this case, a sub-optimal solution is obtained and can be employed in serving the cellular users at time slot $t + L$, without any processing delay at time slot $t + L$. This will beat indeed the raised problem of *channel aging*. Figure 6.2 presents the procedure of the proposed PO approach. As shown in this figure, it consists
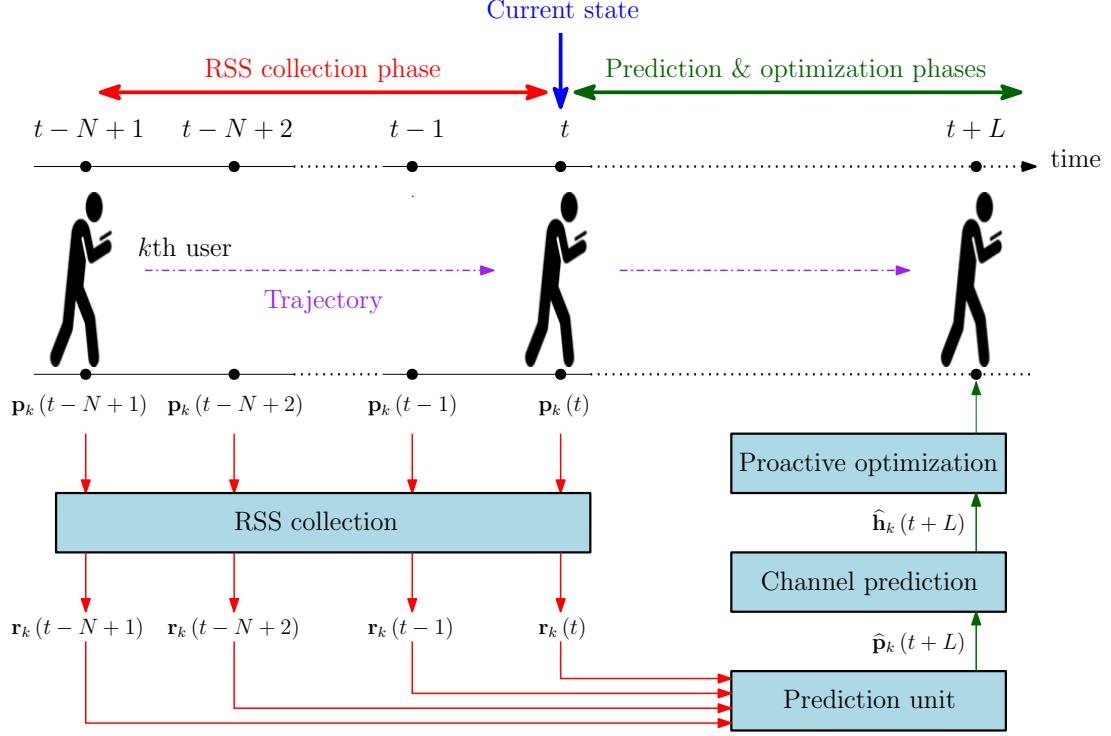
Figure 6.2: Procedure of the proposed PO technique.

mainly of three consecutive phases, which are: 1) RSS collection phase, 2) Prediction phase, and 3) Optimization phase. For the ease of reading, we start with the following notations.

Notations 6.1. *For all $k \in [\![1, K]\!]$, we denote by $\mathbf{p}_k(t) \triangleq [x_k(t), y_k(t), z_k(t), \alpha_k(t), \beta_k(t), \gamma_k(t)]$ the 1×6 vector that contains the exact instantaneous 3D position and orientation of the kth UE at time slot t. Accordingly, we denote by $\widehat{\boldsymbol{p}}_k(t)$ the predicted 3D position orientation of the kth UE at time slot t, respectively.*

The details of each phase of the proposed PO approach are presented in the following subsections.

6.3.2 RSS Collection Phase

In this phase, $N \in \mathbb{N} \backslash \{0\}$ uplink RSS values for each UE are collected over the time slots $[\![t - N + 1, t]\!]$. At each time slot $j \in [\![t - N + 1, t]\!]$, and for all $k \in [\![1, K]\!]$, the kth UE has an instantaneous 3D position and orientation vector $\mathbf{p}_k(j)$. First, in order to cancel any inter-user interference in this phase, the total IR bandwidth B_r is equally divided over all K UEs for the uplink transmissions. At this point, for all $k \in [\![1, K]\!]$, the kth UE needs to transmit a reference signal to the APs. Assuming that the DC-biased PAM with

order M is used, the kth UE broadcasts through its LD a scalar signal $s_k = I_{\text{DC}}$, where I_{DC} denotes the DC bias of the LD. Hence, for all $k \in [\![1, K]\!]$ and $i \in [\![1, N_{\text{r}}]\!]$, the received signal of the kth UE at the ith AP is given by

$$z_{k,i} = \lambda g_{i,k}(j) x_k + n_i, \tag{6.1}$$

where, for all $i \in [\![1, N_{\text{r}}]\!]$ and $j \in [\![1, N_{\text{t}}]\!]$, $g_{i,k}$ is the uplink channel gain between the kth user and the PD ith AP, and n_i is an AWGN experienced at the PD of the ith AP that is $\mathcal{N}(0, \sigma_{\text{n}}^2)$ distributed, such that $\sigma_{\text{n}}^2 = N_{\text{IR}} \frac{B_{\text{IR}}}{K}$ is the noise power, in which N_{IR} is the IR noise power spectral density at the optical receivers and B_{IR} is the IR bandwidth. In addition, as was explained in Section 2.1, $\lambda = T R_{\text{p}} \eta$, in which T is the TIA gain at the AP, R_{p} is the responsivity of the AP's PD, and η is the current-to-power conversion efficiency of the LDs.

Based on the above, for all $k \in [\![1, K]\!]$ and $i \in [\![1, N_{\text{t}}]\!]$, the received SNR of the kth UE at the ith AP at each time slot $j \in [\![t - N + 1, t]\!]$ is expressed as

$$r_{k,i}(j) = \frac{\lambda_{\text{u}}^2 g_{k,i}^2(j) P_{\text{elec}}}{\sigma_{\text{n}}^2}. \tag{6.2}$$

where $P_{\text{elec}} = \frac{I_{\text{DC}}^2}{3} \frac{M-1}{M+1}$ is the electrical power of the transmitted signals. Based on this, for all $k \in [\![1, K]\!]$, the $1 \times N_{\text{r}}$ received SNR vector of the kth UE at the APs at each time slot $j \in [\![t - N + 1, t]\!]$ is expressed as

$$\mathbf{r}_k(j) \triangleq [r_{k,1}(j), r_{k,2}(j), ..., r_{k,M}(j)], \tag{6.3}$$

which depends mainly on the instantaneous 3D position and orientation vector of the kth UE $\mathbf{p}_k(j)$ at time slot j. Consequently, as shown in Figure 6.2, within the time interval $[\![t - N + 1, t]\!]$, and for all $k \in [\![1, K]\!]$, the APs collect a group of N SNR vectors for the kth UE that is expressed as

$$\mathbf{r}_{k,\text{total}}(t) = [\mathbf{r}_k(t - N + 1), \mathbf{r}_k(t - N + 2), ..., \mathbf{r}_k(t)]. \tag{6.4}$$

6.3.3 Prediction Phase

In this phase, the goal is to predict, at each time slot t, the posterior 3D position and orientation for each UE relative to time slot $t + L$, based on its prior RSS values collected between the time slots $t - N + 1$ and t. Specifically, as shown in Figure 6.2, for all $k \in [\![1, K]\!]$, the goal is to predict, at each time slot t, the posterior 3D position and orientation vector $\mathbf{p}_k(t + L)$ of the kth UE, based on its associated vector of RSS values $\mathbf{r}_{k,\text{total}}(t)$ collected between time slots $t - N + 1$ and t. As was mentioned in the RSS collection phase in subsection 6.3.2, for all $k \in [\![1, K]\!]$, the vector of RSS values $\mathbf{r}_{k,\text{total}}(t)$

collected between time slots $t - N + 1$ and t is a function of the instantaneous 3D position orientation vector $\mathbf{p}_k(j)$ of the kth UE at each time slot $j \in [\![t - N + 1, t]\!]$, i.e., there exists a deterministic vector-valued function $\mathbf{F}(\cdot)$ such that

$$\mathbf{p}_k(j) = \mathbf{F}(\mathbf{r}_k(j)). \tag{6.5}$$

In other words, at each time slot t and for all $k \in [\![1, K]\!]$, the vector of total RSS values $\mathbf{r}_{k,\mathrm{total}}(t)$ collected between the time slots $t - N + 1$ and t contains information about the previous realizations of the 3D position and orientation of the kth UE within the time interval $[\![t - N + 1, t]\!]$.

On the other hand, for all $k \in [\![1, K]\!]$, since the kth UE is mobile, then its instantaneous 3D position and orientation vector $\mathbf{p}_k(t)$ is a multivariate random process (RP). In this case, for all $k \in [\![1, K]\!]$, and for every time slot t, there exists a probabilistic vector-valued function $\mathbf{D}(\cdot)$, such that

$$\begin{bmatrix} \mathbf{p}_k(t + L) \\ \mathbf{p}_k(t + L - 1) \\ \vdots \\ \mathbf{p}_k(t) \end{bmatrix} = \mathbf{D}\left(\begin{bmatrix} \mathbf{p}_k(t) \\ \mathbf{p}_k(t - 1) \\ \vdots \\ \mathbf{p}_k(t - N + 1) \end{bmatrix} \right). \tag{6.6}$$

Consequently, based on (6.5) and (6.6), there exists a probabilistic vector-valued function $\mathbf{J}(\cdot)$, such that, for all $k \in [\![1, K]\!]$, and for every time slot t,

$$\begin{bmatrix} \mathbf{p}_k(t + L) \\ \mathbf{p}_k(t + L - 1) \\ \vdots \\ \mathbf{p}_k(t) \end{bmatrix} = \mathbf{J}\left(\begin{bmatrix} \mathbf{r}_k(t) \\ \mathbf{r}_k(t - 1) \\ \vdots \\ \mathbf{r}_k(t - N + 1) \end{bmatrix} \right). \tag{6.7}$$

Based on (6.7), the objective here is to determine the probabilistic vector-valued function $\mathbf{J}(\cdot)$. However, obtaining its exact characterization is not straightforward. In fact, for all $k \in [\![1, K]\!]$, and for every time slot $j \in [\![t - N + 1, t]\!]$, the vector of RSS values $\mathbf{r}_k(j)$ includes the contributions of both the LOS and the NLOS components of the wireless links between the kth UE and the N_{r} APs. Although the contributions of the NLOS components will improve the prediction accuracy, like it was shown in Chapter 5, their inclusion in the prediction process is not straightforward from an optimization point of view, like the case of maximizing an observed predictive likelihood function. This is basically due to the complex expressions of the LiFi channel gain depicted in Section 2.2.

To overcome this issue, an approximate parametric vector-valued function $\widehat{\mathbf{J}}(\mathcal{W}, \cdot)$ will be constructed using an ANN, where $\mathcal{W}$ is the set of parameters of the ANN. In this

case, for all $k \in [\![1, K]\!]$, and at each time slot t, the predicted values of the posterior 3D position and orientation of the kth UE relative to time slot $t + L$ can be obtained as

$$
\begin{bmatrix}
\widehat{\mathbf{p}}_k(t + L) \\
\widehat{\mathbf{p}}_k(t + L - 1) \\
\vdots \\
\widehat{\mathbf{p}}_k(t)
\end{bmatrix}
= \widehat{\mathbf{J}}
\left(
\mathcal{W},
\begin{bmatrix}
\mathbf{r}_k(t) \\
\mathbf{r}_k(t - 1) \\
\vdots \\
\mathbf{r}_k(t - N + 1)
\end{bmatrix}
\right).
\tag{6.8}
$$

The details on how the approximate parametric vector-valued function $\widehat{\mathbf{J}}$ and the optimal set of parameters $\mathcal{W}^*$ are obtained will be presented in Section 6.4.

Based on the above, for all $k \in [\![1, K]\!]$, the predicted 3D position and orientation vector $\widehat{\mathbf{p}}_k(t + L)$ of the kth UE associated to time slot $t + L$ is obtained and its associated predicted $N_{\mathrm{t}} \times 1$ downlink channel gain vector $\widehat{\mathbf{h}}_k(t + L)$ can be calculated at time slot t. Consequently, the predicted $K \times M$ channel matrix $\widehat{\mathbf{H}}(t + L) = \left[\widehat{\mathbf{h}}_1(t + L), \widehat{\mathbf{h}}_2(t + L), ..., \widehat{\mathbf{h}}_K(t + L) \right]^T$ can be obtained at time slot t.

6.3.4 Optimization Phase

In this phase, once the predicted $K \times N_{\mathrm{t}}$ downlink channel matrix $\widehat{\mathbf{H}}(t + L)$ from the N_{t} APs and the K users is obtained, the optimization problem $\mathcal{P} \left[\widehat{\mathbf{H}}(t + L) \right]$ is solved within the time interval $[t, t + L]$. In this case, a sub-optimal solution is obtained and can be employed in serving the LiFi users at time slot $t + L$, without any processing delay at time slot $t + L$, which overcomes the problem of *channel aging* of the considered LiFi system that was raised in Section 6.2.

6.4 Joint Prediction of Indoor LiFi User Position and Orientation

6.4.1 Methodology

In this section, and as discussed in subsection 6.3.3, our objective is to determine an approximate parametric vector-valued function $\widehat{\mathbf{J}}$ along with its optimal set of parameters $\mathcal{W}^*$ that can predict the posterior 3D position and orientation of the LiFi UEs with a good accuracy. To reach this goal, DL techniques, through the use of ANNs, are employed.

The proposed prediction technique consists of two phases: 1) an offline learning (offline phase) and 2) an online deployment (online phase). In the offline learning, a data set of
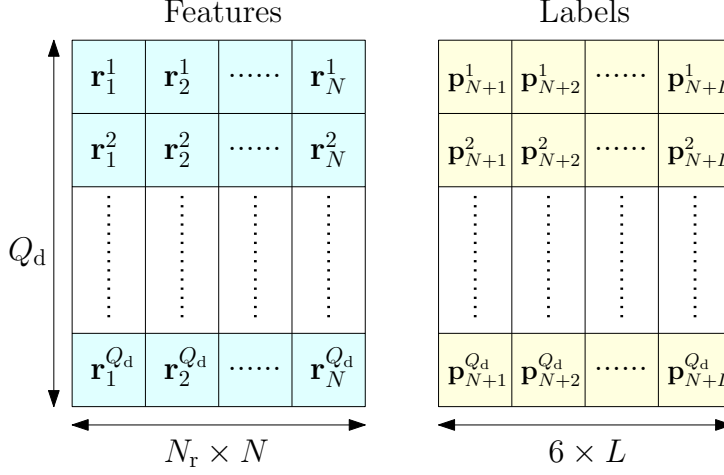
Figure 6.3: Data set structure

Q_{d} random sequences, each of length $N + L_{\max}$, are generated, where $L_{\max}$ denotes the maximum posterior time slot index. Specifically, for all $q \in [\![1, Q_{\mathrm{d}}]\!]$, a random trajectory of length $N + L_{\max}$ steps is generated using a predefined experimental-based indoor mobility model, within which a random 3D experimental-based orientation is generated at each step. For all $q \in [\![1, Q_{\mathrm{d}}]\!]$, the process of generating the qth data point of the data set is as follows.

1. A sequence $\left[\mathbf{p}_1^q, \mathbf{p}_2^q, ..., \mathbf{p}_{N+L_{\max}}^q\right]$ of $N + L_{\max}$ 3D position and orientation vectors is randomly generated using the experimental-based indoor ORWP, where for all $j \in [\![1, N + L_{\max}]\!]$, $\mathbf{p}_j^q$ is the 3D position and orientation vector of the jth time step of the qth sequence. The details of the experimental-based ORWP model employed here are presented in Appendix B. Then, the obtained sequence is recorded.

2. For all $j \in [\![1, N]\!]$, the $1 \times N_{\mathrm{r}}$ SNR vector $\mathbf{r}_j^q$ is calculated based on the 3D position and orientation vector $\mathbf{p}^q(j)$.

3. The features vector of the qth data point is the $1 \times N$ sequence of SNR vectors $[\mathbf{r}_1^q, \mathbf{r}_2^q, ..., \mathbf{r}_N^q]$.

4. The labels vector of the qth data point is the $1 \times L$ sequence of posterior 3D position and orientation vector $\left[\mathbf{p}_{N+1}^q, \mathbf{p}_{N+2}^q, ..., \mathbf{p}_{N+L_{\max}}^q\right]$.

The structure of the data set is shown in Figure 6.3. Afterwards, based on the obtained data set, optimal ANN models that provide the best approximate parametric vector-valued function $\widehat{\mathbf{J}}$ that can map between the received SNR vectors and the posterior

3D position and the orientation vectors are designed. Finally, in the online testing, the obtained approximate parametric vector-valued function $\widehat{\mathbf{J}}$ is deployed. In the following, we will present first the steps of the offline phase and then we will discuss the deployment of the obtained learning models in the online phase.

6.4.2 Prediction Model

The problem at hand is the prediction of future 3D positions and orientations of a LiFi UE based on its prior received SNR values. Since both the position and the orientation of the UE can be modeled as RPs, as discussed in the previous paragraph, the problem can be formulated as a sequence-to-sequence (Seq2Seq) prediction problem [143,144]. Seq2Seq prediction is basically a process of extracting useful information from historical records and then determining future values. Unlike regression predictive modeling, Seq2Seq mapping adds the complexity of sequences dependencies among the input variables [143,144]. A powerful type of neural network designed to handle sequences dependencies is called recurrent neural networks (RNNs). The LSTM network is a category of RNN that is trained using Backpropagation through time and that is known of their capability in alleviating the vanishing gradient problem [145]. As such, LSTM network can be used to create large RNNs that can be used to address difficult Seq2Seq prediction problems. Motivated by this discussion, the approximate parametric vector-valued function $\widehat{\mathbf{J}}$ is an LSTM network that is trained in the offline phase using the generated data set. Hence, its optimal set of parameters $\mathcal{W}^*$ that provide the best prediction accuracy can be obtained.

6.4.3 Online Phase

In the online phase, once the LSTM model is optimized, the obtained parametric vector-valued function $\widehat{\mathbf{J}}\left(\mathcal{W}^*, \cdot\right)$ is deployed at the APs. Consequently, for all $k \in [\![1, K]\!]$, and at each time slot t, the APs track if there is any change in the received SNR values $[\mathbf{r}_k(t - N + 1), \mathbf{r}_k(t - N + 2), ..., \mathbf{r}_k(t)]$ from the kth UE within the interval of time $[\![t - N + 1, t]\!]$. If this is the case, the received SNR values are fed into the obtained parametric vector-valued function $\widehat{\mathbf{J}}\left(\mathcal{W}^*, \cdot\right)$ in order to output the sequence of predicted posterior 3D position and orientation vectors of the kth UE $[\widehat{\mathbf{p}}_k(t), \widehat{\mathbf{p}}_k(t + 1), ..., \widehat{\mathbf{p}}_k(t + L)]$, where $L \in [\![1, L_{\max}]\!]$ is the target posterior time slot index. Consequently, the obtained sequences of predicted posterior 3D positions and orientations vectors are injected into the channel

matrix expression in order to predict the channel matrix of all UEs associated to time slot $t + L$, i.e., $\widetilde{\mathbf{H}}(t + L)$. Finally, assuming a certain transmission strategy and a predefined performance metric, the associated optimization problem $\mathcal{P}\left[\widehat{\mathbf{H}}(t + L)\right]$ is solved within the time interval $[t, t + L]$. In this case, a sub-optimal solution is obtained and can be employed in serving the cellular users at time slot $t + L$ directly, without any processing delay at time slot $t + L$.

6.5 Application: Proactive Sum-Rate Maximisation of Multi-User LiFi Systems

6.5.1 Motivation

The main motivation behind predicting the future channel realizations of mobile UEs is to proactively design near-optimal transmission schemes prior to the target service time slot, which will enable real-time near-optimal service for mobile UEs. As an application for the proposed PO technique, a typical optimization problem is considered, which is the sum-rate maximisation of multi-user LiFi systems with QoS constraints.

6.5.2 Signal Model and Rate Analysis

Consider the same indoor LiFi system presented in Section 6.2, where at each time slot t, the LiFi controller attempts to transmit the vector of messages $\mathbf{u}(t) = [u_1(t), u_2(t), ..., u_K(t)]^T$, in which for all $k \in [\![1, K]\!]$, $u_k(t)$ denotes the message intended to the kth UE at time slot t. Hence, in order to broadcast these messages through the N_{t} APs, the controller multiplexes the messages of the UEs using linear precoding. Based on this, the $N_{\mathrm{t}} \times 1$ vector of signals $\mathbf{s}(t)$ broadcast by the N_{t} APs at each time slot t can be expressed as

$$\mathbf{s}(t) = \mathbf{V}(t)\mathbf{u}(t) = \sum_{k=1}^{K} \mathbf{v}_k(t)u_k(t), \tag{6.9}$$

where for all $k \in [\![1, K]\!]$, $\mathbf{v}_k(t)$ presents the $N_{\mathrm{t}} \times 1$ precoding vector of the kth UE at time slot t and $\mathbf{V}(t) = [\mathbf{w}_1(t), \mathbf{w}_2(t), ..., \mathbf{w}_K(t)]$ presents the $N_{\mathrm{t}} \times K$ precoding matrix at time slot t.

One operating constraint in LiFi systems is the peak-power constraint at the LEDs, also known as the amplitude constraint, [72, 139, 140]. In fact, typical LEDs suffer from nonlinear distortion and clipping effects. Hence, in order to maintain a linear current to

light conversion and to avoid clipping distortion, a peak-power constraint is imposed on the emitted optical power from the APs [32]. This constraint is expressed as

$$||\mathbf{V}\mathbf{u}||_{\infty} \leq \iota I_{\mathrm{DC}}, \tag{6.10}$$

where $\iota \in [0, 1]$ denotes the modulation index of the LiFi system [32, 146]. Now, in order to satisfy the constraint in (6.10), we impose the following constraints on the precoding matrix $\mathbf{V}$ and the total electrical power P_{elec}.

$$||\mathbf{V}||_{\infty} \leq 1, \quad \text{and} \quad ||\mathbf{u}||_{\infty} \leq A, \tag{6.11}$$

where $A = \iota I_{\mathrm{DC}}$. Consequently, for all $k \in [\![1, K]\!]$, the received signal at the kth UE at each time slot t is expressed as

$$y_k(t) = \lambda \mathbf{h}_k^T(t)\mathbf{V}(t)\mathbf{u}(t) + n_k(t) = \underbrace{\lambda \mathbf{h}_k^T(t)\mathbf{v}_k(t)u_k(t)}_{\text{useful signal}} + \underbrace{\lambda \mathbf{h}_k^T(t)\mathbf{V}_k(t)\mathbf{u}_k(t)}_{\text{IUI}} + n_k(t), \tag{6.12}$$

where as was explained in Section 2.1, $\lambda = TR_{\mathrm{p}}\eta N_{\mathrm{LEDs}}$, in which T is the TIA gain at the receiver, R_{p} is the responsivity of the receiver's PD and η is the current-to-power conversion efficiency of the LEDs, and N_{LEDs} is the number of LEDs per AP. In addition, $\mathbf{V}_k(t)$ is the $N_{\mathrm{t}} \times (K-1)$ matrix that is equal to the precoding matrix $\mathbf{V}(t)$ after removing the kth column and $\mathbf{u}_k(t)$ is the $K-1$ vector that is equal to the vector of messages $\mathbf{u}(t)$ after removing the kth element. Moreover, for $k \in [\![1, K]\!]$, n_k is the AWGN experienced at the kth user that is $\mathcal{N}(\mathbf{0}_{N_{\mathrm{r}}}, \sigma_{\mathrm{VL}}^2 \mathbf{I}_{N_{\mathrm{r}}})$ distributed, where the variance of the noise is equal to $\sigma_{\mathrm{VL}}^2 = N_{\mathrm{VL}} B_{\mathrm{VL}}$, where N_{VL} is the noise single sided power spectral density and B_{VL} is the visible light bandwidth available at the APs.

As depicted in the received signal's expression in (6.12), each UE suffers from an inter-user interference (IUI), which is resulting from the transmission of the messages of all UEs within the same time/frequency resource block. One solution to cancels the effects of the IUI at each UE is to employ zero-forcing (ZF) precoding, i.e., to force this interference to be equal to zero at its reception. This cancellation can occur by imposing the following constraints

$$\mathbf{h}_k^T(t)\mathbf{v}_i(t) = 0, \qquad \forall\, (k, i) \in [\![1, K]\!]^2 \,\&\, i \neq k, \tag{6.13}$$

or equivalently $\mathbf{H}(t)\mathbf{V}(t) = $ diagonal matrix, where $\mathbf{H}(t) = [\mathbf{h}_1(t), \mathbf{h}_2(t), ..., \mathbf{h}_k(t)]^T$ denotes the channel matrix of the considered multi-user LiFi system.

Since LiFi systems impose an amplitude constraint (or a peak-power constraint) on the input signals as discussed above, the Gaussian distribution is not admissible for LiFi signals. Due to this, the capacity of LiFi systems remains unknown [147]. Extensive studies have put much effort into obtaining closed-form expressions for the achievable

data rate, and have demonstrated that it can be expressed as $\frac{1}{2}\log\left(1 + c \times \text{SNR}\right)$, where $c = \frac{1}{2\pi e}$ and e is the Euler constant, when the information-bearing signals $\mathbf{u}$ follow the truncated Gaussian distribution [148, 149]. Hence, based on this description and the results of [148, 149], for all $k \in [\![1, K]\!]$, the instantaneous achievable rate at the kth UE at each time slot t can be expressed as

$$R_k\left(\mathbf{h}_k(t), \mathbf{v}_k(t)\right) = \frac{1}{2}\log\left(1 + \rho\left(\mathbf{h}_k(t)^T\mathbf{v}_k(t)\right)^2\right), \tag{6.14}$$

where $\rho = \frac{c\lambda^2 A^2 \sigma_\text{s}^2}{\sigma_\text{n}^2}$, in which $\sigma_\text{s}^2 = \sigma_\text{d}^2 - \dfrac{\sigma_\text{d}\exp\left(\frac{-1}{2\sigma_\text{d}^2}\right)}{\text{erf}\left(\frac{1}{\sigma_\text{d}\sqrt{2}}\right)}$, such that σ_d^2 is the scale parameter of the truncated Gaussian distribution of the input signals.

6.5.3 Problem Formulation

With the objective of maximizing the instantaneous achievable sum-rate of the considered LiFi system while guaranteeing a target QoS for each UE, an optimal design of the instantaneous precoding matrix $\mathbf{V}(t)$ can be obtained through the following optimization problem.

$$\mathcal{P}\left[\mathbf{H}(t)\right]: \quad \max_{\mathbf{V}(t)} \sum_{k=1}^{K} R_k\left(\mathbf{h}_k(t), \mathbf{v}_k(t)\right) \tag{6.15a}$$

$$\text{s.t.} \quad \mathbf{h}_k^T(t)\mathbf{v}_i(t) = 0, \qquad \forall(k, i) \in [\![1, K]\!]^2 \ \& \ i \neq k, \tag{6.15b}$$

$$R_\text{th} \leq R_k\left(\mathbf{h}_k(t), \mathbf{v}_k(t)\right), \quad \forall\, k \in [\![1, K]\!], \tag{6.15c}$$

$$\|\mathbf{V}(t)\|_\infty \leq 1. \tag{6.15d}$$

Problem $\mathcal{P}\left[\mathbf{H}(t)\right]$ is a non-linear non-convex problem and, thus, obtaining its optimal solution is not straightforward. Some heuristic approaches can be employed to obtain suboptimal solutions for problem $\mathcal{P}\left[\mathbf{H}(t)\right]$. However, these approaches require a processing time that may exceed the maximum amount of time allocated to serve the different users, which raises the *channel aging* problem invoked in this chapter. To overcome this issue, the proposed PO approach can be applied. Hence, considering a posterior time slot index L, we are interested in solving the following optimization problem.

$$\mathcal{P}\left[\widehat{\mathbf{H}}(t+L)\right]: \quad \max_{\mathbf{V}(t+L)} \sum_{k=1}^{K} R_k\left(\widehat{\mathbf{h}}_k(t+L), \mathbf{v}_k(t+L)\right) \tag{6.16a}$$

$$\text{s.t.} \quad \widehat{\mathbf{h}}_k^T(t+L)\mathbf{v}_i(t+L) = 0, \qquad \forall\,(k, i) \in [\![1, K]\!]^2 \ \& \ i \neq k, \tag{6.16b}$$

$$R_\text{th} \leq R_k\left(\widehat{\mathbf{h}}_k(t+L), \mathbf{v}_k(t+L)\right), \quad \forall\, k \in [\![1, K]\!], \tag{6.16c}$$

$$\|\mathbf{V}(t+L)\|_\infty \leq 1, \tag{6.16d}$$

at each time slot t and within the time interval $[t, t+L]$, which enables obtaining the optimal precoding matrix $\mathbf{V}^*(t+L)$ prior to the service time slot $t+L$.

Problem $\mathcal{P}\left[\widehat{\mathbf{H}}(t+L)\right]$ is also a non-linear non-convex problem and, thus, obtaining its optimal solution is not straightforward. Alternatively, we propose in the following a solution approach that can reach a near-optimal solution. Consider the change of variable given by $\mathbf{V}(t+L) = \widehat{\mathbf{H}}(t+L)^{\perp}\mathbf{X}$, where $(\cdot)^{\perp}$ denotes the pseudo-inverse operator and $\mathbf{X} = \mathrm{diag}\,(\mathbf{x})$ is a $K \times K$ diagonal matrix, such that $\mathbf{x} = [x_1, x_2, ..., x_K]^T$ is a $K \times 1$ real vector. Based on this, constraint (6.16b) is satisfied and problem $\mathcal{P}\left[\widehat{\mathbf{H}}(t+L)\right]$ can be re-expressed as

$$\mathcal{P}'\left[\widehat{\mathbf{H}}(t+L)\right]: \quad -\min_{\mathbf{x}} \sum_{k=1}^{K} -\frac{1}{2}\log\left(1 + \rho x_k^2(t)\right), \tag{6.17a}$$

$$\text{s.t.} \quad R_{\text{th}} - \frac{1}{2}\log\left(1 + \rho x_k^2\right) \le 0, \qquad \forall\, k \in [\![1, K]\!], \tag{6.17b}$$

$$\left\|\widehat{\mathbf{H}}(t+L)^{\perp}\mathrm{diag}\,(\mathbf{x}(t))\right\|_{\infty} \le 1. \tag{6.17c}$$

The function $x \mapsto f(x) = -\frac{1}{2}\log\left(1 + \rho x^2\right)$ is a smooth function and its second derivative is expressed as $\frac{\partial^2}{\partial x^2}(x) = \frac{\rho(\rho x^2 - 1)}{(\rho x^2 + 1)^2}$, which is positive if $x^2 \ge \frac{1}{\rho}$ and negative otherwise. Hence, the function f is convex if $x^2 \ge \frac{1}{\rho}$ and concave otherwise. Consequently, problem $\mathcal{P}'\left[\widehat{\mathbf{H}}(t+L)\right]$ is not convex. To deal with this issue, we convexify problem $\mathcal{P}'\left[\widehat{\mathbf{H}}(t+L)\right]$ by employing the convex-concave procedure (CCP) proposed in [150]. Using CCP, and based on the description in [150], the objective function (6.17a) and the constraints in (6.17b) are convexified by linearizing them around a certain point $\mathbf{w}_j = [w_{j,1}, w_{j,2}, ..., w_{j,K}]^T$ through the first order Taylor approximation. In this case, the convex form of problem $\mathcal{P}'\left[\widehat{\mathbf{H}}(t+L)\right]$ is given by

$$\mathcal{P}''\left[\widehat{\mathbf{H}}(t+L), \mathbf{w}_j\right]: \quad -\min_{\mathbf{x}} \sum_{k=1}^{K} \left(-\frac{1}{2}\log\left(1 + \rho w_{j,k}^2\right) - \frac{\rho y_{j,k}}{\rho w_{j,k}^2 + 1} \times (x_k(t) - w_{j,k})\right), \tag{6.18a}$$

$$\text{s.t.} \quad R_{\text{th}} - \frac{1}{2}\log\left(1 + \rho y_{j,k}^2\right) - \frac{\rho w_{j,k}}{\rho w_{j,k}^2 + 1} \times (x_k(t) -_{j,k}) \le 0,$$

$$\forall\, k \in [\![1, K]\!], \tag{6.18b}$$

$$\left\|\mathbf{H}^{\perp}(t)\mathrm{diag}\,(\mathbf{x}(t))\right\|_{\infty} \le 1. \tag{6.18c}$$

Problem $\mathcal{P}''\left[\widehat{\mathbf{H}}(t+L), \mathbf{w}_j\right]$ is a convex optimization problem that depends on the linearization point $\mathbf{w}_j$ and can be solved efficiently using standard optimization packages [151, 152]. The detailed iterative algorithm for solving the original problem $\mathcal{P}\left[\widehat{\mathbf{H}}(t+L)\right]$ is given in **Algorithm 1**, where the initial point $\mathbf{w}_1$ is a random feasible point that

---

Algorithm 1 Iterative algorithm for solving $\mathcal{P}\left[\widehat{\mathbf{H}}(t+L)\right]$

---

1. **Initialization**: Choose an initial feasible point $\mathbf{y}_0$.

2. **Set**: $j = 0$.

3. **Repeat**:

    i) Update iteration $j \leftarrow j + 1$.

    ii) Solve $\mathcal{P}''\left[\widehat{\mathbf{H}}(t+L), \mathbf{w}_j\right]$.

    iii) Assign the solution to $\mathbf{w}_{j+1}$.

4. **Termination**: terminate step 3. when

    i) $|g(\mathbf{x}_j, \mathbf{x}_{j-1}) - g(\mathbf{x}_{j-1}, \mathbf{x}_{j-2})| \leq \epsilon$, or

    ii) $j = j_{\max}$.

5. **Assign**: $\mathbf{x}^* = \mathbf{x}_j$.
6. **Construct**: $\mathbf{V}^*(t+L) = \widehat{\mathbf{H}}(t+L)^\perp \mathrm{diag}\left(\mathbf{x}^*\right)$.

---

satisfies the constraints of problem $\mathcal{P}\left[\widehat{\mathbf{H}}(t+L)\right]$, $g(\cdot, \cdot)$ is the objective function in (6.18a) of problem $\mathcal{P}''\left[\widehat{\mathbf{H}}(t+L), \mathbf{y}_j\right]$, ϵ is a gap threshold and $j_{\max}$ is a maximum number of iterations. Finally, once the precoding matrix $\mathbf{V}^*(t)$ is obtained, it is applied directly at time slot $t + L$. Consequently, for all $k \in [\![1, K]\!]$ the instantaneous achievable rate at the kth UE at each time slot t can be expressed as $R_k\left(\mathbf{h}_k(t+L), \mathbf{v}_k(t+L)^*\right)$.

6.6 Simulation Results

In this section, our objective is to evaluate the performance of the proposed PO approach through extensive simulations.

6.6.1 Simulations Parameters

We consider a typical indoor environment with dimensions $L_{\mathrm{r}} \times W_{\mathrm{r}} \times H_{\mathrm{r}} = 10 \times 10 \times 3$ m^3. The indoor environment is equipped with 16 APs which are arranged on the vertices of a square lattice over the ceiling of the room, where each AP is oriented vertically downward. In addition, a LiFi UE, that is equipped with one LD and one PD, is randomly located within the room and its UE may have a random orientation. The UE is a typical smartphone with dimensions $14 \times 7 \times 1$ cm^3. The LD and the PD are adjacent to each

Parameter	Symbol	Value
Room dimension	$L_{\mathrm{r}} \times W_{\mathrm{r}} \times H_{\mathrm{r}}$	5 m $\times$5 m $\times$3 m
Modulation index	ι	0.33
User indoor walking speed	v	1 m/second
Time slot duration	δt	0.5 second
PD responsivity	R_{p}	0.6 A/W
Current-to-power conversion factor	η	0.8 W/A
LED half-power semiangle	$\Phi_{1/2}$	60°
PD geometric area	A_{PD}	1 cm^2
Optical concentrator refractive index	n_c	1
Reflection coefficient of the walls	ξ	0.7
Field of view of the PD	Ψ	90°
VL bandwidth	B_{v}	10 MHz
VL noise power spectral density	N_{v}	10^{-21} W/Hz
IR bandwidth	B_{r}	10 MHz
IR noise power spectral density	N_{r}	10^{-21} W/Hz

Table 6.1: Simulation Parameters.

other and are placed at screen of the smartphone, exactly at 6 cm above the center. The parameters used throughout the chapter are shown in Table 6.1. The CPU of the machine on which all the simulations were performed was an Intel Core i5 from the second generation that has a dual-core, a basic frequency of 2.40 GHz and a maximum turbo frequency of 3.40 GHz.

6.6.2 ANNs Specifications

The architecture of the LSTM model is shown in Table 6.2. For comparison purposes, a CNN model is considered. The design of the considered CNN is optimized and the optimal model consists of an input layer, an output layer and 2 hidden layers, where each hidden layer is composed of 16 filters. In addition, the kernel size of each convolution neuron is composed of 4 parameters. In this CNN model, the structure of each neuron in each hidden layer is the same as the one proposed in Chapter 5. The design of the LSTM and CNN models is performed using the programming environment Python 3 and the Keras library developed by Google's TensorFlow team in 2017 [135].

Prior time slot index	$N = 8$
Maximum posterior time slot index	$L_{\mathrm{max}} = 4$
data set size	$Q_{\mathrm{d}} = 10^6$
(Train, test) partition	$(0.9, 0.1) \times Q_{\mathrm{d}}$
Number of LSTM units	100
LSTM activation function	Hyperbolic tangent (tanh)
LSTM recurrent activation function	Sigmoid
Number CNN hidden layers	2
Number of filters per CNN hidden layer	16
Kernel size for each CNN neuron	4
CNN hidden layer activation	Relu
CNN output layer activation	Linear
Total number of parameters	LSTM: $24,224$ CNN: $25,848$
Optimizer	Adam

Table 6.2: ANNs specifications.

6.6.3 Learning, Prediction, and Computational Complexity Evaluation

Figure 6.4 presents the training and validation losses of the designed LSTM and CNN networks, measured in terms of the MSE, versus the training epoch index. As it can be seen from this figure, the training and validation losses decrease as the epoch index increases, which demonstrates that the designed LSTM and CNN networks are both not overfitting and can generalize well over unseen data points in the online phase.

Figure 6.5 presents the empirical CDF of the instantaneous positioning error resulting from the designed LSTM and CNN models for different values of the posterior time slot index L. This figure shows that the LSTM model provides a higher positioning accuracy than the CNN model. In the same context, as shown in Tables D.1 and D.2 in Appendix D, when the posterior time slot index $L = 1$, the reported average positioning errors are 0.19m and 0.47m for the LSTM and the CNN models, respectively, whereas when $L = 4$, the reported average positioning errors are 0.32m and 0.65m for the LSTM and the CNN models, respectively. Moreover, Figure 6.5 shows that the positioning error increases as the posterior time slot index increases. This result is expected since, as the posterior time slot index increases, more uncertainty about the future positions will be considered.
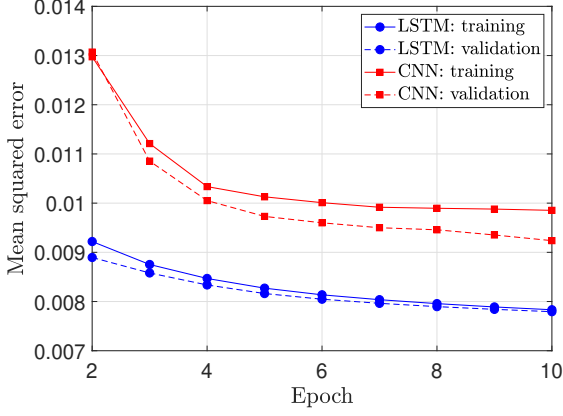
Figure 6.4: Training and validation loss versus the epoch index.
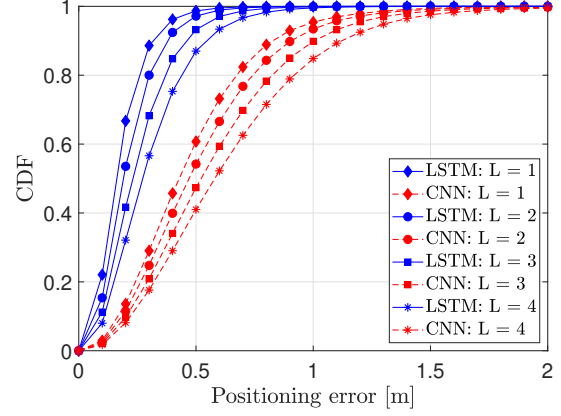
Figure 6.5: CDF of the positioning error for different posterior time slot indices.

Considering the prediction performance of the orientation angles, Figure 6.6 presents the empirical CDFs of the prediction error of the orientation angles yaw α, pitch β, and roll γ. First, the same interpretations established for the positioning error apply for the yaw angle α, where its average prediction error resulting from the LSTM and CNN models are presented in Table D.1 and D.2 in Appendix D. However, for the pitch angle β and the roll angle γ, Figure 6.6 and D.1 and D.2 in Appendix D show that the LSTM model and the CNN model exhibit the same prediction performance. In addition, the prediction performance does not change as the posterior time slot index increases. These observations are basically due to the fact that, from the experimental-based statistics presented in Table 2.1 in Section 2.3, the standard deviation of the pitch angle β and the roll angle γ are very low, i.e., both β and γ fluctuates slightly around their means.

The required time to generate a data set of size $Q_{\mathrm{d}} = 10^5$ data points is approximately 6 hours. In the other hand, the time required to train the designed LSTM and CNN models is 14 mins and 1.5 hours, respectively. Although the time required for the data set generation and the models training is large, this high computational time is not an issue, since the data set generation and the models training is performed in the offline phase and only once prior to the deployment of the APs. Considering the online complexity, the computational time of the designed LSTM and CNN models in the online phase is extremely low. In fact, over the whole test set, which has a size of $0.1 \times Q_{\mathrm{d}} = 10^5$, the total prediction time in the online phase is 3 seconds and 6.56 seconds for the LSTM and CNN models respectively. Therefore, the average prediction time per trial is $\frac{3}{10^5} = 0.03$ millisecond and $\frac{6.56}{10^5} = 0.07$ millisecond for the LSTM and CNN models respectively, i.e.,

(a) Yaw angle α. (b) Pitch angle β. (c) Roll angle γ.
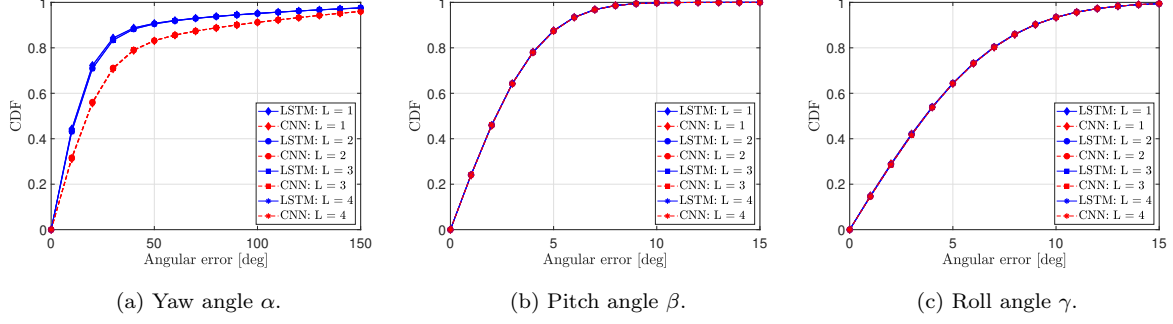
Figure 6.6: CDF of the prediction error of the orientation angles yaw α, pitch β and roll γ.

real-time prediction. In addition, the reported results demonstrates the superiority of the designed LSTM model over the CNN model. This makes the designed LSTM model an auspicious solution for accurate and real-time predictions.

6.6.4   Sum Rate Performance Evaluation

In this subsection, we consider the proactive sum-rate maximisation of the multi-user system considered in Section 6.5 as an application of the proposed PO approach. The results presented within this subsection are obtained from independent Monte-Carlo trials over the whole test set. For a given prior time slot index L, and at each time slot t, four different cases are considered, which are

1. *Baseline 1*: The exact instantaneous channel matrix $\mathbf{H}\left(t+L\right)$ is perfectly estimated at time slot $t+L$ and then the corresponding optimal precoding matrix is obtained at the same time slot without considering any processing delay.

2. *Proposed PO*: The predicted instantaneous channel matrix $\widehat{\mathbf{H}}\left(t+L\right)$ is obtained from the optimized LSTM model at time slot t and then the corresponding optimal precoding matrix is obtained within the time interval $[\![t, t+L]\!]$.

3. *Baseline 2*: The predicted instantaneous channel matrix $\widehat{\mathbf{H}}\left(t+L\right)$ is obtained from the optimized CNN model at time slot t and then the corresponding optimal precoding matrix is obtained within the time interval $[\![t, t+L]\!]$.

4. *Baseline 3*: The exact instantaneous channel matrix $\mathbf{H}\left(t\right)$ is perfectly estimated at time slot t. Then the corresponding optimal precoding matrix is obtained within the time interval $[\![t, t+L]\!]$ and then applied at time slot $t+L$.

101

Baseline 1 is considered here as an upper bound to assess the performance of *Proposed PO* scheme, since at each time slot $t+L$, the idealistic scenario is to obtain the corresponding optimal precoding matrix at the same time slot without any processing delay. Moreover, *Baseline 3* is considered here to demonstrate the performance degradation caused by the *channel aging* problem invoked in this chapter, since the precoding matrix associated to the instantenous channel matrix $\mathbf{H}(t)$ is obtained within the time interval $[\![t, t+L]\!]$, and therefore, applied for the instantaneous channel matrix $\mathbf{H}(t+L)$. On the other hand, for each case discussed above, the associated precoding matrix is obtained using two approaches, which are

- The optimal approach that consists of running an off-the-shelf optimization solver.[1]

- The CCP approach (**Algorithm 1**).

In line with the above, Figure 6.7 presents the average sum rate of the considered multi-user LiFi system versus the number of LiFi UEs K for the different cases presented above, where the posterior time slot index $L = 2$ and the target rate threshold per UE is $R_{\text{th}} = 1$ nats/s/Hz. Figure 6.7 demonstrates that the CCP approaches provides a near-optimal solution for the problem in hand, where the gap between average sum rate obtained from using the optimal solution and the CCP solution is less than 0.01% for all the considered scenarios. On the other hand, by comparing *Baseline 3* to *Baseline 1*, Figure 6.7 shows the performance degradation that is caused by the channel aging problem, where the highest gap between the average sum rates associated to *Baseline 1* and *Baseline 3* is higher than 20% for the considered range of number of UEs. However, the *proposed PO* approach outperforms *Baseline 3* and brings a performance enhancement to the system, where the highest gap between the average sum rates associated to *Baseline 1* and the *proposed PO* is less than 7%. On the other hand, and in accordance with the results obtained in the previous subsection, Figure 6.7 shows that the LSTM model outperforms

---

[1]The adopted solver is `fmincon`, which is a predefined `MATLAB` solver [153]. In addition, 100 distinct initial points were randomly generated within the feasibility region of the optimization variables in order to converge to the optimal solution. Specifically, through the use of the `fmincon` solver, each initial point will lead to a given local extremum. Then, once all local extrema are collected, a simple brute force search over the obtained extrema is applied to obtain the optimal solution. Although this heuristic approach suffers from its high complexity, it was demonstrated that it is very effective in finding the optimal solutions of non-convex problems as shown in [154–157]. Nevertheless, it is important to mention that the optimal solutions of the considered problems can also be obtained using the technique proposed in [158], which has a complexity of $\mathcal{O}\left(\frac{1}{\epsilon^2}\right)$ when the target accuracy of the solution is less than ϵ.
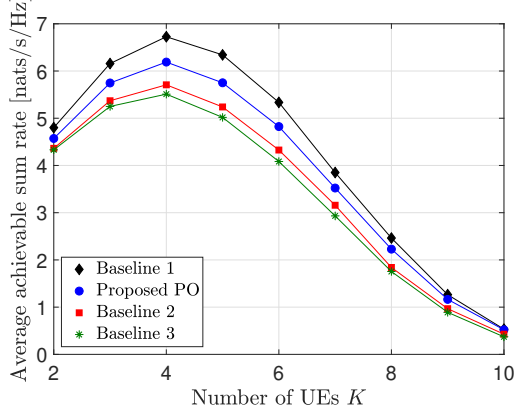
Figure 6.7: Sum rate versus the number of LiFi UEs K, when the posterior time slot index $L = 2$ and the required rate threshold for each LiFi UE $R_{\text{th}} = 2$ nats/s/Hz. Marks denote the CCP results and solid lines denote optimal approach results.
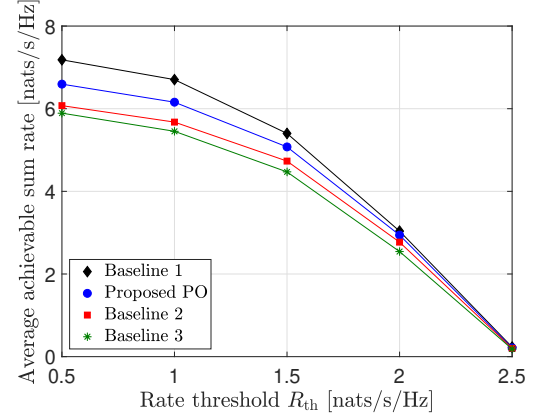
Figure 6.8: Sum rate versus the required rate threshold for each LiFi UE R_{th}, where the considered number of UEs is $K = 4$ and the posterior time slot index $L = 2$. Marks denote the CCP results and solid lines denote optimal approach results.

the CNN model, since the highest gap between the average sum rates associated *Baseline 1* and *Baseline 2* is higher than 10%.

Figure 6.8 presents the average sum rate of the considered multi-user LiFi system versus the target rate threshold per UE R_{th}, when the number of UEs is $K = 4$ and the posterior time slot index $L = 2$. Basically, this figure shows the same conclusions derived from Figure 6.7, which demonstrates the potential of the LSTM model in particular and the proposed PO approach in general. In addition, this figure shows that the sum rate of the system decreases as the rate threshold R_{th}. This is basically expected, since when the rate threshold R_{th} increases, the number of users that are admitted to the networks increases, and this is due to the fact that their channel realizations can not satisfy the target QoS.

Figure 6.9 presents the average computational time of the optimal optimization approach and the CCP approach for obtaining the best precoding matrix $\mathbf{V}$ for the considered LiFi system versus the number of LiFi UEs. This figure shows that the computational time increases as the number of UEs increases, which is expected, since as the number of UEs increases, the number of optimization variables increases. In addition, this figure demonstrates that the CCP approach has a lower computational time than the one of the optimal optimization approach (at least 50% less). In addition, recall that the CCP approach provides a performance gap that is less than 0.01% from the optimal approach.
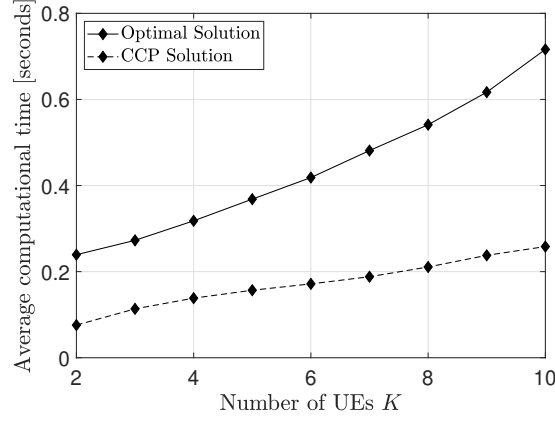
Figure 6.9: Average computational time versus the number of LiFi UEs K, when the required rate threshold for each LiFi UE $R_{\mathrm{th}} = 1$ nats/s/Hz.

This demonstrates the potential of the CCP approach in providing an optimal solution with a low computational time for the considered problem. Moreover, since the duration of one time slot is 0.5 seconds, the solution of the CCP approach can be obtained within one time slot. Therefore, the proposed PO approach can be applied even for a posterior time slot index $L = 1$, i.e., at each time slot t, the a near-optimal solution can be provided using the LSTM model and the CCP approach in the time interval $[\![t, t+1]\!]$. Therefore, for each time slot t, a near optimal precoding matrix $\mathbf{V}$ can be applied directly at time slot $t+1$ without any processing delay.

6.7 Conclusion

With the objective of overcoming the LiFi channel aging problem, a PO approach for indoor LiFi systems is proposed in this chapter. The core of the proposed technique is one LSTM network that is capable of predicting posterior positions and orientations of mobile users following random trajectories in indoor environments. Afterwards, these predicted posterior positions and orientations are used to predict the channel coefficients of mobile wireless links. Finally, the obtained predicted channel coefficients are exploited for deriving near-optimal power allocation schemes prior to the intended service time, which enables near-optimal and real-time service for mobile LiFi users. Through various simulations, the performance of the proposed PO approach is investigated in a typical optimization problem, which is the sum rate maximization of multi-user LiFi systems with QoS constraints. For this case, a performance gap of less than 7% is achieved, while

saving guaranteed real-time service. This demonstrates the potential of the proposed PO approach in providing near-optimal and real-time service of mobile LiFi users and in alleviating the LiFi *channel aging* problem.

The focus of Chapters 5 and 6 is providing some solutions for the CSI acquisition procedure, either CSI estimation or prediction. Hence, the goal of these two last chapters is preparing the floor for improving the performance of LiFi systems in order to meet the requirements of 6G networks, especially in terms high data rates and massive connectivity. To this end, the next chapter focuses on developing advanced multiple access techniques in order to meet these demands.

Chapter 7

CoMP-Assisted NOMA and Cooperative NOMA in Indoor LiFi Cellular Systems

7.1 Motivation and Related Works

As a wireless broadband technology, LiFi must support a high number of users with simultaneous network access [31]. Traditional multiple access techniques, referred to as orthogonal multiple access (OMA) techniques, allocate the available resources to coexisting users in an orthogonal manner in order to cancel the IUI. Such multiple access techniques include time division multiple access (TDMA), and frequency division multiple access (FDMA) [31]. The main drawback of the aforementioned techniques is that the maximum number of users that can be served is limited by the number of available orthogonal resources. In other words, the OMA techniques cannot provide sufficient resource reuse when the number of coexisting users is high. This makes OMA techniques unable to support a massive number of users, and hence, unable to provide a massive connectivity, which is one of the main requirements of 6G networks.

In an effort to increase the throughput and improve the fairness of LiFi systems, the non-orthogonal multiple access (NOMA) technique was introduced in the literature. In contrast to OMA techniques, NOMA allows multiple users to exploit the same time/frequency resource blocks at the expense of some IUI, leading to an efficient resource utilization. In particular, downlink power-domain NOMA relies on the superposition coding (SC) concept at the transmitter side to multiplex the data streams of different users

106

in the power domain, and on the successive interference cancellation (SIC) concept at the end users to decode their received data [159].[1] NOMA operates by allocating different power levels to users based on their channel gains. On the other side, the strong users, which are the users with high channel gains, first apply SIC to decode the weak users' data, which are the users with low channel gains, cancel it from their respective receptions, and then decode their data, whereas the weak users proceed to decode their data directly, and hence, suffer from IUI resulting from the superposition of the strong users' data.

Despite the great benefits that LiFi offers, it suffers from various shortcomings that make the current technology still far from satisfying the demands of 6G networks. The first limitation is the short communication range resulting from the short wavelengths of the visible light waves. This results in high propagation losses as the LiFi channel gain significantly deteriorates when the distance between transmitting and receiving devices increases, in addition to the fact that the visible light can be easily blocked by obstacles [34, 160, 161]. Moreover, unlike conventional RF wireless systems, the LiFi channel is not isotropic, meaning that the orientations of the transmitting and receiving devices affect the channel gains significantly [34, 160, 161]. As a result, the LiFi channel quality fluctuates and the performance of advanced multiple access techniques, such as NOMA, is significantly affected when applied to LiFi systems [34, 160, 161].

A large body of work has been produced in the application of NOMA in LiFi systems, such as [52, 162–165] to name a few. In [52, 162], it was shown that NOMA outperforms the traditional orthogonal frequency division multiple access (OFDMA) scheme in indoor LiFi systems that are serving multiple users with fixed positions and orientations. Both works prove the superiority of NOMA over OMA for stationary users but refrain from studying the performance of NOMA for mobile users with random positions and orientations. In [163], NOMA was investigated in a downlink multi-user LiFi system with mobile and randomly oriented users, where the sum-rate and the outage probability were derived. Recently, an overview of the key multiple access techniques used in single-cell LiFi systems, such as NOMA and space-division-multiple-access (SDMA), was provided in [164]. In [165], a system model consisting of one AP serving multiple users simultaneously was established, where users are served using the cooperative NOMA (C-NOMA) scheme. C-

---

[1]In this chapter, the term "NOMA" is restricted to power-domain NOMA as distinct from its code-domain NOMA counterpart.

NOMA is an enhanced version of NOMA that takes advantage of the desirable attributes of NOMA and device-to-device (D2D) communication. By exploiting the SIC capabilities, each strong user can act as a relay to assist the communication between the transmitter and the weak user through an RF D2D link. Hence, each weak user receives multiple versions of his data, one through the LiFi link coming from the transmitter and the remaining from the RF links coming from the associated strong users. In [165], the LiFi system sum-rate was maximized by optimizing the strong/weak user pairing, the LiFi/RF link selection, and the transmitted power, where it was shown that C-NOMA outperforms the conventional NOMA scheme. The main drawback with the works in [52, 162–165] is that the performance of NOMA was investigated in a single-cell setup, and the extension to multi-cell configuration was not considered

For 6G wireless networks, cell densification has been demonstrated to be an effective method to increase the network capacity. The main motivation behind cell densification is reducing the path loss and allowing the reuse of partial or total spectrum by small cells within a given coverage area. In the context of LiFi, the concept of optical attocell was first introduced in [166]. However, similar to the cell densification concept, the main drawback of the use of multiple optical attocells in indoor environments is the severe ICI. Precisely, an indoor environment can be composed of multiple optical attocells, each having a radius of around 3 m [52]. These optical attocells are adjacent to each other. Therefore, when the optical attocells are exploiting the same frequency resources, the users within one attocell can experience severe ICI from adjacent cells.

The application of NOMA in multi-cell LiFi systems was studied in [167,168]. In [167], a user grouping scheme based on users locations was proposed to reduce the ICI effects in NOMA-based multi-cell LiFi networks. With the residual interference from the SIC process in NOMA taken into account, the power allocation within each attocell was optimized to improve the achievable rate per user under a QoS constraint. Recently, a multi-cell LiFi system was considered in [168], where each attocell consists of an AP that serves two users coexisting within its coverage using C-NOMA. However, the main drawback of the schemes proposed in [167, 168] is that the LiFi users still suffer from the ICI effects since no ICI mitigation techniques were employed. In order to mitigate the ICI effects, the concept of cooperative cellular systems has been introduced in practical LiFi systems, where multiple LiFi APs coordinate together in serving multiple users within the resulting

illuminated area [75, 76, 78, 169–171]. In this context, the users that are highly prone to ICI effects can be jointly served by a set of adjacent APs. This ICI mitigation technique is referred to as the coordinated multipoint (CoMP) or the coordinated broadcasting technique [75, 76, 78, 169–172].

The performance of CoMP transmission in multi-cell downlink RF networks has been investigated in [155–157, 172–174], where different system configurations and various performance metrics were considered. However, different from RF systems, a constraint is imposed on the amplitude of the transmitted LiFi signals, which is referred to as the peak-power constraint, rather than on their average power. Due to this, the power allocation schemes developed for multi-user multi-cell RF systems do not apply for LiFi systems, which is the case in [31, 168] to name a few. On the other hand, the performance of CoMP transmission in LiFi systems was also investigated in the literature [75, 76, 78, 169–171]. The authors in [169] considered the problem of joint resource and power allocation in OFDMA-based coordinated multi-cell network. OFDMA is an OMA technique and it was demonstrated in the literature that NOMA techniques offer a higher spectral efficiency and a greater connectivity when compared to OMA techniques. In [75], it was demonstrated that the CoMP technique can achieve higher signal-to-interference-plus-noise ratios (SINRs) for ICI prone users in comparison to the frequency reuse (FR) technique. In [76, 170], two linear precoders based on the minimum mean square error (MMSE) method were proposed to minimize the MSE in multiple coordinated LiFi attocells under imperfect channel state information (CSI), where all the LED transmitters are assumed to be coordinated through an optical power line communication (PLC) link. Considering multi-user multi-cell MIMO LiFi systems, a coordinated ZF precoding technique was proposed in [78, 171] in a way to cancel the ICI, where the objective was to minimize the MSE in [78] and to maximize the achievable sum-rate of the cellular users in [171].

The integration between CoMP and NOMA was investigated in multi-user multi-cell LiFi systems [80, 175]. In [175], a downlink multi-user multi-cell LiFi system was considered and a joint NOMA transmission scheme was proposed, where the users in the overlapping regions are jointly served by all the corresponding LiFi APs. In this context, the authors developed two subcarrier allocation techniques, namely, area-based subcarrier allocation and user-based subcarrier allocation. However, the power allocation scheme, which is a crucial factor in the considered system, was not optimized, and suboptimal

power allocation coefficients were employed instead. In [80], the authors proposed a hybrid NOMA and ZF precoding technique to manage multiple users in multi-cell LiFi networks. The proposed approach consists of employing ZF precoding to cancel the ICI at the cell-edge users, while using NOMA to deal with the IUI. However, the authors have ignored the effects of ICI at the cell-center users, which may affect significantly the performance of the system. In fact, in downlink multi-cell LiFi systems, the cell-center users may experience ICI as well since typical users may have random orientation and the distance between the APs is typically small, i.e., the corresponding adjacent cells are very close to each other.

Based on the above background, one can see that both NOMA and C-NOMA are auspicious multiple access techniques that can boost the network connectivity, while the CoMP technique is an effective ICI mitigation technique. Motivated by this, it is expected that the integration between CoMP and NOMA/C-NOMA techniques can improve the performance of multi-user multi-cell LiFi systems and can make the LiFi technology a promising candidate for 6G wireless networks. However, against the above background, the optimal power allocation schemes that enhance typical performance metric, such as the sum data rate and the minimum data rate, in multi-user multi-cell LiFi systems under the promising CoMP-assisted NOMA and CoMP-assisted C-NOMA techniques were not investigated in the literature, which is the focus of the chapter.

7.2   Contributions and Outcomes

In this chapter, we consider a downlink LiFi system consisting of two adjacent LiFi attocells that utilize the same frequency resources. Each attocell contains one AP used for illumination and data communication simultaneously. The coverage areas of the two attocells are overlapped. Within this system, three stationary LiFi users are communicating simultaneously with the two APs, where each user is equipped with a randomly oriented UE. The first and second UEs are located near the center of each attocell, whereas the third UE is located near the edge of the two attocells, i.e., in the area of overlapping coverage. Therefore, the first and second UEs are associated to the first and second APs, respectively, whereas the third UE is associated to both APs. In this setup, two multiple access techniques are proposed, which are defined as follows.

- **CoMP-assisted NOMA**: Each AP employs NOMA to serve its associated UEs. Hence, the first and second UEs are the strong NOMA UEs in their respective cells, whereas the third UE is the weak UE in both cells. Since the two attocells utilize the same frequency resources, the UEs suffer from ICI. To overcome this issue, the joint-transmission (JT) CoMP technique is employed to mitigate the ICI at the weak UE, whereas the coordinated ZF precoding technique is used to cancel the ICI at the strong UEs.

- **CoMP assisted C-NOMA**: Each AP employs C-NOMA to serve its associated UEs. Hence, the first and second UEs are the strong NOMA UEs in their respective cells, whereas the third UE is the weak UE in both cells. Moreover, the strong UEs have the ability to harvest the energy from the light intensity broadcast from the APs. Therefore, by harnessing the SIC capabilities, the strong UEs can work as relays and forward the decoded weak UE's signal through RF D2D links using the harvested energy. Furthermore, similar to the CoMP-assisted NOMA scheme, the coordinated ZF precoding technique is used at the two APs to cancel the ICI at the strong UEs.

For each proposed multiples access scheme, two optimization frameworks are considered. The first aims to maximize the network sum data rate, under QoS, SIC and power constraints, whereas the second aims to maximize the minimum achievable data rate within the multi-cell LiFi network. For each optimization problem, an optimal and low-complexity power control policy is proposed. In the simulation results, the optimality of the proposed low-complexity power control schemes are verified. In addition, three baseline schemes are considered for comparison purpose, which are the CoMP-assisted OMA scheme, the C-NOMA scheme and the NOMA scheme, and our results demonstrate the superiority of the proposed schemes. Finally, the performance of the proposed schemes and the considered baselines is evaluated while varying various system parameters.

The rest of this chapter is organized as follows. Section 7.3 introduces the system model and the proposed multiple access schemes. Section 7.4 presents the problems formulations and the proposed solutions. Sections 7.5 and 7.6 present the simulation results and the conclusion, respectively.
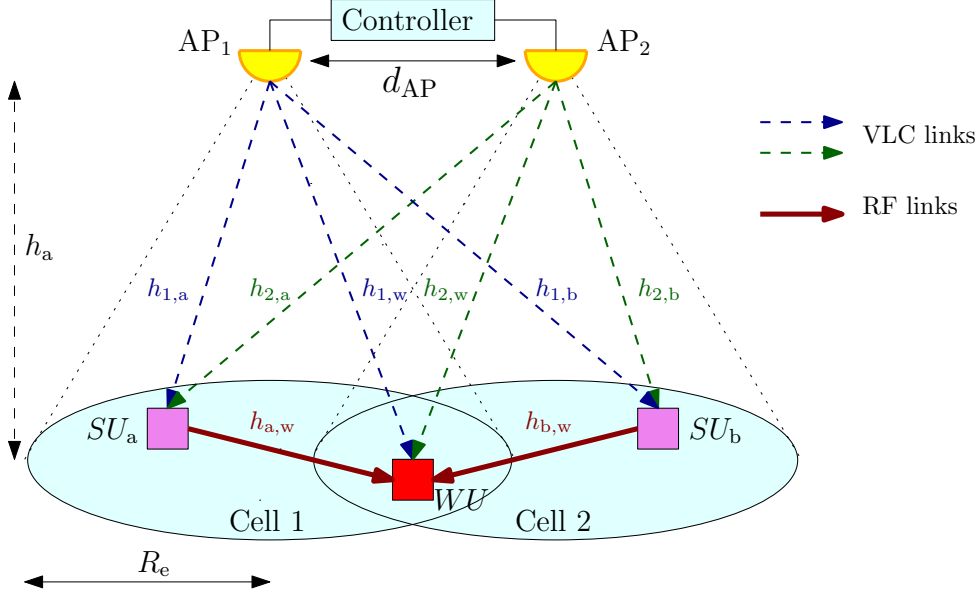
Figure 7.1: System Model.

7.3   System Model and Transmission Schemes

7.3.1   System Model

The system model considered in this chapter is shown in Figure 7.1, where two APs, each equipped with a set of LEDs, are installed at the ceiling of an indoor environment at a height h_a from the ground.[2] Hence, the circular coverage area of each AP has a radius $R_\text{e} = h_\text{a} \times \tan\left(\Phi_{1/2}\right)$, where $\Phi_{1/2}$ represents the half-power semi-angle of the LEDs [33]. The two APs are jointly monitored by a LiFi controller and they share the same frequency bandwidth B_VL. Two UEs, denoted by SU_a and SU_b, respectively, are located around the centers of the first and second cells, respectively, i.e., around the centers of the coverage areas of AP_1 and AP_2, respectively. On the other hand, since the two APs are adjacent, their resulting coverage areas may be overlapping. In this context, one UE, denoted by WU, is located within the edge of both cells, i.e., within the overlapping region between the coverage areas of AP_1 and AP_2. The area of the resulting overlapping region depends on the radius R_e of each cell, and hence, depends on the height h_a, the half-power semi-angle $\Phi_{1/2}$, and the distance between the two APs, which is denoted by d_AP. In practical

---

[2]In practical LiFi systems, the number of deployed APs might be greater than two. In such a case, the APs can be clustered into pairs of adjacent APs and the proposed multiple access schemes can be applied within each pair. In addition, the main reason behind limiting the number of APs to two in this study is that this chapter proposes a proof of concept of the CoMP-assisted NOMA and the CoMP-assisted C-NOMA schemes for indoor LiFi systems.

use cases, wide angle LEDs are required in order to provide uniform illumination within the indoor environments. Hence, typical values of the LEDs half-power semi-angle $\Phi_{1/2}$ can go up to $60°$ in practical use cases [176]. On the other hand, the separation distance between the different APs in practical scenarios depends mainly on the dimensions of the indoor environments as well as the required number of APs that provide the target uniform illuminations. In this context, typical values of the distance between the APs can range from 1m to 5m in practical use cases [177].

7.3.2 Transmission Model

Since they are located around the centers of their associated cells, the UEs SU_{a} and SU_{b} are associated with AP_1 and AP_2, respectively. However, the UE WU is associated with both APs since it is located within the intersection of their coverage areas. In this considered cellular system, the LiFi controller applies NOMA to serve the UEs within each cell, where SU_{a} and WU are the NOMA UEs associated with AP_1 and SU_{b} and WU are the NOMA UEs associated with AP_2. In this context, when applying the NOMA principle, SU_{a} and SU_{b} are considered as strong UEs in their respective cells since they are located around their centers, whereas WU is considered as the weak UE in both cells. Based on this, the superimposed signals of SU_{a} and WU at AP_1 and of SU_{b} and WU at AP_2 are expressed, respectively, as

$$s_1 = \sqrt{(1-\alpha_1)P_{\mathrm{elec}}}s_{\mathrm{a}} + \sqrt{\alpha_1 P_{\mathrm{elec}}}s_{\mathrm{w}}, \tag{7.1a}$$

$$s_2 = \sqrt{(1-\alpha_2)P_{\mathrm{elec}}}s_{\mathrm{b}} + \sqrt{\alpha_2 P_{\mathrm{elec}}}s_{\mathrm{w}}, \tag{7.1b}$$

where s_{a}, s_{b}, and s_{w} represent the messages intended to SU_{a}, SU_{b}, and WU, respectively, such that for all $k \in \{\mathrm{a}, \mathrm{b}, \mathrm{w}\}$, the message $s_k \in [-1, 1]$, P_{elec} represents the total electrical power, and α_1, $\alpha_2 \in [0, 1]$ represent the power allocation factors assigned by AP_1 and AP_2 to WU, respectively, which should be designed by the LiFi controller. Afterwards, the LiFi controller applies linear precoding to the signals broadcast by AP_1 and AP_2. As such, the 2×1 vector of optical signals broadcast from the two APs is given by

$$\mathbf{x} = \mathbf{V}\mathbf{s} + I_{\mathrm{DC}}\mathbf{1}_2, \tag{7.2}$$

where $\mathbf{x} = [x_1, x_2]^T$, such that x_1 and x_2 are the total optical signals broadcast from AP_1 and AP_2, respectively, $\mathbf{V}$ is the 2×2 precoding matrix of the considered LiFi cellular system that should be designed by the LiFi controller, $\mathbf{s} = [s_1, s_2]^T$, and I_{DC} represents the electrical direct-current (DC) provided to each AP. The constant term $I_{\mathrm{DC}}\mathbf{1}_2$ is added

in (7.2) in order to ensure the positivity of the transmitted signals $\mathbf{Vs}$.

One operating constraint in LiFi systems is the peak-power constraint at the LEDs, also known as the amplitude constraint, [72, 139, 140]. In fact, typical LEDs suffer from nonlinear distortion and clipping effects. Hence, in order to maintain a linear current to light conversion and to avoid clipping distortion, a peak-power constraint is imposed on the emitted optical power from the APs [32]. This constraint is expressed as

$$||\mathbf{Vs}||_\infty \leq \iota I_{\mathrm{DC}}, \tag{7.3}$$

where $\iota \in [0, 1]$ denotes the modulation index of the LiFi system [32, 146]. Now, in order to satisfy the constraint in (7.3), we impose the following constraints on the precoding matrix $\mathbf{V}$ and the total electrical power P_{elec}.

$$||\mathbf{V}||_\infty \leq 1, \tag{7.4a}$$

$$P_{\mathrm{elec}} \leq \frac{(\iota I_{\mathrm{DC}})^2}{2}. \tag{7.4b}$$

In this case, by applying the constraints in (7.4), the constraint in (7.3) is satisfied.

7.3.3 Received Signals

For all $i \in 1, 2$, let $h_{i,\mathrm{a}}$, $h_{i,\mathrm{b}}$ denote the positive-valued downlink LiFi channel gains from AP_i to SU_a and SU_b, respectively, where the expression of each channel gain can be found in Section 2.2. Therefore, the received signals at SU_a, SU_b can be expressed in a matrix form as [32, 146]

$$\mathbf{y} = \lambda \mathbf{H}_{\mathrm{a,b}} \mathbf{Vs} + \lambda I_{\mathrm{DC}} \mathbf{H} \mathbf{1}_2 + \mathbf{n}, \tag{7.5}$$

where $\mathbf{y} = [y_\mathrm{a}, y_\mathrm{b}]^T$ is the vector of the received signals, such that y_a and y_b are the received signals at SU_a and SU_b, respectively, and $\mathbf{H}_{\mathrm{a,b}}$ denotes the channel matrix between the two APs and the strong UEs, which is expressed as

$$\mathbf{H}_{\mathrm{a,b}} = \begin{bmatrix} h_{1,\mathrm{a}} & h_{2,\mathrm{a}} \\ h_{1,\mathrm{b}} & h_{2,\mathrm{b}} \end{bmatrix}, \tag{7.6}$$

and $\mathbf{n} = [n_\mathrm{a}, n_\mathrm{b}]^T$, in which n_a and n_b represent the AWGN experienced at SU_a and SU_b, respectively. In addition, for all $k \in \{\mathrm{a}, \mathrm{b}\}$, the noise n_k is $\mathcal{N}(0, \sigma_{\mathrm{VL}}^2)$ distributed, where $\sigma_{\mathrm{VL}}^2 = N_{\mathrm{VL}} B_{\mathrm{VL}}$ is the noise power, in which N_{VL} is the noise power spectral density. In addition, as was explained in Section 2.1, $\lambda = T R_\mathrm{p} \eta N_{\mathrm{LEDs}}$, in which T is the TIA amplifier gain at the receiver, R_p is the responsivity of the receiver's PD, η is the current-to-power conversion efficiency of the LEDs, and N_{LEDs} is the number of LEDs per AP.

One key parameter in the considered cellular system is the design of the precoding

matrix $\mathbf{V}$ at the LiFi controller in a way that boosts the overall performance of the system. As discussed above, and as it can be seen from Figure 7.1, the considered cellular system suffers from ICI. In fact, since both APs are exploiting the same frequency bandwidth, the strong UE at each cell suffers from ICI that is broadcast from the other cell. Precisely, SU_a, which is associated to cell 1 and served by AP_1, is experiencing ICI generated from AP_2 through the wireless channel $h_{2,a}$, and SU_b, which is associated to cell 2 and served by AP_2, is experiencing ICI generated from AP_1 through the wireless channel $h_{1,b}$. One way to overcome this issue is to cancel the ICI realizations at both strong UEs through ZF precoding. As such, by taking into account the imposed amplitude constraint $||\mathbf{V}||_\infty \leq 1$, the ZF precoding matrix for the considered cellular system can be expressed as [178]

$$\mathbf{V} = \frac{\mathbf{H}_{a,b}^\perp}{||\mathbf{H}_{a,b}^\perp||_\infty}. \tag{7.7}$$

Based on this, the received signals at SU_a and SU_b are expressed, respectively, as

$$y_a = \frac{\lambda\sqrt{(1-\alpha_1)P_{elec}}}{||\mathbf{H}_{a,b}^\perp||_\infty}s_a + \frac{\lambda\sqrt{\alpha_1 P_{elec}}}{||\mathbf{H}_{a,b}^\perp||_\infty}s_w + \lambda I_{DC}\left(h_{1,a} + h_{2,a}\right) + n_a, \tag{7.8a}$$

$$y_b = \frac{\lambda\sqrt{(1-\alpha_2)P_{elec}}}{||\mathbf{H}_{a,b}^\perp||_\infty}s_b + \frac{\lambda\sqrt{\alpha_2 P_{elec}}}{||\mathbf{H}_{a,b}^\perp||_\infty}s_w + \lambda I_{DC}\left(h_{1,b} + h_{2,b}\right) + n_b. \tag{7.8b}$$

Considering the weak UE, let $h_{i,w}$, for all $i \in \{1, 2\}$, denotes the positive-valued downlink LiFi channel gains from AP_i to WU, where its expression can be found in Section 2.2. In addition, let $\mathbf{h}_w = [h_{1,w}, h_{2,w}]^T$ and $\tilde{\mathbf{h}}_w = \left[\tilde{h}_{1,w}, \tilde{h}_{2,w}\right]^T = \mathbf{V}^T\mathbf{h}_w$. Based on this, the received signal at WU through the direct transmission from the two APs is expressed as

$$\begin{aligned} y_w &= \lambda\mathbf{h}_w^T\mathbf{V}\mathbf{s} + \lambda I_{DC}\mathbf{h}_w^T\mathbf{1}_2 + n_w, \\ &= \frac{\lambda\sqrt{(1-\alpha_1)P_{elec}}}{||\mathbf{H}_{a,b}^\perp||_\infty}\tilde{h}_{1,w}s_a + \frac{\lambda\sqrt{(1-\alpha_2)P_{elec}}}{||\mathbf{H}_{a,b}^\perp||_\infty}\tilde{h}_{2,w}s_b \\ &\quad + \frac{\lambda\sqrt{P_{elec}}}{||\mathbf{H}_{a,b}^\perp||_\infty}\left(\tilde{h}_{1,w}\sqrt{\alpha_1} + \tilde{h}_{2,w}\sqrt{\alpha_2}\right)s_w + \lambda I_{DC}\left(h_{1,w} + h_{2,w}\right) + n_w, \end{aligned} \tag{7.9}$$

where n_w represents the AWGN experienced at WU that is $\mathcal{N}(0, \sigma_{VL}^2)$ distributed.

7.3.4 Data rate Analysis

7.3.4.1 CoMP-Assisted NOMA

The data rates received at the UEs are governed by the NOMA technique employed by the APs. Accordingly, SU_a and SU_b will first use SIC to decode the message of WU and then decode their own messages. Based on this, and according to [148,165], the achievable

data rate of SU_a to decode the signal of WU is expressed as

$$R_{a \to w}(\alpha_1) = \frac{B_{VL}}{2} \log\left(1 + \frac{c\alpha_1}{c(1 - \alpha_1) + \frac{1}{\gamma_{RX}}}\right), \tag{7.10}$$

where $\gamma_{Rx} = \frac{\lambda^2 P_{elec} \sigma_s^2}{\left\|\mathbf{H}_{a,b}^\perp\right\|_\infty^2 \sigma_{VL}^2}$, in which $\sigma_s^2 = \sigma_d^2 - \frac{\sigma_d \exp\left(\frac{-1}{2\sigma_d^2}\right)}{\text{erf}\left(\frac{1}{\sigma_d \sqrt{2}}\right)}$, such that σ_d^2 is the scale parameter of the truncated Gaussian distribution of the input signals s_a, s_b and s_w, respectively, and erf $(\cdot)$ is the error function. After that SU_a performs SIC and cancels the message of WU from its reception, its achievable data rate to decode its own message is expressed as

$$R_a(\alpha_1) = \frac{B_{VL}}{2} \log\left(1 + c\gamma_{RX}(1 - \alpha_1)\right). \tag{7.11}$$

Similarly, the achievable data rate of SU_b to decode the signal of WU is expressed as

$$R_{b \to w}(\alpha_2) = \frac{B_{VL}}{2} \log\left(1 + \frac{c\alpha_2}{c(1 - \alpha_2) + \frac{1}{\gamma_{RX}}}\right), \tag{7.12}$$

and its achievable data rate to decode its own message after performing SIC is expressed as

$$R_b(\alpha_2) = \frac{B_{VL}}{2} \log\left(1 + c\gamma_{RX}(1 - \alpha_2)\right). \tag{7.13}$$

For WU, and following the NOMA principle, it will treat the messages of SU_a and SU_b as noise and will decode directly its own message. Hence, the achievable data rate of WU to decode its own message is expressed as

$$R_{w \to w}^{VL}(\alpha_1, \alpha_2) = \frac{B_{VL}}{2} \log\left(1 + \frac{c(\tilde{h}_{1,w}\sqrt{\alpha_1} + \tilde{h}_{2,w}\sqrt{\alpha_2})^2}{c\tilde{h}_{1,w}^2(1 - \alpha_1) + c\tilde{h}_{2,w}^2(1 - \alpha_2) + \frac{1}{\gamma_{RX}}}\right). \tag{7.14}$$

Finally, to ensure a successful SIC at the strong UEs, the WU's message should be detectable at each strong UE [179–183]. Thus, the achievable data rate of WU is given by [179–183]

$$R_w^{VL} = \min\left(R_{a \to w}(\alpha_1), R_{w \to w}^{VL}(\alpha_1, \alpha_2), R_{b \to w}(\alpha_2)\right). \tag{7.15}$$

7.3.4.2 CoMP-Assisted C-NOMA

In this scheme, and similar to the CoMP-assisted NOMA scheme, each strong UE performs SIC and cancels the message of the weak UE from its reception. In this context, the achievable data rates of SU_a and SU_b to decode the signal of WU and to decode their own signals are given in (7.10)-(7.13). However, different from the CoMP-assisted NOMA scheme, it is assumed that the strong NOMA UEs SU_a and SU_b can work as relays that have the ability to harvest the energy from the light intensity broadcast from the APs and then to utilize it to forward the decoded weak UE's signal. To harvest the energy, a capacitor separates the DC component from the received electrical signal at each strong UE and forwards it to its energy harvesting circuit [184, 185]. The received energy at the

the strong user $k \in \{a, b\}$ is given by [186]

$$E_k = f V_t I_{\mathrm{DC},k}^{\mathrm{r}} \log \left[1 + \frac{I_{\mathrm{DC},k}^{\mathrm{r}}}{I_0} \right], \tag{7.16}$$

where $I_{\mathrm{DC},k}^{\mathrm{r}} = \lambda I_{\mathrm{DC}} (h_{1,k} + h_{2,k})$ is the received DC at the strong user k, V_t is the thermal voltage, f is the fill factor, and I_0 is the dark saturation current of the PD. At this stage, each transmission time-slot is divided into two equidistant mini-time slots. In the first time slot, each strong UE harvest the energy and charge its battery, whereas in the second mini-time slot, it discharge the harvested energy and transmit the data of WU through an RF link. In this case, for all $k \in \{a, b\}$, the RF transmission power from SU_k is given by $P_k^{\mathrm{RF}} = E_k$ and the achievable data rate of WU that can be offered by the strong UEs SU_{a} and SU_{b} through the RF D2D links is given by

$$R_{\mathrm{a,b}\to\mathrm{w}}^{\mathrm{RF}} = \frac{B_{\mathrm{RF}}}{2} \log \left(1 + \frac{|g_{\mathrm{a,w}}^{\mathrm{D2D}}|^2 P_{\mathrm{a}}^{\mathrm{RF}} + |g_{\mathrm{b,w}}^{\mathrm{D2D}}|^2 P_{\mathrm{b}}^{\mathrm{RF}}}{\sigma_{\mathrm{RF}}^2} \right), \tag{7.17}$$

where, for all $k \in \{a, b\}$, $g_{k,\mathrm{w}}^{\mathrm{D2D}}$ is the RF channel coefficient between the strong UE SU_k and WU and $\sigma_{\mathrm{RF}}^2 = N_{\mathrm{RF}} B_{\mathrm{RF}}$ is the RF noise power, in which N_{RF} is the power spectral density of the RF noise and B_{RF} is the RF modulation bandwidth. Using the same RF D2D channel model in indoor environments adopted in [187], the RF channel coefficients between the strong UEs and the weak UE are modeled by the Nakagami-m fading channel, i.e., for all $k \in \{a, b\}$, the RF channel coefficient $g_{k,\mathrm{w}}^{\mathrm{D2D}} \sim Nakagami\left(F, d_{k,w}^{-\mu}\right)$, where F represents the fading parameter, $d_{k,w}$ represents the Euclidean distance between the strong UE SU_k and the weak UE WU, and μ represents the path-loss exponent.

The weak UE WU is receiving two copies of his message through two different links, one from SU_{a} and one from SU_{b}. Hence, WU can combine these two copies using the maximum-ratio-combining (MRC) technique and then decodes his own message, which results in the achievable data rate $R_{\mathrm{a,b}\to\mathrm{w}}^{\mathrm{RF}}$. However, this data rate is achievable if and only if the copies transmitted from the strong UEs are truly the exact message s_{w} of WU, i.e., if and only if the strong UEs are able to decode the message s_{w} of WU. Therefore, the data rate achieved at the weak UE is constrained by the achievable data rates of the strong UEs to decode the message s_{w} of the WU, which are the data rates $R_{\mathrm{a}\to\mathrm{w}}(\alpha_1)$ and $R_{\mathrm{b}\to\mathrm{w}}(\alpha_2)$. Consequently, in line with the results of [157,174], the resulting achievable data rate of the weak UE WU from the cooperative diversity of the strong UEs is expressed as

$$R_{\mathrm{w}}^{\mathrm{RF}}(\alpha_1, \alpha_2) = \min \left(R_{\mathrm{a}\to\mathrm{w}}(\alpha_1), R_{\mathrm{a,b}\to\mathrm{w}}^{\mathrm{RF}}, R_{\mathrm{b}\to\mathrm{w}}(\alpha_2) \right). \tag{7.18}$$

7.4 Problems Formulation and Proposed Solutions

In this section, we investigate the sum data rate and the minimum data rate maximization problems for the considered LiFi cellular system for both the CoMP-assisted NOMA and the CoMP-assisted C-NOMA schemes. The sum data rate maximization problem is investigated in subsection 7.4.1, whereas the minimum data rate maximization problem is considered in subsection 7.4.2.

7.4.1 Sum Data Rate Maximization

The first objective of this chapter is to maximize the sum data rate of the considered LiFi cellular system under both the CoMP-assisted NOMA and the CoMP-assisted C-NOMA schemes, while a target QoS should be guaranteed for each UE in terms of its required data rate threshold, denoted by R_{th}.

7.4.1.1 CoMP-Assisted NOMA

For this scheme, the preset objective can be reached by solving the following optimization problem.

$$\mathcal{P}_1 : R_{\text{sum}}^{\text{VL}^*} = \max_{\alpha_1, \alpha_2} \ R_{\text{a}}(\alpha_1) + R_{\text{b}}(\alpha_2) + R_{\text{w}}^{\text{VL}}(\alpha_1, \alpha_2), \tag{7.19a}$$

$$\text{s.t.} \quad 0 \leq \alpha_i \leq 1, \quad \forall \ i \in \{1, 2\}, \tag{7.19b}$$

$$R_{\text{a}\rightarrow\text{w}}(\alpha_1) \geq R_{\text{th}}, \tag{7.19c}$$

$$R_{\text{a}}(\alpha_1) \geq R_{\text{th}}, \tag{7.19d}$$

$$R_{\text{b}\rightarrow\text{w}}(\alpha_2) \geq R_{\text{th}}, \tag{7.19e}$$

$$R_{\text{b}}(\alpha_2) \geq R_{\text{th}}, \tag{7.19f}$$

$$R_{\text{w}\rightarrow\text{w}}^{\text{VL}} \geq R_{\text{th}}. \tag{7.19g}$$

Based on the data rate expressions presented in (7.10)-(7.14), problem $\mathcal{P}_1$ is a non-linear non-convex problem that cannot be solved in a straightforward manner. Alternatively, we propose in the following an efficient and low complexity approach to solve problem $\mathcal{P}_1$. First, in order to be able to solve problem $\mathcal{P}_1$, the conditions under which at least one feasible solution exists must be derived. In this context, the feasibility conditions of problem $\mathcal{P}_1$ are presented in the following theorem.

Theorem 7.1. *Problem $\mathcal{P}_1$ is feasible if and only if the following conditions hold:*

$$\text{Condition 1: } \alpha_{\min} \leq \alpha_{\max}, \tag{7.20a}$$

$$\text{Condition 2: } 0 \leq g\left(\alpha_{\max}, \alpha_{\max}\right), \tag{7.20b}$$

where $\alpha_{\min} == \frac{t_{\mathrm{v}}(c\gamma_{\mathrm{RX}}+1)}{c\gamma_{\mathrm{RX}}(1+t_{\mathrm{v}})}$ and $\alpha_{\max} = 1 - \frac{t_{\mathrm{v}}}{c\gamma_{\mathrm{RX}}}$, such that $t_{\mathrm{v}} = \exp\left(\frac{2R_{\mathrm{th}}}{B_{\mathrm{VL}}}\right) - 1$, and the function $g\left(\cdot,\cdot\right)$ is expressed, for all $(\alpha_1, \alpha_2) \in \mathbb{R}^2$, as

$$\begin{aligned} g\left(\alpha_1, \alpha_2\right) = &\, c\left(1 + t_{\mathrm{v}}\right)\tilde{h}_{1,\mathrm{w}}^2\alpha_1 + c\left(1 + t_{\mathrm{v}}\right)\tilde{h}_{2,\mathrm{w}}^2\alpha_2 + c\tilde{h}_{1,\mathrm{w}}\tilde{h}_{2,\mathrm{w}}\sqrt{\alpha_1\alpha_2} \\ &- t\left(c\tilde{h}_{1,\mathrm{w}}^2 + c\tilde{h}_{2,\mathrm{w}}^2 + \frac{1}{\gamma_{\mathrm{RX}}}\right). \end{aligned} \tag{7.21}$$

Proof. See Appendix E.1. ∎

Based on **Theorem 7.1** and its proof in Appendix E.1, the feasibility region of the optimization problem $\mathcal{P}_1$ is defined by the set $\left\{(\alpha_1, \alpha_2) \in [\alpha_{\min}, \alpha_{\max}]^2 \,\middle|\, g\left(\alpha_1, \alpha_2\right) \geq 0\right\}$. Now that the feasibility conditions are set, our objective is to find the optimal solution of problem $\mathcal{P}_1$, i.e., the optimal values of the power allocation fractions α_1 and α_2 that maximize the network sum data rate $R_{\mathrm{sum}}^{\mathrm{VL}} = R_{\mathrm{a}} + R_{\mathrm{b}} + R_{\mathrm{w}}^{\mathrm{VL}}$. In this setup, since SU_{a} and SU_{b} are the strong UEs and WU is the weak UE, the optimal power allocation strategy that maximizes the network sum data rate is the one that allocates the lowest possible power to the weak UE WU while guaranteeing its required data rate threshold R_{th}, and the remaining of the power to the strong UEs SU_{a} and SU_{b} [154, 157]. Therefore, since the expressions of the achievable data rates R_{a} and R_{b} are decreasing functions of α_1 and α_2, respectively, and the expression of the achievable data rate $R_{\mathrm{w}}^{\mathrm{VL}}$ is an increasing function with respect to α_1 and α_2, then the optimal power allocation strategy is the one that satisfies the inequality $g\left(\alpha_1, \alpha_2\right) \geq 0$ with the lowest possible values of α_1 and α_2 within the square $[\alpha_{\min}, \alpha_{\max}]^2$.

In order to determine the optimal power allocation coefficients (α_1^*, α_2^*), we opt for a discrete line search technique within the segment $[\alpha_{\min}, \alpha_{\max}]$. Let $K \in \mathbb{N}$ be the number of discrete points within $[\alpha_{\min}, \alpha_{\max}]$. Based on this, the discrete line search technique within the segment $[\alpha_{\min}, \alpha_{\max}]$ works as follows. For all $i \in [\![0, K-1]\!]$, we calculate $\alpha_1^i = \alpha_{\min} + \frac{\alpha_{\max}-\alpha_{\min}}{K-1} \times i$. Then, we determine the lowest value of α_2^i that satisfies the inequality $g(\alpha_1^i, \alpha_2^i) \geq 0$ using the approach presented in Appendix E.2. Afterwards, we calculate the corresponding network sum data rate $R_i(\alpha_1^i, \alpha_2^i) = R_{\mathrm{a}}(\alpha_1^i) + R_{\mathrm{b}}(\alpha_2^i) + R_{\mathrm{w}}^{\mathrm{VL}}(\alpha_1^i, \alpha_2^i)$. Finally, the optimal power allocation fractions (α_1^*, α_2^*), solution of problem $\mathcal{P}_1$, is the one that achieves the highest network sum data rate, i.e.,

$$(\alpha_1^*, \alpha_2^*) = \underset{(\alpha_1^i, \alpha_2^i)}{\mathrm{argmax}} \; R_i(\alpha_1^i, \alpha_2^i), \tag{7.22}$$

119

which can be obtained through a brute force search over the set $\left\{R_i(\alpha_1^i, \alpha_2^i) \middle| i \in [\![0, K-1]\!]\right\}$. As it can be seen, the proposed solution approach is based on a discrete line search technique over a set of K points, which has a complexity of $\mathcal{O}(K)$, i.e., a linear complexity. This fact demonstrates the low complexity of the proposed solution approach.

7.4.1.2 CoMP-Assisted C-NOMA

Under this scheme, the objective of maximizing the sum data rate of the considered LiFi cellular system while guaranteeing the required data rate threshold R_{th} at each UE can be reached by solving the following optimization problem.

$$\mathcal{P}_2 : R_{\text{sum}}^{\text{VL/RF}^*} = \max_{\alpha_1, \alpha_2} R_{\text{a}}(\alpha_1) + R_{\text{b}}(\alpha_2) + R_{\text{w}}^{\text{RF}}(\alpha_1, \alpha_2), \tag{7.23a}$$

$$\text{s.t.} \qquad (7.19\text{b}) - (7.19\text{f}), \tag{7.23b}$$

$$R_{\text{a,b}\to\text{w}}^{\text{RF}} \geq R_{\text{th}}. \tag{7.23c}$$

Based on the rate expressions presented in (7.10)-(7.13), problem $\mathcal{P}_2$ is a non-linear non-convex problem that cannot be solved in a straightforward manner. Alternatively, we propose in the following an efficient and low complexity approach to solve problem $\mathcal{P}_2$. First, and similar to the CoMP-assisted NOMA scheme, the conditions under which at least one feasible solution for problem $\mathcal{P}_2$ exists must be derived. In this context, the feasibility conditions of problem $\mathcal{P}_2$ are presented in the following theorem.

Theorem 7.2. *Problem $\mathcal{P}_2$ is feasible if and only if the following conditions hold:*

$$\text{Condition 1: } \alpha_{\min} \leq \alpha_{\max}, \tag{7.24a}$$

$$\text{Condition 2: } t_{\text{r}} \leq \frac{|g_{\text{a,w}}^{\text{D2D}}|^2 P_{\text{a}}^{\text{RF}} + |g_{\text{b,w}}^{\text{D2D}}|^2 P_{\text{b}}^{\text{RF}}}{\sigma_{\text{RF}}^2}, \tag{7.24b}$$

where $t_{\text{r}} = \exp\left(\frac{2R_{\text{th}}}{B_{\text{RF}}}\right) - 1$.

Proof. The proof can be easily deducted from the one of **Theorem 7.1** in Appendix E.1. ∎

It is important to mention that the condition in (7.24b) is related to the RF relaying links from the strong UEs to the weak UE and is not related to the power allocation fractions (α_1, α_2). Specifically, the RF relaying links are governed by the RF channel conditions, represented by the channel coefficients $g_{\text{a,w}}^{\text{D2D}}$ and $g_{\text{a,b}}$, the electrical powers P_{a}^{RF} and P_{b}^{RF} that are resulting from the harvested optical powers at the strong UEs, the available RF bandwidth B_{RF} and the electrical noise power σ_r^2 at the WU. When combined together, these parameters have to make the resulting RF data rate at WU

that is given by $R^{\mathrm{RF}}_{\mathrm{a,b} \to \mathrm{w}}$ greater than the required data rate threshold R_{th}, which is the focus of the condition in (7.24b). In this context, assuming that the condition in (7.24b) is satisfied, and based on **_Theorem_ 7.2**, the feasibility region of problem $\mathcal{P}_2$ is the square $[\alpha_{\min}, \alpha_{\max}]^2$.

Now that the feasibility conditions are set, our objective is to find the optimal solution of problem $\mathcal{P}_2$, i.e., the optimal values of the power allocation fractions α_1 and α_2 that maximize the network sum data rate $R^{\mathrm{VL/RF}}_{\mathrm{sum}} = R_{\mathrm{a}} + R_{\mathrm{b}} + R^{\mathrm{RF}}_{\mathrm{w}}$. In this context, $R^{\mathrm{VL/RF}^*}_{\mathrm{sum}}$ can be expressed as

$$R^{\mathrm{VL/RF}^*}_{\mathrm{sum}} = \max_{\alpha_1,\alpha_2} \; \left[R_{\mathrm{a}}(\alpha_1) + R_{\mathrm{b}}(\alpha_2) + R^{\mathrm{RF}}_{\mathrm{w}}(\alpha_1, \alpha_2) \right], \tag{7.25a}$$

$$= \max_{\alpha_1,\alpha_2} \; \left[R_{\mathrm{a}}(\alpha_1) + R_{\mathrm{b}}(\alpha_2) + \min \left(R_{\mathrm{a} \to \mathrm{w}}(\alpha_1), R^{\mathrm{RF}}_{\mathrm{a,b} \to \mathrm{w}}, R_{\mathrm{b} \to \mathrm{w}}(\alpha_2) \right) \right], \tag{7.25b}$$

$$= \max_{\alpha_1,\alpha_2} \; \min \left(R_{\mathrm{a}}(\alpha_1) + R_{\mathrm{b}}(\alpha_2) + R_{\mathrm{a} \to \mathrm{w}}(\alpha_1), R_{\mathrm{a}}(\alpha_1) + R_{\mathrm{b}}(\alpha_2) + R^{\mathrm{RF}}_{\mathrm{a,b} \to \mathrm{w}}, \right.$$
$$\tag{7.25c}$$

$$\left. R_{\mathrm{a}}(\alpha_1) + R_{\mathrm{b}}(\alpha_2) + R_{\mathrm{b} \to \mathrm{w}}(\alpha_2) \right)$$

$$= \max_{\alpha_1,\alpha_2} \; \min \left(R_{\mathrm{b}}(\alpha_2) + \frac{B_{\mathrm{VL}}}{2} \log \left(1 + c\gamma_{\mathrm{RX}} \right), R_{\mathrm{a}}(\alpha_1) + R_{\mathrm{b}}(\alpha_2) + R^{\mathrm{RF}}_{\mathrm{a,b} \to \mathrm{w}}, \right.$$
$$\tag{7.25d}$$

$$\left. R_{\mathrm{a}}(\alpha_1) + \frac{B_{\mathrm{VL}}}{2} \log \left(1 + c\gamma_{\mathrm{RX}} \right) \right). \tag{7.25e}$$

Since the expressions of the achievable data rates $R_{\mathrm{a}}(\alpha_1)$ and $R_{\mathrm{b}}(\alpha_2)$ are decreasing functions with respect to α_1 and α_2, respectively, the first term inside the min operator in (7.25) is maximized when $\alpha_2 = \alpha_{\min}$, the second is maximized when $(\alpha_1, \alpha_2) = (\alpha_{\min}, \alpha_{\min})$, and the third term is maximized when $\alpha_1 = \alpha_{\min}$. Based on this, we conclude that the optimal solution of problem $\mathcal{P}_2$ is $(\alpha_1^*, \alpha_2^*) = (\alpha_{\min}, \alpha_{\min})$.

7.4.2 Minimum Data Rate Maximization

The second objective of this chapter is to maximize the minimum data rate of the UEs within the considered LiFi cellular system under the CoMP-assisted NOMA and the CoMP-assisted C-NOMA schemes.

7.4.2.1 CoMP-Assisted NOMA

For this scheme, and by recalling the expression of $R_{\mathrm{w}}^{\mathrm{VL}}$ in (7.15), the target objective can be reached by solving the following optimization problem.

$$\mathcal{P}_3 : R_{\min}^{\mathrm{VL}^*} = \max_{\alpha_1, \alpha_2} \left[\min \left\{ R_{\mathrm{a} \to \mathrm{w}}(\alpha_1), R_{\mathrm{a}}(\alpha_1), R_{\mathrm{b} \to \mathrm{w}}(\alpha_2), R_{\mathrm{b}}(\alpha_2), R_{\mathrm{w} \to \mathrm{w}}^{\mathrm{VL}}(\alpha_1, \alpha_2) \right\} \right], \quad \text{(7.26a)}$$

$$\text{s.t.} \qquad 0 \le \alpha_i \le 1, \quad \forall \, i \in \{1, 2\}. \qquad \text{(7.26b)}$$

Based on the rate expressions presented in (7.10)-(7.14), problem $\mathcal{P}_3$ is a non-linear non-convex problem that cannot be solved in a straightforward manner. Alternatively, we propose in the following an efficient and low complexity approach to solve problem $\mathcal{P}_3$, which is feasible over the entire set $[0, 1]^2$. First, it can be easily demonstrated that, for $\alpha_1, \alpha_2 \in [0, 1]$, we have

$$R_{\mathrm{a} \to \mathrm{w}}(\alpha_1) \ge R_{\mathrm{a}}(\alpha_1) \Leftrightarrow \alpha_1 \ge \alpha_0, \qquad \text{(7.27a)}$$

$$R_{\mathrm{b} \to \mathrm{w}}(\alpha_2) \ge R_{\mathrm{b}}(\alpha_2) \Leftrightarrow \alpha_2 \ge \alpha_0, \qquad \text{(7.27b)}$$

where $\alpha_0 = \frac{(c\gamma_{\mathrm{RX}}+1) - \sqrt{c\gamma_{\mathrm{RX}}+1}}{c\gamma_{\mathrm{RX}}}$. Consequently, for all $(\alpha_1, \alpha_2) \in [\alpha_0, 1]^2$, we have

$$\min \left\{ R_{\mathrm{a} \to \mathrm{w}}(\alpha_1), R_{\mathrm{a}}(\alpha_2), R_{\mathrm{b} \to \mathrm{w}}(\alpha_1), R_{\mathrm{b}}(\alpha_2), R_{\mathrm{w} \to \mathrm{w}}^{\mathrm{VL}} \right\} = \min \left\{ R_{\mathrm{a}}(\alpha_2), R_{\mathrm{b}}(\alpha_2), R_{\mathrm{w} \to \mathrm{w}}^{\mathrm{VL}} \right\}.$$

$$\text{(7.28)}$$

At this stage, we apply the discrete line search approach within the segment $[\alpha_0, 1]$ in order to maximize $\min \left\{ R_{\mathrm{a}}(\alpha_2), R_{\mathrm{b}}(\alpha_2), R_{\mathrm{w} \to \mathrm{w}}^{\mathrm{VL}} \right\}$. Specifically, let $K \in \mathbb{N}$ be the number of discrete points within $[\alpha_0, 1]$. Based on this, the discrete line search technique within the segment $[\alpha_0, 1]$ works as follows. For all $i \in [\![0, K - 1]\!]$, we calculate $\alpha_1^i = \alpha_0 + \frac{1 - \alpha_0}{K - 1} \times i$. Then, we determine the lowest value of $\alpha_2^i \in [\alpha_0, 1]$ that satisfies the inequality $R_{\mathrm{w} \to \mathrm{w}}^{\mathrm{VL}}(\alpha_1^i, \alpha_2^i) \ge R_{\mathrm{b}}(\alpha_2^i)$ using the same approach of the sum data rate maximization problem presented in Appendix E.2. Afterwards, we calculate the corresponding minimum data rate $R_{\min}^i(\alpha_1^i, \alpha_2^i) = \min \left\{ R_{\mathrm{a} \to \mathrm{w}}(\alpha_1^i), R_{\mathrm{a}}(\alpha_1^i), R_{\mathrm{b} \to \mathrm{w}}(\alpha_2^i), R_{\mathrm{b}}(\alpha_2^i), R_{\mathrm{w} \to \mathrm{w}}^{\mathrm{VL}}(\alpha_1^i, \alpha_2^i) \right\}$. Finally, the optimal power allocation fractions (α_1^*, α_2^*), solution of problem $\mathcal{P}_3$, is the one that achieves the highest minimum data rate, i.e.,

$$(\alpha_1^*, \alpha_2^*) = \operatorname*{argmax}_{(\alpha_1^i, \alpha_2^i)} R_{\min}^i(\alpha_1^i, \alpha_2^i), \qquad \text{(7.29)}$$

which can be obtained through a brute force search over the set $\left\{ R_{\min}^i(\alpha_1^i, \alpha_2^i) \middle| i \in [\![0, K - 1]\!] \right\}$. As it can be seen, the proposed solution approach is based on a discrete line search technique over a set of K points, which has a complexity of $\mathcal{O}(K)$, i.e., a linear complexity, This fact demonstrates the low complexity of the proposed solution approach.

7.4.2.2 CoMP-Assisted C-NOMA

Since the achievable data rate $R_{a,b \to w}^{RF}$ is related to the RF relaying links from the strong UEs to the weak UE and is not related to the power allocation fractions (α_1, α_2), the maximum minimum data rate of the UEs for the considered LiFi cellular system under the CoMP-assisted C-NOMA scheme is given by $R_{min}^{VL/RF^*} = \min \left\{ R_{a,b \to w}^{RF}, R_{min}^{a,b^*} \right\}$, where R_{min}^{a,b^*} is obtained by solving the following optimization problem.

$$\mathcal{P}_4 : R_{min}^{a,b^*} = \max_{\alpha_1, \alpha_2} \left[\min \left\{ R_{a \to w}(\alpha_1), R_a(\alpha_1), R_{b \to w}(\alpha_2), R_b(\alpha_2) \right\} \right], \qquad (7.30a)$$

$$\text{s.t.} \qquad 0 \leq \alpha_i \leq 1, \quad \forall\, i \in \{1, 2\}. \qquad (7.30b)$$

It can be easily verified that problem $\mathcal{P}_4$ is a non-linear non-convex problem, due to the non-convexity of the data rate expressions in (7.10)-(7.13), hence, it can not be solved in a straightforward manner. Alternatively, we propose an efficient and low complexity approach to solve problem $\mathcal{P}_4$, which is feasible over the entire set $[0, 1]^2$. It can be easily noticed that the maximum value of $\min \{R_{a \to w}(\alpha_1), R_a(\alpha_1), R_{b \to w}(\alpha_2), R_b(\alpha_2)\}$ is achieved if and only if $R_{a \to w}(\alpha_1) = R_a(\alpha_1)$ and $R_{b \to w}(\alpha_2) = R_b(\alpha_2)$, which, based on (7.27), is reached if and only if $(\alpha_1, \alpha_2) = (\alpha_0, \alpha_0)$. Consequently, the optimal solution of problem $\mathcal{P}_4$ is $(\alpha_1^*, \alpha_2^*) = (\alpha_0, \alpha_0)$.

7.5 Simulation Results

In this section, our objective is to evaluate the performance of the proposed CoMP-assisted NOMA and CoMP-assisted C-NOMA schemes for the considered indoor LiFi cellular system through extensive simulations.

7.5.1 Simulations Settings

We consider the LiFi cellular system presented in section 7.3.1. Each AP is oriented vertically downward, whereas each UE has a random orientation that is generated using the measurements-based orientation models proposed in [28, 34, 161]. Moreover, the first and second UEs are randomly located around the center of the first and the second attocells, respectively, whereas the third UE is randomly located near the edge of both attocells. Therefore, using the proposed CoMP-assisted NOMA and CoMP-assisted C-NOMA schemes, the first and second UEs are associated to the first and second attocells, respectively, and each one of them is communicating with the AP of its associated attocell,

Table 7.1: Simulation Parameters

Parameter	Symbol	Value	Parameter	Symbol	Value
APs height	h_{a}	3m	Modulation index	ι	0.33
Current-to-power conversion factor	η	0.6 W/A	PD responsivity	R_{p}	0.58 A/W
Half-power semi-angle	$\Phi_{1/2}$	60°	PD geometric area	A_{PD}	1 cm^2
Optical concentrator refractive index	n_c	1	Field of view of the PD	Ψ	90°
VL bandwidth	B_{VL}	20 MHz	Noise power spectral density	N_{VL}	10^{-21} W/Hz
DC component	I_{DC}	25 dBm	data rate threshold	R_{th}	10 Mbit/s
UE's height	h_{u}	0.9m	Number of discrete points	K	1000
TIA gain	T	1	Thermal voltage	V_t	25 mV
Fill factor	f	0.75	Dark saturation current of the PD	I_0	10^{-10} A
RF fading parameter	F	1	Path loss exponent	μ	2
RF bandwidth	B_{RF}	16 MHz	RF Noise power spectral density	N_{RF}	10^{-21} W/Hz

whereas the third UE is associated to the two attocells. Unless otherwise stated, the simulation parameters and settings used throughout the chapter are shown in Table 7.1. All the results are generated through 10^4 independent Monte Carlo trials, where in each trial the locations and the orientations of the UEs are generated randomly as discussed above. Finally, for comparison purposes, three baselines are considered, which are

- **CoMP-assisted OMA**: The two cells are coordinating together to serve the weak UE, whereas, unlike the proposed CoMP-assisted NOMA and CoMP-assisted C-NOMA schemes, each cell adopts frequency division multiple access (FDMA) to serve its associated UEs.

- **C-NOMA**: Each cell adopts C-NOMA to serve its associated UEs. Specifically, each strong UE has the ability to harvest the energy from the light intensity broadcast from the APs. Therefore, by harnessing the SIC capabilities, each strong UE forwards the decoded weak UE's signal through RF D2D link using the harvested energy. In addition, the two cells exploit the same frequency bandwidth but without any coordination between them, unlike the proposed CoMP-assisted C-NOMA scheme.

- **NOMA**: Each cell adopts NOMA to serve its associated UEs. In addition, the two cells exploit the same frequency bandwidth but without any coordination between them, unlike the proposed CoMP-assisted NOMA scheme.
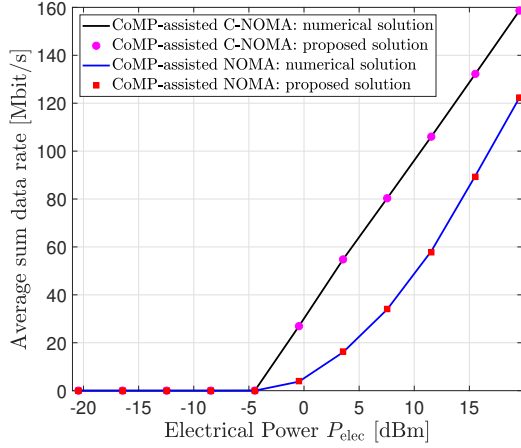
Figure 7.2: Average sum data rate achieved by the numerical and the proposed solution approaches for the CoMP-assisted NOMA and the CoMP-assisted C-NOMA schemes versus the transmit electrical power P_{elec} at the APs.
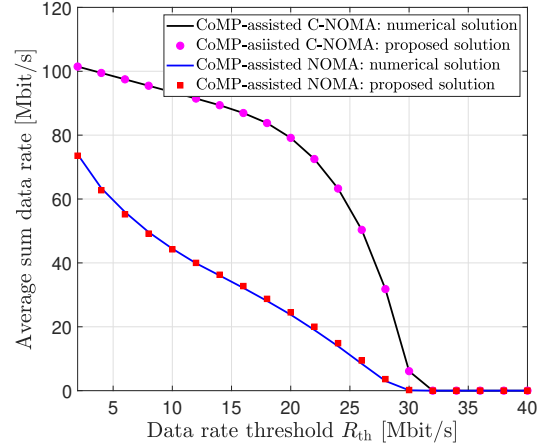
Figure 7.3: Average sum data rate achieved by the numerical and the proposed solution approaches for the CoMP-assisted NOMA and the CoMP-assisted C-NOMA schemes versus the required data rate threshold R_{th} at the APs.

7.5.2 Sum Data Rate Performance

7.5.2.1 On the Optimality of the Proposed Solution Approaches

Figure 7.2 presents the average sum data rate, achieved by the proposed CoMP-assisted NOMA and CoMP-assisted C-NOMA schemes, versus the transmit electrical power P_{elec}, when the required data rate threshold is $R_{\text{th}} = 10$ [Mbit/Hz]. On the other hand, Figure 7.3 presents the average sum data rate, achieved by the proposed CoMP-assisted NOMA and CoMP-assisted C-NOMA schemes, versus the required data rate threshold R_{th}, when the transmit electrical power is $P_{\text{elec}} = 9.5$ dBm. For the two proposed schemes, the results of both the numerical solutions and the proposed solutions of the power allocation coefficients are presented. The numerical solutions of problems $\mathcal{P}_1$ and $\mathcal{P}_2$ are obtained using an off-the-shelf optimization solver, whereas the analytical solutions are obtained through our proposed power allocation schemes.[3] Figure 7.2 and 7.3 show that

---

[3]The adopted solver is `fmincon`, which is a predefined `MATLAB` solver [153]. In addition, 100 distinct initial points were randomly generated within the feasibility region of the optimization variables in order to converge to the optimal solution. Specifically, through the use of the `fmincon` solver, each initial point will lead to a given local extremum. Then, once all local extrema are collected, a simple brute force search over the obtained extrema is applied to obtain the optimal solution. Although this heuristic approach suffers from its high complexity, it was demonstrated that it is very effective in finding the optimal solutions of non-convex problems as shown in [154–157]. Nevertheless, it is important to mention that the optimal solutions of the considered problems can also be obtained using the technique proposed

the proposed solutions of the power allocation coefficients of the proposed CoMP-assisted NOMA and CoMP-assisted C-NOMA schemes match perfectly the numerical solutions, which demonstrates their optimality. Moreover, it demonstrates the superiority of the CoMP-assisted C-NOMA scheme over the CoMP-assisted NOMA scheme. This is basically due to the additional power at the strong UEs that is harvested from the APs and then used to relay the data of the weak UE. This harvested energy is resulting from the DC component received at the strong UEs, which is unexploited in the CoMP-assisted NOMA scheme.

7.5.2.2 Effect of the Transmit Electrical Power P_{elec}

Figure 7.4 presents the average sum data rate per cell, achieved by the proposed CoMP-assisted NOMA and CoMP-assisted C-NOMA schemes, the CoMP-assisted OMA scheme, the C-NOMA scheme and the NOMA scheme, versus the transmit electrical power P_{elec}, for different values of the distance between the APs d_{AP} and the LEDs half-power semi-angle $\Phi_{1/2}$. The required data rate threshold is $R_{\text{th}} = 10$ [Mbit/Hz]. The results of Figure 7.4 can be divided into two regimes. namely, the low power regime and the high power regime. When the transmit electrical power is low, the C-NOMA scheme outperforms the CoMP-assisted C-NOMA scheme and the NOMA scheme outperforms the CoMP-assisted NOMA scheme, with C-NOMA being the best scheme that achieves the highest sum data rate per cell. However, when the transmit electrical power is high, the CoMP-assisted C-NOMA scheme outperforms the C-NOMA scheme and the CoMP-assisted NOMA scheme outperforms the NOMA scheme, with CoMP-assisted C-NOMA being the scheme that achieves the highest sum data rate per cell. In fact, when the transmit electrical power is low, the power of the interfering signals coming from the adjacent cell is low, and therefore, the use of the coordinated ZF precoding between the APs in the CoMP-assisted schemes is meaningless. However, when the transmit electrical power is high, the power of the interfering signals coming from the adjacent cell is high. Due to this, the performance of the NOMA and the C-NOMA schemes starts to stagnate when the transmit electrical power increases, whereas accounting to the use of the coordinated ZF precoding, the performance of the CoMP-assisted schemes increases continuously when the transmit electrical power increases.

---

in [158], which has a complexity of $\mathcal{O}\left(\frac{1}{\epsilon^2}\right)$ when the target accuracy of the solution is less than ϵ.

(a) $d_{\mathrm{AP}} = 4$m, $\Phi_{1/2} = 45°$.

(b) $d_{\mathrm{AP}} = 4$m, $\Phi_{1/2} = 60°$.

(c) $d_{\mathrm{AP}} = 5$m, $\Phi_{1/2} = 45°$.

(d) $d_{\mathrm{AP}} = 5$m, $\Phi_{1/2} = 60°$.

Figure 7.4: Average achievable sum data rate per cell, achieved by the proposed CoMP-assisted NOMA and CoMP-assisted C-NOMA schemes, the CoMP-assisted OMA scheme, the C-NOMA scheme and the NOMA scheme, versus the transmit electrical power P_{elec}.

7.5.2.3 Effect of the Data Rate Threshold R_{th}

Figure 7.5 presents the average sum data rate per cell, achieved by the proposed CoMP-assisted NOMA and CoMP-assisted C-NOMA schemes, the CoMP-assisted OMA scheme, the C-NOMA scheme and the NOMA scheme, versus the required data rate threshold per UE R_{th} for different values of the distance between the APs d_{AP} and the LEDs half-power semi-angle $\Phi_{1/2}$, where the transmit electrical power is $P_{\mathrm{elec}} = 9.5$ dBm. Figure 7.5 shows that, for all the considered cases of $\left(d_{\mathrm{AP}}, \Phi_{1/2}\right)$, the proposed CoMP-assisted C-NOMA scheme outperforms all the considered baselines, which demonstrates the capability of integrating CoMP with C-NOMA in beating the ICI effects and increasing the network sum data rate simultaneously. On the other hand, we remark that the average sum data

(a) $d_{AP} = 4$m, $\Phi_{1/2} = 45°$.

(b) $d_{AP} = 4$m, $\Phi_{1/2} = 60°$.

(c) $d_{AP} = 5$m, $\Phi_{1/2} = 45°$.

(d) $d_{AP} = 5$m, $\Phi_{1/2} = 60°$.

Figure 7.5: Average achievable sum data rate per cell, achieved by the proposed CoMP-assisted NOMA and CoMP-assisted C-NOMA schemes, the CoMP-assisted OMA scheme, the C-NOMA scheme and the NOMA scheme, versus the required data rate threshold per UE R_{th}.

rate per cell achieved by all the considered schemes decrease when the rate threshold R_{th} increases. This is basically due to the fact that as R_{th} increases, the number of UEs that satisfy the target QoS decreases, and therefore, the number of UEs that can be served by the two APs decreases. The high slope of the drop in the achieved sum data rates by all schemes is mainly resulting from the 1/2 pre-log penalties in the achievable data rate expression derived in the literature [148].

In Figure 7.5, one can see that the average achievable sum data rates achieved by all the considered schemes decrease as the distance between the APs d_{AP} decreases and/or the LEDs half-power semi-angle $\Phi_{1/2}$ increases. In fact, when d_{AP} decreases and/or $\Phi_{1/2}$ increases, the coverage area of each AP increases, and hence, the area of the overlapping region between the two APs increases. Therefore, the ICI effects from one cell

to the other increases, which explains the performance degradation for the C-NOMA and the NOMA schemes. On the other hand, despite the exploitation of the coordinated broadcasting technique between the two APs, the performance degradation of the CoMP-assisted schemes is resulting from the use of the ZF precoding and the peak-power constraint imposed on LiFi systems. Specifically, the use of the JT and the ZF precoding eliminates the ICI effects at the strong and weak UEs. However, as the coverage area of each AP increases, the channel coefficients from the two APs to the strong UEs increases, and hence, the coefficients of the channel matrix $\mathbf{H}_{a,b}$ in (7.6) increases. Consequently, the multiplicative term $\frac{1}{||\mathbf{H}_{a,b}^{\perp}||_{\infty}}$, which is required to make the ZF precoding matrix satisfy the peak-power constraint at the LEDs of the APs, decreases. Therefore, when the distance between the APs d_{AP} decreases and/or the LEDs half-power semi-angle $\Phi_{1/2}$ increases, the average received SNR at the UEs \$$\gamma_{Rx} = \frac{\lambda^2 P_{elec} \sigma_s^2}{||\mathbf{H}_{a,b}^{\perp}||_{\infty}^2 \sigma_{VL}^2}$, which explains the performance degradation for the CoMP-assisted schemes, despite the use of the ICI mitigation techniques.

7.5.2.4 Effects of the Area of the PD A_{PD}

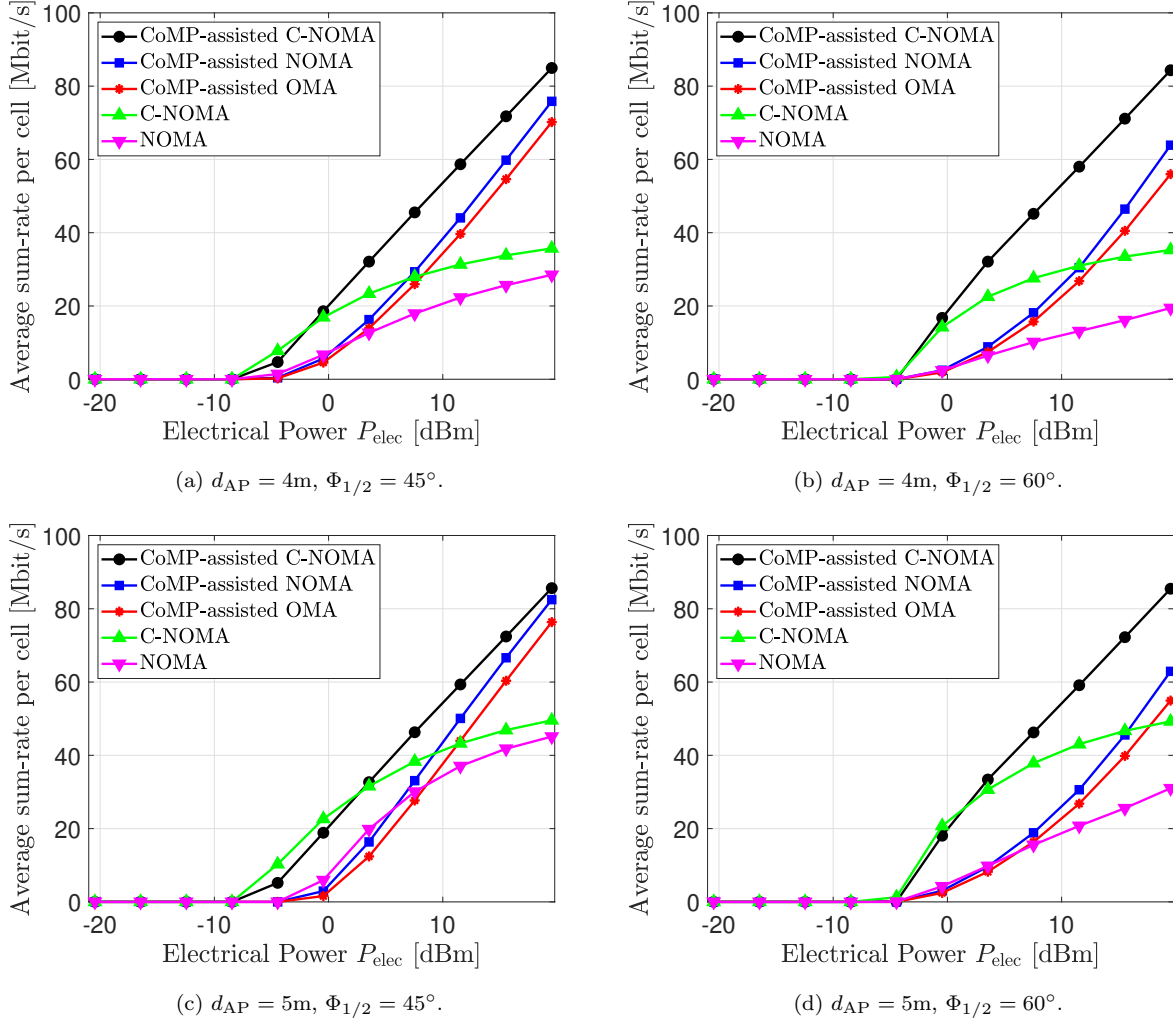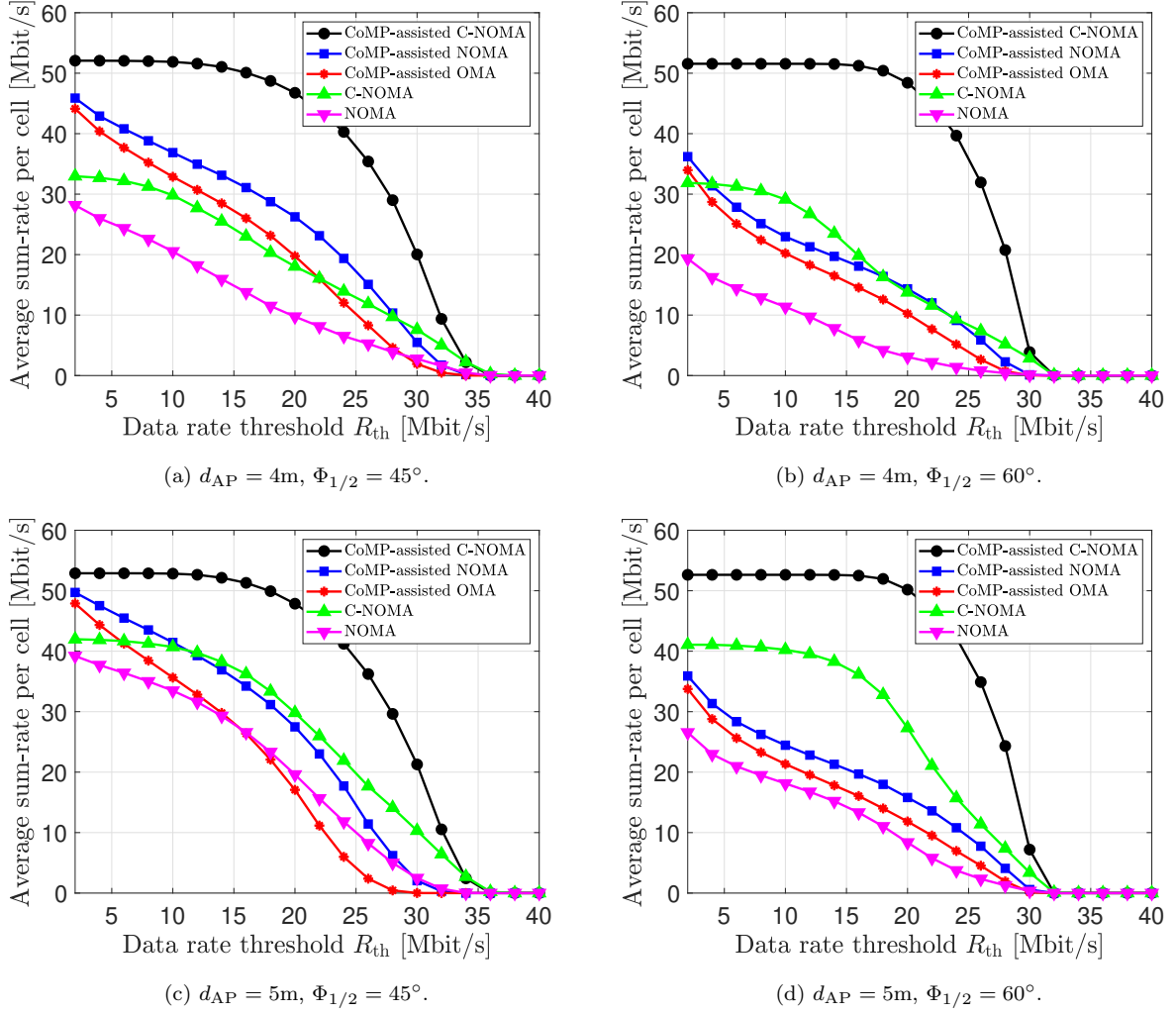The area of the PD A_{PD} at each UE is an important factor whose effects in the system performance should be analyzed. In this context, Figure 7.6 presents the average sum data rate per cell, achieved by the proposed CoMP-assisted NOMA and CoMP-assisted C-NOMA schemes, the CoMP-assisted OMA scheme, the C-NOMA scheme and the NOMA scheme, versus the area of the PD of each UE A_{PD}, when the transmit electrical power is $P_{elec} = 9.5$ dBm and the required data rate threshold is $R_{th} = 10$ [Mbit/Hz]. This figure demonstrates the superiority of the proposed CoMP-assisted schemes compared to the considered baselines and shows that the system performance increases when the area of the PD increases. This can be explained as follows. When the area of the PD increases, the received optical power from the APs at each UE increases, and hence, the power of the received signals increases, which increases the performance of the system. However, this is not the case for the C-NOMA and NOMA schemes, where at a certain point, increasing the area of the PD will increase the received optical power of both the useful and the interfering signals. Due to this, after a certain value of the PD's area, the sum data rate achieved by the C-NOMA and NOMA schemes starts stagnating.
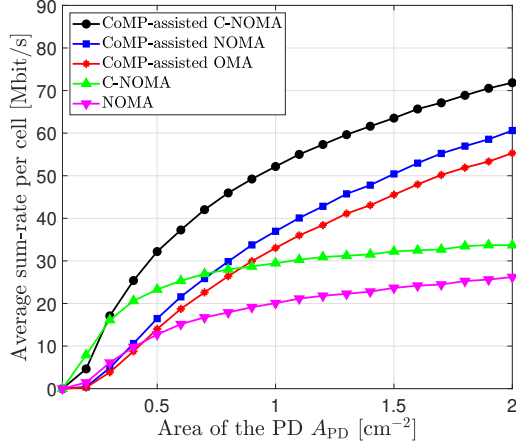
Figure 7.6: Average achievable sum data rate per cell, achieved by the proposed CoMP-assisted NOMA and CoMP-assisted C-NOMA schemes, and the considered baselines, versus the area of the PD of each UE A_{PD}.

Figure 7.7: Average achievable sum data rate achieved by the proposed CoMP-assisted NOMA and CoMP-assisted C-NOMA schemes versus the required data rate threshold per R_{th} for different UC techniques.

7.5.2.5 The Case of Multiple Users Per Cell

In this part, we consider the case where six UEs are coexisting within the proposed network model, where the first two UEs are strong UEs located near the center of the first cell, and hence, associated to the first cell, the second two UEs are strong UEs located near the center of the second cell, and hence, associated to the second cell, and the remaining two UEs are weak UEs located near the edge of both cells, and hence, associated to both cells. Specifically, the locations of the strong UEs are generated randomly near the centers of the coverage areas of the APs, whereas the locations of the weak UEs are generated randomly near the edges of the cells, in which the orientation of each UE is randomly generated using the measurements-based orientation models proposed in [28, 34, 161]. As such, four UEs are associated to each AP. In this case, the UEs can be clustered into groups of three UEs. Each cluster consists of one strong UE associated to the first AP, one strong UE associated to the second AP, and one weak UE served jointly by the two APs. Since multiple clusters are constructed by the two APs, a promising technique to avoid the inter-cluster interference within each cell is to utilize a hybrid multiple access technique, in which the proposed CoMP-assisted NOMA and CoMP-assisted C-NOMA schemes are combined with the conventional FDMA scheme. In particular, the proposed CoMP-assisted NOMA and CoMP-assisted C-NOMA schemes are applied within each cluster of UEs, whereas different clusters are served through different sub-bandwidths. In
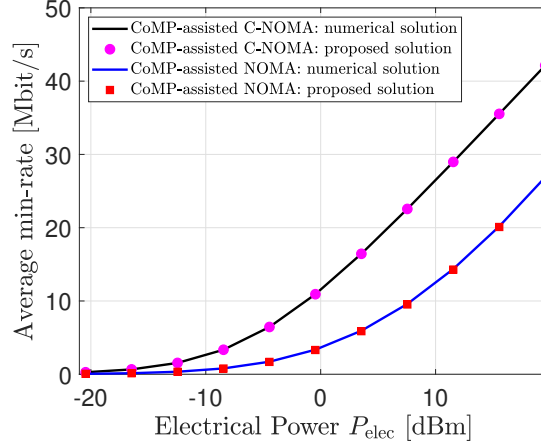
Figure 7.8: Average minimum data rate achieved by the numerical and the proposed solution approaches for the CoMP-assisted NOMA and the CoMP-assisted C-NOMA schemes versus the transmit electrical power P_{elec} at the APs.

this context, the UE clustering (UC) policy is another dimension to optimize along with the power allocation scheme. As such, two UC policies are considered for this purpose. The optimal UC and the random UC, which are defined as follows.

- **Optimal UC**: The optimal power allocation coefficients that maximize the sum data rate are obtained for all possible clusters using the proposed power allocation schemes. Then, the *Hungarian* method is applied to obtain the optimal UC policy [154, 156].

- **Random UC**: Random disjoint clusters of UEs are generated and then the optimal power allocation coefficients that maximize the sum data rate are obtained for each cluster using the proposed power allocation schemes.

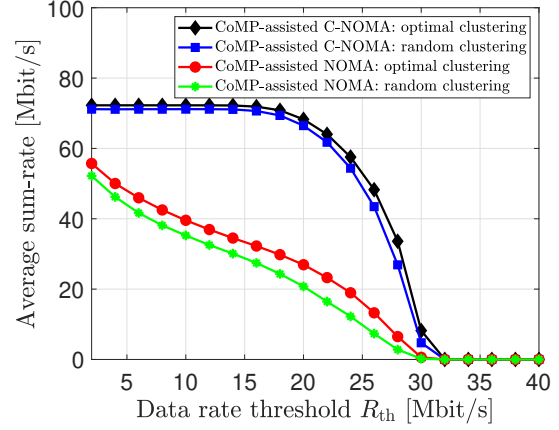Figure 7.7 presents the average overall sum data rate of the LiFi network achieved by the proposed CoMP-assisted NOMA and CoMP-assisted C-NOMA schemes versus the required data rate threshold per UE R_{th} for the considered UC techniques. This figure shows that the optimal UC policy achieves better performance than the random clustering.

7.5.3 Minimum Data Rate Performance

7.5.3.1 On the Optimality of the Proposed Solution Approaches

Figure 7.8 presents the average minimum data rate, achieved by the proposed CoMP-assisted NOMA and the CoMP-assisted C-NOMA schemes, versus the transmit electrical

power P_{elec}. For the two proposed schemes, the results of both the numerical solutions and the proposed solutions of the power allocation coefficients are presented. The numerical solutions are obtained by solving problems $\mathcal{P}_3$ and $\mathcal{P}_4$ using an off the-shelf optimization solver, whereas the analytical solutions are obtained through our proposed power allocation schemes. Figure 7.8 shows that the proposed solutions of the power allocation coefficients of the proposed CoMP-assisted NOMA and CoMP-assisted C-NOMA schemes match perfectly the numerical solutions, which demonstrates their optimality. Moreover, and as was shown by Figure 7.2, Figure 7.8 demonstrates the superiority of the CoMP-assisted C-NOMA scheme over the CoMP-assisted NOMA scheme due to the additional power at the strong UEs that is harvested from the APs and then used to relay the data of the weak UE.

7.5.3.2 Effect of the Transmit Electrical Power P_{elec}

Figure 7.9 presents the average minimum data rate per cell, achieved by the proposed CoMP-assisted NOMA and CoMP-assisted C-NOMA schemes, the CoMP-assisted OMA scheme, the C-NOMA scheme and the NOMA scheme, versus the transmit electrical power P_{elec}, for different values of the distance between the APs d_{AP} and the LEDs half-power semi-angle $\Phi_{1/2}$. Basically, the same observations and interpretation that were remarked for the sum data rate performance in Figure 7.4 are also valid for the minimum data rate performance.

7.6 Conclusion

This chapter studies the performance of CoMP transmission in downlink multi-cell NOMA/C-NOMA LiFi systems. For a system consisting of two adjacent attocells serving three coexisting users, optimal and low-complexity power control schemes that maximizes the network sum data rate, while guaranteeing target QoS at the end users, and the minimum data rate within the network are derived. In the simulation results, the optimality of the derived power control schemes is verified and the performance of the proposed CoMP-assisted NOMA and CoMP-assisted C-NOMA schemes are compared with those of the CoMP-assisted FDMA scheme, the C-NOMA scheme and the NOMA scheme, where the superiority of the proposed schemes is demonstrated. The extension of the proposed CoMP-assisted NOMA and CoMP-assisted C-NOMA schemes to multiple

(a) $d_{\text{AP}} = 4\text{m}$, $\Phi_{1/2} = 45°$.

(b) $d_{\text{AP}} = 4\text{m}$, $\Phi_{1/2} = 60°$.

(c) $d_{\text{AP}} = 5\text{m}$, $\Phi_{1/2} = 45°$.

(d) $d_{\text{AP}} = 5\text{m}$, $\Phi_{1/2} = 60°$.
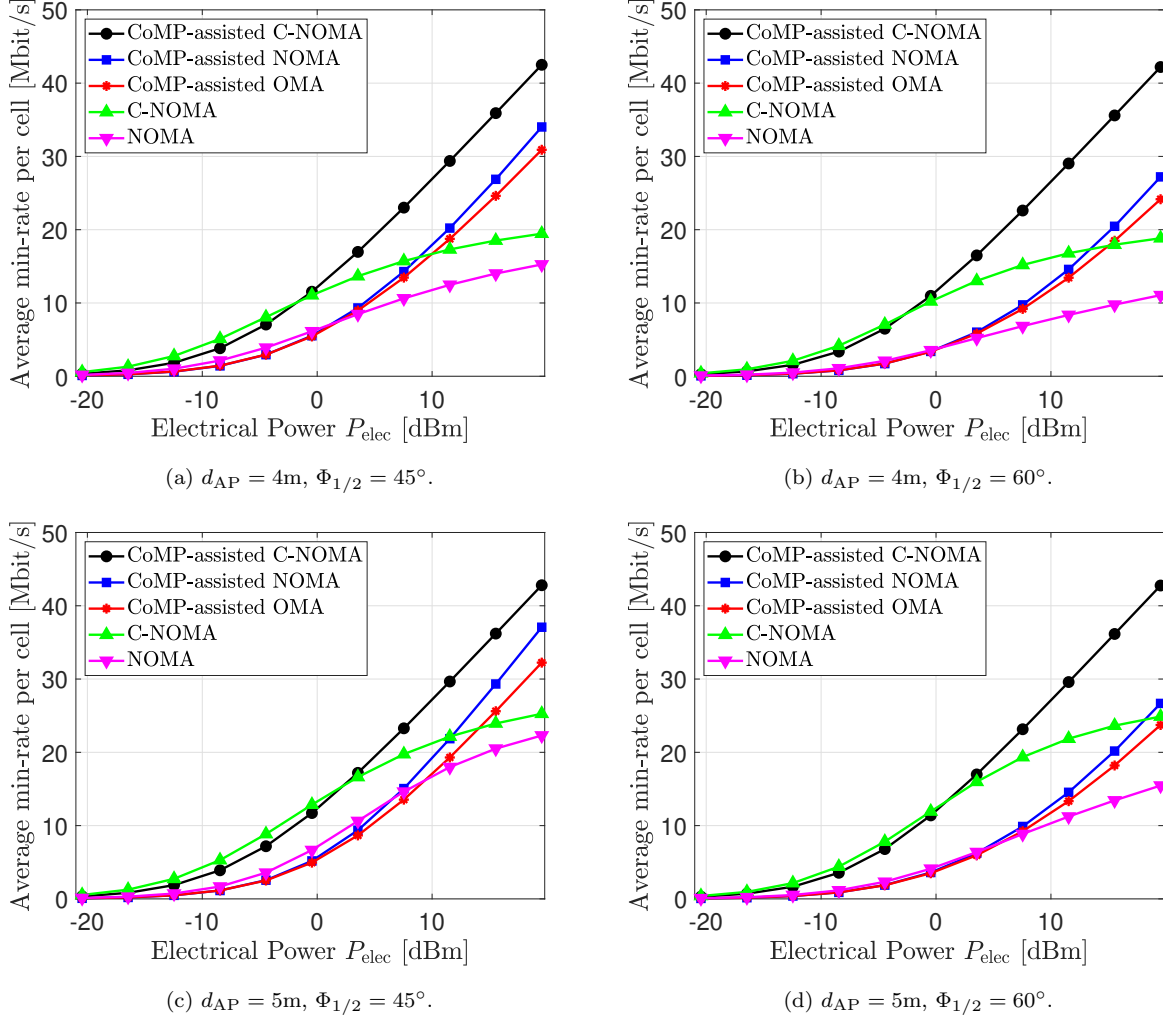
Figure 7.9: Average minimum data rate per cell, achieved by the proposed CoMP-assisted NOMA and CoMP-assisted C-NOMA schemes, the CoMP-assisted OMA scheme, the C-NOMA scheme and the NOMA scheme, versus the transmit electrical power P_{elec}.

coordinating attocells, i.e., a number of APs higher than two, can be considered as a potential future research direction. In such a case, although the dynamic power control and the interference management become more challenging, it is expected that a performance enhancement of LiFi cellular systems can be achieved.

Chapter 8

Conclusions and Future Research Directions

8.1 Conclusion

LiFi is an emerging wireless communication technology that will boost the emergence of 6G wireless networks. However, this technology suffers from some shortcomings that should be carefully investigated. In this dissertation, we aimed at making the LiFi technology tailored to real-world settings and we presented the vision of bringing the deployment of LiFi-based systems closer than ever.

In Chapter 3, we have developed novel, realistic and measurement-based channel models for indoor LiFi systems. Precisely, the statistics of the channel gain are derived for the case of stationary and mobile users with random device orientation. For stationary users, two channel models were proposed, which are the MTL model and the MB model, and for mobile users, two channel models were also proposed, which are the SMTG model and the SMB model. Based on the derived models, the impact of random orientation and spatial distribution of users was investigated, where we showed that the aforementioned factors can strongly affect the channel gain and the system performance. Furthermore, in Chapter 4, aiming to alleviate the effects of mobility, random device orientation, and blockage, we have proposed a novel MDR design. We tested the performance of the proposed design using measurement-based channel models. In addition, we have adopted SM as a modulation scheme and we showed that MDR outperforms the benchmark structure by over 10 dB at BER of 3.8×10^{-3}. We further demonstrated that the proposed designs and techniques outperforms the conventional spatial multiplexing system.

In Chapter 5, the joint estimation of user 3D position and orientation in indoor LiFi systems with unknown emission power was investigated. We have adopted fingerprinting as an estimation technique and the received SNR as an estimation metric, where all components of the LiFi channel are considered. Motivated by the success of DL techniques in solving several complex estimation and prediction problems, we have employed two deep ANN models that can map efficiently the instantaneous received SNR with the user 3D position and the UE orientation. The first model is based on MLP and the second model is based on CNN. Through numerous examples, we have investigated the performance of the proposed models in terms of the average estimation error, precision, computational time, and the BER. We have also compared this performance to that of the KNN technique, which is widely used in solving wireless localization problems. It is demonstrated that the proposed models achieve significant gains and are superior to the KNN scheme. Moreover, In Chapter 6, we have proposed a proactive optimization approach that can alleviate the LiFi channel aging problem for mobile users. The core idea is designing an LSTM network that is capable of predicting posterior positions and orientations of mobile users, which can be then used to predict their channel coefficients. Consequently, the obtained channel coefficients can be exploited for deriving near-optimal transmission-schemes prior to the intended service-time, which enables real-time service. Through various simulations, the performance of the designed LSTM model is evaluated in terms of prediction accuracy and time. Finally, the performance of the proposed approach is investigated in the sum rate maximization problem of multi-user LiFi systems with quality-of-service constraints, where a performance gap of less than 7% is achieved, while maintaining a real time service.

Finally, in Chapter 7, aiming to provide broadband connectivity for multiple users within LiFi cellular systems, we have proposed two multiple access techniques, namely, CoMP-assisted NOMA scheme and CoMP-assisted C-NOMA. In a multi-cell setting, the coordinated ZF precoding is used to cancel the ICI at the users located near the centers of the cells, whereas the JT is employed to eliminate the ICI at the users located at the edge of both cells and to improve their receptions as well. Furthermore, NOMA and C-NOMA where employed to serve users within each cell. For each scheme, two power allocation frameworks are formulated each as an optimization problem, where the objective of the former is maximizing the network sum data rate while guaranteeing a

certain QoS for each user, whereas the goal of the latter is to maximize the minimum data rate among all coexisting users. The formulated optimization problems are not convex, and hence, difficult to be solved directly unless using heuristic methods, which comes at the expense of high computational complexity. To overcome this issue, optimal and low complexity power allocation schemes are derived. In the simulation results, the performance of the proposed CoMP-assisted NOMA and CoMP-assisted C-NOMA schemes are compared with those of the CoMP-assisted OMA scheme, the C-NOMA scheme, and the NOMA scheme, where the superiority of the proposed schemes are demonstrated. Finally, the performance of the proposed schemes and the considered baselines is evaluated while varying various system parameters.

8.2 Future Research Directions

8.2.1 Channel Models

The channel models proposed in Chapter 3, albeit being fundamental, they serve as a starting point for developing realistic transmission techniques and transceiver designs tailored to real-world set-ups. In Chapter 3, only the statistics of the LOS channel gain were considered whereas those of the NLOS channel gain were ignored. In fact, deriving closed-form statistical models for the total LiFi channel gain, i.e., including both LOS and NLOS components, especially when the LiFi AP is close to the walls, i.e., when the NLOS components are not negligible compared to the LOS component, and while considering the random orientation and motion of users is quite challenging [44]. In fact, the expression of the NLOS channel gain is very complex, since it is based on summing over all possible reflections through all possible objects [44]. Due to this, an alternative in deriving the channel statistics of the total channel gain that encompass the random orientation and motion of users is by performing empirical studies based on extensive experiments and semi-analytical results, which can be considered as a key future research direction.

8.2.2 Rate Splitting Multiple Access

Motivated by the mobile applications and connected devices that are expected to increase exponentially in the IoT, multiple access techniques are supposed to be amalgamated into the communication model to accommodate multiple users and devices [9,188].

Among various methods for multiple access, rate splitting multiple access (RSMA), considered as a key type of the next generation multiple access, has attracted sustained attentions recently due to its advantages of rate-wise, robustness, spectral efficiency, and lower computation complexity [189]. RSMA is originally proposed for two-user single-input single-output systems in [190], where it aims to achieve new rate regions. In the recent years since 2016, to address the multi-user interference (MUI) problem and to reduce the CSI feedback, RSMA is introduced afresh and extended to multi-user MIMO systems [191], massive MIMO systems [192], and multiple-input single-output broadcast (MISO BC) systems [193]. With the RSMA scheme, the transmitted messages are split into common parts and private parts, where the common parts of all users are jointly encoded into a single common stream intended to be decoded by all users at the receiver, and the private parts are separately encoded into multiple streams that will only be decoded by their corresponding users. To accomplish this splitting design, the linear precoding method is employed at the transmitters and the SIC is adopted at the receivers, which enables RSMA to partially treat interference as noise and to partially decode the interference. With such a splitting design, RSMA subsumes SDMA and NOMA as special cases and outperforms them in terms of spectral efficiency and QoS enhancements at a lower complexity [194]. To benefit from RSMA, the resource allocation, precoding design, and application extension are required to be thoroughly explored.

Most of the existing researches focus on the investigations of RSMA in the context of RF communications [189–193], while only sporadic researches are designed for LiFi [164, 195–198]. Motivate by the above background, optimizing and boosting the performance of multi-user LiFi systems under the RSMA technique is a key future research area. The main objective is enhancing the performance of multi-user multi-cell LiFi systems, with respect to some typical performance metrics, such as the sum-rate or the minimum rate, through an optimal design of the resource allocation and the precoding design. The secrecy performance of the considered system can be also considered as a potential future research direction.

8.2.3 Outdoor LiFi Systems

Outdoor LiFi applications are less explored when compared to their indoor counterparts. This is mainly due to two facts: 1) the dual use of LEDs is not always practical in

an outdoor LiFi environments, and 2) the level of interference and noise is considerably higher in outdoor environments. Nevertheless, several outdoor LiFi applications have been identified in the literature. The adoption of LiFi in outdoor applications was reviewed in [199], where the authors revealed the issues that arise in the outdoor usage of LiFi and identified emerging challenges. In this context, LiFi outdoor applications include, but are not limited to [200]:

1. Vehicle-to-everything (V2X) communication.

2. Pedestrian-to-infrastructure (P2I) communication.

3. Building-to-building (B2B) communication.

V2X communications is a new concept that uses the latest generation of information and communication technology that connect vehicles to everything. In its turn, V2X communication includes [201]:

1. Vehicle-to-infrastructure (V2I) communication, also known as road to vehicle (R2V) communication.

2. Vehicle-to-vehicle (V2V) communication.

The V2X technology links and interconnects the various elements of transportation, such as pedestrians, vehicles, roads, and cloud environments. This leads to the building of an intelligent transportation system and promoting the development of new modes and new forms of automobiles and transportation services by gathering more information and promote the innovation and application of automated driving technologies [202]. In addition, V2X communication is of great significance for improving traffic efficiency, saving resources, reducing accidents, and improving traffic management [202, 203]. Additionally, in outdoor environment, the LiFi technology can be incorporated in the building of smart city to provide green and ubiquitous wireless connection [204]. Specifically, in a large scale outdoor domain, the LED street luminaries can be modified and networked to provide various and low-cost services (video broadcasting, stream media, real time voice, high precision positioning and so on) to the pedestrians and the grounding vehicles in moving or static status [205, 206]. On the other hand, B2B communications define all the communications technologies that enable connection between buildings. Both RF and OWC (including the visible light and the IR spectra) can used for this type of mission.

Therefore, LiFi may be used to connect buildings situated within a reasonable distance from each other, such as campuses, bank buildings, and headquarters, to provide access to information, data and media. Some fundamental features should be clearly defined and deeply investigated before performing security analysis. These features include:

- The framework and the network configuration, such as distances, dimensions, transmit light sources, optical receivers, etc.

- Realistic and measurement-based channel models should be derived. These channel models should encompass the effect of interference as there are fewer physical barriers in outdoor environments (unlike the indoor environment).

- The effect of sunlight during the day, outdoor illumination during the night, and weather conditions should be studied. It has been shown that solar irradiance does not prevent high speed LiFi communication [207]. However, careful considerations and system design are required to minimize the effect of those sources of impairment on the performance of LiFi systems.

Appendices

Appendix A

Proofs and Derivations for Chapter 3

A.1 Proof of Theorem 3.1

At first, let us determine the range of the LOS channel gain H_{LOS}. Recall that H_{LOS} is expressed as

$$H_{\mathrm{LOS}} = H_0 \frac{(h_a - h_u)^m \cos(\psi)}{d^{m+2}} \times \mathcal{U}_{[\cos(\Psi),0]}\left(\cos\left(\psi\right)\right), \tag{A.1}$$

where $\cos(\psi) = \frac{r\cos(\Omega - \alpha)\sin(\theta) + (h_a - h_u)\cos(\theta)}{d}$. Since $\Psi \in [0, \frac{\pi}{2}]$, we have $H_{\mathrm{LOS}} \geq 0$ and the minimum value of H_{LOS} is equal to $h_{\min} = 0$. A set of values that can yield in $h_{\min} = 0$ is given as $d = d_{\min}$, $\Omega - \alpha = \pm k\frac{\pi}{2}$ s.t. $k = 1, 3$ and $\theta \geq \Psi$, which corresponds to the case where $\cos\left(\psi\right) \leq \cos\left(\Psi\right)$. On the other hand, the maximum value of H_{LOS} is equal to $h_{\max} = \frac{H_0}{(h_a - h_u)^2}$. A set of values that can yield in $h_{\max}$ is expressed as $d = h_a - h_u$, $\Omega - \alpha = \pm\frac{\pi}{2}$ s.t. $k = 1, 3$ and $\theta = 0$, which corresponds to the case where $\cos\left(\psi\right) = 0$.

Since the range of the LOS channel gain H_{LOS} is now determined, the CDF of the LOS channel gain H_{LOS} is expressed as

$$F_{H_{\mathrm{LOS}}}(h) \tag{A.2a}$$

$$= \Pr\left(H_{\mathrm{LOS}} \leq h\right) \tag{A.2b}$$

$$= \Pr\left(\left(\left(a(\theta)\frac{\sqrt{d^2 - (h_a - h_u)^2}}{d^{m+3}}\cos(\Omega - \alpha) + \frac{b(\theta)}{d^{m+3}}\right) \times \mathcal{U}_{[\cos(\Psi),0]}\left(\cos\left(\psi\right)\right) \leq h\right) \tag{A.2c}$$

$$= \Pr\left(a(\theta)\frac{\sqrt{d^2 - (h_a - h_u)^2}}{d^{m+3}}\cos(\Omega - \alpha) + \frac{b(\theta)}{d^{m+3}} \leq h, \cos(\Psi) \leq \cos(\psi)\right) \tag{A.2d}$$

$$+ \Pr\left(0 \leq h, \cos(\psi) \leq \cos(\Psi)\right)$$

$$= \int_{d_{\min}}^{d_{\max}} \int_0^{\frac{\pi}{2}} \Pr\left(\frac{l\cos(\Psi) - b'(\theta)}{a'(\theta)\sqrt{d^2 - (h_a - h_u)^2}} \leq \cos(\Omega - \alpha)\right)$$

$$\leq \frac{d^{m+3}h - b}{a(\theta)\sqrt{d^2 - (h_a - h_u)^2}} \Bigg| \theta, d \Bigg) f_\theta(\theta) f_d(l) \mathrm{d}\theta \mathrm{d}l + F_{\cos(\psi)}(\cos(\Psi)) \mathcal{U}_{[0,\infty]}(h) \quad \text{(A.2e)}$$

$$= \int_{d^*_{\min}(h)}^{d_{\max}} \int_0^{\frac{\pi}{2}} I_H(\theta, l) f_\theta(\theta) f_d(l) \mathrm{d}\theta \mathrm{d}l + F_{\cos(\psi)}(\cos(\Psi)) \mathcal{U}_{[0,\infty]}(h), \quad \text{(A.2f)}$$

where $a'(\theta) = \sin(\theta)$, $b'(\theta) = (h_a - h_u)\cos(\theta)$ and the function I_H is expressed as

$$I_H(\theta, l) = F_{\cos(\Omega-\alpha)}\left(\frac{l^{m+3}h - b(\theta)}{a(\theta)\sqrt{l^2 - (h_a - h_u)^2}}\right) - F_{\cos(\Omega-\alpha)}\left(\frac{l\cos(\Psi) - b'(\theta)}{a'(\theta)\sqrt{l^2 - (h_a - h_u)^2}}\right). \quad \text{(A.3)}$$

Equality (A.2f) follows from the fact that the conditional probability under the integral in (A.2e) is not null if and only if

$$\frac{l\cos(\Psi) - b'(\theta)}{a'(\theta)\sqrt{l^2 - (h_a - h_u)^2}} \leq \frac{l^{m+3}h - b(\theta)}{a(\theta)\sqrt{l^2 - (h_a - h_u)^2}}, \quad \text{(A.4)}$$

i.e., $\left(\frac{H_0(h_a - h_u)^m \cos_\Psi}{h}\right)^{\frac{1}{m+2}} \leq l$. Or, l is constrained within the range $[d_{\min}, d_{\max}]$. Therefore, the conditional probability in (A.2e) is not null if and only if $l \in [d^*_{\min}(h), d_{\max}]$, where $d^*_{\min}(h) = \max(d_0(h), d_{\min})$ such that $d_0(h) = \left(\frac{H_0(h_a - h_u)^m \cos(\Psi)}{h}\right)^{\frac{1}{m+2}}$. Additionally, since l_0 should be always lower than $d_{\max}$, we conclude that the channel gain H_{LOS} under the integral in (A.2f) should satisfy $h^*_{\min} \leq h$, where $h^*_{\min} = \frac{H_0(h_a - h_u)^m \cos(\Psi)}{d_{\max}^{m+2}} \in [h_{\min}, h_{\max}]$. Furthermore, $F_{\cos(\psi)}(\cos(\Psi))$ in is expressed as

$$F_{\cos(\psi)}(\cos(\Psi)) = \Pr(\cos(\psi) \leq \cos(\Psi)) \quad \text{(A.5a)}$$

$$= \int_{d_{\min}}^{d_{\max}} \int_0^{\frac{\pi}{2}} F_{\cos(\Omega-\alpha)}\left(\frac{l\cos(\Psi) - (h_a - h_u)\cos(\theta)}{\sin(\theta)\sqrt{l^2 - (h_a - h_u)^2}}\right) f_\theta(\theta) f_d(l) \mathrm{d}\theta \mathrm{d}l. \quad \text{(A.5b)}$$

Based on this, the corresponding PDF of the LOS channel gain H_{LOS} is obtained by differentiating equality (A.2f) with respect to H_{LOS}. Using Leibniz integral rule for differentiation, the PDF of the LOS channel gain H_{LOS} is expressed as

$$f_H(h) = \frac{\partial}{\partial h}[\Pr(H \leq h)] \quad \text{(A.6a)}$$

$$= \int_{d^*_{\min}}^{d_{\max}} \int_0^{\frac{\pi}{2}} \frac{l^{m+3}}{a(\theta)\sqrt{l^2 - (h_a - h_u)^2}} f_{\cos(\Omega-\alpha)}\left(\frac{l^{m+3}h - b(\theta)}{a(\theta)\sqrt{l^2 - (h_a - h_u)^2}}\right) f_\theta(\theta) f_d(l) \mathrm{d}\theta \mathrm{d}l \quad \text{(A.6b)}$$

$$+ v(h) \int_0^{\frac{\pi}{2}} J_H(\theta, l) f_\theta(\theta) \mathrm{d}\theta + F_{\cos(\psi)}(\cos(\Psi))\delta(h),$$

for $h \in [h^*_{\min}, h^*_{\max}]$, and 0 otherwise, such that $h^*_{\max} = h_{\max}\cos(\Psi) \in [h_{\min}, h_{\max}]$. This completes the proof.

A.2   Proof of Theorem 3.2

Based on the results of **Theorem 3.1**, the PDF of the LOS channel gain H_{LOS} is given by

$$f_{H_{\mathrm{LOS}}}(h) = g_H(h)\mathcal{U}\left(h^*_{\min}, h_{\max}\right) + F_{\cos(\psi)}(\cos(\Psi))\delta(h)$$

$$= \left(1 - F_{\cos(\psi)}(\cos(\Psi))\right) f_Z(h) + F_{\cos(\psi)}(\cos(\Psi))\delta(h), \qquad (A.7)$$

where f_Z is a PDF, with support range $[h^*_{\min}, h_{\max}]$. The PDF f_Z is associated to the random variable Z that is expressed as $Z = XY$, where $X = \frac{c}{d^{m+2}}$ such that $c = H_0\left(h_{\mathrm{a}} - h_{\mathrm{u}}\right)^m$ and $Y = \cos(\psi)$ for $\psi \in [0, \Psi]$. Note that X and Y are two random variables that reflect the effects of the random spatial distribution of the user and the random orientation of the UE on the LOS channel gain, respectively. For the case of stationary users, and using the PDF transformation of random variables, the PDF of the random variable X is expressed as

$$f_X(x) = \frac{c^{\frac{1}{m+2}}}{(m+2)}\left(\frac{1}{x}\right)^{\frac{m+3}{m+2}} f_d\left(\left(\frac{c}{x}\right)^{\frac{1}{m+2}}\right) = \frac{2c^{\frac{2}{m+2}}}{R^2(m+2)}\left(\frac{1}{x}\right)^{\frac{m+4}{m+2}}\mathcal{U}_{\left[c/d^{m+2}_{\max}, c/d^{m+2}_{\min}\right]}(x). \qquad (A.8)$$

Obviously, X and Y are correlated since they are a function of the distance l, which is also a random variable. However, such correlation can be weak in most of the cases. In fact, for high values of d, the effect of the random orientation on the LOS channel gain H_{LOS} is negligible compared to the one of the distance, whereas for the case of low values of l, the effect of the distance is negligible compared to the one of random orientation. Due to this, as an approximation, we assume that the random variables X and Y are uncorrelated. Based on this, using the theorem of the PDF of the product of random variables [208], the PDF of the random variable Z can be approximated as

$$f_Z(h) \approx \int_{y_{\min}(h)}^{y_{\max}(h)} f_X\left(\frac{h}{y}\right) f_Y(y)\frac{\mathrm{d}y}{y} = \left(\frac{1}{h}\right)^{\frac{m+4}{m+2}}\int_{y_{\min}(h)}^{y_{\max}(h)} \frac{2c^{\frac{2}{m+2}}}{R^2(m+2)}y^{\frac{2}{m+2}} f_Y(y)\,\mathrm{d}y, \qquad (A.9)$$

where f_Y denotes the PDF of the random variable Y and it is given in (19) and (22) of [28]. Based on this, the PDF f_Z has the form $f_Z(h) \approx \frac{1}{h^\nu}\tilde{f}(h)$, where $\nu > 0$ and $\tilde{f}$ is a function with support range $[h^*_{\min}, h_{\max}]$ that is expressed as

$$\tilde{f}(h) = \int_{y_{\min}(h)}^{y_{\max}(h)} \frac{2c^{\frac{2}{m+2}}}{R^2(m+2)}y^{\frac{2}{m+2}} f_Y(y)\,\mathrm{d}y. \qquad (A.10)$$

Consequently, by substituting $f_Z(h)$ in (A.7) by its expression and defining the function g, for $h \in [h^*_{\min}, h_{\max}]$, as $g(h) = \left(1 - F_{\cos(\psi)}(\cos(\Psi))\right)\tilde{f}(h)$, we obtain the result of Theorem 2, which completes the proof.

A.3 Proof of Theorem 3.3

Using the same notation adopted in Appendix B, the PDF of the random variable X for the case of mobile users is expressed as

$$f_X(x) = \frac{c^{\frac{1}{m+2}}}{(m+2)} \left(\frac{1}{x}\right)^{\frac{m+3}{m+2}} f_d\left(\left(\frac{c}{x}\right)^{\frac{1}{m+2}}\right) = \sum_{i=1}^{3} \frac{a_i c^{b_i + \frac{2}{m+2}}}{(m+2)R^{b_i+1}} \left(\frac{1}{x}\right)^{b_i + \frac{m+4}{m+2}} \mathcal{U}_{\left[c/d_{\max}^{m+2},\, c/d_{\min}^{m+2}\right]}(x).$$

$$(\text{A.11})$$

Therefore, the PDF of the random variable Z can be approximated by

$$f_Z(h) \approx \int_{y_{\min}(h)}^{y_{\max}(h)} f_X\left(\frac{h}{y}\right) f_Y(y) \frac{\mathrm{d}y}{y} = \sum_{i=1}^{3} \left(\frac{1}{h}\right)^{b_i + \frac{m+4}{m+2}} \int_{y_{\min}(h)}^{y_{\max}(h)} \left[\frac{a_i c^{b_i + \frac{2}{m+2}}}{(m+2)R^{b_i+1}} y^{b_i + \frac{m+4}{m+2}} f_Y(y)\right] \mathrm{d}y,$$

$$(\text{A.12})$$

which has the form $f_Z(h) \approx \sum_{j=1}^{3} \frac{1}{z^{\nu_i}} \tilde{f}_j(h)$, where, for $j = 1, 2, 3$, $\nu_j > 0$ and $\tilde{f}_j$ is a function with support range $[h_{\min}^*, h_{\max}]$ that is expressed as

$$\tilde{f}_j(h) = \int_{y_{\min}(h)}^{y_{\max}(h)} \left[\frac{a_i c^{b_i + \frac{2}{m+2}}}{(m+2)R^{b_i+1}} y^{b_i + \frac{m+4}{m+2}} f_Y(y)\right] \mathrm{d}y. \qquad (\text{A.13})$$

Consequently, by substituting $f_Z(h)$ in (A.7) by its expression and defining $g_j(h)$, for $j = 1, 2, 3$ and for $h \in [h_{\min}^*, h_{\max}]$, as $g_j(h) = \left(1 - F_{\cos(\psi)}(\cos(\Psi))\right) \tilde{f}_j(h)$, we obtain the result of Theorem 3, which completes the proof.

A.4 Proof of Corollary 3.1

Based on the PDF of the LOS channel gain H_{LOS} provided in Theorem 1 and the expression of the probability of error of M-pulse amplitude modulation [209, 210], the average probability of error of the considered LiFi system is expressed as

$$P_e = \int_{h_{\min}}^{h_{\max}} f_H(h) P_{e,h}\left(P_{\mathrm{opt}}, h\right) \mathrm{d}h \qquad (\text{A.14a})$$

$$= \int_{h_{\min}^*}^{h_{\max}} g_H(h) \frac{2(M-1)}{M} \mathcal{Q}\left(\frac{h P_{\mathrm{opt}}}{\sigma(M-1)}\right) \mathrm{d}h$$

$$+ F_{\cos(\psi)}(\cos(\Psi)) \int_{h_{\min}}^{h_{\max}} \delta(h) \mathcal{Q}\left(\frac{h P_{\mathrm{opt}}}{\sigma(M-1)}\right) \mathrm{d}h, \quad (\text{A.14b})$$

where $P_{e,h}\left(P_{\mathrm{opt}}, h\right)$ is the instantaneous probability of error for a given channel gain H_{LOS} and $\gamma_{\mathrm{TX}} = \frac{P_{\mathrm{elec}}}{\sigma^2} = \frac{P_{\mathrm{opt}}^2}{\sigma^2}$ is the transmitted SNR, such that P_{elec} is the transmitted electrical signal and σ^2 is the average noise power at the receiver. Now, since the function $h \mapsto g_H(h) \frac{2(M-1)}{M} \mathcal{Q}\left(\frac{h P_{\mathrm{opt}}}{\sigma(M-1)}\right)$ is a smooth function within $[h_{\min}^*, h_{\max}]$, and using the

Lebesgue's dominated convergence theorem, we get

$$\lim_{P_{\mathrm{opt}} \to \infty} \int_{h_{\min}}^{h_{\max}} g_H(h) \frac{2(M-1)}{M} \mathcal{Q}\left(\frac{hP_{\mathrm{opt}}}{\sigma(M-1)}\right) \mathrm{d}h$$

$$= \int_{h_{\min}}^{h_{\max}} \lim_{P_{\mathrm{opt}} \to \infty} g_H(h) \frac{2(M-1)}{M} \mathcal{Q}\left(\frac{hP_{\mathrm{opt}}}{\sigma(M-1)}\right) \mathrm{d}h \qquad (\mathrm{A}.15)$$

$$= 0.$$

Furthermore, since $h_{\min} = 0$, we have $\int_{h_{\min}}^{h_{\max}} \delta(h) \mathcal{Q}\left(\frac{hP_{\mathrm{opt}}}{\sigma(M-1)}\right) \mathrm{d}h = \mathcal{Q}(0) = \frac{1}{2}$, which implies that $\lim_{P_{\mathrm{opt}} \to \infty} \int_{h_{\min}}^{h_{\max}} \delta(h) \mathcal{Q}\left(\frac{hP_{\mathrm{opt}}}{\sigma(M-1)}\right) \mathrm{d}h = \frac{1}{2}$. Therefore, we conclude that $\lim_{P_{\mathrm{opt}} \to \infty} P_e(P_{\mathrm{opt}}) = \frac{F_{\cos(\psi)}(\cos(\Psi))}{2}$, which completes the proof.

Appendix B

Orientation-Based Random Waypoint

The random waypoint (RWP) mobility model is one of the most widely used and simple models, which is utilized for the simulation-based studies of wireless networks [211]. The RWP mobility model specifies the following characterizations, i) destinations are chosen randomly following a uniform distribution in the room area, and ii) users move with a constant speed on a straight line between two consecutive waypoints [211]. The RWP model is identified as a discrete-time stochastic random process (RP). Mathematically, it can be denoted as an infinite sequence of triples, $\{(\mathbf{P}_{n-1}, \mathbf{P}_n, v_n) \mid n \in \mathbb{N}\}$, where n shows the nth movement period. The UE moves from $\mathbf{P}_{n-1} = (x_{n-1}, y_{n-1})$ to $\mathbf{P}_n = (x_n, y_n)$ with a constant speed of v. The angle between the direction of movement and the positive direction of the X-axis is defined as the user direction, $\Omega = \tan^{-1}(\frac{y_n - y_{n-1}}{x_n - x_{n-1}})$.

In order to provide a more realistic framework for analyzing the performance of mobile wireless networks in LiFi, it is required to combine the conventional RWP with the random orientation model. An orientation-based random waypoint (ORWP) mobility model is introduced in [28], where the elevation angle of the UE is included during the user's movement. An altered version of ORWP, where the yaw angle α, the pitch angle β, and the roll angle γ, are encompassed, is used in this study to evaluate the system performance metrics (such as received SNR) more accurately for mobile users. The ORWP can be modeled as an infinite sequence of quadruples, $\{(\mathbf{P}_{n-1}, \mathbf{P}_n, v_n, \mathbf{\Theta}_n) \mid n \in \mathbb{N}\}$, where $\mathbf{\Theta}_n = (\alpha_n, \beta_n, \gamma_n)$ is a random vector process describing the UE's orientation during the movement from waypoint $\mathbf{P}_{n-1}$ to waypoint $\mathbf{P}_n$. The entities, α, β and γ are RPs. The ORWP is summarized in the **Algorithm** 2.

It is shown in Section 2.3 that α, β and γ for walking activities follow a Gaussian distribution with the parameters given in Table 2.1. According to the experimental measurements, the adjacent samples of the RPs α, β and γ are correlated. Hence, to incorporate the device orientation with the RWP mobility model, a correlated Gaussian RP which statistically follows the experimental measurements should be generated. It should be noted that the random orientation process considered here can be applied to

---

Algorithm 2 Orientation-based random waypoint (ORWP)

1: Initialization:

$n \longleftarrow 1$; $k \longleftarrow 1$;

Denote $\mathbf{P}_n = (x_n, y_n)$ and $\mathbf{P}_0 = (x_0, y_0)$ as the nth and initial UE's positions, respectively;

N as the number of simulation runs; v as the average speed of UE; $T_{c,\alpha}$, $T_{c,\beta}$ and $T_{c,\gamma}$ as the coherence time of α, β and γ, respectively; Set $T_c = \min\{T_{c,\alpha}, T_{c,\beta}, T_{c,\gamma}\}$;

μ_α, μ_β and μ_γ as the mean and σ_α^2, σ_β^2 and σ_γ^2 as the variance of Gaussian RPs α, β and γ;

2: **for** $n = 1 : N$ **do**

3:     Choose a random location $\mathcal{P}_n = (x_n, y_n)$

4:     Compute $\mathcal{D}_n = \|\mathcal{P}_n - \mathcal{P}_{n-1}\|$

5:     Compute $\Omega = \tan^{-1}\left(\frac{y_n - y_{n-1}}{x_n - x_{n-1}}\right)$

6:     $t_{\text{move}} \longleftarrow 0$;

7:     **while** $t_{\text{move}} \leq \frac{\mathcal{D}_n}{v}$ **do**

8:         Compute $\mathbf{P}_k = (x_k, y_k)$ with $x_k = x_{k-1} + vT_c \cos\Omega$ and $y_k = y_{k-1} + vT_c \sin\Omega$

9:         Generate $\mathbf{\Theta}_k = (\alpha_k, \beta_k, \gamma_k)$ based on the AR(1) model

10:        Return $(\mathbf{P}_{k-1}, \mathbf{P}_k, v, \mathbf{\Theta}_k)$ as ORWP specifications

11:        $k \longleftarrow k + 1$

12:        $t_{\text{move}} \longleftarrow t_{\text{move}} + T_c$

13:    **end while**

14:    **if** $t_{\text{move}} \neq \frac{\mathcal{D}_n}{v} - T_c$ & $t_{\text{move}} \geq \lfloor \frac{\mathcal{D}_n}{v} \rfloor T_c - T_c$ **then**

15:        Generate $\mathbf{\Theta}_k = (\alpha_k, \beta_k, \gamma_k)$ based on the AR(1) model

16:        $\mathbf{P}_k \longleftarrow \mathcal{P}_n$

17:        Return $(\mathbf{P}_{k-1}, \mathbf{P}_k, v, \mathbf{\Theta}_k)$ as ORWP specifications

18:        $k \longleftarrow k + 1$

19:    **end if**

20:    $n \longleftarrow n + 1$

21: **end for**

---

any other mobility models. Methods to generate a correlated Gaussian RP are discussed in [212,213] and references therein. A simple way of producing a correlated Gaussian RP is to use a linear time-invariant (LTI) filter and passing a white noise process through it, e.g., a linear autoregressive (AR) filter. Thus, after passing the white noise process, $w[k]$, through the LTI filter, the kth time sample of the correlated Gaussian RP, $\alpha[k]$, is expressed as:

$$\alpha[k] = c_0 + \sum_{i=1}^{p} c_i \alpha[k-i] + w[k], \tag{B.1}$$

where c_i for $i = 0, \ldots, p$ are constant coefficients of the AR model with order p, i.e., AR(p), and c_0 specifies the bias level. To characterize the AR(p) model, we need to determine $p+2$ unknown parameters that are: $c_0, c_1, \ldots, c_p, \sigma_w^2$, and σ_w^2 is the variance of white noise RP, w. These parameters can be obtained by matching the generated random process to the moments and the correlation lag between the samples [214]. Here, we use the moments obtained through experimental measurements. Hence, a first-order AR model is sufficient to be considered as a method for generating the correlated Gaussian RP as the mean and variance of the produced samples match the measurement results. The kth sample of the AR(1) model is given as:

$$\alpha[k] = c_0 + c_1 \alpha[k-1] + w[k]. \tag{B.2}$$

To guarantee the RP of α is wide-sense stationary, the condition $|c_1| < 1$ should be fulfilled. The mean, variance and autocorrelation function of AR(1) are given respectively as [215]:

$$\mu_\alpha = \frac{c_0}{1 - c_1}, \qquad \sigma_\alpha^2 = \frac{\sigma_w^2}{1 - c_1^2}, \qquad \mathcal{R}_\alpha(k) = c_1^k.$$

Note that $\mathcal{R}_\alpha(\frac{T_{c,\alpha}}{T_s}) = 0.05$ where $T_{c,\alpha}$ is the coherence time of α and T_s is the sampling time [28]. Using the above equations:

$$c_0 = (1 - c_1)\mu_\alpha, \qquad \sigma_w^2 = (1 - c_1^2)\sigma_\alpha^2, \qquad c_1 = 0.05^{\frac{T_s}{T_{c,\alpha}}}. \tag{B.3}$$

Then, the kth time sample of the correlated Gaussian RP, α, can be obtained based on (B.2) and using the parameters of the AR(1) model given in (B.3). The same method can be applied to both β and γ to determine the kth time sample of the device orientation, $\mathbf{\Theta}_n[k] = (\alpha_n[k], \beta_n[k], \gamma_n[k])$. According to the approach explained above, the ORWP is described in **Algorithm** 2.

Appendix C

Performance of the Proposed MLP and CNN Models versus the Benchmark KNN Technique.

This appendix presents the average error and the precision of the position, yaw angle α, pitch angle β, and roll angle γ, achieved by the proposed CNN and MLP models, along with the benchmark KNN model. the results of the CNN, MLP and KNN models are depicted in Table C.1, C.2, and C.3, respectively.

Table C.1: Performance of the proposed CNN model.

			$N = 10^5$	$N = 10^6$
Position	Average Error [cm]	LOS	**21.83**	**16.49**
		LOS + NLOS	**14.55**	**10.53**
	Precision [cm]	LOS	**38.7**	**29.8**
		LOS + NLOS	**23.9**	**17.15**
Yaw angle α	Average Error [Deg]	LOS	**15.15**	**11.9**
		LOS + NLOS	**12.28**	**9.07**
	Precision [Deg]	LOS	**25**	**16.9**
		LOS + NLOS	**18.5**	**12.5**
Pitch angle β	Average Error [Deg]	LOS	**1.55**	**1.42**
		LOS + NLOS	**1.35**	**0.96**
& roll angle γ	Precision [Deg]	LOS	**3.47**	**3.19**
		LOS + NLOS	**2.96**	**2.135**

Table C.2: Performance comparison of the proposed MLP model.

			$N = 10^5$	$N = 10^6$
Position	Average Error [cm]	LOS	29.73	21.93
		LOS + NLOS	15.05	13.04
	Precision [cm]	LOS	49.9	37.8
		LOS + NLOS	25.1	21.4
Yaw angle α	Average Error [Deg]	LOS	16.40	11.68
		LOS + NLOS	12.56	10.09
	Precision [Deg]	LOS	25.5	16.67
		LOS + NLOS	18.9	15.5
Pitch angle β	Average Error [Deg]	LOS	1.61	1.5
		LOS + NLOS	1.40	0.98
& roll angle γ	Precision [Deg]	LOS	3.57	3.4
		LOS + NLOS	3.09	2.17

Table C.3: Performance comparison of the proposed KNN technique.

			$N = 10^5$	$N = 10^6$
Position	Average Error [cm]	LOS	34.71	22.16
		LOS + NLOS	27.30	17.34
	Precision [cm]	LOS	61.7	40
		LOS + NLOS	46.5	29.5
Yaw angle α	Average Error [Deg]	LOS	19.05	13.30
		LOS + NLOS	21.37	14.49
	Precision [Deg]	LOS	36.1	17.2
		LOS + NLOS	55	17.7
Pitch angle β	Average Error [Deg]	LOS	1.88	1.7
		LOS + NLOS	1.88	1.8
& roll angle γ	Precision [Deg]	LOS	4.1	3.86
		LOS + NLOS	4.07	3.925

Appendix D

Performance of the Proposed LSTM Model versus the Benchmark CNN Model

This appendix presents the average error of the position, yaw angle α, pitch angle β, and roll angle γ, achieved by the proposed LSTM models, along with the benchmark CNN model for different values of posterior time slot index L. The cases when $L = 1$ and 2 are presented in Table D.1, whereas the cases when $L = 3$ and 4 are prsented in Table D.2.

Table D.1: Average prediction error of the position and the orientation angles yaw α, pitch β, and roll γ.

	$L = 1$		$L = 2$	
	LSTM	CNN	LSTM	CNN
Position	0.1789 m	0.4742 m	0.2136 m	0.5192 m m
Yaw angle α	22.4266°	32.6992°	22.8108°	32.4743°
Pitch angle β	2.5974°	2.6003°	2.6013°	2.6068°
Roll angle γ	4.3254°	4.3262°	4.3212°	4.3338°

Table D.2: Average prediction error of the position and the orientation angles yaw α, pitch β, and roll γ.

	$L = 3$		$L = 4$	
	LSTM	CNN	LSTM	CNN
Position	0.2565 m	0.5750 m	0.3046 m	0.6385 m
Yaw angle α	22.8551°	32.5409°	22.4539°	32.4700°
Pitch angle β	2.5983°	2.5991°	2.6003°	2.6063°
Roll angle γ	4.3314°	4.3401°	4.3405°	4.3381°

Appendix E

Proofs and Derivations for Chapter 7

E.1   Proof of Theorem 7.1

Considering the constraints (7.19c) and (7.19e), and by substituting R_{a} and R_{b} with their expressions into (7.19c) and (7.19e), and then solving the resulting inequality, we obtain $\alpha_1 \leq \alpha_{\max}$ and $\alpha_2 \leq \alpha_{\max}$. Now, considering the constraints (7.19d) and (7.19f), and by substituting $R_{\mathrm{a} \to \mathrm{w}}$ and $R_{\mathrm{b} \to \mathrm{w}}$ with their expressions into (7.19d) and (7.19f), and then solving the resulting inequality, we obtain $\alpha_{\min} \leq \alpha_1$ and $\alpha_{\min} \leq \alpha_2$. Based on this, constraints (7.19b)-(7.19f) are satisfied if and only if $\alpha_{\min} \leq \alpha_{\max}$, which constitutes the first feasibility condition of problem $\mathcal{P}_1$. Finally, we focus on constraint (7.19g). By substituting $R_{\mathrm{w} \to \mathrm{w}}^{\mathrm{VL}}$ with its expression into constraint (7.19g), and solving the resulting inequality, we obtain the inequality $g\left(\alpha_1, \alpha_2\right) \geq 0$. Obviously, the last inequality is feasible if and only if it is satisfied by the highest values of α_1 and α_2, i.e., $\alpha_1 = \alpha_{\max}$ and $\alpha_2 = \alpha_{\max}$, which constitutes the second and last feasibility condition of problem $\mathcal{P}_1$.

E.2   Line Search Method for the Sum Data Rate Maximization

We assume that the power allocation coefficient α_1 is fixed and we consider the change of variable $\beta = \sqrt{\alpha_2}$. Hence, solving the inequality $g\left(\alpha_1, \alpha_2\right) \geq 0$ is equivalent to solving the inequality $c_1 \beta^2 + c_2 \beta + c_3 \geq 0$ over the segment $\left[\sqrt{\alpha_{\min}}, \sqrt{\alpha_{\max}}\right]$, where $c_1 = c\left(1 + t_{\mathrm{v}}\right) \tilde{h}_{2,\mathrm{w}}^2$, $c_2 = c \tilde{h}_{1,\mathrm{w}} \tilde{h}_{2,\mathrm{w}} \sqrt{\alpha_1}$, and $c_3 = c\left(1 + t_{\mathrm{v}}\right) \tilde{h}_{1,\mathrm{w}}^2 \alpha_1 - t\left(c \tilde{h}_{1,\mathrm{w}}^2 + c \tilde{h}_{2,\mathrm{w}}^2 + \frac{1}{\gamma_{\mathrm{RX}}}\right)$. We compute the discriminant $\Delta = c_2^2 - 4 c_1 c_2$. If $\Delta \leq 0$, and since $c_1 \geq 0$, then the lowest value of α_2 that satisfies $g\left(\alpha_1, \alpha_2\right) \geq 0$ is $\alpha_{\min}$. Otherwise, we compute the ordered roots

$\beta_1 = \min\left(\frac{-c_2-\sqrt{\Delta}}{2c_1}, \frac{-c_2+\sqrt{\Delta}}{2c_1}\right)$ and $\beta_2 = \max\left(\frac{-c_2-\sqrt{\Delta}}{2c_1}, \frac{-c_2+\sqrt{\Delta}}{2c_1}\right)$. In this case, the lowest value of α_2 that satisfies $g(\alpha_1, \alpha_2) \geq 0$ is $\alpha_{\min}$, except the two following two cases. The first case is when $\beta_1 \leq \sqrt{\alpha_{\min}}$ and $\sqrt{\alpha_{\max}} \leq \beta_2$. In this case, there is no feasible solution for α_2 and the associated achievable sum data rate is zero. The second case if when $\beta_1 \leq \sqrt{\alpha_{\min}}$ and $\sqrt{\alpha_{\min}} \leq \beta_2 \leq \sqrt{\alpha_{\max}}$. In this case, the lowest value of α_2 that satisfies $g(\alpha_1, \alpha_2) \geq 0$ is β_2^2.

Bibliography

[1] W. Saad, M. Bennis, and M. Chen, "A vision of 6G wireless systems: Applications, trends, technologies, and open research problems," *IEEE network*, vol. 34, no. 3, pp. 134–142, Oct. 2019.

[2] Z. Zhang, Y. Xiao, Z. Ma, M. Xiao, Z. Ding, X. Lei, G. K. Karagiannidis, and P. Fan, "6G wireless networks: Vision, requirements, architecture, and key technologies," *IEEE Vehicular Tech. Mag.*, vol. 14, no. 3, pp. 28–41, Sep. 2019.

[3] M. Kamel, W. Hamouda, and A. Youssef, "Ultra-dense networks: A survey," *IEEE Communications Surveys & Tutorials*, vol. 18, no. 4, pp. 2522–2545, 2016.

[4] A. F. Molisch, V. V. Ratnam, S. Han, Z. Li, S. L. H. Nguyen, L. Li, and K. Haneda, "Hybrid beamforming for massive mimo: A survey," *IEEE Communications magazine*, vol. 55, no. 9, pp. 134–141, 2017.

[5] S. Elhoushy, M. Ibrahim, and W. Hamouda, "Cell-free massive mimo: A survey," *IEEE Communications Surveys & Tutorials*, 2021.

[6] Q. Wu and R. Zhang, "Towards smart and reconfigurable environment: Intelligent reflecting surface aided wireless network," *IEEE Communications Magazine*, vol. 58, no. 1, pp. 106–112, 2019.

[7] Y. Liu, X. Liu, X. Mu, T. Hou, J. Xu, M. Di Renzo, and N. Al-Dhahir, "Reconfigurable intelligent surfaces: Principles and opportunities," *IEEE Communications Surveys & Tutorials*, vol. 23, no. 3, pp. 1546–1577, 2021.

[8] C. Huang, S. Hu, G. C. Alexandropoulos, A. Zappone, C. Yuen, R. Zhang, M. Di Renzo, and M. Debbah, "Holographic mimo surfaces for 6g wireless networks: Opportunities, challenges, and trends," *IEEE Wireless Communications*, vol. 27, no. 5, pp. 118–125, 2020.

[9] L. Dai, B. Wang, Z. Ding, Z. Wang, S. Chen, and L. Hanzo, "A survey of non-orthogonal multiple access for 5g," *IEEE communications surveys & tutorials*, vol. 20, no. 3, pp. 2294–2323, 2018.

[10] Z. Lin, M. Lin, T. De Cola, J.-B. Wang, W.-P. Zhu, and J. Cheng, "Supporting iot with rate-splitting multiple access in satellite and aerial-integrated networks," *IEEE Internet of Things Journal*, vol. 8, no. 14, pp. 11 123–11 134, 2021.

[11] X. Wang, L. Kong, F. Kong, F. Qiu, M. Xia, S. Arnon, and G. Chen, "Millimeter wave communication: A comprehensive survey," *IEEE Communications Surveys & Tutorials*, vol. 20, no. 3, pp. 1616–1653, 2018.

[12] S. Ghafoor, N. Boujnah, M. H. Rehmani, and A. Davy, "Mac protocols for tera-hertz communication: A comprehensive survey," *IEEE Communications Surveys & Tutorials*, vol. 22, no. 4, pp. 2236–2282, 2020.

[13] M. A. Khalighi and M. Uysal, "Survey on free space optical communication: A communication theory perspective," *IEEE communications surveys & tutorials*, vol. 16, no. 4, pp. 2231–2258, 2014.

[14] S. Arai, M. Kinoshita, and T. Yamazato, "Optical wireless communication: A candidate 6g technology?" *IEICE Transactions on Fundamentals of Electronics, Communications and Computer Sciences*, vol. 104, no. 1, pp. 227–234, 2021.

[15] P. H. Pathak, X. Feng, P. Hu, and P. Mohapatra, "Visible light communication, networking, and sensing: A survey, potential and challenges," *IEEE communications surveys & tutorials*, vol. 17, no. 4, pp. 2047–2077, 2015.

[16] H. aas, L. Yin, Y. Wang, and C. Chen, "What is LiFi?" *Journal of lightwave tech.*, vol. 34, no. 6, pp. 1533–1544, Mar. 2015.

[17] K. David and H. Berndt, "6G vision and requirements: Is there any need for beyond 5G?" *IEEE Vehicular Tech. Mag.*, vol. 13, no. 3, pp. 72–80, Jul. 2018.

[18] I. Tavakkolnia, C. Chen, R. Bian, and H. Haas, "Energy-efficient adaptive MIMO-VLC technique for indoor LiFi applications," in *Proc. IEEE ICT*, St. Malo, France, Jun. 2018, pp. 331–335.

[19] M. Obeed, A. M. Salhab, M.-S. Alouini, and S. A. Zummo, "Survey on physical layer security in optical wireless communication systems," in *2018 Seventh International Conference on Communications and Networking (ComNet)*. IEEE, 2018, pp. 1–5.

[20] C. Medina, M. Zambrano, and K. Navarro, "Led based visible light communication: Technology, applications and challenges-a survey," *International Journal of Advances in Engineering & Technology*, vol. 8, no. 4, p. 482, 2015.

[21] T. Yamazato, I. Takai, H. Okada, T. Fujii, T. Yendo, S. Arai, M. Andoh, T. Harada, K. Yasutomi, K. Kagawa *et al.*, "Image-sensor-based visible light communication for automotive applications," *IEEE Communications Magazine*, vol. 52, no. 7, pp. 88–97, 2014.

[22] R. Perez-Jimenez, J. Rufo, C. Quintana, J. Rabadan, and F. Lopez-Hernandez, "Visible light communication systems for passenger in-flight data networking," in *2011 IEEE International Conference on Consumer Electronics (ICCE)*. IEEE, 2011, pp. 445–446.

[23] M. Sui, Z. Xia, W. Zhu, J. Shen, and J. Chen, "A visible light communication based aircraft cabin wireless network demo system," in *Asia Communications and Photonics Conference*. Optica Publishing Group, 2015, pp. AM1E–1.

[24] H. Kaushal and G. Kaddoum, "Underwater optical wireless communication," *IEEE access*, vol. 4, pp. 1518–1547, 2016.

[25] X. Huang, J. A. Zhang, R. P. Liu, Y. J. Guo, and L. Hanzo, "Airplane-aided integrated networking for 6g wireless: Will it work?" *IEEE Vehicular Technology Magazine*, vol. 14, no. 3, pp. 84–91, 2019.

[26] S. K. Rao, "Advanced antenna technologies for satellite communications payloads," *IEEE Transactions on Antennas and Propagation*, vol. 63, no. 4, pp. 1205–1217, 2015.

[27] A. Al-Kinani, C.-X. Wang, L. Zhou, and W. Zhang, "Optical wireless communication channel measurements and models," *IEEE Communications Surveys & Tutorials*, vol. 20, no. 3, pp. 1939–1962, 2018.

[28] M. D. Soltani, A. A. Purwita, Z. Zeng, H. Haas, and M. Safari, "Modeling the Random Orientation of Mobile Devices: Measurement, Analysis and LiFi Use Case," *IEEE Trans. Commun.*, vol. 67, no. 3, pp. 2157–2172, 2019.

[29] Y. Zhuang, L. Hua, L. Qi, J. Yang, P. Cao, Y. Cao, Y. Wu, J. Thompson, and H. Haas, "A survey of positioning systems using visible led lights," *IEEE Communications Surveys & Tutorials*, vol. 20, no. 3, pp. 1963–1988, 2018.

[30] Qualcomm, "Lumicast lights the way to a more personal retail experience," [Online]. Available: https://www.qualcomm.com/news/onq/2017/03/20/lumicast-lights-way-more-personal-retail-experience, Jun. 2018.

[31] M. Obeed, A. M. Salhab, M.-S. Alouini, and S. A. Zummo, "On optimizing vlc networks for downlink multi-user transmission: A survey," *IEEE Communications Surveys & Tutorials*, vol. 21, no. 3, pp. 2947–2976, 2019.

[32] M. A. Arfaoui, M. D. Soltani, I. Tavakkolnia, A. Ghrayeb, M. Safari, C. Assi, and H. Haas, "Physical layer security for visible light communication systems: A survey," *IEEE Commun. Surveys & Tutorials*, vol. 22, no. 3, pp. 887 – 1908, Apr. 2020.

[33] M. A. Arfaoui, M. D. Soltani, I. Tavakkolnia, A. Ghrayeb, C. Assi, H. Haas, and M. Safari, "SNR Statistics for Indoor VLC Mobile Users with Random Orientation," in *Proc. IEEE ICC*, Shanghai, China, May. 2019.

[34] M. A. Arfaoui, M. D. Soltani, I. Tavakkolnia, A. Ghrayeb, C. Assi, M. Safari, and H. Haas, "Measurements-based channel models for indoor LiFi systems," *IEEE Trans. Wireless Commun.*, vol. 20, no. 2, pp. 827 – 842, Oct. 2020.

[35] I. Tavakkolnia, M. D. Soltani, M. A. Arfaoui, , A. Ghrayeb, C. Assi, M. Safari, and H. Haas, "MIMO System with Multi-directional Receiver in Optical Wireless Communications," in *Proc. IEEE ICC*, Shanghai, China, May. 2019.

[36] M. D. Soltani, M. A. Arfaoui, I. Tavakkolnia, A. Ghrayeb, M. Safari, C. M. Assi, M. O. Hasna, and H. Haas, "Bidirectional Optical Spatial Modulation for Mobile Users: Towards a Practical Design for LiFi Systems," *IEEE JSAC SI Spatial Modulation in Emerging Wireless Systems*, vol. 37, no. 9, pp. 2069 – 2086, Aug. 2019.

[37] M. A. Arfaoui, M. D. Soltani, I. Tavakkolnia, A. Ghrayeb, C. M. Assi, M. Safari, and H. Haas, "Invoking deep learning for joint estimation of indoor LiFi user position and orientation," *IEEE Journal on Selected Areas in Communications*, vol. 39, no. 9, pp. 2890–2905, Mar. 2021.

[38] M. A. Arfaoui, A. Ghrayeb, and C. Assi, "Cascaded Artificial Neural Networks for Proactive Power Allocation in Indoor LiFi Systems," in *Proc. IEEE ICC*, Montreal, QC, Canada, Jun. 2021.

[39] M. A. Arfaoui, A. Ghrayeb, and C. Assi, "Deep learning based proactive optimization for indoor lifi systems with channel aging," *IEEE Trans. on Wireless Commun.*, Apr. 2021, *submitted*.

[40] M. A. Arfaoui, A. Ghrayeb, C. Assi, and M. Qaraqe, "CoMP-Assisted NOMA and Cooperative NOMA in Indoor VLC Cellular Systems," *IEEE Trans. on Commun.*, July. 2022 (*Early Access*).

[41] H. Elgala, R. Mesleh, and H. Haas, "Predistortion in optical wireless transmission using ofdm," in *2009 Ninth International Conference on Hybrid Intelligent Systems*, Shenyang, China, Aug. 2009.

[42] T. Fath and H. Haas, "Performance comparison of MIMO techniques for optical wireless communications in indoor environments," *IEEE Trans. Commun.*, vol. 61, no. 2, pp. 733–742, Feb. 2013.

[43] J. M. Kahn and J. R. Barry, "Wireless infrared communications," *Proc. IEEE*, vol. 85, no. 2, pp. 265–298, Feb. 1997.

[44] H. Schulze, "Frequency-Domain Simulation of the Indoor Wireless Optical Communication Channel," *IEEE Trans. Commun.*, vol. 64, no. 6, pp. 2551–2562, Jun. 2016.

[45] M. D. Soltani, H. Kazemi, M. Safari, and H. Haas, "Handover Modeling for Indoor Li-Fi Cellular Networks: The Effects of Receiver Mobility and Rotation," in *Proc. IEEE WCNC*, San Fransisco, USA, Mar. 2017.

[46] Vieyra Software. Physics toolbox sensor suite. [Online]. Available: https://play.google.com/store/apps/details?id=com.chrystianvieyra.physicstoolboxsuite

[47] Z. Zeng, M. D. Soltani, H. Haas, and M. Safari, "Orientation Model of Mobile Device for Indoor VLC and Millimetre Wave Systems," in *IEEE 88nd Veh. Technol. Conf. (VTC2018-Fall)*, Chicago, USA, August 2018.

[48] A. A. Purwita, M. D. Soltani, M. Safari, and H. Haas, "Impact of terminal orientation on performance in LiFi systems," in *Proc. IEEE WCNC*, Barcelona, Spain, Apr. 2018.

[49] S. Kotz, T. Kozubowski, and K. Podgorski, *The Laplace Distribution and Generalizations: a Revisit with Applications to Communications, Economics, Engineering, and Finance.* Springer Science & Business Media, 2012.

[50] R. Murray Spiegel, *Theory and Problems of Statistics in SI Units.* McGraw-Hill International Book Company; Singapore, 1972.

[51] F. J. Massey Jr, "The kolmogorov-smirnov test for goodness of fit," *Journal of the American statistical Association*, vol. 46, no. 253, pp. 68–78, 1951.

[52] L. Yin, W. O. Popoola, X. Wu, and H. Haas, "Performance evaluation of non-orthogonal multiple access in visible light communication," *IEEE Trans. on Commun.*, vol. 64, no. 12, pp. 5162–5175, Sep. 2016.

[53] A. Gupta, N. Sharma, P. Garg, and M.-S. Alouini, "Cascaded FSO-VLC communication system," *IEEE Wireless Commun. Letters*, vol. 6, no. 6, pp. 810–813, Aug. 2017.

[54] S. Cho, G. Chen, and J. P. Coon, "Physical layer security in visible light communication systems with randomly located colluding eavesdroppers," *IEEE Wireless Commun. Letters*, vol. 7, no. 5, pp. 768 – 771, Oct. 2018.

[55] Y. Yapici and I. Guvenc, "Non-orthogonal multiple access for mobile vlc networks with random receiver orientation," in *Proc. IEEE Globecom*, Waikoloa, HI, USA, USA, Dec. 2019.

[56] K. Govindan, K. Zeng, and P. Mohapatra, "Probability density of the received power in mobile networks," *IEEE Trans. Wireless Commun.*, vol. 10, no. 11, pp. 3613–3619, Dec. 2011.

[57] V. A. Aalo, C. Mukasa, and G. P. Efthymoglou, "Effect of mobility on the outage and BER performances of digital transmissions over Nakagami-m fading channels," *IEEE Trans. Vehicular Tech.*, vol. 65, no. 4, pp. 2715–2721, Apr. 2016.

[58] A. Gupta and P. Garg, "Statistics of SNR for an indoor VLC system and its applications in system performance," *IEEE Commun. Letters*, vol. 22, no. 9, pp. 1898 – 1901, Jul. 2018.

[59] M. D. Soltani, X. Wu, M. Safari, and H. Haas, "Access point selection in li-fi cellular networks with arbitrary receiver orientation," in *Proc. IEEE ICC*, Valencia, Spain, 2016.

[60] A. A. Purwita, M. D. Soltani, M. Safari, and H. Haas, "Handover Probability of Hybrid LiFi/RF-Based Networks with Randomly-Oriented Devices," in *Proc. IEEE VTC*, Porto, Portugal, Jun Jun. 2018.

[61] J.-Y. Wang, Q.-L. Li, J.-X. Zhu, and Y. Wang, "Impact of receiver's tilted angle on channel capacity in VLCs," *Electronics Letters*, vol. 53, no. 6, pp. 421–423, Mar. 2017.

[62] J.-Y. Wang, J.-B. Wang, B. Zhu, M. Lin, Y. Wu, Y. Wang, and M. Chen, "Improvement of BER performance by tilting receiver plane for indoor visible light communications with input-dependent noise," in *Proc. IEEE ICC*, Paris, France, May 2017.

[63] Z. Wang, C. Yu, W.-D. Zhong, and J. Chen, "Performance improvement by tilting receiver plane in M-QAM OFDM visible light communications," *Optics express*, vol. 19, no. 14, pp. 13 418–13 427, Jun. 2011.

[64] A. A. Matrawy, M. A. El-Shimy, M. R. Rizk, and Z. A. El-Sahn, "Optimum angle diversity receivers for indoor single user MIMO visible light communication systems," in *Proc. Asia Communications and Photonics Conference.* Wuhan, China: Optical Society of America, 2016.

[65] Y. S. Eroğlu, Y. Yapıcı, and I. Güvenç, "Impact of random receiver orientation on visible light communications channel," *IEEE Transactions on Commun.*, vol. 67, no. 2, pp. 1313–1325, Nov. 2018.

[66] A. A. Purwita, M. D. Soltani, M. Safari, and H. Haas, "Impact of terminal orientation on performance in LiFi systems," in *Proc. IEEE WCNC*, Barcelona, Spain, Apr. 2018.

[67] Z. Zeng, M. D. Soltani, H. Haas, and M. Safari, "Orientation Model of Mobile Device for Indoor VLC and Millimetre Wave Systems," in *Proc. IEEE VTC*, Chicago, USA, Aug. 2018.

[68] M. D. Soltani, "Analysis of Random Orientation and User Mobility in LiFi Networks," *The University of Edinburgh*, 2019.

[69] M. D. Soltani, A. A. Purwita, I. Tavakkolnia, H. Haas, and M. Safari, "Impact of device orientation on error performance of LiFi systems," *IEEE Access*, vol. 7, pp. 41 690–41 701, Mar. 2019.

[70] L. Zeng, D. O'Brien, H. Le-Minh, K. Lee, D. Jung, and Y. Oh, "Improvement of data rate by using equalization in an indoor visible light communication system," in *Proc. IEEE ICCSC*, Shanghai, China, Jun. 2008.

[71] L. Zeng, D. C. O'Brien, H. Le Minh, G. E. Faulkner, K. Lee, D. Jung, Y. Oh, and E. T. Won, "High data rate multiple input multiple output (MIMO) optical wireless communications using white LED lighting," *IEEE J. Select. Areas in Commun.*, vol. 27, no. 9, pp. 1654 – 1662, Dec. 2009.

[72] M. A. Arfaoui, A. Ghrayeb, and C. Assi, "Secrecy rate closed-form expressions for the SISO VLC wiretap channel with discrete input signaling," *IEEE Commun. Letters*, vol. 22, no. 7, pp. 1382 – 1385, Apr. 2018.

[73] C. Chen, R. Bian, and H. Haas, "Omnidirectional transmitter and receiver design for wireless infrared uplink transmission in LiFi," in *Proc. IEEE ICC*, Kansas City, Missouri, USA, May 2018.

[74] C. Chen, W.-D. Zhong, H. Yang, S. Zhang, and P. Du, "Reduction of sinr fluctuation in indoor multi-cell vlc systems using optimized angle diversity receiver," *Journal of Lightwave Technology*, vol. 36, no. 17, pp. 3603–3610, 2018.

[75] C. Chen, D. Tsonev, and H. Haas, "Joint transmission in indoor visible light communication downlink cellular networks," in *2013 IEEE Globecom Workshops (GC Wkshps).* IEEE, 2013, pp. 1127–1132.

[76] H. Ma, L. Lampe, and S. Hranilovic, "Coordinated broadcasting for multiuser indoor visible light communication systems," *IEEE Transactions on Communications*, vol. 63, no. 9, pp. 3313–3324, 2015.

[77] T. V. Pham, H. Le Minh, and A. T. Pham, "Multi-cell vlc: Multi-user downlink capacity with coordinated precoding," in *2017 IEEE International Conference on Communications Workshops (ICC Workshops).* IEEE, 2017, pp. 469–474.

[78] H. Yang, C. Chen, W.-D. Zhong, and A. Alphones, "Joint precoder and equalizer design for multi-user multi-cell mimo vlc systems," *IEEE Transactions on Vehicular Technology*, vol. 67, no. 12, pp. 11 354–11 364, 2018.

[79] S. Tao, H. Yu, Q. Li, and Y. Tang, "Performance analysis of user association strategy based on power-domain non-orthogonal multiple access in visible light communication multi-cell networks," *EURASIP Journal on Wireless Communications and Networking*, vol. 2020, no. 1, pp. 1–13, 2020.

[80] M. W. Eltokhey, M. A. Khalighi, A. S. Ghazy, and S. Hranilovic, "Hybrid noma and zf pre-coding transmission for multi-cell vlc networks," *IEEE Open Journal of the Communications Society*, 2020.

[81] *IEEE 802.15.7: IEEE Standard for Local and Metropolitan Area Networks–Part 15.7: Short-Range Wireless Optical Communication Using Visible Light*, IEEE-SA Std., Sep. 2011.

[82] M. S. Mossaad, S. Hranilovic, and L. Lampe, "Visible light communications using OFDM and multiple LEDs," *IEEE Trans. Commun.*, vol. 63, no. 11, pp. 4304–4313, Nov. 2015.

[83] H. Chun, S. Rajbhandari, G. Faulkner *et al.*, "LED based wavelength division multiplexed 10 Gb/s visible light communications," *J. Lightw. Technol.*, vol. 34, no. 13, pp. 3047–3052, Jul. 2016.

[84] R. Mesleh, H. Haas, C. W. Ahn, and S. Yun, "Spatial modulation - a new low complexity spectral efficiency enhancing technique," in *2006 First Int. Conf. on Commun. and Netw. in China*, Beijing, China, Oct 2006, pp. 1–5.

[85] M. Di Renzo, H. Haas, A. Ghrayeb, S. Sugiura, and L. Hanzo, "Spatial modulation for generalized MIMO: Challenges, opportunities, and implementation," *Proc. IEEE*, vol. 102, no. 1, pp. 56–103, Jan. 2014.

[86] R. Mesleh, H. Elgala, and H. Haas, "Optical spatial modulation," *IEEE/OSA J. Opt. Commun. Netw.*, vol. 3, no. 3, pp. 234–244, 2011.

[87] J. Jeganathan, A. Ghrayeb, L. Szczecinski, and A. Ceron, "Space shift keying modulation for MIMO channels," *IEEE Trans. Wireless Commun.*, vol. 8, no. 7, pp. 3692–3703, Jul. 2009.

[88] R. Y. Mesleh, H. Haas, S. Sinanovic, C. W. Ahn, and S. Yun, "Spatial modulation," *IEEE Trans. Vehicular Tech.*, vol. 57, no. 4, pp. 2228–2241, Jul. 2008.

[89] J. Jeganathan, A. Ghrayeb, and L. Szczecinski, "Generalized space shift keying modulation for MIMO channels," in *Proc. IEEE PIMRC*, Cannes, France, Dec. 2008, pp. 1–5.

[90] W. O. Popoola and H. Haas, "Demonstration of the merit and limitation of generalised space shift keying for indoor visible light communications," *J. Lightw. Technol.*, vol. 32, no. 10, pp. 1960–1965, May 2014.

[91] M. D. Soltani, Z. Zeng, I. Tavakkolnia, H. Haas, and M. Safari, "Random Receiver Orientation Effect on Channel Gain in LiFi Systems," in *Proc. IEEE WCNC*, Marrakech, Morocco, April 2019, pp. 1–6.

[92] A. A. Purwita, M. D. Soltani, M. Safari, and H. Haas, "Handover probability of hybrid LiFi/RF-based networks with randomly-oriented devices," in *87nd Veh. Technol. Conf. (VTC2018-Spring)*, Porto, Portugal, June 2018.

[93] J. Y. Wang, J. B. Wang, B. Zhu, M. Lin, Y. Wu, Y. Wang, and M. Chen, "Improvement of BER performance by tilting receiver plane for indoor visible light communications with input-dependent noise," in *Proc. IEEE ICC*, Paris, France, May. 2017, pp. 1–6.

[94] M. D. Soltani, A. A. Purwita, I. Tavakkolnia, H. Haas, and M. Safari, "Impact of device orientation on error performance of LiFi systems," *IEEE Access*, vol. 7, pp. 41 690–41 701, Mar. 2019.

[95] C. Chen, M. D. Soltani, M. Safari, A. A. Purwita, X. Wu, and H. Haas, "An Omni-directional User Equipment Configuration to Support Mobility in LiFi Networks," in *Proc. IEEE ICC*, Shanghai, China, May. 2019.

[96] M. D. Soltani, X. Wu, M. Safari, and H. Haas, "Access Point Selection in Li-Fi Cellular Networks with Arbitrary Receiver Orientation," in *IEEE 27th Annual Int. Symp. on Personal, Indoor, and Mobile Radio Communications (PIMRC)*, Valencia, Spain, Sept 2016, pp. 1–6.

[97] S. Jivkova and M. Kavehrad, "Shadowing and blockage in indoor optical wireless communications," in *Proc. IEEE Globecom*, San Francisco, USA, Dec. 2003.

[98] L. Chevalier, S. Sahuguede, and A. Julien-Vergonjanne, "Performance evaluation of wireless optical communication for mobile body area network scenario with blocking effects," *IET Optoelectronics*, vol. 9, no. 5, pp. 211–217, Oct. 2015.

[99] V. Raghavan *et al.*, "Statistical blockage modeling and robustness of beamforming in millimeter wave systems," [Online]. Available: https://arxiv.org/abs/1801.03346, Jan. 2018.

[100] P. Yang, M. D. Renzo, Y. Xiao, S. Li, and L. Hanzo, "Design guidelines for spatial modulation," *IEEE Communications Surveys Tutorials*, vol. 17, no. 1, pp. 6–26, Firstquarter 2015.

[101] I. Tavakkolnia, A. Yesilkaya, and H. Haas, "OFDM-based spatial modulation for optical wireless communications," in *Proc. IEEE Globecom*, Abu Dahbi, UAE, Dec. 2018.

[102] R. Mesleh, M. D. Renzo, H. Haas, and P. M. Grant, "Trellis coded spatial modulation," *IEEE Trans. Wireless Commun.*, vol. 9, no. 7, pp. 2349–2361, Jul. 2010.

[103] A. Younis, S. Sinanovic, M. D. Renzo, R. Mesleh, and H. Haas, "Generalised sphere decoding for spatial modulation," *IEEE Trans. Commun.*, vol. 61, no. 7, pp. 2805–2815, Jul. 2013.

[104] E. Basar, U. Aygolu, E. Panayirci, and H. V. Poor, "Performance of spatial modulation in the presence of channel estimation errors," *IEEE Commun. Lett.*, vol. 16, no. 2, pp. 176–179, Feb. 2012.

[105] R. Rajashekar, K. Hari, and L. Hanzo, "Reduced-complexity ML detection and capacity-optimized training for spatial modulation systems," *IEEE Trans. Commun.*, vol. 62, no. 1, pp. 112–125, Jan. 2014.

[106] W. M. Gifford, M. Z. Win, and M. Chiani, "Diversity with practical channel estimation," *IEEE Trans. Wireless Commun.*, vol. 4, no. 4, pp. 1935–1947, Jul. 2005.

[107] A. Yassin *et. al.*, "Recent advances in indoor localization: A survey on theoretical approaches and applications," *IEEE Commun. Surveys & Tutorials*, vol. 19, no. 2, pp. 1327–1346, Nov. 2016.

[108] F. Yao, A. Keller, M. Ahmad, B. Ahmad, R. Harrison, and A. W. Colombo, "Optimizing the scheduling of autonomous guided vehicle in a manufacturing process," in *Proc. IEEE INDIN*, Porto, Portugal, Sep. 2018.

[109] C. Eppner, S. Höfer, R. Jonschkowski, R. Martín-Martín, A. Sieverling, V. Wall, and O. Brock, "Lessons from the amazon picking challenge: Four aspects of building robotic systems," in *Robotics: science and systems*, 2016.

[110] B. Zhou and Q. Chen, "On the particle-assisted stochastic search mechanism in wireless cooperative localization," *IEEE Trans. on Wireless Commun.*, vol. 15, no. 7, pp. 4765–4777, Mar. 2016.

[111] N. U. Hassan, A. Naeem, M. A. Pasha, T. Jadoon, and C. Yuen, "Indoor positioning using visible led lights: A survey," *ACM Computing Surveys*, vol. 48, no. 2, pp. 1–32, Sep. 2015.

[112] S.-H. Yang, H.-S. Kim, Y.-H. Son, and S.-K. Han, "Three-dimensional visible light indoor localization using AOA and RSS with multiple optical receivers," *Journal of Lightwave Technology*, vol. 32, no. 14, pp. 2480–2485, Jul. 2014.

[113] H. Sharifi, A. Kumar, F. Alam, and K. M. Arif, "Indoor localization of mobile robot with visible light communication," in *Proc. IEEE ASME International Conference on MESA*, Auckland, New Zealand, 2016.

[114] W. Zhang, M. S. Chowdhury, and M. Kavehrad, "Asynchronous indoor positioning system based on visible light communications," *Optical Engineering*, vol. 53, no. 4, pp. 045 105–1–045 105–9, Apr. 2014.

[115] Z. Zhou, M. Kavehrad, and P. Deng, "Indoor positioning algorithm using light-emitting diode visible light communications," *Optical engineering*, vol. 51, no. 8, p. 085009, Aug. 2012.

[116] L. Yin *et. al.*, "Indoor visible light positioning with angle diversity transmitter," in *Proc. IEEE VTC*, Boston, USA, Sep. 2015.

[117] K. Qiu, F. Zhang, and M. Liu, "Visible light communication-based indoor localization using Gaussian process," in *2015 IEEE IROS*, Hamburg, Germany, Dec. 2015.

[118] B. Zhou, A. Liu, and V. Lau, "Joint user location and orientation estimation for visible light communication systems with unknown power emission," *IEEE Trans. on Wireless Commun.*, vol. 18, no. 11, pp. 5181–5195, Aug. 2019.

[119] B. Zhou, Y. Zhuang, and Y. Cao, "On the Performance Gain of Harnessing Non-Line-Of-Sight Propagation for Visible Light-Based Positioning," *IEEE Trans. on Wireless Commun.*, 2020.

[120] T. Wang, C.-K. Wen, H. Wang, F. Gao, T. Jiang, and S. Jin, "Deep learning for wireless physical layer: Opportunities and challenges," *China Commun.*, vol. 14, no. 11, pp. 92–111, Dec. 2017.

[121] G. Zhu, D. Liu, Y. Du, C. You, J. Zhang, and K. Huang, "Toward an intelligent edge: wireless communication meets machine learning," *IEEE Commun. Magazine*, vol. 58, no. 1, pp. 19–25, Jan. 2020.

[122] Y. Sun, M. Peng, Y. Zhou, Y. Huang, and S. Mao, "Application of machine learning in wireless networks: Key techniques and open issues," *IEEE Commun. Surveys & Tutorials*, vol. 21, no. 4, pp. 3072–3108, Jun. 2019.

[123] H. Q. Tran and C. Ha, "High Precision Weighted Optimum K-Nearest Neighbors Algorithm for Indoor Visible Light Positioning Applications," *IEEE Access*, vol. 8, pp. 114 597–114 607, Jun. 2020.

[124] Y. Chen, W. Guan, J. Li, and H. Song, "Indoor real-time 3-D visible light positioning system using fingerprinting and extreme learning machine," *IEEE Access*, vol. 8, pp. 13 875–13 886, Dec. 2019.

[125] A. Zappone, M. Di Renzo, and M. Debbah, "Wireless networks design in the era of deep learning: Model-based, AI-based, or both?" *IEEE Trans. Commun.*, vol. 67, no. 10, pp. 7331–7376, Jun. 2019.

[126] Z. Qin, H. Ye, G. Y. Li, and B.-H. F. Juang, "Deep learning in physical layer communications," *IEEE Wireless Commun.*, vol. 26, no. 2, pp. 93–99, Mar. 2019.

[127] H. Ye, G. Y. Li, and B.-H. F. Juang, "Deep reinforcement learning based resource allocation for V2V communications," *IEEE Trans. on Vehicular Tech.*, vol. 68, no. 4, pp. 3163–3173, Feb. 2019.

[128] F. Tang, B. Mao, Z. M. Fadlullah, and N. Kato, "On a novel deep-learning-based intelligent partially overlapping channel assignment in SDN-IoT," *IEEE Commun. Magazine*, vol. 56, no. 9, pp. 80–86, Sep. 2018.

[129] F. Tang, B. Mao, Z. M. Fadlullah, N. Kato, O. Akashi, T. Inoue, and K. Mizutani, "On removing routing protocol from future wireless networks: A real-time deep learning approach for intelligent traffic control," *IEEE Wireless Commun.*, vol. 25, no. 1, pp. 154–160, Oct. 2017.

[130] S. e. t. Ali, "6g white paper on machine learning in wireless communication networks," [Online]. Available: https://arxiv.org/abs/2004.13875, Apr. 2020.

[131] S. Sonoda and N. Murata, "Neural network with unbounded activation functions is universal approximator," *Applied and Computational Harmonic Analysis*, vol. 43, no. 2, pp. 233–268, Spr. 2017.

[132] P. Grover, "Five regression loss functions all machine learners should know,"," [Online]. Available: https://heartbeat.fritz.ai/5-regression-loss-functions-all-machine-learners-should-know-4fb140e9d4b0, Jun. 2018.

[133] S. Ruder, "An overview of gradient descent optimization algorithms," *arXiv preprint*, Jun. 2017.

[134] N. Srivastava, G. Hinton, A. Krizhevsky, I. Sutskever, and R. Salakhutdinov, "Dropout: a simple way to prevent neural networks from overfitting," *The journal of machine learning research*, vol. 15, no. 1, pp. 1929–1958, Jan. 2014.

[135] K. Team, "Keras: Deep Learning for humans," [Online]. Available: https://github.com/keras-team/keras, 2017.

[136] H. Inoue, "Multi-sample dropout for accelerated training and better generalization," [Online]. Available: https://arxiv.org/abs/1905.09788, Oct. 2020.

[137] T. V. Pham and A. T. Pham, "Energy efficient artificial noise-aided precoding designs for secured visible light communication systems," *IEEE Trans. Wireless Commun.*, vol. 20, no. 1, Oct. 2020.

[138] L. Zhao, K. Cai, and M. Jiang, "Multiuser precoded mimo visible light communication systems enabling spatial dimming," *Journal of Lightwave Techn.*, vol. 38, no. 20, pp. 5624–5634, Jun. 2020.

[139] M. A. Arfaoui, A. Ghrayeb, and C. M. Assi, "Secrecy performance of the MIMO VLC wiretap channel with randomly located eavesdropper," *IEEE Trans. Wireless Commun.*, vol. 19, no. 1, pp. 265–278, Oct. 2019.

[140] M. A. Arfaoui, H. Zaid, Z. Rezki, A. Ghrayeb, A. Chaaban, and M.-S. Alouini, "Artificial noise-based beamforming for the MISO VLC wiretap channel," *IEEE Trans. Commun.*, vol. 67, no. 4, pp. 2866–2879, Dec. 2018.

[141] A. K. Papazafeiropoulos, "Impact of general channel aging conditions on the downlink performance of massive MIMO," *IEEE Trans. on Vehicular Tech.*, vol. 66, no. 2, pp. 1428–1442, May. 2016.

[142] J. Yuan, H. Q. Ngo, and M. Matthaiou, "Machine learning-based channel prediction in massive MIMO with channel aging," *IEEE Trans. Wireless Commun.*, vol. 19, no. 5, pp. 2960–2973, Feb. 2020.

[143] G. Shen, J. Kurths, and Y. Yuan, "Sequence-to-sequence prediction of spatiotemporal systems," *Chaos: An Interdisciplinary Journal of Nonlinear Science*, vol. 30, no. 2, pp. 1–10, Feb. 2020.

[144] Y. Hua *et. al.*, "Deep learning with long short-term memory for time series prediction," *IEEE Commun. Mag.*, vol. 57, no. 6, pp. 114–119, Mar. 2019.

[145] M. Sundermeyer *et. al.*, "LSTM neural networks for language modeling," in *Proc. INTERSPEECH*, Portland, OR, USA, Sep. 2012.

[146] A. Mostafa and L. Lampe, "Physical-layer security for MISO visible light communication channels," *IEEE J. on Selected Areas in Commun.*, vol. 33, no. 9, pp. 1806–1818, May. 2015.

[147] A. Lapidoth, S. M. Moser, and M. A. Wigger, "On the capacity of free-space optical intensity channels," *IEEE Trans. Inform. Theory*, vol. 55, no. 10, pp. 4449–4461, Sep. 2009.

[148] A. Chaaban, Z. Rezki, and M.-S. Alouini, "On the capacity of the intensity-modulation direct-detection optical broadcast channel," *IEEE Trans. Wireless Commun.*, vol. 15, no. 5, pp. 3114–3130, Jan. 2016.

[149] J. Zhou and W. Zhang, "Bounds on the capacity region of the optical intensity multiple access channel," *IEEE Transactions on Communications*, vol. 67, no. 11, pp. 7629–7641, 2019.

[150] T. Lipp and S. Boyd, "Variations and extension of the convex–concave procedure," *Optimization and Engineering*, vol. 17, no. 2, pp. 263–287, Nov. 2015.

[151] M. Grant, S. Boyd, and Y. Ye, "Cvx: Matlab software for disciplined convex programming," *Web page and software available at http://cvxr.com/cvx/*, Dec. 2017.

[152] J. Lofberg, "Yalmip: A toolbox for modeling and optimization in matlab," in *Proc IEEE ICRA*, New Orleans, LA, USA, Sep. 2004.

[153] S. Ebbesen *et. al.*, "A generic particle swarm optimization matlab function," in *Proc. IEEE ACC*, Montréal, Quebec, Canada, Oct. 2012.

[154] P. Hũu *et al.*, "A low-complexity framework for joint user pairing and power control for cooperative NOMA in 5G and beyond cellular networks," *IEEE Trans. on Commun.*, vol. 68, no. 11, pp. 6737–6749, Jul. 2020.

[155] M. Elhattab, M. A. Arfaoui, and C. Assi, "Power allocation in comp-empowered c-noma networks," *IEEE Networking Letters*, vol. 3, no. 1, pp. 10–14, 2020.

[156] M. Elhattab, M. A. Arfaoui, C. Assi, and A. Ghrayeb, "Ris-assisted joint transmission in a two-cell downlink noma cellular system," *IEEE Journal on Selected Areas in Communications*, 2022.

[157] M. Elhattab, M. A. Arfaoui, and C. Assi, "Joint clustering and power allocation in coordinated multipoint assisted c-noma cellular networks," *IEEE Transactions on Communications*, 2022.

[158] V. K. Papanikolaou, P. D. Diamantoulakis, P. C. Sofotasios, S. Muhaidat, and G. K. Karagiannidis, "On optimal resource allocation for hybrid vlc/rf networks with common backhaul," *IEEE Transactions on Cognitive Communications and Networking*, vol. 6, no. 1, pp. 352–365, 2020.

[159] X. Zhang and M. Haenggi, "The performance of successive interference cancellation in random wireless networks," *IEEE Trans. on Inform. Theory*, vol. 60, no. 10, pp. 6368–6388, Jul. 2014.

[160] Z. Zeng *et al.*, "Angle diversity receiver in LiFi cellular networks," in *Proc. IEEE ICC Workshops*, Shanghai, China, May. 2019.

[161] M. D. Soltani, M. A. Arfaoui, I. Tavakkolnia, A. Ghrayeb, M. Safari, C. M. Assi, M. O. Hasna, and H. Haas, "Bidirectional optical spatial modulation for mobile users: Toward a practical design for lifi systems," *IEEE Journal on Selected Areas in Communications*, vol. 37, no. 9, pp. 2069–2086, Aug. 2019.

[162] R. C. Kizilirmak, C. R. Rowell, and M. Uysal, "Non-orthogonal multiple access (NOMA) for indoor visible light communications," in *Proc. IEEE IWOW*, Istanbul, Turkey, Sep. 2015.

[163] Y. Yapıcı and I. Güvenç, "NOMA for VLC downlink transmission with random receiver orientation," *IEEE Trans. Communications*, vol. 67, no. 8, pp. 5558–5573, Apr. 2019.

[164] S. Naser, P. C. Sofotasios, L. Bariah, W. Jaafar, S. Muhaidat, M. Al-Qutayri, and O. A. Dobre, "Rate-splitting multiple access: Unifying noma and sdma in miso vlc channels," *IEEE Open Journal of Vehicular Technology*, vol. 1, pp. 393–413, 2020.

[165] M. Obeed, H. Dahrouj, A. M. Salhab, S. A. Zummo, and M.-S. Alouini, "User pairing, link selection and power allocation for cooperative NOMA hybrid VLC/RF systems," *IEEE Trans. on Wireless Commun.*, vol. 20, no. 3, Nov. 2020.

[166] H. Haas, "High-speed wireless networking using visible light," *Spie Newsroom*, vol. 1, no. 1, pp. 1–3, Apr. 2013.

[167] X. Zhang, Q. Gao, C. Gong, and Z. Xu, "User grouping and power allocation for NOMA visible light communication multi-cell networks," *IEEE commun. letters*, vol. 21, no. 4, pp. 777–780, Dec. 2016.

[168] M. Obeed, H. Dahrouj, A. M. Salhab, A. Chaaban, S. A. Zummo, and M.-S. Alouini, "Power allocation and link selection for multicell cooperative NOMA hybrid VLC/RF systems," *IEEE Commun. Letters*, Oct. 2020.

[169] H. Yang *et al.*, "Coordinated resource allocation-based integrated visible light communication and positioning systems for indoor iot," *IEEE Trans. Wireless Commun.*, vol. 19, no. 7, pp. 4671–4684, 2020.

[170] H. Ma, L. Lampe, and S. Hranilovic, "Integration of indoor visible light and power line communication systems," in *Proc. IEEE ISPLC*, Johannesburg, South Africa, Mar. 2013.

[171] T. V. Pham, H. Le Minh, and A. T. Pham, "Multi-cell VLC: Multi-user downlink capacity with coordinated precoding," in *Proc. ICC Workshops*. Paris, France: IEEE, May 2017.

[172] M. S. Ali, E. Hossain, A. Al-Dweik, and D. I. Kim, "Downlink power allocation for comp-noma in multi-cell networks," *IEEE Transactions on Communications*, vol. 66, no. 9, pp. 3982–3998, 2018.

[173] M. Elhattab, M.-A. Arfaoui, and C. Assi, "Comp transmission in downlink noma-based heterogeneous cloud radio access networks," *IEEE Transactions on Communications*, vol. 68, no. 12, pp. 7779–7794, 2020.

[174] M. Elhattab, M. A. Arfaoui, and C. Assi, "A joint comp c-noma for enhanced cellular system performance," *IEEE Communications Letters*, vol. 24, no. 9, pp. 1919–1923, 2020.

[175] V. S. Rajput, D. Ashok, and A. Chockalingam, "Joint noma transmission in indoor multi-cell vlc networks," in *2019 IEEE 30th Annual International Symposium on Personal, Indoor and Mobile Radio Communications (PIMRC)*.   IEEE, 2019, pp. 1–6.

[176] S. Tech, "Narrow vs Wide Angle LEDs, What's the difference?"   [Online]. Available: https://www.signal-tech.com/information-center/news-and-articles/ 83-Narrow-vs-Wide-Angle-LEDs-Whats-the-difference, Aug. 2020.

[177] S. Alfattani, "Review of lifi technology and its future applications," *Journal of Optical Communications*, vol. 42, no. 1, pp. 121–132, 2021.

[178] T. V. Pham, H. Le-Minh, and A. T. Pham, "Multi-user visible light communication broadcast channels with zero-forcing precoding," *IEEE Trans. on Commun.*, vol. 65, no. 6, pp. 2509–2521, Apr. 2017.

[179] R. Jiao and L. Dai, "On the max-min fairness of beamspace mimo-noma," *IEEE Transactions on Signal Processing*, vol. 68, pp. 4919–4932, 2020.

[180] R. Jiao, L. Dai, W. Wang, F. Lyu, N. Cheng, and X. Shen, "Max-min fairness for beamspace mimo-noma: From single-beam to multi-beam," *IEEE Transactions on Wireless Communications*, 2021.

[181] S. Timotheou and I. Krikidis, "Fairness for non-orthogonal multiple access in 5g systems," *IEEE signal processing letters*, vol. 22, no. 10, pp. 1647–1651, 2015.

[182] M. F. Hanif *et al.*, "A minorization-maximization method for optimizing sum rate in the downlink of non-orthogonal multiple access systems," *IEEE Transactions on Signal Processing*, vol. 64, no. 1, pp. 76–88, 2015.

[183] Q. Zhang, Q. Li, and J. Qin, "Robust beamforming for nonorthogonal multiple-access systems in miso channels," *IEEE Transactions on Vehicular Technology*, vol. 65, no. 12, pp. 10 231–10 236, 2016.

[184] Z. Wang, D. Tsonev, S. Videv, and H. Haas, "On the design of a solar-panel receiver for optical wireless communications with simultaneous energy harvesting," *IEEE Journal on Selected Areas in Communications*, vol. 33, no. 8, pp. 1612–1623, 2015.

[185] P. D. Diamantoulakis, G. K. Karagiannidis, and Z. Ding, "Simultaneous lightwave information and power transfer (slipt)," *IEEE Transactions on Green Communications and Networking*, vol. 2, no. 3, pp. 764–773, 2018.

[186] C. Li, W. Jia, Q. Tao, and M. Sun, "Solar cell phone charger performance in indoor environment," in *2011 IEEE 37th Annual Northeast Bioengineering Conference (NEBEC)*. IEEE, 2011, pp. 1–2.

[187] Y. Xiao, P. D. Diamantoulakis, Z. Fang, Z. Ma, L. Hao, and G. K. Karagiannidis, "Hybrid lightwave/rf cooperative noma networks," *IEEE Transactions on Wireless Communications*, vol. 19, no. 2, pp. 1154–1166, 2019.

[188] S. Feng, R. Zhang, W. Xu, and L. Hanzo, "Multiple access design for ultra-dense vlc networks: Orthogonal vs non-orthogonal," *IEEE Transactions on Communications*, vol. 67, no. 3, pp. 2218–2232, 2018.

[189] Y. Mao, E. Piovano, and B. Clerckx, "Rate-splitting multiple access for overloaded cellular internet of things," *IEEE Transactions on Communications*, 2021.

[190] T. Han and K. Kobayashi, "A new achievable rate region for the interference channel," *IEEE transactions on information theory*, vol. 27, no. 1, pp. 49–60, 1981.

[191] B. Clerckx, H. Joudeh, C. Hao, M. Dai, and B. Rassouli, "Rate splitting for mimo wireless networks: A promising phy-layer strategy for lte evolution," *IEEE Communications Magazine*, vol. 54, no. 5, pp. 98–105, 2016.

[192] M. Dai, B. Clerckx, D. Gesbert, and G. Caire, "A rate splitting strategy for massive mimo with imperfect csit," *IEEE Transactions on Wireless Communications*, vol. 15, no. 7, pp. 4611–4624, 2016.

[193] H. Joudeh and B. Clerckx, "Robust transmission in downlink multiuser miso systems: A rate-splitting approach," *IEEE Transactions on Signal Processing*, vol. 64, no. 23, pp. 6227–6242, 2016.

[194] Y. Mao, B. Clerckx, and V. O. Li, "Rate-splitting multiple access for downlink communication systems: bridging, generalizing, and outperforming sdma and noma," *EURASIP journal on wireless communications and networking*, vol. 2018, no. 1, pp. 1–54, 2018.

[195] S. Ma, H. Zhou, Y. Mao, X. Liu, Y. Wu, B. Clerckx, Y. Wang, and S. Li, "Robust beamforming design for rate splitting multiple access-aided miso visible light communications," *arXiv preprint arXiv:2108.07014*, 2021.

[196] S. Tao, H. Yu, Q. Li, Y. Tang, and D. Zhang, "One-layer rate-splitting multiple access with benefits over power-domain noma in indoor multi-cell visible light communication networks," in *2020 IEEE International Conference on Communications Workshops (ICC Workshops)*. IEEE, 2020, pp. 1–7.

[197] S. A. Naser, P. C. Sofotasios, S. Muhaidat, and M. Al-Qutayri, "Rate-splitting multiple access for indoor visible light communication networks," in *2021 IEEE Wireless Communications and Networking Conference Workshops (WCNCW)*. IEEE, 2021, pp. 1–7.

[198] F. Xing, S. He, V. C. Leung, and H. Yin, "Energy efficiency optimization for rate-splitting multiple access-based indoor visible light communication networks," *IEEE Journal on Selected Areas in Communications*, vol. 40, no. 5, pp. 1706–1720, 2022.

[199] A.-M. Căilean and M. Dimian, "Current challenges for visible light communications usage in vehicle applications: A survey," *IEEE Commun. Surveys & Tutorials*, vol. 19, no. 4, pp. 2681–2703, May. 2017.

[200] A. Ndjiongue and H. C. Ferreira, "An overview of outdoor visible light communications," *Trans. on Emerging Telecommunications Technologies*, vol. 29, no. 7, pp. 1–15, Jul. 2018.

[201] J. Wang, Y. Shao, Y. Ge, and R. Yu, "A Survey of Vehicle to Everything (V2X) Testing," *Sensors*, vol. 19, no. 2, p. 334, Jan. 2019.

[202] S. Chen, J. Hu, Y. Shi, Y. Peng, J. Fang, R. Zhao, and L. Zhao, "Vehicle-to-everything (v2x) services supported by LTE-based systems and 5G," *IEEE Commun. Standards Magazine*, vol. 1, no. 2, pp. 70–76, Jul. 2017.

[203] 5GAA, "An assessment of LTE-V2X (PC5) and 802.11p direct communications technologies for improved road safety in the EU," [Online]. Available: http://5gaa. org/wp-content/uploads/2017/12/5GAA-Road-safety-FINAL2017-12-05.pdf, Dec. 2017.

[204] I. Yaqoob, I. A. T. Hashem, Y. Mehmood, A. Gani, S. Mokhtar, and S. Guizani, "Enabling communication technologies for smart cities," *IEEE Commun. Magazine*, vol. 55, no. 1, pp. 112–120, Jan. 2017.

[205] T. H. Do and M. Yoo, "Visible light communication based vehicle positioning using LED street light and rolling shutter CMOS sensors," *Optics Commun.*, vol. 407, pp. 112–126, Jan. 2018.

[206] N. Zhu, Z. Xu, Y. Wang, H. Zhuge, and J. Li, "Handover method in visible light communication between the moving vehicle and multiple LED streetlights," *Inter. J. for Light and Electron Optics*, vol. 125, no. 14, pp. 3540–3544, Jul. 2014.

[207] M. S. Islim, S. Videv, M. Safari, E. Xie, J. J. McKendry, E. Gu, M. D. Dawson, and H. Haas, "The impact of solar irradiance on visible light communications," *J. of Lightwave Technology*, vol. 36, no. 12, pp. 2376–2386, Jun. 2018.

[208] A. G. Glen, L. M. Leemis, and J. H. Drew, "Computing the distribution of the product of two continuous random variables," *J. of Computational statistics & data analysis*, vol. 44, no. 3, pp. 451–464, Jan. 2004.

[209] J. M. Kahn and J. R. Barry, "Wireless infrared communications," *Proc. of the IEEE*, vol. 85, no. 2, pp. 265–298, Feb. 1997.

[210] C.-C. Yeh and J. R. Barry, "Approximate minimum bit-error rate equalization for pulse-amplitude and quadrature-amplitude modulation," in *Proc. IEEE ICC*, Atlanta, GA, USA, Jun. 1998.

[211] C. Bettstetter, H. Hartenstein, and X. Perez-Costa, "Stochastic properties of the random waypoint mobility model," *ACM Wireless Netw.*, vol. 10, no. 5, pp. 555–567, Sep. 2004.

[212] R. F. Fox, I. R. Gatland, R. Roy, and G. Vemuri, "Fast, accurate algorithm for numerical simulation of exponentially correlated colored noise," *Physical review A*, vol. 38, no. 11, p. 5938, Dec. 1988.

[213] G. N. Tavares and A. Petrolino, "On the generation of correlated Gaussian random variates by inverse DFT," *IEEE Trans. Commun.*, vol. 59, no. 1, pp. 45–51, Jan. 2011.

[214] M. Levin, "Generation of a sampled Gaussian time series having a specified correlation function," *IEEE Trans. Inf. Theory*, vol. 6, no. 5, pp. 545–548, Dec. 1960.

[215] G. E. Box *et al.*, *Time series analysis: forecasting and control.* John Wiley & Sons, 2015.